# Edge-perturbations and Strain Effects on the Magnetic Properties of Graphene Nanoribbons.

**Jack P C Baldwin**

Doctor of Philosophy

University of York
Physics

November 2015

# Abstract

Graphene is important in the study of 2D systems and has a number of unique properties and advantages: High charge-carrier mobilities and ballistic transport at room temperature, high structural stability, relativistic properties and a relatively simple production method. The potential of a tunable band-gap in graphene nanoribbons suggests that it could become a leading electrical component. One method that has emerged for modelling nanogaphene systems is the extended tight-binding model with Hubbard-$U$. Within a real-space formalism, this model can be easily and efficiently applied to increasingly more complicated systems, where any number of edge defects, impurities and even patterning can be included, giving a more realistic description. This thesis investigated methods of structurally perturbing the ideal graphene nanoribbon device and probed the spin-dependent properties that arose: Random-edge vacancies, asymmetrical notches, uniaxial strain, magnetic inhomogeneity, chevron ZGNRs and patterned AGNRs. Random edge-vacancies have been used to perturb the electronic conductance in order to introduce the conductance gap observed in experimental results. These studies use the non-interacting tight-binding model, ignoring coulomb interactions. Introducing coulomb interactions within ideal ZGNRs has been shown to intrinsically include a conductance gap without edge-vacancies. The work presented in this thesis investigated the effects of edge-vacancies on the interacting model and demonstrated that, in general, the non-interacting model is insufficient to describe the physics of disordered ZGNRs. Controllable, asymmetric perturbations (i.e., notches and magnetic inhomogeneity) were added to interacting ideal ZGNRs to determine if the spin-dependent properties can be controlled. Asymmetrical perturbations exhibited spin-dependent conductance. In particular, magnetic inhomogeneity showed a transition from semi-conductive to half-metallic, suggesting a possible avenue for spin-filtering in spintronic devices. Finally, bottom-up synthesised GNRs were investigated (chevron ZGNRs and patterned AGNRs) and demonstrated controllable conductance properties and further work involving these systems was presented.

# Contents

# List of Tables

# List of Figures

# Acknowedgments

This thesis would not have been possible without the help and support I have gained over my years (Count them, FIVE!) producing this document.

First I would like thank Dr Yvette Hancock. Without her, this project would not have existed in the first place! I would also like to thank her for her support producing this document, particularly in the last year and a half.

I would like to thank the EPSRC for funding this project and making it all possible.

The thanks also extend to the friends I made during my 9 year sentence at the University of York as well as at the Physics by the Sea summer school.

My thanks go to Brigantes and York Brewery for providing me an income during my last year of my PhD. Without the job you provided me, I could not have afforded to stay in York and finish off my thesis.

To Dr Fair, for supporting me when I was at my lowest and helping me get back on my feet.

I would also like to thank Neil, Chris and Mark, Kaleigh and Jonna, and Andy and Rach for putting up with a house mate like me.

To Ali, for making me smile and keeping me on the right side of sane for the last 6 months.

To Badger and Barley, Who are good dogs?? You are!

Finally, I would like to thank my parents. My Mum and Dad have provided me with so much support, both financially, but more importantly emotionally. I know I have not spent as much time at home as you would like but you can't underestimate how much this thesis is due to you. You were the first to spot when things were going wrong and you supported me throughout.

# Declaration

This thesis has not previously been accepted in substance for any degree and is not being concurrently submitted in candidature for any degree other than Doctor of Philosophy of the University of York. This thesis is the result of my own investigations, except where otherwise stated. Other sources are acknowledged by explicit references.

I hereby give consent for my thesis, if accepted, to be made available for photocopying and for inter-library loan, and for the title and summary to be made available to outside organisations.

A list of publications based on the research in this is thesis is below:

**Baldwin J**, Hancock Y. Effect of asymmetric edge-perturbation and strain on spin-conduction in zigzag graphene nanoribbons. Physica Status Solidi (c). 2014 May;11(5-6):1011-1015. - Chapter 6

**Baldwin J**, Hancock Y. Effect of Random Edge-vacancy Disorder in Zigzag Graphene Nanoribbons. In Preparation. - Chapter 4

Gerates, J, **Baldwin J**, Twarock R, Hancock Y, A proposed method for directed self-assembly of graphene nanoribbons. In Preparation. - Chapter 6. Joint work. Author carried out computational modelling of the devices investigated. In particular, the author calculated band- and conductance- gaps with the generalised tight-binding model.

# Chapter 1

# Introduction

## 1.1 Abstract

Graphene, a single layer of the carbon allotrope graphite, has been demonstrated, both experimentally and theoretically, to have properties of interest to condensed matter theory, and in particular, future device miniaturisation. This literature review gives a general overview of bulk graphene properties before moving on to the focus of this thesis, graphene nanoribbons. This review discusses the mechanisms for gap opening due to quantum confinement in graphene nanoribbons along with the semi-conducting transport observed in both theoretical and experimental results. A brief review into density functional theory and tight-binding methods of modelling graphene nanoribbons is also carried out. Finally, the effects of structural perturbations, in particular, random edge-vacancies, asymmetrical patterning and uniaxial strain are discussed.

## 1.2 Overview

There is a demand for the trend suggested by Moore's Law to continue. This law requires the number of transistors per chip to double every two years [1]. Materials such as silicon, a fundamental material in the electronics industry, cannot keep up with this growing demand for miniaturisation [2] due to the silicon oxide insulating layer inside the transistor losing its insulating behaviour at roughly 5 silicon layers thick, causing a loss of charge [3]. Initially studies showed that ionised Metal-Oxide-Silicon (MOS) transistors lose their transistor properties below 50 nm [4]. The lower limit for silicon devices has been improved to 10nm but there have been significant problems with the cost and reliability of mass production, for example, issues with gate leakage [5].

One possible material for silicon replacement is graphene [6, 7]. Graphene is a single atomic layer of graphite as shown in Figure 1.1. Graphite is a honeycomb carbon lattice structure constructed from a series of hybridised sp-2 bonds, with stacked layers coupled by

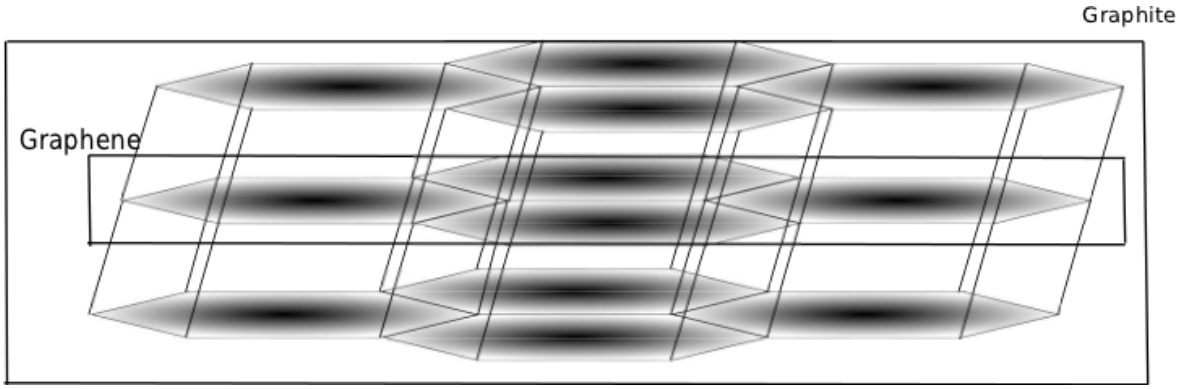


Figure 1.1: Graphene's relationship to graphite. In graphite, each honeycomb layer is sp-2 bonded within the plane of the layers and coupled via Van der Waals forces between layers. Graphene is a single, independent layer of the graphite structure.

Van der Waals forces [8]. In graphene, the sp-2 bonds create very strong and stable covalent bonds in-plane, with a single 2p orbital out of plane. It is this out of plane 2p orbital that gives rise to graphene's properties as will be discussed in Section 1.3.

## 1.3 Properties of Bulk Graphene

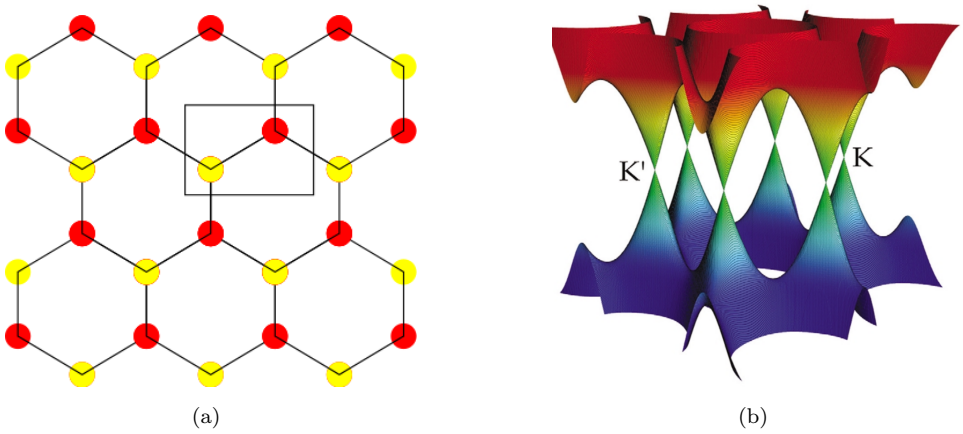


(a) (b)

Figure 1.2: (a) The real-space unit cell of bulk graphene can be described using a two atom basis. The square highlights the unit cell. (b) The 2D band structure of bulk graphene showing the linear dispersion relation between wave vector and energy around two points, $K$ and $K'$, about the Fermi energy. Reproduced from Katsnelson. [9].

The properties of bulk graphene were first formulated using the tight-binding model by Wallace [10] which modelled the electronic structure and assumed a single $2p_z$ conduction electron. The band structure of graphene can be approximated using a unit cell of two carbon atoms as demonstrated in Figure 1.2(a)). This two atom basis is required to fully map the honeycomb structure. As Figure 1.2(b) shows, this honeycomb structure leads to a linear dispersion relation around two points in k-space, $K$ and $K'$, where the valence and the conductance bands meet at the Fermi level [9, 10]. These two non-equivalent points in k-space arise due to the two atom basis [9, 10]. Figure 1.3(a) demonstrates there is also a

direct mapping of the honeycomb structure to the Brillouin zone of this system. This linear dispersion relation has been supported by experimental results, for example, the electron and hole cyclotron masses both have a square root dependence on carrier concentration implying a linear dispersion relation [7, 11]. The square root dependence implies a linear dispersion as the effective cyclotron mass is proportional to $\frac{\partial A}{\partial E_F}$, where $A$ is the area within the Fermi surface, an energy surface within reciprocal space due to the crystal lattice, and $E_F$ is the Fermi energy [12]. $\frac{\partial A}{\partial E_f}$ is proportional to the square root of carrier concentration for massless Dirac fermions [13]. The solution to the tight-binding model for bulk graphene also predicts in a zero-gap semiconductor [10, 14]. This means that the valence and conduction bands meet at a single point at the Fermi level. As Figure 1.3(b) shows, the linear dispersion relation is only valid within ±1eV of the Fermi level [15].

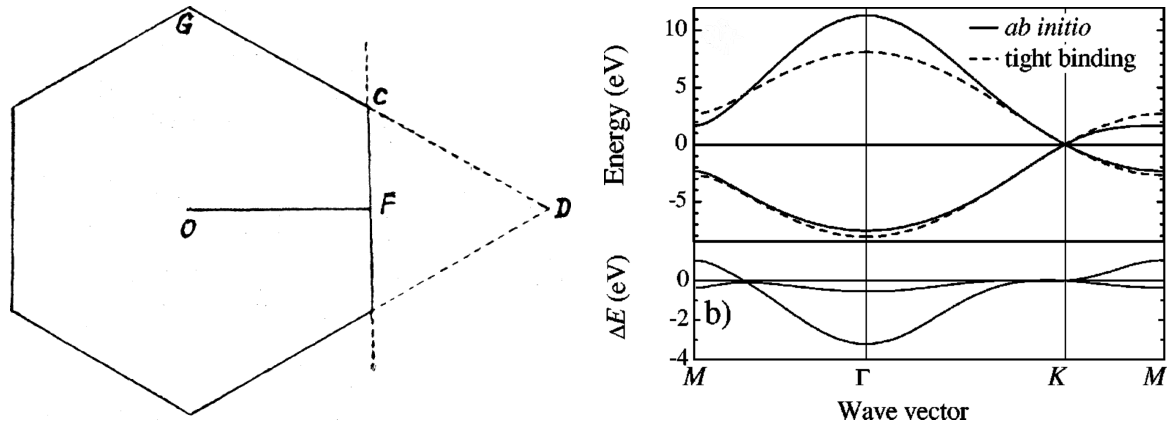


(a) (b)

Figure 1.3: (a) The hexagonal brillouin zone for graphene. Reproduced from Wallace [10]. (b) The 1D band structure of bulk graphene showing the linear dispersion relation between wave vector and energy about the Fermi level. As the image shows, the linear dispersion is only valid within ±1eV of the Fermi level (0eV) at wave vector = K. Also shown, the difference between the simple tight-binding model and *ab initio* Density Functional Theory (DFT) within the local density approximation (LDA) using the SIESTA package [16]. Reproduced from Reich *et al.* [15].

The linear dependence of energy on wave vector suggests that the speed of the electrons is constant and independent of momentum, analogous to the constant speed of photons [17], therefore suggesting the electrons are moving relativistically. The low-energy linear dispersion about $K$ and $K'$ can be recreated using the Dirac equation of quantum mechanics [18, 19]:

$$(\beta mc^2 + \sum_{k=1}^{3} \alpha_k p_k c)\psi(\mathbf{x}, t) = i\hbar \frac{\partial \psi(\mathbf{x}, t)}{\partial t} \tag{1.1}$$

Where $m$ is the rest mass of an electron, $c$ is the speed of light, $p$ is the momentum, $\mathbf{x}$ is the space coordinate, $t$ is the time coordinate and $\hbar = \frac{h}{2\pi}$, where $h$ is the Planck constant [18, 19]. The importance of the Dirac equation is that it describes relativistic particles with spin 1/2 as well as predicting anti-particles [9, 18, 19, 20]. To recreate the zero

gap band structure, massless Dirac fermions are required as normal Dirac fermions lead to a gap equal to $2mc^2$ [9, 18, 19, 20]. The Dirac equation maps onto the linear dispersion and the gapless semiconductor suggesting graphene exhibits relativistic qualities, with the quasi-particle being a massless, Dirac-like fermion [9, 18, 19, 21]. The zero-gap semiconductor nature has been confirmed through graphene-based transport experiments [7, 11] and shows that bulk graphene is still conductive even at extremely low temperatures [22] or in the limit of zero charge carrier concentration [7].

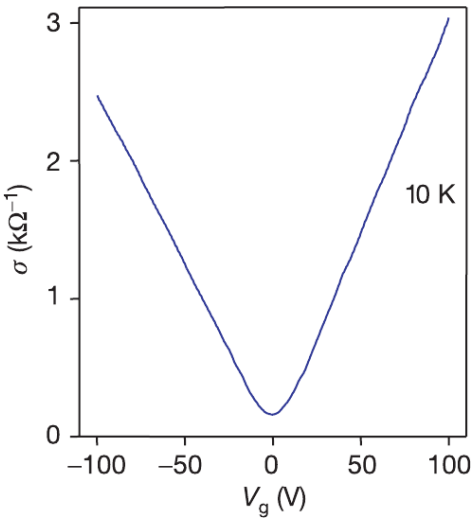


Figure 1.4: Experimental evidence of the non-zero conductance at very low temperatures (10 k). The conductance is $\sim$0.1K $\Omega^{-1}$ at this relatively low temperature. Reproduced from Novoselov *et al* [7]

.

The crystalline structure, and therefore the Dirac-like fermions, gives rise to the particle chirality of graphene [9, 17]. When solving the Dirac equation for graphene the two atoms inside the unit cell must be solved together. The solution to the Hamiltonian of a two atom unit cell is a two component wavefunction where the components gives the weights on the two atoms. The two components in the wavefunction give rise to a pseudospin, an extra degree of freedom due to the two atom basis. These two solutions can be identified by a quantum index which, within the formalism, is similar to the spin index in quantum electrodynamics where site A is pseudospin-up and site B is pseudospin-down.

This peusdospin defines the chirality of the particles. When the peusdospin lies parallel (anti-parallel) to the direction of travel it corresponds to an electron (hole). The transformation between these two states gives the parity and, due to the Dirac nature of these particles, the invariance under parity for this system leads to chiral symmetry [23, 24, 25].

Another important property of graphene, particularly for applications, is its high charge-carrier mobility. The high mobilities together with a high carrier concentration ($10^{11} - 10^{13} cm^{-2}$ [7]) provide evidence for the existence of ballistic transport in graphene on the submicrometre scale at room temperatures [6, 26, 27]. Ballistic transport is an important

effect as it suggests that the only resistance occurring in graphene devices is from the lead-device contacts; this has been confirmed experimentally at very low temperatures on a $1\mu$ m length scale (Figure 1.4) [7, 28, 29, 30].

## 1.4 Properties of Nanographene

The band-gap of graphene can be opened and then tuned when the material is produced as a nanoribbon [29, 31, 32]. A graphene nanoribbon (GNR) is a graphene sample that is finite in one direction and bulk-like in the other. Figure 1.5 demonstrates that the direction of the finite dimension gives rise to two distinct types of nanoribbon, zig-zag graphene nanoribbon (ZGNR) and armchair graphene nanoribbon (AGNR).

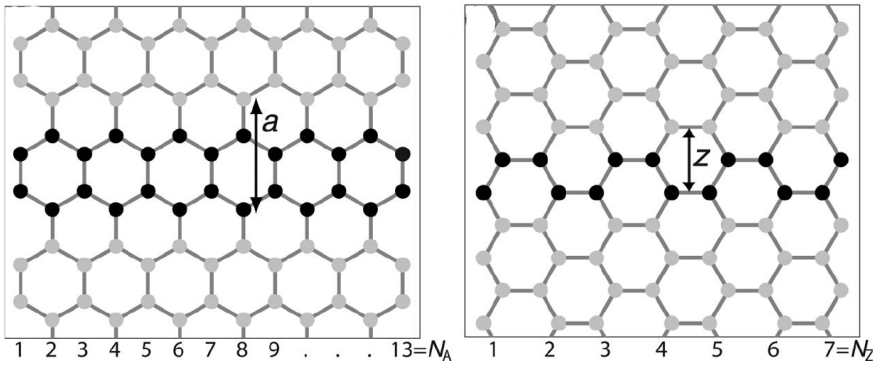


(a) 13-AGNR (b) 7-ZGNR

Figure 1.5: The two distinct edge-structures of a graphene nanoribbon. (a) 13-AGNR (armchair graphene nanoribbon), (b) 7-ZGNR (zig-zag graphene nanoribbon). The unit cell distance and ribbon width are represented by $a$, $N_A$ and $z$, $N_Z$ for an AGNR and ZGNR, respectively [32, 33]. The symbol $N$ in each case give a classification of the GNRs, with $N$ being the number of dimer lines crossed or zig-zag chains across the ribbon for AGNR and ZGNR, respectively. These systems are examples of the ideal unit cell defined in this investigation as the smallest possible unit cell to describe a perfect ribbon. Reproduced from Hancock *el al* [33].

The width of a zig-zag and armchair GNR can be described using the following convention. $N_A$-AGNR describes an armchair ribbon with a width of $N_A$, where $N_A$ is defined as the number of dimer lines that are crossed along the width of the ribbon. $N_Z$-ZGNR describes a zig-zag ribbon with a width of $N_Z$, with $N_Z$ defined as the number of zig-zag chains across the ribbon width [33]. Figure 1.5 demonstrates the ideal unit cell for both AGNR and ZGNR. In this work an extra variable, $U_{a(z)}$, is included to describe the size of the unit cell for AGNR(ZGNR). The variable $U_{a(z)}$ describes the number of ideal unit cells used to approximate the total system. AGNR systems are defined as $U_a$-$N_A$-AGNR and ZGNR systems as $U_z$-$N_z$-ZGNR such that the full GNRs (including bold and grey sites) in Figure 1.5 can be described as 3-13-AGNR (Figure 1.5(a)) and 5-7-ZGNR (Figure 1.5(b)).

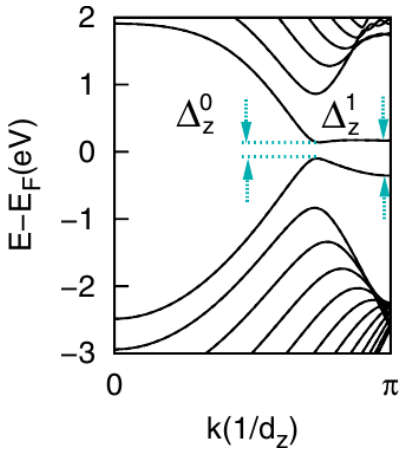


(a) 12-ZGNR band structure

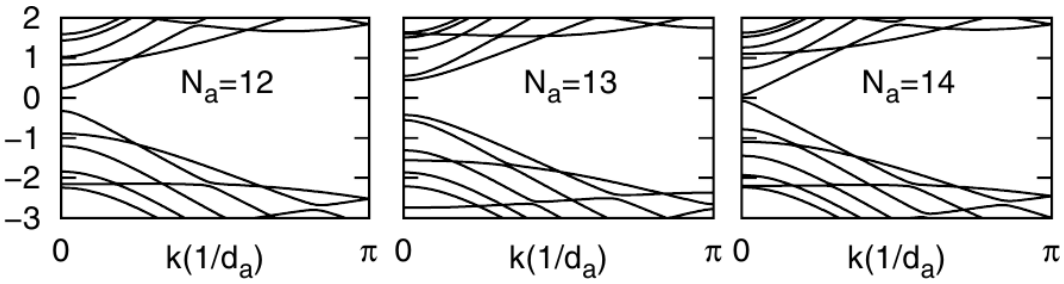


(b) Three trends of AGNR band structure

Figure 1.6: Comparison between the band structures of two types of edge-structure, (a) ZGNR and (b) AGNR produced using DFT calculations within the local spin density approximation (LSDA) using the SIESTA package [16, 32]. Three armchair graphs are used to demonstrate the three trends shown in Figure 1.8(a). Figure 1.6(a) includes both the direct ($\Delta_z^0$) and the indirect ($\Delta_z^1$) band-gap. Reproduced from Son *el al.* [32].

### 1.4.1 Models

This thesis shall discuss two methods of modeling these GNRs. The most accurate of the two models used is the density functional theory (DFT) *ab initio* method [34] which attempts to model the system from first principles. DFT uses functionals to represent the density of electrons and calculates the various internal and external potentials using these functionals [34]. One can calculate the functionals using the local spin-density approximation (LSDA). LSDA uses the homogeneous electron model, a model that assumes the positive charge from the nucleus is uniformly distributed throughout the electron gas, to approximate the electron density for both electron spin types at a specific point in space [35]. Another DFT method is the generalised gradient approximation, (GGA) [36, 37]. GGA introduces a density gradient correction into the LSDA approximation [36, 37]. See Ref [37] for a more detailed description into the GGA approximation. These methods all calculate different results for the sizes of the band gaps. Dalosto and Levine [38] calculated the difference in band-gap between LSDA and spin-polarised GGA and found that the LSDA calculates the band-gap to be 1.5 times smaller with respect to the Perdew-Burke-Ernzerhof GGA [38]. In general both methods are extremely accurate but computationally expensive. DFT calculations are therefore limited to

small, ideal systems or small systems containing only a small density of single point defects and impurities due to the small unit cell limitations of the computationally costly DFT.

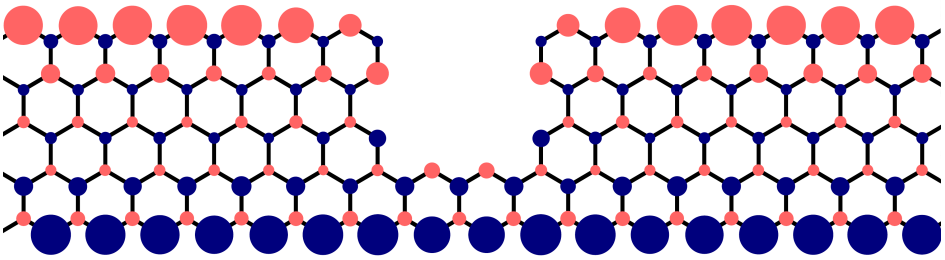

Figure 1.7: Example of a mixed-edge system, which was produced by Hancock *et al.* [33] to test the generalised tight-binding model. Coloured lattice points demonstrate the spin-polarisation. Red gives spin down and blue spin up and the radii is proportional to the degree of spin-localisation.

An alternative method to DFT is the tight-binding model. This model can be solved with a simple matrix solver and thus is extremely efficient computationally. The parameters for the model are obtained by fitting the band-gap and band structure solutions to DFT results. For the parameters, we can use a separate set for ZGNRs and AGNRs, but this is an issue if we have mixed edge structures, for example notches (Figure 1.7). Hancock *et al.* [33] put forward a method that uses a single set of parameters fitted to the band-gap and band structures of both AGNR and ZGNR, allowing systems with different mixes of the two edge types to be simulated. There is an issue with both of these fitting methods as any fundamental errors in the DFT results, when compared to experiments, will be transferred to the tight-binding results. Unfortunately due to the complexity of experimental structures, DFT is still the only method used to find the tight-binding parameters.

### 1.4.2 Band Structure

The properties of graphene nanoribbons are dependent on the edge-structure, which can be seen by comparing the band structures [32, 39, 40] (Figure 1.6). For ZGNRs, the flat bands, and therefore very small electron group velocity, close to the Fermi energy (Figure 1.6(a)) suggests a localised edge-state. AGNR does not have a flat band near the band-gap and thus does not display the same localisation.

In general, the energy band-gaps for both AGNRs and ZGNRs are inversely proportional to the width of the ribbons [29]. Figure 1.8(a) demonstrates that, for the AGNR system, the band-gap results split into three separate trends as a function of the nanoribbon width. The first trend occurs at $N_a = p*3$, the second at $N_a = p*3+1$, and the third at $N_a = p*3+2$, where $p$ is $> 0$ and an integer [32]. Figure 1.8(b) shows that ZGNRs have two key trends, the direct band-gap trend and the indirect edge band-gap trend at $k = \frac{\pi}{a}$. The band-gap trends in Figure 1.8 are from DFT, LSDA calculations using the SIESTA package [16, 32].

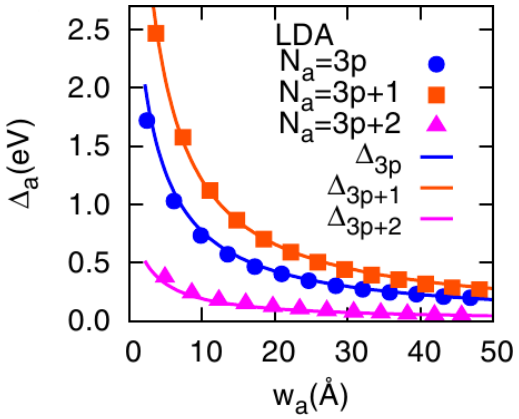


(a) Band-gap vs ribbon width for AGNRs

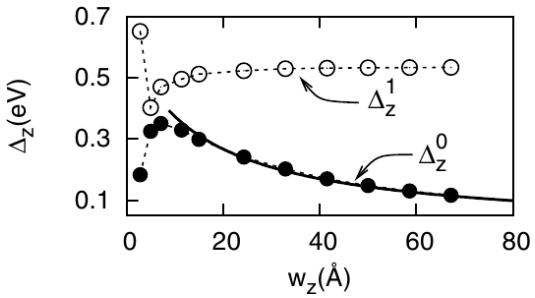


(b) Band-gap vs ribbon width for ZGNRs

Figure 1.8: *Ab initio* calculations for the band-gap vs ribbon width for (a) AGNR, and (b) ZGNR. The two trends shown in (b), $\Delta_z^0$ and $\Delta_z^1$, are for the direct band and the band at $k = \frac{\pi}{a}$, the band edge, respectively. These calculations were carried out by Son *et al.* using DFT, LSDA calculations using the SIESTA package [16, 32]. Reproduced from Son *et al.* [32].

The band-gap trends are significant as the simple tight-binding model used for bulk systems, using only 1st nearest-neighbour and no Hubbard-$U$, does not recreate DFT results. ZGNRs have semi-metal properties, i.e., conduction and valence bands touch at a single point at the Fermi energy, when described using the simple tight-binding model [40, 42, 43]. Son *et al.* [32] demonstrated this by comparing the simple tight-binding model with *ab inito* DFT LSDA calculations using the SIESTA package [16] for AGNRs. They reported that the gap vs width trends predicted by DFT were not found. Instead two trends, both as a function of ribbon width, were seen, one inverse trend and one semi-metal trend, Figure 1.9(a). The two trends as a function of ribbon width within AGNRs is significant as a number of authors base their predictions on this nearest neighbour tight-binding model [40, 42, 43, 44, 45]. White *et al.* [46] first demonstrated that single-electron interactions across the ribbon, i.e., 3rd nearest-neighbour interactions, contribute significantly and will open the semi-metal gap seen in the simple tight-binding model [46]. Gunlycke and White [41] demonstrated that edge distortions would also affect the band-gap and would increase the agreement between the extended tight-binding model and DFT results [41]. In both of these papers, 2nd nearest-neighbour interactions were ignored. The effect from the third nearest-neighbour hopping was also demonstrated by Reich *et al.* [15], however, this paper focused on nanotubes. Yamashiro

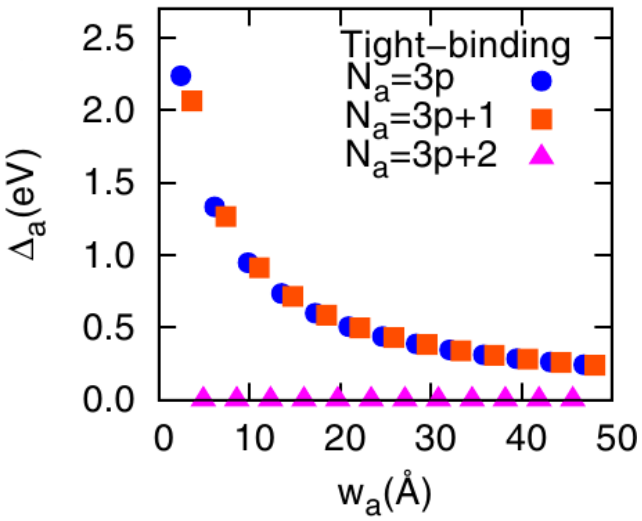


(a) Band-gap vs ribbon width for AGNRs, 1st nearest-neighbour hopping only

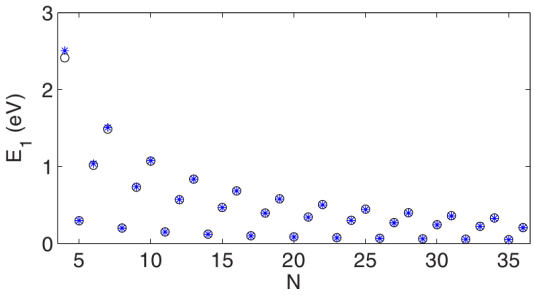


(b) Band-gap vs ribbon width for AGNRs , up to 3rd nearest-neighbour hopping

Figure 1.9: (a) The three shapes, triangle, square and circle, demonstrate the three trends predicted for AGNR. Image reproduced from Son *et al.* [32]. (b) Analytical tight-binding results for the extended model (stars) compared to numerical first principle local-density-functional (LDF) results (circles). Image reproduced from Gunlycke and White [41]. Included as a comparison between a simple tight-binding model and the extended tight-binding model with up to 3rd nearest-neighbour hopping.

*et al.* [47] were able to demonstrate the effects of the Hubbard-$U$ term, i.e., the electron-electron interaction term, on the electronic structure of ZGNRs. This paper did not look at the effects of the Hubbard-$U$ on band-gap but was however able to to show that the Hubbard-$U$ term could be applicable to ZGNRs. Fernández-Rossier [48] demonstrated that the Hubbard-$U$ term opens the semi-metal band-structure predicted by the simplified tight-binding model. This is in agreement with DFT LSDA results [32]. In Figure 1.10, work by Hancock *et al.* [33] demonstrates these effects by introducing the Hubbard-$U$ term and the extended hopping parameters and comparing the results with DFT LSDA results produced using the SIESTA package [16]. As Figure 1.10 shows, introducing the Hubbard-$U$ has no effect on the AGNR system however it opens the gap in ZGNR. The 2nd nearest-neighbour hopping has a small effect on the band structure of AGNR. The noticeable effect of the 2nd nearest-neighbour hopping is the breaking of the symmetry seen in the band structure of the AGNR. Finally the 3rd nearest-neighbour hopping term opens the semi-metal gap seen

in AGNRs. Hancock *et al.* uses the same tight-binding parameters for both ZGNR and AGNR [33].

The band-gap predictions using the LSDA DFT have yet to be shown experimentally in any great detail and as of yet there has only been a single inverse dependence found [29, 31]. Another issue with these band-gaps is that, when compared to experimental results of exfoliated samples, the theoretical results are an order of magnitude too small [29]. This suggests missing physics in even the most fundamental models, for example *ab initio* DFT calculations.

The method laid out by Han *et al.* [29] involves using a mask to protect the ribbon area before using an oxygen plasma to etch away the unwanted areas. The widths investigated ranged from 10-100nm and the ribbons were 1-2 $\mu$m long. Using this method there is a relatively large error when attempting to produce widths of specific sizes. Han *et al.* report errors in the etched samples to be between 8%-17%.

The band-gaps found using chemically derived nanographene agree with theory [31]. The chemical synthesis method involves exfoliating the material by heating it for 60s to $1000°C$ in a forming gas of 3% hydrogen in argon. The exfoliated graphite is then dispersed in a 1,2-dichloroethane solution of poly(m-phenylenevinylene-co-2,5-dioctoxy-p-phenylenevinylene) (PmPV) by sonication for 30 min [31]. Li *et al.* were able to produce ultrasmooth GNRs smaller than 10nm [31]. Figure 1.12 demonstrates that the trend found by Li *et al.* agrees with the Son *et al.* [32] predictions to a good approximation. The samples tested by Li *et al.* fall around the four trends predicted by Son *et al.*, the three for AGNR and the single trend for the direct band-gap in ZGNR. The samples produced by Li *et al.* were characterised using transmission electron microscopy, electron diffraction and Raman spectroscopy and were reported to be of very good quality, especially when compared to the roughness of the exfoliated ribbons. The precise edge type of each of the samples were unknown to the group and as such the trend for ZGNR could not be separated from the one for AGNR [31]. The fact chemically derived nanographene agrees more directly with theory compared to exfoliated graphene may be due to the method of synthesis, I.E., bottom up compared to top down, and due to the quality of the nanographene edges.

Although magnetisation has been theoretically predicted in the case of ZGNRs [32, 49], there is an issue with its experimental confirmation due to the sensitivity of the magnetisation on the structural quality of the GNR sample, its purity and the edge structure [50].

### 1.4.3 Transport

As discussed in Section 1.3, bulk graphene demonstrates ballistic transport. This can be modeled with the Landauer-Büttiker (LB) formalism [51]. This formalism was developed for mesocopic systems and assumes ballistic, coherent transport. Mesoscopic systems are larger

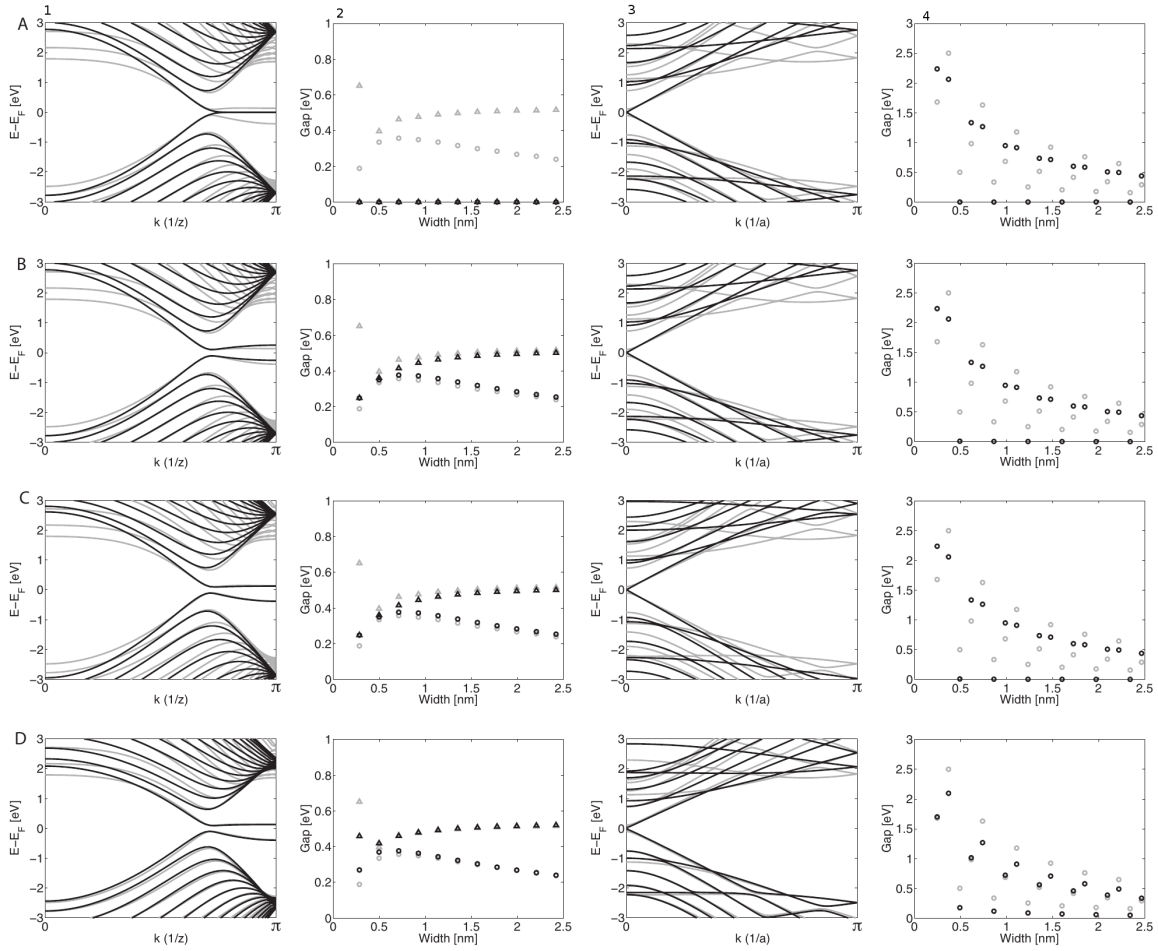


Figure 1.10: Columns: 1, 16-ZGNR band structure. 2, ZGNR band-gap trend. Circles for direct band-gap, triangles for the band -gap at the band edge. 3, 14-AGNR band structure. 4, ZGNR band-gap trend. For all graphs black gives tight-binding results and grey gives DFT LSDA results produced using the SIESTA package [16]. Rows: A, Simple tight-binding model only. B, Simple tight-binding model with Hubbard-$U$. C, Extended tight-binding model with up to 2nd nearest-neighbour with Hubbard-$U$. D, Full extended tight-binding model with Hubbard-$U$. Reproduced from Hancock *et al.* [33]

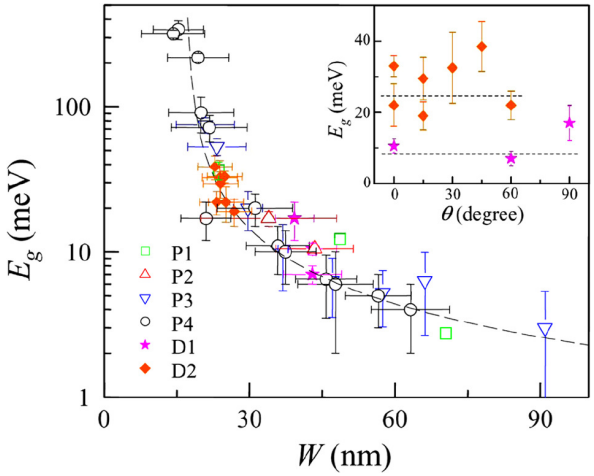


Figure 1.11: Experimental results produced by Han *et al.* demonstrating a single dependence of band-gap on width observed for these GNR systems. The six systems tested are detailed in ref [29], P 1-4 are parallel ribbons and D1 and D2 are ribbons with varying orientations relative to the parallel ribbons. There should be a periodic dependence of the energy gap on the orientation for GNRs with similar edge-structures. This periodic dependence is not observed suggesting it is not possible to control the edge-type with this production method yet [29]. Reproduced from Han *et al.* [29]

then the microscopic atomic systems but incorporate deviations from Ohm's law [51].

Areshkin *et al.* [52] used the simple tight-binding model to show that substrate induced disorder would not affect the predicted ballistic transport properties in AGNRS due to their narrow widths leading to energetically isolated bands at the Fermi energy. Edge-disorder, for example edge-vacancies or edge-impurities, would break the ballistic properties in AGNR systems [52].

Li *et al.* [31] measured the conductivity and whilst they did not find values consistent with ballistic transport they did get values larger than traditional semiconductors [31]. This could be due to the chemically derived graphene ribbon.

DFT calculations using GGA with the SIESTA [16] package by Dubois *et al.* [53] and experimental results by Molitor *et al.* [54] have been used to find zero transport resulting from the band-gap predicted for these GNRs [29, 32], Figure 1.13. The system calculated by Dubois *et al.*, 35-AGNR, would demonstrate a semi-metal band structure if modeled with the simple tight-binding model, highlighting the limitation of the simplified model. Kim and Kim [55] also uses DFT calculations to demonstrate the zero conductance in ZGNR ribbons using the non-equilibrium Greens function method, see ref [55] for more details. They suggest that either LSDA or GGA can be used but do not go into detail.

Figure 1.14 demonstrates further work by Dubois *et al.* [53] showing a zero conduction-gap in the transport results for ZGNR DFT GGA calculations. These results qualitatively agree with experimental results demonstrating a band-gap [29, 31] and zero conductance [54] but it must be noted that the experimental results include a voltage bias not included in the study by Dubois *et al.* [53].

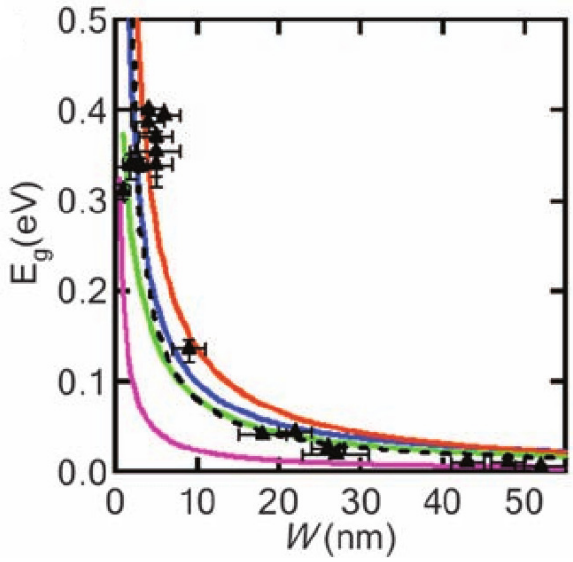


Figure 1.12: Experimental results produced by Li *et al.* [31] The image shows a single dependence observed for these GNR systems as the group were unable to determine the edge structure of their devices [31]. The black symbols give the experimental data [31], the four bold lines are the results predicted by Son *et al.* [32] and the dotted line is fitted to the experimental results, where $E_g = \frac{0.8}{W}$. The Son *et al.* results are, from the left to the right, 3p+2 AGNR, ZGNR, 3p AGNR, and 3p+1 AGNR, respectively where p is an integer and is used to define the AGNR trends. Reproduced from Li *et al.* [31].

### 1.4.4 Random Edge-Defects

Cresti *et al.* [56] carried out a review on the effects of edge-disorder, for example edge-vacancies and edge-impurities, on transport but, even though they showed 3rd nearest-neighbour hopping has an effect on the band-gaps of AGNR and mention the opening of the ZGNR gap using spin-polarisation, they did not use the extended model for their transport measurements. This is a common practice in the literature for GNR transport investigations [44, 56, 57, 58, 59]. Many researchers apply Anderson localisation [52, 57, 60, 61, 62, 63, 64, 65, 66, 67, 68], to these systems. Anderson localisation applies to metallic systems and uses random defects and impurities to cause a strong localisation of electrons [69]. This strong localisation leads to a metallic/insulator transition. These papers suggest Anderson localisation could be the cause of the zero conductance and band-gap in experimental results [29, 31, 52, 57, 62, 63, 64, 65, 66, 67, 68]. This ignores evidence that shows that the extended hopping terms and Coulomb repulsion [32, 33, 46] will open the semi-metal gap without the need of this Anderson localisation.

Huang *et al.* [50] have demonstrated using LSDA DFT VASP calculations [70] that removing atoms along the edge of a ZGNR system would reduce the edge-polarisation and thus edge-magnetisation (Figure 1.15) until the system becomes paramagnetic at 33.33% edge-vacancy concentration. This investigation is limited by the computational cost of *ab initio* calculations and is thus restricted to small systems with systematic defects. A more realistic system would introduce random defects and use a large sample of systems for ensemble

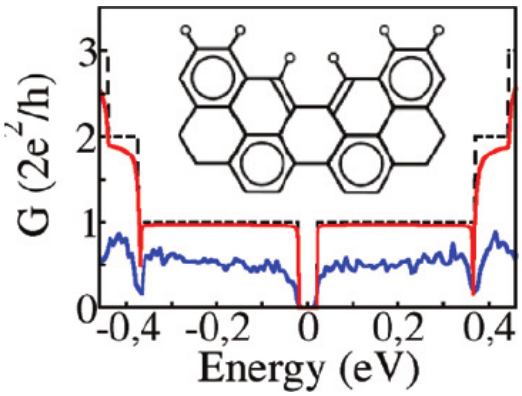


(a) Dubois *et al.* [53]

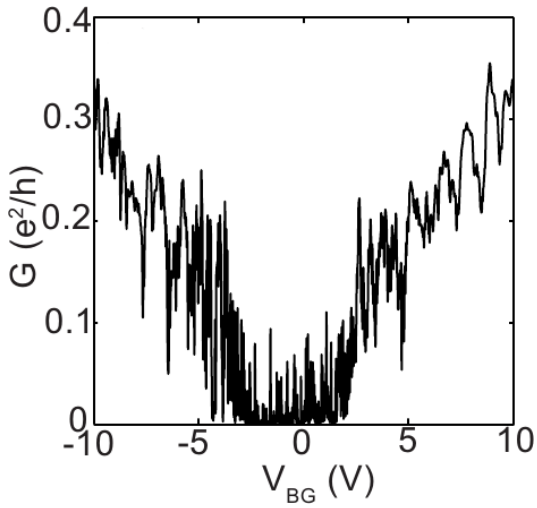


(b) Molitor *et al.* [54]

Figure 1.13: Comparison between DFT GGA results and experimental results for electronic transport of GNR devices. (a) Produced using DFT calculations with GGA using the SIESTA package [16] to model a 35-AGNR. The dotted black line gives the perfect ribbon, red gives a single defect, i.e., the removal of a two atoms, and blue gives average conductance for a 500 nm long AGNR with 30 defects. The insert demonstrates the edge structure. Reproduced from Dubois *et al.* [53]. (b) Produced using experimental techniques. Dimensions for the experimental system were, W=85 nm and L=500 nm, a bias voltage of 300 $\mu$V was used. There is a lot of noise inside the gap but by tuning the voltage bias [54] (i.e., controlling the electrical charge at the gate of the device) this noise can be reduced and an accurate gap found. Reproduced from Molitor *et al.* [54]. The experimental and the defected theoretical results have a qualitative agreement of the main features.

averaging. This approach requires a less computationally expensive model, for example, the extended, interacting tight-binding model. Random edge-defects are of particular interest due to current production methods, as it is extremely difficult to produce perfect edge structures using top-down methods [29, 71, 72].

Modelling such edge-defects in realistic systems requires a fast and accurate description of the properties of nanographene that is not restricted to a specific type of GNR. For this reason, a more generalised theoretical approach is required to introduce more realistic effects and thus produce more accurate predictions. Due to the large cells required for realistic edge-defects, for example edge-vacancies and edge-disorder, a computationally efficient model is

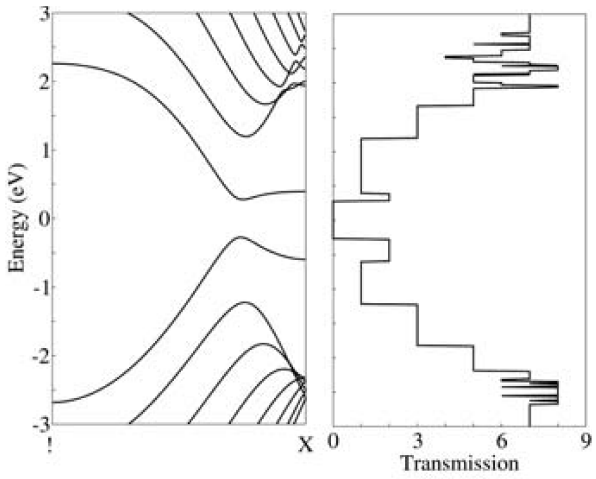


Figure 1.14: Results produced using DFT GGA calculations in the SIESTA package [16]. The ZGNR results are for the anti-ferromagnetic system. Graph demonstrates the conduction-gap in a spin-polarised ZGNR structure. Images reproduced from Dubois *et al.* [53].

also required. Large unit cells are also required to model the effects of "patterning", i.e., the deliberate introduction of notches and defects rather than introducing them randomly though production methods.

Edge-vacancies have also been used to perturb the transport properties [52, 54, 56, 58, 59, 62, 63, 64, 65, 66, 67, 68, 73, 74] with Anderson localisation being linked to the decrease in the overall transport properties [52, 67]. Edge-vacancies are of significance due to the resolution limits of top down methods leading to highly disordered systems [29, 71, 72] particularly when compared to bottom up techniques [31, 75, 76, 77, 78]. Huang *et al.* [50] was able to calculate the formation energies of edge-vacancies in ZGNR graphene samples and showed that the energy required for a defect concentration of $0.10\text{Å}^{-1}$ was accessible at room temperature.

Evaldsson *et al.* [79] assumed for AGNR edge-disordered devices that a conductance of less than $0.01 * 2e^2/h$ was equivalent to zero conductance based on the experimental results of Han *et al.* [29]. This criterion was also later applied to 16-ZGNR devices studied by Cresti and Roche [59]. Areshkin *et al.* [52] studied 64-ZGNR devices of length 1 $\mu$m that had random edge-vacancies, random edge-disorder (implemented by random variations in the on-site atomic energies), and variable bond lengths using the STB model. In these studies, the ballistic conductance of the significantly wide 64-ZGNR systems was determined to be robust even at a large edge-vacancy concentration of 50% and with an "edge" defined as 4 atoms deep. In comparison, Cresti and Roche [59] used the STB model to show that a 16-ZGNR device having a smaller width and length of 500nm exhibited greater sensitivity to the effect of edge-vacancies with significant perturbation to the conductance at only 7.5% edge-vacancy concentration. Specifically they demonstrated that the spin-independent conductance in 16-ZGNR devices would be significantly reduced to below the $0.01 * 2e^2/h$ criterion, thereby generating the appearance of a conductance gap of $\approx 1.75\ eV$ at lengths greater than 470nm.

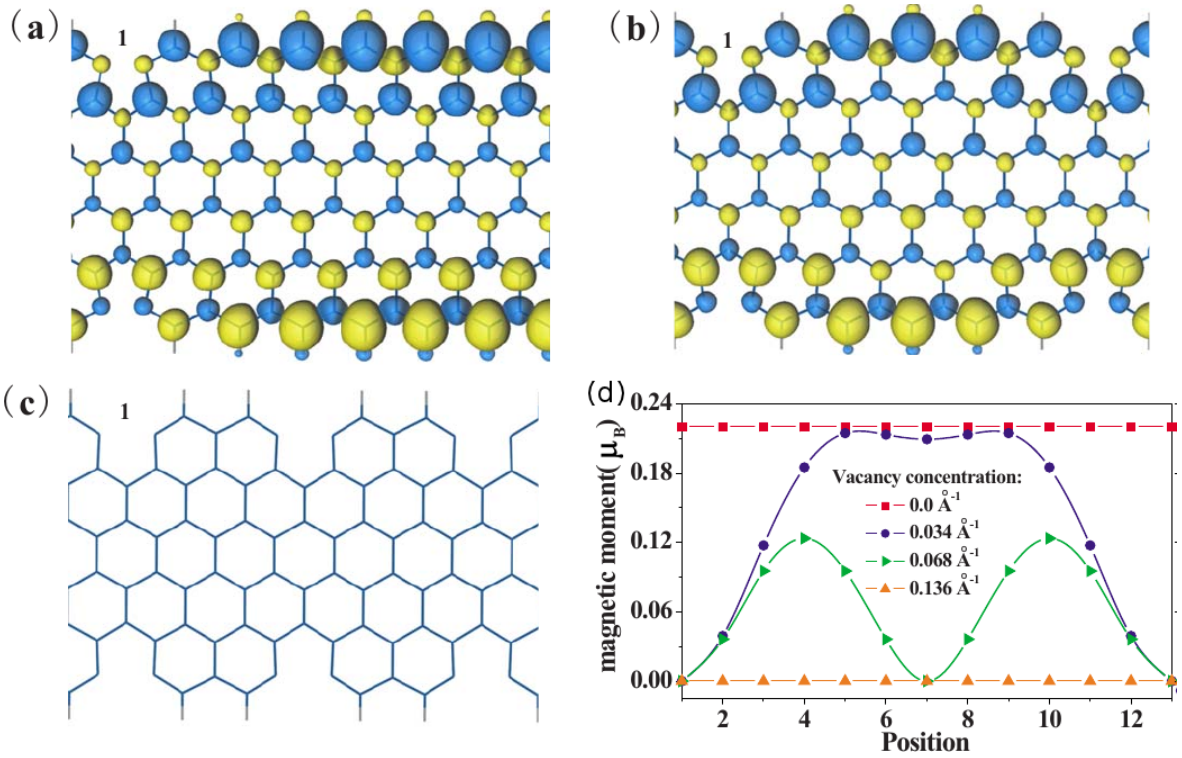


Figure 1.15: Effects of systematic edge-vacancies on the edge-magnetisation of a 12-6-ZGNR system found using DFT LSDA calculations within VASP [70]. (a)-(c): System map demonstrating the decrease in edge-magnetisation as the number of edge-defects increase. (d) Value of the magnetisation at each site along the edge of the system. As vacancies are introduced, the magnetisation around the vacancy decreases. Note, system is periodic such that site 13 is equal to site 1. Adapted from Huang *et al.* [50]

The increased robustness of conduction at increased device width compared to the 16-ZGNR studied by Cresti and Roche [59] has also been demonstrated using the STB model by Haskins *et al.* [64] for a 70-ZGNR system with a length of 100 nm. Li and Lu [62] used the STB model to study ZGNR devices with increasing widths from 5 Å to 55 Å and demonstrated that, for edge-vacancies with one, two or three edge-atoms, the conductance remained unperturbed as a function of the increasing device-width. In comparison, AGNR devices of equivalent widths demonstrated greater relative perturbation to the conductance compared to ZGNRs having same number of edge-vacancies. ZGNRs in this study became immune to edge-vacancy perturbation at widths $> 30$ $\mathring{A}$, thereby providing further evidence of the robustness of ZGNRs against edge-vacancy perturbation.

Mucciolo *et al.* [67] introduced edge-disorder to a 40-ZGNR device with length 45 $nm$ and width of 4.7 $nm$ width that was modelled using the STB model where edge roughness was defined such that $r = (W - \bar{W})P/a_0$, where $\bar{W}$ is the average ribbon width, $W$ is the undefected ribbon width, $P$ is the probability of an edge-vacancy and $a_0$ is the lattice constant. Mucciolo *et al.* [67] found that the conductance of the 40-ZGNR device was robust to small edge-roughness ($r = 0.01$), however, became more sensitive as the edge-roughness increased ($r = 0.50$). At which point, the conductance at the Fermi energy dropped by

approximately four orders of magnitude relative to the undefected device. They were also able to demonstrate the increased sensitivity of the conductance in ZNGRs with 45 $nm$ length on edge-roughness as a function of decreasing ribbon-width with the conductance gap decreasing by half an order of magnitude as the width of the ribbon was increased from $\sim 2.5 - 12$ $nm$.

Saloriutta *et al.* used the TranSIESTA package that employs spin-dependent, non-equilibrium Green's function-density functional theory (NEGF-DFT) within the PBE-GGA [80] to demonstrate that a hydrogen-passivated structural protrusion on the edge of a 12-5-ZGNR device reduced the transport conduction relative for both spin directions. A significant decrease in spin-conduction near the first conductance step within the range of $\pm 1.5$ $eV$ along with a decrease in the conductance spikes either side of the conductance gap was observed. The largest decrease in spin-conduction was close to 100% at $\pm\, 1.4$ $eV$. Saloriutta *et al.* also demonstrated a stability in the conductance gap, with the gap staying the same size independent of the introduction of these protrusions. Such protrusions are relevant to the work in this thesis as these can occur in random edge-vacancy systems having edge-vacancy concentrations greater than 50%.

Molitor *et al.* [54] carried out experimental transport and band gap measurements on etched GNRs. Similar to Han *et al.* [29], the edge-type (AGNR or ZGNR) could not be determined, however, a band gap and conductance gap was measured at all widths. Molitor *et al.* [54] use edge-roughness to explain the presence of the measured gaps, however, this explanation is not in agreement with other experimental studies, for example Li *et al.* [31], who measured a band gap in structurally pristine, chemically derived GNRs. As the GTB model predicts a intrinsic gap [32], edge-vacancies will be incorporated into the GTB model to test the stability of the transport-gap with the introduction of edge-vacancies in Chapter 4.

### 1.4.5 Asymmetric Edge-Perturbations

The transport results for ZGNRs are of particular interest due to the strong localisation and, therefore, spin-polarisation. In an ideal system there is no spin-dependent transport in either ZGNR or AGNR [55, 81], whereas breaking the structural symmetry of the system, with structural perturbations like notches, defects or protrusions, can add spin-dependence into the transport results [33, 74, 82, 83, 84]. Figure 1.16 demonstrates this spin-dependent transport in two different ZGNR systems through the addition of a notch [82]. Hancock *et al.* [82] modeled a 21-16-ZGNR system, a system large enough such that, at the time, the computational cost for DFT would be high, Figure 1.16(a) [82]. The extended tight-binding model was used to calculate the transport properties and show a large spin-dependent channel. This is due to spin-down being suppressed by the notch and thus removing the available

channel, Figure 1.16(b) [82]. This is of particular interest for spintronic devices as it may allow the "turning off" of a particular spin channel.

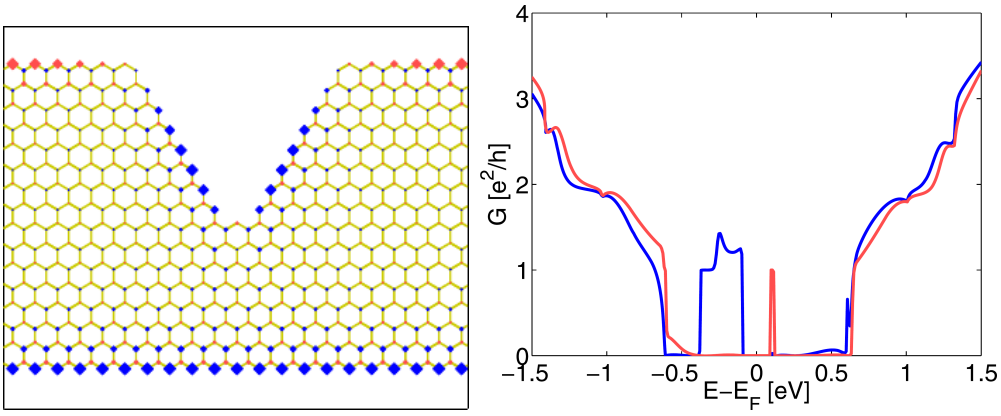


(a) (b)

Figure 1.16: Demonstration of "turning off" a spin by the addition of a large notch. (a) System map of the notched 21-16-ZGNR system. Blue(red) gives spin up(down) and the radii gives the relative magnitude of the spin-polarisation. (b) The spin dependent transport. Blue give spin up and red gives spin down. As we can see the spin down conductance is suppressed by the notch. System was calculated using the generalised tight-binding model. The Hubbard-$U$ term is included leading to spin-polarisation. Images reproduced from Hancock *et al.* [82]

Asymmetric magnetic impurities can be introduced the GTB model though perturbing the Hubbard-$U$ value relative to the value for carbon in the ZGNR devices, 2.0eV [82]. These magnetic impurities have been studied in bulk graphene by Hu *et al.* [85] using quantum Monte Carlo methods within the STB model. Yang et. al. [86] introduced pertubations to the Hubbard-U value in bulk graphene via proximity effect to a metallic substrate and determined an opening of the band-gap. Pedersen and Pedersen [87] introduced B and N doping into a self-consistent TB model for bulk graphene and determined that a variable Hubbard-U can be used to describe these impurities.

Power *et. al.* [88] used both the 1st nearest neighbour Hubbard model along with DFT, GGA calculations within the SIESTA program to investigate the introduction of single magnetic impurities into ZGNR and AGNR devices. Power *et. al.* [88] determined good agreement between DFT and using the 1st nearest neighbour Hubbard model for a Mn impurity. Power *et. al.* [88] assume that the only non-zero value of $U$ in the device is for the transition metal impurity. This assumption would lead to zero magnetic properties when applied to a ZGNR graphene device without impurities. Krychowski *et. al.* [89] carried out DFT, GGA calculations within the VASP program for a single Co adatom in 4-ZGNR. The Co adatom in this investigation is placed on a ''hollow site", i.e., in the middle of a hexagonal ring of carbon. Mao *et. al.* [90] introduced K adatoms at various concentrations using GGA-PBE DFT calculations within the VASP program to 8-ZGNR and found that, 1.56% adatom concentration, the device becomes FM instead of AFM. Zhang *et. al.* [91] introduces regular Fe adatoms to the ''hollow site" both at the edge and in the middle of a 4-ZGNR device.

GGA-PBE DFT calculations are carried out using the atomistix toolkit (ATK). For regular Fe atoms along the edge ''hollow sites", there is a decrease in the magnetic moment near to the Fe adatom, and the introduction of a spin-dependent transport gap.

Chevron GNRs result from self-assembly bottom-up fabrication methods that use small precursor molecules to construct atomically clean graphene ribbons [78, 92]. 6'11-dibromo-1,2,3,4-tetraphenyltriphenylene is double annealed on a Au(111) substrate and produces chevron AGNR samples with alternating N=6 and N=9 widths [78]. These chevron samples have been investigated using both DFT [93, 94, 95] and TB methods [96], with the AGNR edged chevron being the focus of most studies [78, 92, 94, 96].

Wang and Wang [94] used DFT, LDA methods to investigate optical properties of AGNR chevron graphene nanoribbons (CAGNR), and found that there was an overall increase in the band gap of the chevron GNR compared to the ideal GNR. Fa and Zhou [93] investigated oxygen terminated ZGNR chevron devices (CZGNR) using DFT, GGA with spin-polarisation and demonstrated a transition from AFM to FM magnetic properties. Unfortunately, this paper does not draw any conclusions for ideal chevron ZGNR. Finally Cuong et. al. [95] investigated 120 degree angled CZGNR structures using DFT LDA methods but ignored the spin degrees of freedom and determined that the formation energies of these CZGNR devices was less than that of straight ZGNR structures. This supports the idea that CZGNR devices would be produced during the bottom-up synthesis of ZGNR devices and that these would be more energetically favorable than ideal, straight ZGNR devices. Cuong et al [95] also determined that a band-gap opening would occur but, as spin-degrees of freedom are ignored, conclusions cannot be drawn until compared to spin-polarised calculations.

In terms of TB calculations, Chen et. al. [96] focuses on thermal properties of CAGNR devices but they do determine a decrease in conductance compared to ideal AGNR devices due to the reduction in conductance channels. Girao *et al.* [97] has investigated both AGNR and mixed edge ZGNR using the Hubbard-$U$ model in term of band gaps but this work does not go into detail concerning the spin-dependent properties. The main conclusion drawn in this study is that different spin-properties lead to different conductance results, but they do not determine the ground state magnetic state and assume that all magnetic states are energetically equal.

Patterned AGNR (PAGNR) devices introduce internal patterning to ideal AGNR devices though self-assembly. The self-assembly occurs when smaller ''building block" carbon molecules, tetrabenzathracence and benzene, combine together to form the patterned devices observed in Figure 1.17. Based on the concentration of these smaller component molecules, the width and length of the device can be controlled [99]. The band and transport gaps of the patterned and ideal AGNR devices can be compared using the GTB model as the patterned devices form with AGNR edges. Experimentally, these patterned devices have been probed

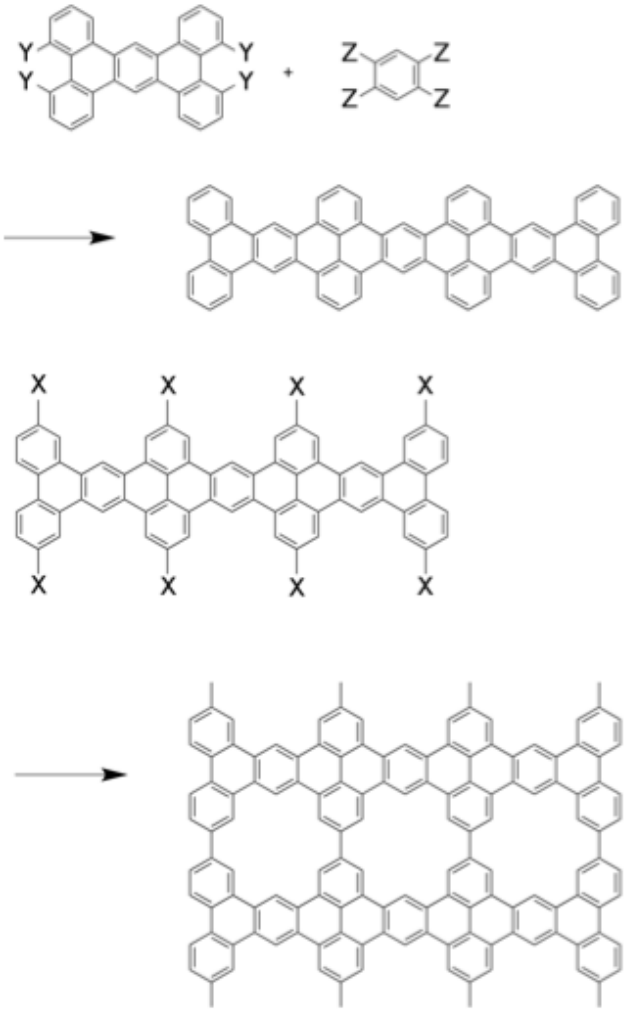


Figure 1.17: Self assembly example for the formation of the patterned AGNR device. Ribbon grows in the direction of the x-x coupling resulting in regular holes along the device. Reproduced from Gerates *et. al.* [98]

in depth [99, 100, 101], but with fewer studies into the theoretical electronic properties.

Due to the regular nature of the patterning, along with the shape of the hole, the closest studies being carried out computationally to those studied here are for graphene antidot structures. Topsakal *et. al.* [102] carried out DFT GGA-PAW calculations using the VASP package on AGNR devices with small antidots. The devices investigated by Topsakal *et. al.* [102] assume a single antidot in a wide device and vary the location of the antidot across the width. The closest approximation to the patterned devices in Figure 6.12 is that of a antidot in location 1, i.e., the center of the device for the smallest widths investigated by Topsakal *et. al.* [102]. For 34- 36- and 38-AGNR devices, there is an increase in band gap with the introduction of the antidot. Ma *et. al.* [103] carried out transport calculations on AGNR and ZGNR devices with two triangular antidots. Ma *et. al.* [103] used the STB model, and assumed that the introduction of the two triangular anti-dots opened a conductance gap in the device. Rosales *et. al.* [104] carried out STB model transport calculations on antidots within 11-AGNR devices. The antidots are repeated along the length of the device with

period d. Rosales *et. al.* [104] demonstrated that, as the period of the antidots increases, the conductance gap decreases, with a large increase in the gap when a small period (d=3) is examined. Again, Rosales *et. al.* [104] uses the STB model for the calculations but models a semi-conductive (within the STB model) AGNR device. This allows easier comparison with the GTB model compared to a metallic (within the STB model) device.

### 1.4.6 Uniaxial Strain

The effect of uniaxial strain on the transport properties of graphene structures is another area that has been studied in depth using both DFT and tight-binding methods. Uniaxial strain can control the properties of graphene devices in a predictable, controllable way [105, 106, 107, 108, 109, 110, 111, 112, 113, 114, 115]. For example, uniaxial strain can lead to a metal/semiconductor transition in both bulk and nanographene [110, 111] as well as provide a controllable way of perturbing the band-gap [106, 110, 111, 114, 115] and electronic transport [107, 111]. Uniaxial strain can arise due to a lattice mismatch with the substrate [116, 117, 118] or via direct application [119, 120, 121]. AGNR systems have an sawtooth like trend for band-gap vs energy [114], whereas ZGNR systems have a more linear trend [115]. This uniaxial strain can be introduced intrinsically though lattice mismatch between the graphene sample and the substrate in which it is deposited [116, 117, 118], as well as directly applied, though the application of uniaxial tensile strain on suspended samples [120, 121].

Harrison scaling of the parameters in the tight binding model was initially used for uniaxial strain, in bulk, nano and non-graphene [108, 109, 115, 122] devices. This approach was first proposed by Harrison in 1980 [123]. Harrison scaling allows general trends to be probed as uniaxial strain was introduced to various devices. Exponential scaling of the parameters in the tight binding model was introduced in 1998 [124] and was demonstrated to be a more accurate description of uniaxial strain in graphene devices [106]. Currently, exponential scaling is more widely used than Harrison scaling for detailed probing of properties, with each paper generally using a fitting parameter, $A$, unique to the system investigated. Due to the various structural perturbations being studied in this work, the Harrison scaling method is used.

The linear dependence of electronic conductance gap (which is equivalent to the energy band gap at zero bias) on unixaial strain has been demonstrated by Li *et al.* [115] for12-ZGNR using DFT with GGA via VASP [70] for small uniaxial strain in the x-direction (less than 10%). A slightly curving linear dependence was also shown for 6-ZGNR by Zhang *et al.* [125] with DFT, GGA and HSE06 via VASP [70] between $|\pm 10\%|$ in the y-direction. Lu and Guo [126] used the interacting tight-binding model to calculate energy band gaps for 5-, 10-, 16- and 32-ZGNR and found a slightly curved linear dependence between $|\pm 15\%|$ in the

x-direction (Figure 5.12(a)). Lu and Guo [126] parametrised the model using the hopping and Hubbard-$U$ values found by Gunlycke and White [127], and used Harrison scaling and used a Poisson ratio of 0.165.

Poetschke *et al.* uses the STB model to model a 10-ZGNR device under strain but finds no metallic/semiconductive transition in the ZGNR device. When compared to the DFT results of Li *et al.* [115], Zhang *et al.* [125] and Su *et al.* [128] it is clear that the STB model is insufficient to accurately model the effects of strain on a ZGNR system. The lack of an interacting term is a serious enough deficiency to disregard the STB model for these studies.

## 1.5 Conclusion

In this chapter we have discussed the fundamental properties of bulk graphene, and thus demonstrated the advantage of using graphene nanoribbons to open the semi-metallic band-gap. We have also briefly described the theoretical and experimental evidence of the semi-conductive band- and conduction-gaps. Structural perturbations were explored and the effects of random-edge vacancies, asymmetrical patterning and uniaxial strain were covered. Comparing the band-structure and band-gaps of density functional theory, tight-binding models and experimental evidence demonstrates that physics is missing in the commonly used simple tight-binding model and there are significant results predicted for structural perturbations that must be reconsidered within the extended, interacting, tight-binding model, as we do in this thesis. The next Chapter will describe the interacting generalised tight-binding model used for our calculations along with the Landauer-Büttiker formalism used to calculate the transport properties.

# Chapter 2

# Theory

## 2.1 Abstract

This chapter describes the underlying theory used in this work. The Hartree-Fock mean-field approximation, second quantisation of fermions and Bloch's theorem are introduced as they lay the foundations for the tight-binding formalism and Hubbard model discussed later in the chapter. The Hubbard model, i.e. the tight-binding model with Hubbard-$U$ is discussed in detail, with particular attention paid to the effects of the Hubbard-$U$ term. The stability of the mean-field approximation of the Hubbard-$U$ term is discussed and a method for reducing the likelihood of calculations becoming trapped in metastable energy states though an adiabatic Hubbard-$U$ is laid out. The final discussion into the Hubbard model deals with the mean-field approximation and the predicted lowest-energy state phase transitions with varying band filling and U/t ratio for both square and hexagonal lattices.

The Landauer-Büttiker (coherent) transport formalism and its solution via the Green's function method is introduced and derived, with particular care paid to the discontinuities in the edge spin-localisation between the device and the leads. The density of states is also introduced and derived, with a focus on the quasi-2D nature of GNRs. An important tool, the **GR**aphene **U**ser **I**nterface, is introduced and briefly discussed. Finally, the mathematical details of density functional theory (DFT) and the local spin-density approximation are laid out, with a description of the two DFT packages, VASP and ONETEP, that are used in this work.

## 2.2 The Hartree-Fock Approximation

For a many electron system, the full many body Schrödinger eigenproblem is [123]:

$$[-\frac{\hbar^2}{2m}\sum_i \nabla_i^2 + \sum_i V(\boldsymbol{r}_i) + \frac{1}{2}\sum_i \sum_{j\neq i} \frac{e^2}{|\boldsymbol{r}_i - \boldsymbol{r}_j|}]\boldsymbol{\Psi}(\boldsymbol{r_1}, \boldsymbol{r_2}, \ldots, \boldsymbol{r_N}) = E\boldsymbol{\Psi}(\boldsymbol{r_1}, \boldsymbol{r_2}, \ldots, \boldsymbol{r_N}) \quad (2.1)$$

where $\hbar$ is the reduced Planck constant, $m$ is the mass of an electron, $e$ is the electronic charge, $\boldsymbol{r_i}$ is a vector describing the location of electron $i$, $\nabla^2$ is the Laplacian operator, $V(\boldsymbol{r_i})$ is the position-dependent, potential energy operator, which takes into account the interaction of each electron with the ionic potential at $r_i$, and $E$ is the total energy. $|\boldsymbol{r_i} - \boldsymbol{r_j}|$ is the distance between electrons $i$ and $j$. The left-hand-side of this equation contains three terms: The first term is the sum of the kinetic energy contributions from each electron; the second term is the sum of the interaction energies from the ion and electron interactions; and the third term is the energy associated with the Coulomb interaction between each electron defined at $r_i$ and the other electrons defined at $r_j$ in the solid. In addition to these terms, the anti-symmetry arising from the interchange of two electrons (i.e., indistinguishable particles) must also be taken into account [123]. The many-body Schroedinger problem cannot be solved exactly and hence certain approximations need to be made. The Hartree approximation assumes that the overall Hamiltonian of the of a many-body system can be written as the sum of the individual electron Hamiltonians [123]:

$$[-\frac{\hbar^2}{2m}\nabla^2 + V(\boldsymbol{r}) + \sum_{j\neq i} e^2 \int \frac{\psi_j^*(\boldsymbol{r'})\psi_j(\boldsymbol{r'})d\tau}{|\boldsymbol{r} - \boldsymbol{r'}|}]\psi_i(\boldsymbol{r}) = \epsilon_i\psi_i(\boldsymbol{r}) \tag{2.2}$$

where $j$ is summed over all occupied states except i. Here, $\psi_i$ is the individual wave function corresponding to an electron $i$, $\psi^*$ is the complex conjugate of this wave function. $\boldsymbol{r}$ and $\boldsymbol{r'}$ are the vectors describing the location of electrons i and j respectively and the $\epsilon_i$ values are variational parameters in the form of one-electron energy eigenvalues. The Hartree approximation does not include the anti-symmetry requirement of the wave function as [123]:

$$\boldsymbol{\Psi(r_1, r_2, \ldots, r_N)} = \sum_i \psi_i(\boldsymbol{r_i}) \tag{2.3}$$

a Slater determinant of $\psi$s will produce an antisymmetic wavefunction [123, 129]:

$$\boldsymbol{\Psi(r_1, r_2, \ldots, r_N)} = \frac{1}{\sqrt{N!}} \begin{vmatrix} \psi_1(\boldsymbol{r_1}) & \psi_1(\boldsymbol{r_2}) & \ldots & \psi_1(\boldsymbol{r_N}) \\ \psi_2(\boldsymbol{r_1}) & \ldots & \ldots & \ldots \\ \ldots & \ldots & \ldots & \ldots \\ \psi_N(\boldsymbol{r_1}) & \ldots & \ldots & \psi_N(\boldsymbol{r_N}) \end{vmatrix} \tag{2.4}$$

with $\Psi$ giving the total wavefunction, $\psi$ the individual wavefunctions and N the total number of electrons. Substituting Equation 2.4 into Equation 2.1 leads to the Hartree-Fock equa-

tion [123]:

$$[-\frac{\hbar^2}{2m}\nabla^2 + V(\boldsymbol{r}) + \sum_j e^2 \int \frac{\psi_j^*(\boldsymbol{r}')\psi_j(\boldsymbol{r}')d\tau'}{|\boldsymbol{r}-\boldsymbol{r}'|}]\psi_i(\boldsymbol{r}) - \sum_j e^2\psi_j(\boldsymbol{r}) \int \frac{\psi_j^*(\boldsymbol{r}')\psi_i(\boldsymbol{r}')d\tau'}{|\boldsymbol{r}-\boldsymbol{r}'|} = \epsilon_i\psi_i(\boldsymbol{r}) \tag{2.5}$$

the new term in Equation 2.5 is the fourth term on the left-hand-side, which denotes the exchange interaction [123].

## 2.3 Introduction to Second Quantisation for Fermions

The second quantisation of quantum mechanics for fermions (in this example, electrons) involves replacing individual electron wave functions with operators.

The Pauli exclusion principle states that, for fermions, each state may only contain up to 1 particle [130, 131]. The Fermi statistics that arise from this principle can be enforced by making the fields anticommute, as demonstrated by Jordan and Wigner [130, 132][1] :

$$\Psi(\mathbf{r})\Psi^\dagger(\mathbf{r}') + \Psi^\dagger(\mathbf{r}')\Psi(\mathbf{r}) \equiv \{\Psi(\mathbf{r}), \Psi^\dagger(\mathbf{r}')\} = \delta(\mathbf{r}-\mathbf{r}') \tag{2.6}$$

$$\{\Psi(\mathbf{r}), \Psi(\mathbf{r}')\} = 0 \tag{2.7}$$

$$\{\Psi^\dagger(\mathbf{r}), \Psi^\dagger(\mathbf{r}')\} = 0 \tag{2.8}$$

by expanding the wave functions, $\Psi(\mathbf{r})$ and $\Psi^\dagger(\mathbf{r})$, in a basis set, $\phi_i(\mathbf{r})$ [130],

$$\Psi(\mathbf{r}) = \sum_i c_i\phi_i(\mathbf{r}) \tag{2.9}$$

$$\Psi^\dagger(\mathbf{r}) = \sum_i c_i^\dagger\phi_i^*(\mathbf{r}), \tag{2.10}$$

the creation, $c_i^\dagger$, and annihilation, $c_i$, operators can be defined. These obey the same anti-commutation demonstrated by Jordan and Wigner [130, 132]:

$$\{c_i, c_{i'}^\dagger\} = \delta(i-i') \tag{2.11}$$

$$\{c_i, c_{i'}\} = 0 \tag{2.12}$$

$$\{c_i^\dagger, c_{i'}^\dagger\} = 0 \tag{2.13}$$

the operators create an electron in state $i$ ($c_i^\dagger$) or annihilate an electron from state $i$ ($c_i$).

[1] Ref [132] is covered, in English, in "Selected topics in field quantization" by Pauli [131].

For example, if state $i$ with zero particles is $|0\rangle_i$, and state $i$ with 1 particle is $|1\rangle_i$, then [130]:

$$c_i|1\rangle_i = |0\rangle_i \tag{2.14}$$

$$c_i|0\rangle_i = 0 \tag{2.15}$$

$$c_i^\dagger|0\rangle_i = |1\rangle_i \tag{2.16}$$

$$c_i^\dagger|1\rangle_i = 0 \tag{2.17}$$

$c_i^\dagger$ and $c_i$ can be used to construct the number operator for state $i$, $n_i$, as follows [123, 130]:

$$n_i = c_i^\dagger c_i \tag{2.18}$$

where $n_i$ is an eigenvalue equal to one if the state $i$ is occupied [123, 130]:

$$n_i c_i^\dagger|0\rangle_i = c_i^\dagger|0\rangle_i. \tag{2.19}$$

Finally, the creation and annihilation operators for electrons can be transformed to the wavevector representation via [123, 133, 134]:

$$\begin{aligned} c_{k\sigma} &= N^{-\frac{1}{2}} \sum_i e^{-ik\cdot\mathbf{R}_i} c_{i\sigma} \\ c_{k\sigma}^\dagger &= N^{-\frac{1}{2}} \sum_i e^{ik\cdot\mathbf{R}_i} c_{i\sigma}^\dagger \end{aligned} \tag{2.20}$$

where i is the lattice site and $R_i$ is the lattice position within the tight-binding description.

## 2.4 Bloch's Theorem and the Tight-Binding Model

### 2.4.1 Bloch's Theorem

Bloch's theorem states that the eigenstates of the one-electron Hamiltonian [12],

$$H = -\frac{\hbar^2}{2m}\nabla^2 + U(\boldsymbol{r}), \tag{2.21}$$

where [12],

$$U(\boldsymbol{r}) = U(\boldsymbol{r} + \mathbf{R}), \tag{2.22}$$

for all Bravais lattice vectors, $\mathbf{R}$, are such that they are plane waves multiplied by the function $u_{nk}(\mathbf{r})$ which has the periodicity of the Bravais lattice [12]:

$$\psi_{\mathbf{k}}(\mathbf{r}) = e^{i\mathbf{k}\cdot\mathbf{R}} u_{\mathbf{k}}(\mathbf{r}) \tag{2.23}$$

$$u_{\mathbf{k}}(\mathbf{r}) = u_{\mathbf{k}}(\mathbf{r} + \mathbf{R}). \tag{2.24}$$

The Bravais lattice specifies the periodicity of the crystal such that the geometry of the underlying periodic structure is described. A 3D Bravais lattice, for example, consists of all points with position vectors, R [12]:

$$\mathbf{R} = n_1\mathbf{a}_1 + n_2\mathbf{a}_2 + n_3\mathbf{a}_3 \tag{2.25}$$

such that the vectors $\mathbf{a}_{1,2,3}$ are not linearly dependent and $n_{1,2,3}$ can be any set of integers.

The Bloch condition, Equation 2.24 can also be written as:

$$\psi_{\mathbf{k}}(\mathbf{r}+\mathbf{R}) = e^{i\mathbf{k}\cdot\mathbf{R}}\psi_{\mathbf{k}}(\mathbf{r}) \tag{2.26}$$

### 2.4.2 Tight Binding Approximation

The tight-binding approximation (TBA) is used to describe the overlap of atomic wavefunctions in systems where the atomic description is still valid but a correction to the isolated electron model is required [12]. For example, when two sodium atoms are brought within 3.7Å of each other, the overlap of the 3s-level atomic wavefunction is such that the actual electronic levels are significantly different to the atomic levels [12].

Assuming the ground state of an electron within potential $U(\mathbf{r})$ of an isolated atom is $\phi(\mathbf{r})$, then, if the interaction between two neighbouring atoms is small, the approximate wavefunction for an electron in the crystal becomes [135]:

$$\psi_{\mathbf{k}}(\mathbf{r}) = \sum_i C_{\mathbf{k}i}\phi(\mathbf{r}-\mathbf{R}_i) \tag{2.27}$$

where the sum is over all lattice points, $i$, and $\mathbf{R}_i$ is the Bravais lattice vector for $i$. The function fulfills Bloch's condition (Equation 2.24) when [135],

$$C_{\mathbf{k}i} = N^{-\frac{1}{2}}e^{i\mathbf{k}\cdot\mathbf{R}_i}, \tag{2.28}$$

where N is the number of lattice points, and therefore [135]:

$$\psi_{\mathbf{k}}(\mathbf{r}) = \sum_i N^{-\frac{1}{2}}e^{i\mathbf{k}\cdot\mathbf{R}_i}\phi(\mathbf{r}-\mathbf{R}_i). \tag{2.29}$$

The Bloch condition for Equation 2.29 can be confirmed by applying a translation in the

vector direction, $\mathbf{T}$ [135],

$$\psi_{\mathbf{k}}(\mathbf{r}+\mathbf{T}) = \sum_i N^{-\frac{1}{2}} e^{i\mathbf{k}\cdot\mathbf{R}_i}\phi(\mathbf{r}+\mathbf{T}-\mathbf{R}_i) \tag{2.30}$$

$$= e^{i\mathbf{k}\cdot\mathbf{T}} \sum_i N^{-\frac{1}{2}} e^{i\mathbf{k}\cdot(\mathbf{R}_i-\mathbf{T})}\phi(\mathbf{r}-(\mathbf{R}_i-\mathbf{T})) \tag{2.31}$$

$$= e^{i\mathbf{k}\cdot\mathbf{T}}\psi_{\mathbf{k}}(\mathbf{r}) \tag{2.32}$$

where Equation 2.32 is the same as the alternative form of the Bloch condition, Equation 2.26.

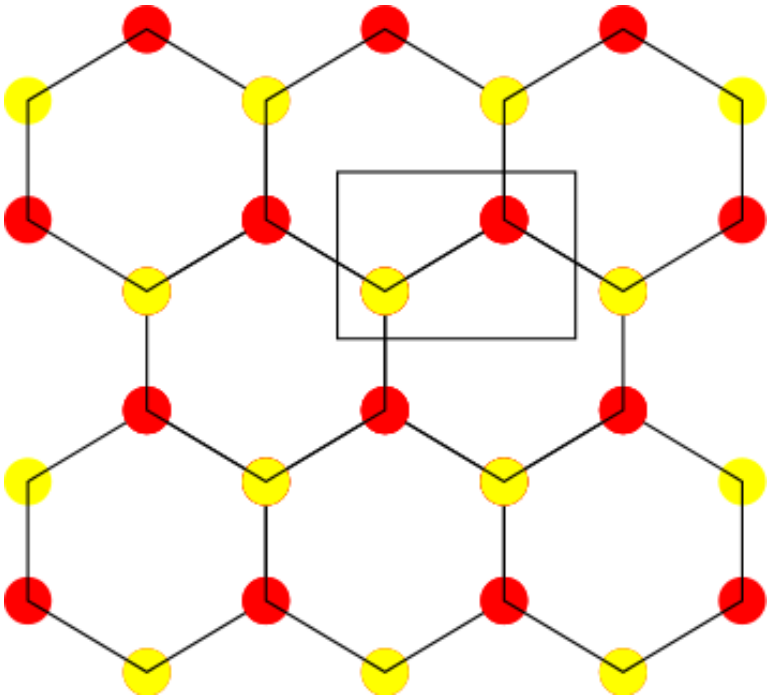

Figure 2.1: The real-space unit cell of bulk graphene can be described using a two atom basis. The rectangle highlights the two atom basis. The red and yellow atoms are labelled A and B respectively .

The tight-binding approximation was first applied to bulk graphene (Figure 2.1) by Wallace in 1947 [10]. Wallace modelled the normalised $2p_z$ orbital wavefunction, $X(r)$, for an isolated atom [10] which, within the TBA, has the form:

$$\Psi = \phi_1 + \lambda\phi_2 \tag{2.33}$$

where [10],

$$\phi_1(\mathbf{r}) = \sum_A e^{2\pi i\boldsymbol{k}\cdot\boldsymbol{R}_A} X(\boldsymbol{r}-\boldsymbol{R_A}), \tag{2.34}$$

$$\phi_2(\mathbf{r}) = \sum_B e^{2\pi i\boldsymbol{k}\cdot\boldsymbol{R}_B} X(\boldsymbol{r}-\boldsymbol{R_B}), \tag{2.35}$$

$\lambda$ is a constant and the sum in Equation 2.34(2.35) is taken over A(B) and all lattice points generated though Bravais lattice vector ($\mathbf{R}_{A(B)}$) translations. Neglecting the overlap of the

$p_z$ wave functions centred on different atoms by assuming [10],

$$S = \int X(\boldsymbol{r} - \boldsymbol{R}_A)X(\boldsymbol{r} - \boldsymbol{R}_B)d\tau = 0, \tag{2.36}$$

Equation 2.33 can be inserted into,

$$H\Psi = E\Psi, \tag{2.37}$$

and by following the method detailed in Ref [10], the elements of the matrix Hamiltonian become [10]:

$$H_{11} + \lambda H_{12} = EN \tag{2.38}$$

$$H_{21} + \lambda H_{22} = \lambda EN \tag{2.39}$$

where [10]:

$$H_{11} = \int \phi_1^* H \phi_1 d\tau \tag{2.40}$$

$$H_{12} = H_{21}^* = \int \phi_1^* H \phi_2 d\tau \tag{2.41}$$

$$H_{22} = \int \phi_2^* H \phi_2 d\tau \tag{2.42}$$

$$N = \int \phi_1^* \phi_1 d\tau = \int \phi_2^* \phi_2 d\tau. \tag{2.43}$$

Eliminating $\lambda$ gives the secular equation [10]:

$$\begin{vmatrix} H_{11} - EN & H_{12} \\ H_{21} & H_{22} - EN \end{vmatrix} = 0 \tag{2.44}$$

this secular equation is used to find E [10]:

$$E = \frac{1}{2N}[H_{11} + H_{22} \pm ((H_{11} - H_{22})^2 + 4H_{12}^2)^{\frac{1}{2}}]. \tag{2.45}$$

Due to the symmetry of the systems, $H_{11} = H_{22}$, a new set of matrix elements can be defined and thus the energy function can be rewritten [10]:

$$H'_{11} = H'_{22} = \frac{1}{N}H_{11} = \frac{1}{N}H_{22} \tag{2.46}$$

$$H'_{12} = \frac{1}{N}H_{12} \tag{2.47}$$

$$\therefore \; E = H'_{11} \pm |H'_{12}| \tag{2.48}$$

As $H'_{11} = H'_{22}$, the diagonal elements of the matrix are constant. Using this, $H'_{11}$ and $H'_{22}$ can be set to zero. In addition, $H_{12}$ is assumed to be summed over nearest neighbouring atoms only, for example A(B) atoms only interact with the nearest B(A) atoms [10].

Now, from Equations 2.34, 2.35, 2.41 and 2.47:

$$H'_{12} = e^{2\pi i \boldsymbol{k}\cdot(\mathbf{r}_A - \mathbf{r}_B)} \int X^*(\boldsymbol{r} - \boldsymbol{R_A}) H X(\boldsymbol{r} - \boldsymbol{R_B}) d\tau. \tag{2.49}$$

Now, following the details laid out in Ref [10], $|H_{12}|$, and therefore $\pm E$, becomes:

$$|H_{12}| = t\sqrt{1 + 4\cos^2(\pi k_y a + 4cos(\pi k_y a)\cos(\pi k_x \sqrt{3} a)} \tag{2.50}$$

where t is the hopping integral within the tight-binding approximation,

$$t = \int X^*(\mathbf{r} - \mathbf{AB}) H X(\mathbf{r}) d\tau, \tag{2.51}$$

a is the magnitude of the fundamental lattice distance, $k_{x(y)}$ is the x(y)-component of $\mathbf{k}$ and $\mathbf{A}(\mathbf{B})$ is the lattice vector of site A(B).

Wallace neglected the overlap integral in his initial deviation and thus assumed an orthonormal basis [10]. By including overlap integrals, nonorthogonality is introduced. Wannier functions, introduced next section, can be used tofix this nonorthogonality.

## 2.5 Extended Tight-Binding Model with Hubbard-*U*

The Hubbard model within the tight binding approximation was first purposed in 1963 by J. Hubbard [134]. In this paper, Hubbard studied the narrow 3d bands of transition metals. For simplicity his method was described as it applies to an s-band. This convention will also be used in this derivation.

By rewriting the Hartree-Fock approximation, Equation 2.5, in second quantised notation Hubbard derived the full Hamiltonian for a many-electron system [134]:

$$\begin{aligned} H = \sum_{k_1,\sigma} \varepsilon_{k_1} c^\dagger_{k_1,\sigma} c_{k_1,\sigma} + \frac{1}{2} \sum_{k_1,k_2,k'_1,k'_2} \sum_{\sigma_1,\sigma_2} \langle k_1 k_2 | \frac{1}{r} | k'_1 k'_2 \rangle c^\dagger_{k_1\sigma_1} c_{k_2\sigma_2} c^\dagger_{k'_1\sigma_1} c_{k'_2\sigma_2} \\ - \sum_{k_1,k'_1} \sum_{\sigma} \{2\langle k_1 k'_1 | \frac{1}{r} | k_1 k'_1 \rangle - \langle k_1 k'_1 | \frac{1}{r} | k'_1 k_1 \rangle) \upsilon_{k'_1} c^\dagger_{k_1\sigma} c_{k'_1\sigma} \end{aligned} \tag{2.52}$$

where the summation over $k_{1(2)}$ is across the first Brillouin zone, $\sigma$ is the electron spin ($\sigma = \uparrow, \downarrow$), $c^\dagger_{i(j)}$ and $c_{j(i)}$ are the creation and annihilation operators respectively and [134]:

$$\langle k_1 k_2 | \frac{1}{r} | k'_1 k'_2 \rangle = e^2 \int \frac{\psi^*_{k_1}(\boldsymbol{r'}) \psi_{k'_1}(\boldsymbol{r}) \psi_{k_2}(\boldsymbol{r}) \psi^*_{k'_2}(\mathbf{r'})}{|\boldsymbol{r} - \boldsymbol{r'}|} d\boldsymbol{r} d\boldsymbol{r'}. \tag{2.53}$$

The Hamiltonian is comprised of three parts, the first term in Equation 2.52 is the band energies of the electrons, the second term is the interaction energy of the electrons and the last term subtracts the potential energy of the electrons in the Hartree-Fock field arising

from the electrons in the s-band. The term is subtracted to avoid counting the interactions of the electrons twice, once implicitly from the Hartree-Fock term and once explicitly from the interaction energy term of the Hamiltonian. $v_k$ is the occupation number and its effects are discussed in more detail in Section 2.6.

The wavefunctions used in the tight-binding approximation, $\psi_{k_{1(2)}}$, are not exact solutions to the one-electron problem [123, 133, 136]. There is a lack of orthogonality of the atomic orbitals. The overlap terms are non-zere due to this non-orthogonality and thus a linear combination of atomic orbitals on different sites must be taken to remove them. This linear combination can be carried out using the Wannier function [134, 137]:

$$\phi(\mathbf{r}) = N^{-\frac{1}{2}} \sum_{k} \psi_{\mathbf{k}}(\boldsymbol{r}). \tag{2.54}$$

This can be transformed to obtain the eigenstates in terms of Equation 2.5 [133, 134]:

$$\psi_{\mathbf{k}}(\boldsymbol{r}) = N^{-\frac{1}{2}} \sum_{i} e^{i\mathbf{k}\cdot\mathbf{R}_i} \phi(\boldsymbol{r} - \mathbf{R}_i) \tag{2.55}$$

where the sum is over all atomic positions, $\mathbf{R}_i$. These wavefunctions are in the form of the tight-binding states but are now exact and orthogonal.

The creation and annihilation operators for electrons with spin $\uparrow, \downarrow$ can be transformed from the wavevector form to the lattice site form using Equation 2.20 [123, 133, 134]. Equation 2.52 now becomes [134]:

$$\begin{aligned} H = &\sum_{ij}\sum_{\sigma} T_{ij} c^{\dagger}_{i\sigma} c_{j\sigma} + \frac{1}{2}\sum_{ijlm}\sum_{\sigma\sigma'} \langle ij|\frac{1}{r}|lm\rangle c^{\dagger}_{i\sigma} c^{\dagger}_{j\sigma'} c_{m\sigma'} c_{l\sigma} \\ &-\frac{1}{2}\sum_{ijlm}\sum_{\sigma} [2\langle ij|\frac{1}{r}|lm\rangle - \langle ij|\frac{1}{r}|ml\rangle\} v_{jm} c^{\dagger}_{i\sigma} c_{l\sigma} \end{aligned} \tag{2.56}$$

where $i, j, l$ and $m$ are at lattice sites $R_i, R_j, R_l$ and $R_m$ [123, 134, 133],

$$T_{i,j} = N^{-1} \sum_{\mathbf{k}} \epsilon_{\mathbf{k}} e^{i\mathbf{k}\cdot(\mathbf{R}_i - \mathbf{R}_j)}, \tag{2.57}$$

$$\langle ij|\frac{1}{r}|lml\rangle = e^2 \int \phi^*(\boldsymbol{r} - \mathbf{R}_i)\phi(\boldsymbol{r} - \mathbf{R}_j)\phi^*(\boldsymbol{r} - \mathbf{R}_l)\phi(\boldsymbol{r} - \mathbf{R}_m)\frac{d\boldsymbol{r}d\boldsymbol{r'}}{|\boldsymbol{r} - \boldsymbol{r'}|}, \tag{2.58}$$

$$v_{jm} = N^{-1} \sum_{\mathbf{k}} v_{\mathbf{k}} e^{i\mathbf{k}\cdot(\mathbf{R}_j - \mathbf{R}_m)}, \tag{2.59}$$

and $\epsilon_{\mathbf{k}}$ is the energy associated with $\psi_{\mathbf{k}}$. The integral $\langle ij|\frac{1}{r}|lm\rangle$ only gives a significantly large value when i=j=l=m [134]. This was shown by Hubbard to be correct as $I = \langle ii|1/r|ii\rangle$ is of the order of approximately 20eV whereas the next largest, l=i, m=j, is approximately 2-3eV due to Coulomb screening [134].

Now, using the approximation that i=j=l=m, Equation 2.56 becomes [134]:

$$H = \sum_{,j} \sum_{\sigma} T_{ij} c^{\dagger}_{i\sigma} c_{j\sigma} + \frac{1}{2} I \sum_{i} \sum_{\sigma \neq \sigma'} n_{i\sigma} n_{i\sigma'} - I \sum_{i\sigma} v_{ii} n_{i\sigma} \tag{2.60}$$

where $n_{i\sigma} = c^{\dagger}_{i\sigma} c_{i\sigma}$ is the number operator as described in Section 2.2. The third term on the RHS of Equation 2.60 is a constant for homogeneous systems as $v_{ii}$ and I are site dependent. This term can therefore also introduce inhomogeneity into the system if required. Now,

$$T_{ij} = -t_{ij}, \tag{2.61}$$

$$\frac{1}{2} I = U, \tag{2.62}$$

$$-I v_{ii} = E_i, \tag{2.63}$$

where $-t_{ij}$, $U$ and $E_i$ are constants [134]. The convention in Equation 2.61 defines $t_{ij}$ as positive and Equation 2.63 defines $E_i$ as negative. This leads to [134]:

- The tight-binding kinetic energy term [134]:

$$-\sum_{ij} \sum_{\sigma} t_{ij} c^{\dagger}_{i\sigma} c_{j\sigma} \tag{2.64}$$

- The Hubbard-$U$ potential term [134]:

$$\sum_{i} U_i n_{i\uparrow} n_{i\downarrow} \tag{2.65}$$

- The on-site energy term [134]:

$$\sum_{i} \sum_{\sigma} E_i c^{\dagger}_{i\sigma} c_{i\sigma} \tag{2.66}$$

The overall Hamiltonian is given by [134]:

$$H_{hub} = -\sum_{ij} \sum_{\sigma=\downarrow\uparrow} (t_{ij} c^{\dagger}_{i\sigma} c_{j\sigma} + H.c.) + \sum_{i} \sum_{\sigma=\downarrow\uparrow} E_i c^{\dagger}_{i\sigma} c_{i\sigma} + \sum_{i} U_i n_{i\uparrow} n_{i\downarrow}. \tag{2.67}$$

The on-site terms in the Hamiltonian, the on-site energy (second term) and the Hubbard-$U$ (third term), are site-dependent, which introduces inhomogeneity into the system allowing for different local properties at each atomic site. All values of $E_i$ are relative to the dominant atom, which has an on-site energy of $E_i$=0.

The potential term of the Hamiltonian contains the number operator, $n_{i,\sigma} = c^{\dagger}_{i,\sigma} c_{i,\sigma} = \{0..1\}$, and the site-dependent Hubbard-$U$ term which is the Coulomb interaction energy between two electrons of opposite spin at the same atomic site, $i$. With $U_i = 0$, the Hubbard Hamiltonian then reduces to a single-particle extended tight-binding model, which can easily be solved using matrix algebra to produce the eigenenergy band solutions.

The introduction of the Hubbard-$U$ term results in a difficult two-body interaction term, with the Hamiltonian needing to be solved using a full many-body treatment. One method of approximation to the many-body problem is to use a mean-field method. The method used in this work involves an average spin-dependent field such that inter-spin interactions are replaced by interactions between individual spins and the average field of the opposite spin. This has been shown to be an effective method of finding an approximate solution to Equation 2.67 [134, 138, 139]. For this we must first linearise the Hamiltonian using [123, 134]:

$$n_{i\sigma} = n_{i\sigma} - \langle n_{i\sigma}\rangle + \langle n_{i\sigma}\rangle \tag{2.68}$$

$$n_{i\sigma} = \delta(n_{i\sigma}) + \langle n_{i\sigma}\rangle \tag{2.69}$$

$$\delta(n_{i\sigma}) = n_{i\sigma} - \langle n_{i\sigma}\rangle \tag{2.70}$$

where $n_{i\sigma}$ is the number operator at site i with spin $\sigma$ and $\langle n_{i,\sigma}\rangle$ is the value taken within the quantum average. The Coulomb interaction term can be written as [123, 134]:

$$H = \sum_i U_i(\langle n_{i\uparrow}\rangle n_{i\downarrow} + n_{i\uparrow}\langle n_{i\downarrow}\rangle - \langle n_{i\uparrow}\rangle\langle n_{i\downarrow}\rangle) \tag{2.71}$$

where it is assumed that $\delta(n_{i\downarrow})\delta(n_{i\uparrow})$ is too small to be significant and -$\sum_i U_i\langle n_{i\uparrow}\rangle\langle n_{i\downarrow}\rangle$ is the mean-field, Hartree-Fock correction term. The complete Hamiltonian can then be written as a set of two coupled equations [123, 134]:

$$H_{up} = -\sum_{ij} t_{ij} c^\dagger_{i\uparrow} c_{j\uparrow} + \sum_i U_i n_{i\uparrow}\langle n_{i\downarrow}\rangle \tag{2.72}$$

$$H_{down} = -\sum_{ij} t_{ij} c^\dagger_{i\downarrow} c_{j\downarrow} + \sum_i U_i n_{i\downarrow}\langle n_{i\uparrow}\rangle. \tag{2.73}$$

The total energy can be calculated using Equation 2.74 [123, 134]:

$$E_{total} = E_{up} + E_{down} - \sum_i U_i\langle n_{i\uparrow}\rangle\langle n_{i\downarrow}\rangle \tag{2.74}$$

where $E_{up(down)}$ denotes the total energy of the spin-up(down) eigensolution found though solving $H_{up(down)}$

This gives us a final, mean-field equation of [123, 134]:

$$H_{hub} = -\sum_{ij\sigma}(t_{ij} c^\dagger_{i\sigma} c_{j\sigma} + H.c.) + \sum_{i\sigma} E_i c^\dagger_{i\sigma} c_{i\sigma} \tag{2.75}$$

$$+ \sum_i U_i(\langle n_{i\uparrow}\rangle n_{i\downarrow} + n_{i\uparrow}\langle n_{i\downarrow}\rangle - \langle n_{i\uparrow}\rangle\langle n_{i\downarrow}\rangle). \tag{2.76}$$

Equations 2.72 and 2.73 must be solved self-consistently, initially solving for Equation 2.72 using a preset texture (for example an antiferromagnetic texture) of $\langle n_{i\uparrow}\rangle$, cal-

culating $\langle n_{i\downarrow} \rangle$ then substituting it into Equation 2.73 to find $\langle n_{i\uparrow,new} \rangle$. The convergence criterion between the new value of $\langle n_{i\sigma} \rangle$ and the old value in the self-convergence step has been determined though initial convergence testing to be 0.0001%. This converged value is generally system independent as it is more closely linked to the machine accuracy. $\langle n_{i\sigma} \rangle$ is calculated by summing up the occupied eigenstates [134]:

$$\langle n_{i\sigma} \rangle = \int_{-\infty}^{\mu} D_{i\sigma}(E) dE \tag{2.77}$$

where $D_{i\sigma}(E)$ is the spin-dependent density of states and $\mu$ is the chemical potential. For a zero temperature model, the chemical potential is defined as the Fermi level [140].

The Hubbard-$U$ term must be controlled very carefully. The energy landscape of this model is such that it is very easy to converge into metastable states resulting in an energy which is larger than the lowest possible energy due to the variational principle [141]. This states that model wavefunctions , for example Equation 2.76, gives energies such that [141]:

$$E_{model} \geq E_{actual}. \tag{2.78}$$

This is an issue when dealing with systems that do not yet have a well defined ground state. One solution is the inclusion of an adiabatic Hubbard-$U$ term that is slowly turned on. This will explore more of the energy landscape and increase the chances of finding the global energy minima. The initial, antiferromagnetic, texture of the system can also guide the model in finding the global minima. Both of these methods, when used together, greatly increase the accuracy and efficiency of the model but can still result in a metastable state. To prevent this, multiple starting textures, for example antiferromagnetic, ferromagnetic and paramagnetic, and paths though the landscape must be tested in order to confirm the lowest total energy found is the actual lowest total energy achievable. $U$ is adiabatically "turned on" by initially randomly assigning $U_i(0)$ such that:

$$\sum_i U_i(0)/N = 0 \tag{2.79}$$

where $U_i(0)$ is the initially randomly assigned, site dependent, $U$. The random values of $U_i(0)$ are linearly distributed within a range of 1eV. The model is then self-consistently solved and a new set of values for $U_i$ are calculated such that $U_i(t)$ is increased over a total number of steps, T, found though initial tests (T ranging from 1 to 200 depending on the complexity of the system), with each site converging to the site dependent $U_i(T)$:

$$U_i(t) = \frac{t}{T}(U_i(T)\sqrt{t/T} + U_i(0)[1 - t/T]) \tag{2.80}$$

where t is the current step number. As each adiabatic $U$ step is carried out, the final $U_i(T)$

increases in weighting, while the initial, random, $U_i(0)$ decreases in weighting. This also leads to the range of random values shrinking until the range is zero at $t = T$. The weightings in Equation 2.80, $\sqrt{t/T}$ and $[1 - t/T]$, were found though initial tests into different weightings, for example a linear increase with $t$, and $\sqrt{t/T}$ and $[1 - t/T]$ were determined to most consistently avoid a metastable state.

Due to the possible spin-separation in the interacting systems, the degree of polarisation must be considered. This can be analysed using a spin-distribution diagram. The spin-polarisation on any site is defined as [82]:

$$\langle n_{inet} \rangle = \langle n_{i\uparrow} \rangle - \langle n_{i\downarrow} \rangle. \tag{2.81}$$

By defining spin-up to be positive and spin-down as negative it is possible to associate a radius with the magnitude of $|n_{net}|$ and a color with the sign of $\langle n_{inet} \rangle$. Plotting these radii on their respective atomic site, given by i, a spin-distribution diagram is formed. The polarisation can also be used to define the ordering of the spin leading to edge-magnetisation. This edge-magnetisation is defined as:

$$\begin{aligned} M_{edge_\uparrow} &= \sum_{i=edge} \theta(\langle n_{inet} \rangle) \langle n_{inet} \rangle \\ M_{edge_\downarrow} &= \sum_{i=edge} \theta(-\langle n_{inet} \rangle) |\langle n_{inet} \rangle| \end{aligned} \tag{2.82}$$

where $\theta(x)$ is the Heaviside step function [142]:

$$\theta(x) = \begin{cases} 1 & \text{if x} > 0 \\ 0.5 & \text{if x} = 0 \\ 0 & \text{if x} < 0 \end{cases} \tag{2.83}$$

## 2.6 Hubbard Model

An exact solution of the Hubbard model was investigated by Lieb and Mattis [143] in 1962 and by Lieb and Wu [144] in 1968 for an infinite 1D lattice at half-filling and then by Hirsch [139] in 1985 for an infinite 2D square lattice using the mean-field approximation. Lieb and Mattis [143] demonstrated that for an infinite 1D lattice ferromagnetism cannot occur with only 1st nearest-neighbour hopping. Lieb and Wu [144] demonstrated that in a 1D system for $U \neq 0$ the Mott transition does not occur. The Mott transition is the transition from a metallic band structure to a insulating structure [145]. Hirsch [139] discussed the Hartree-Fock phase diagram and used numerical calculations to predict the diagram though Monte Carlo methods (Figures 2.2 and 2.3). The Hartree-Fock phase diagram (Figure 2.2) demonstrates the phase transitions from a lowest energy paramagnetic state to a lowest energy

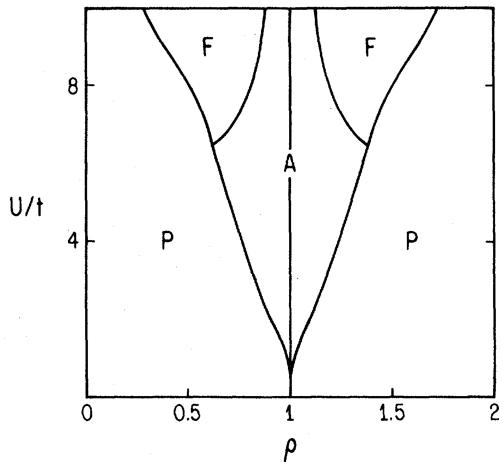


Figure 2.2: Hartree-Fock phase diagram for a Hubbard model on a 2D square lattice. P, F and A denotes paramagnetic, ferromagnetic and antiferromagnetic lowest energy states respectively. $U/t$ is the ratio between the value of Hubbard-$U$ and the nearest-neighbour hopping parameter and $\rho$ is the band filling. Reproduced from Hirsch [139].

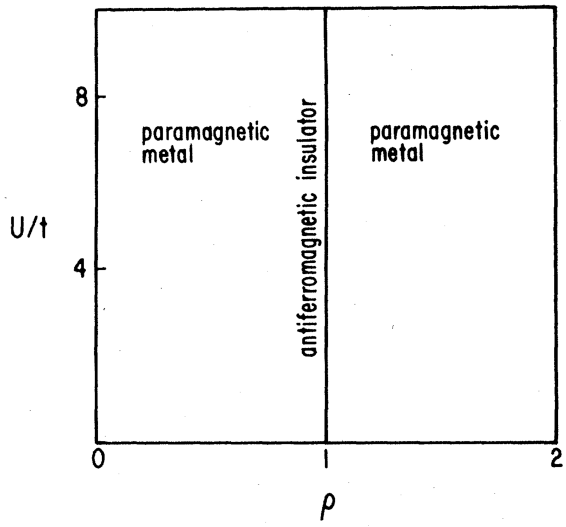


Figure 2.3: Lowest energy-state phase diagram found though numerical calculations by Hirsch [139]. $U/t$ is the ratio between the value of Hubbard-$U$ and the nearest-neighbour hopping parameter and $\rho$ is the band filling. Reproduced from Hirsch [139].

antiferromagnetic or ferromagnetic state as the $U$/t ratio and band filling increases. For this, $U$ is the Hubbard-$U$ and t is the first nearest-neighbour hopping parameter and the square lattice is a Mott-insulator [145] for all $U \neq 0$. Figure 2.2 shows that at half-filling and for $U << \infty$ the system is predicted to have an antiferromagnetic lowest energy-state phase [139]. The antiferromagnetic nature will lead to the spin-distribution observed in Figure 2.4. It is not until $U$ is very large [139] that a ferromagnetic lowest energy-state phase transition occurs at half-filling, in agreement with the more rigorous solution by Nagaoka [146], who demonstrated a ferromagnetic lowest energy-state solution when $U{=}\infty$. This ferromagnetic state is due to the repositioning of holes though the system giving rise to a linear combination of spin-configurations and therefore ferromagnetism [146, 147]. This "Nagaoka ferromagnetism" only

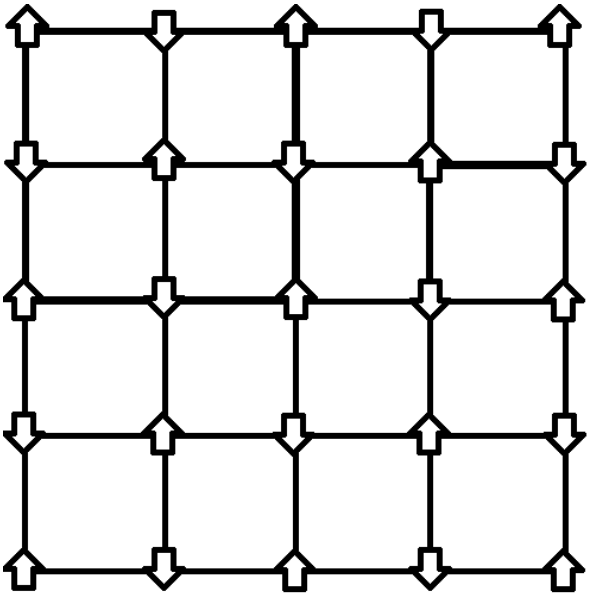

Figure 2.4: Antiferromagnetic spin-distribution diagram for a 2D square lattice grid using a mean-field Hubbard model at half-filling.

occurs in 2D square lattices when $U{=}\infty$ and thus it would be of interest to find a system in which this occurs at finite $U$ and finite density holes [146, 147]. Unfortunately, the numerical simulations carried out by Hirsch [139] into an exact solution via Monte Carlo methods does not give the same phase diagram (Figure 2.3) as the Hartree-Fock approximation. Hirsch [139] carried out Monte Carlo numerical calculations for a half-filled system and various U/t ratios and for a non-half-filled system with U/t=4 and 8 and used the results to predict the phase diagram in Figure 2.3. Hirsch [139] was unable to demonstrate a ferromagnetic lowest energy-state phase regardless of the band filling or $U$/t ratio. Hirsch [139] concluded that the Hartree-Fock approximation was therefore a better approximation as Monte Carlo numerical results do not describe itinerant magnetism as it is an incompetent description of the physics involved.

Sorella and Tosatti [149] demonstrated in 1992 that, for a hexagonal lattice, there is a Mott transition between the nonmagentic semi-metal lowest energy state and the antiferromagnetic insulator lowest energy state at $U/t = 4.5 \pm 0.5$, found using quantum Monte Carlo methods. Peres *et al.* [148] carried out similar Hartree-Fock phase diagram calculations for a infinite hexagonal 2D lattice (Figure 2.5), both with 1st nearest-neighbour hopping only (Figure 2.5(a)) and with 1st and 2nd nearest-neighbour hopping (Figure 2.5(b)). They found similar lowest energy-state phase transitions, with a large paramagnetic lowest energy-state phase in the 1st nearest-neighbour hopping only model for $n < 0.74$ compared to a large Nagaoka ferromagnetic lowest energy-state phase in the 1st and 2nd nearest-neighbour hopping model for $n < 0.9$. This is of interest as previously Nagaoka ferromagnetism had only occurred at infinite $U$, at least for square lattices. Hanisch *et al.* [150] have also demonstrated Nagaoka ferromagnetism in triangular, Kagome and hexagonal lattices. As Figure 2.5 shows,

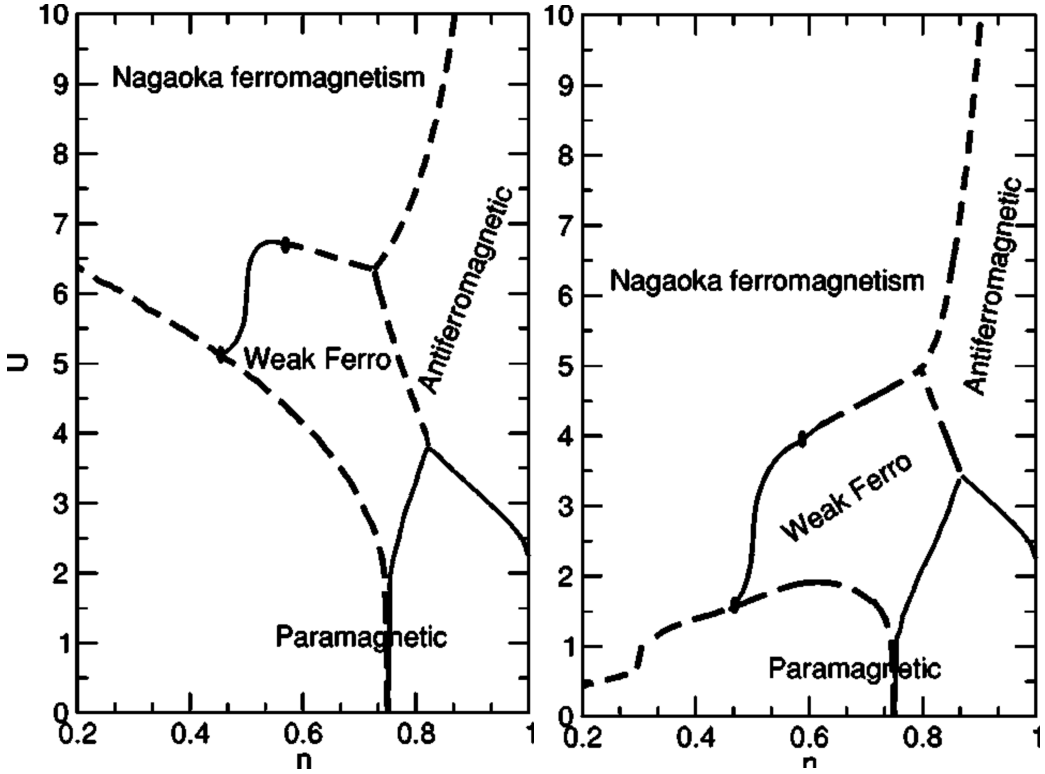


(a) (b)

Figure 2.5: Hartree-Fock phase diagram for a 2D Hubbard model of a hexagonal lattice. (a) 1st-nearest neighbour Hubbard model. (b) 1st and 2nd nearest-neighbour Hubbard model. Reproduced from Peres *et al.* [148].

at half filling (n=1) and $U$=2, the bulk hexagonal system is predicted to be paramagnetic for both the 1st nearest-neighbour hopping only and for 1st and 2nd nearest-neighbour hopping models. Due to the finite nature of graphene nanoribbons, this prediction cannot be assumed to be accurate outside of the bulk limit, as demonstrated by Son *et al.* [32], who predicted a antiferromagnetic lowest energy state using DFT LSDA calculations.

## 2.7 Landauer-Büttiker (Coherent) Transport Formalism

The transport calculations are carried out using the Landauer-Büttiker (LB) Formalism [51]:

$$G_\sigma(E) = \frac{e^2}{h}\bar{T}_\sigma(E) \tag{2.84}$$

where $G_\sigma$ is the spin-dependent conductance, i.e., the inverse of the resistance of the system. $\bar{T}_\sigma$ is the spin-dependent transmission function, the probability that an electron with spin $\sigma$ from one lead will transmit to the other and not be reflected and $e^2/h$ is defined as the unit of quantum conductance. The LB formalism assumes the system to be ballistic so that there is no reflection of electrons inside the device and any resistance is due to the lead-device contacts [51]. Ballistic transport has been experimentally confirmed for bulk graphene [28, 29]. For this investigation coherent transport is assumed in GNRs. Coherent

transport ignores electron-electron and electron-phonon interactions [51].

Following Ref [51] it is possible to derive Equation 2.84 from the electrical current from the electrons in the lead:

$$I_{\alpha nE} = \frac{e}{L}\sum_{k} T_{n\sigma}(E)v(k)f(E-\mu_{\sigma}) \tag{2.85}$$

where $v(k)$ is the group velocity of the electrons, $f(E-\mu_{\alpha})$ is the Fermi-Dirac distribution of the population of the states, with $\mu$ the chemical potential of each of the leads, $\alpha = 1, 2$. $T_{n\sigma}$ is the spin-dependent transmission function for channel n with energy E(k) and spin $\sigma$. By summing the difference in current between the two leads over all quantum channels and assuming current flows from lead 1 to lead 2, the net current can be found [51]:

$$I = \sum_{n}[I_{1nE} - I_{2nE}] \tag{2.86}$$

$$I = \frac{e}{L}\sum_{nk} T_{n\sigma}(E)v(k)(f(E-\mu_1) - f(E-\mu_2)) \tag{2.87}$$

with $f(E-\mu_{1(2)})$ the Fermi-Dirac distribution in lead 1(2). By assuming current from the lead to the device is positive and [51]:

$$\sum_{k} \rightarrow \frac{L}{2\pi}\int dk \tag{2.88}$$

$$v(k) = \frac{dE}{\hbar dk}. \tag{2.89}$$

Equation 2.87 becomes [51]:

$$I = \frac{e}{h}\sum_{n}\int dE T_{n\sigma}(E)(f(E-\mu_1) - f(E-\mu_2)). \tag{2.90}$$

Assuming low temperature and voltage, V, ($Ve = \mu_1 - \mu_2$), $f(E-\mu_1) - f(E-\mu_2)$ can be Taylor expanded around the Fermi energy [51]:

$$f(E-\mu_1) - f(E-\mu_2) \approx \delta(E-E_F)(\mu_1-\mu_2) \tag{2.91}$$

where $\delta$ is a delta function. Using this and Equation 2.90, the conductance though the system becomes [51]:

$$G(E_F) = \frac{I}{V} = \frac{\frac{e}{h}\sum_n \int dE T_{n\sigma}(E)\delta(E-E_F)(\mu_1-\mu_2)}{V} \tag{2.92}$$

$$G(E_F) = \frac{e^2}{h}\sum_{n} T_{n\sigma}(E_F) = \frac{e^2}{h}\bar{T}_{\sigma}(E_F) \tag{2.93}$$

where $\bar{T}_{\sigma}$ is the sum of all spin-dependent transmission probabilities.

To solve Equation 2.84 it is possible to calculate the transmission function using Green's functions (following Ref[51]):

$$[E - H]G(\mathbf{r}, \mathbf{r'}, E) = \delta(\mathbf{r\text{-}r'}) \tag{2.94}$$

where H is a Hamiltonian, in this study the GTB Hamiltonian, E is the energy associated with H and G(**r**,**r'**,E), the Green's function for two points, **r** and **r'**. The Green's function can be rewritten as an operator [51]:

$$G(\mathbf{r}, \mathbf{r'}, E) = \langle \mathbf{r}|G(E)|\mathbf{r'}\rangle. \tag{2.95}$$

When E is not an eigenvalue of the Hamiltonian, H, then the Green's function is formally written in terms of the Green's function operator [51]:

$$G(E) = [E - H]^{-1} \tag{2.96}$$

Green's functions can describe the effect of an excitation in one lead at the other lead; The retarded Green's function, $G(E)^R$, is the solution to the Green's function such that an excitation causes an outgoing wavefunction starting at the point of excitation. The advanced Green's function, $G(E)^A$, is the solution to the Green's function such that an excitation causes an incoming wavefunction disappearing at the point of excitation. The two solutions can be distinguished by the inclusion of an infinitesimally small imaginary term, $\eta$, such that a positive term gives the retarded solution and the complex conjugate gives the advanced solution [51]:

$$G(E)^R = G(E)^{A*} = [(E + i\eta)I - H]^{-1} \tag{2.97}$$

where I is the identity matrix.

The spin-dependent transmission function, Equation 2.84, can be written in terms of Green's function operators using the Fisher-Lee relation[51, 151] such that the spin-dependent transmission function between two leads (left (l) and right (r)) is [51]:

$$\bar{T}(E)_\sigma = Tr[\Gamma(E)_{l,\sigma} G(E)^R_\sigma \Gamma(E)_{r,\sigma} G(E)^A_\sigma] \tag{2.98}$$

where $\bar{T}(E)_\sigma$ is the spin-dependent transmission function, $\Gamma(E)_{l(r),\sigma}$ is the spin-dependent Gamma function, describing the coupling of the device to the left(right) lead. This spin-dependent broadening term can written as [51]:

$$\Gamma(E)_{l(r),\sigma} = i[\Sigma(E)^R_{l(r),\sigma} - \Sigma(E)^A_{l(r),\sigma}] \tag{2.99}$$

where $\Sigma(E)^R(A)_{l(r),\sigma}$ is the retarded(advanced) spin-dependent self-energy for the left(right)

lead. This spin-dependent self-energy describes the interactions between the device and leads. This can be expressed in terms of the surface Green's function for the leads and the coupling between the device and leads [51]:

$$\Sigma(E)^{R(A)}_{l(r),\sigma} = V^{\dagger}_{l(r)\ sys} g(E)^{R(A)}_{l(r)} V_{l(r)\ sys} \tag{2.100}$$

$V_{l(r)}$ gives the coupling between the device region and the left(right) lead, and $g(E)^{R(A)}$ is the retarded/advanced surface Green's function for the leads. The self-energy describes the effect of the semi-infinite leads on the device as these semi-infinite leads cannot be solved analytically.

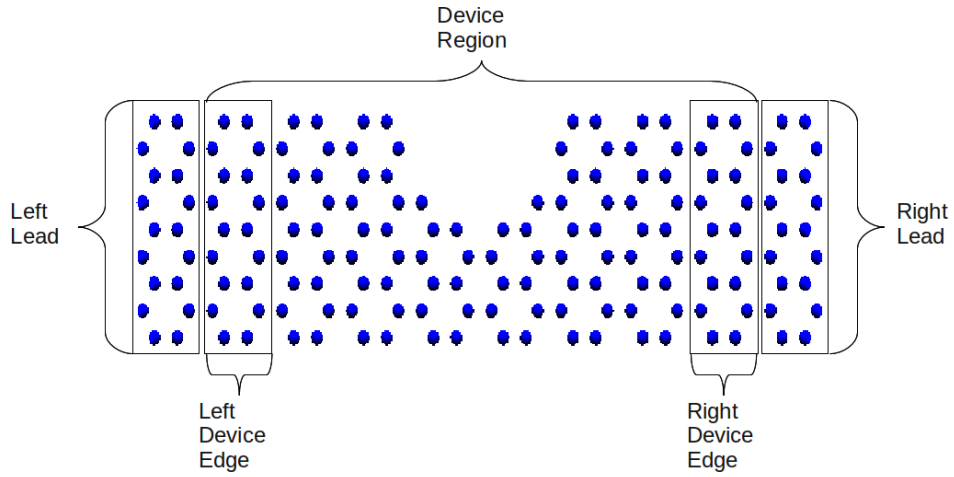


Figure 2.6: Diagram to demonstrate the five regions used in the model, the device region, the left and right device edges, and the left and right leads.

The Hamiltonian in Equation 2.97 can be broken down into its components (Figure 2.6) [152, 153, 51]:

$$H = \begin{pmatrix} H_{\text{left lead}} & H_{\text{left lead/device}} & 0 \\ H_{\text{device/left lead}} & H_{device} & H_{\text{device/right lead}} \\ 0 & H_{\text{right lead/device}} & H_{\text{right lead}} \end{pmatrix} \tag{2.101}$$

where $H_{\text{left lead/right lead}}$ is assumed to be zero. If this is not the case, then there are interactions between the two leads in this theoretical approach and the device must be increased in length such that the two leads are decoupled [152, 153].

The Green's function associated with the device region is defined as [51, 152]:

$$G^{R}_{\sigma}(E) = [(E + i\eta)I - H_{device} - \Sigma(E)^{R}_{l,\sigma} - \Sigma(E)^{R}_{r,\sigma}]^{-1} \tag{2.102}$$

$g(E)^{R/A}$ and therefore, $\Sigma(E)^{R}_{l,\sigma}$, can be calculated using a decimation method [154]. This is an iterative method that incorporates the semi-infinite leads into the device.

Using the decimation method, Equations 2.99 and 2.102, and $\Sigma^{A}_{l/r} = \Sigma^{R*}_{l/r}$, $\Gamma(E)_{l,\sigma}$ can be found and therefore, via Equation 2.98, $\bar{T}_{\sigma}$.

### 2.7.1 Device/Lead Convergence

One important factor that can influence the transport properties in the LB formalism is discontinuities in the spin-polarisation (Equation 2.81) between the lead and the device. Disorder can reduce the spin-polarisation of the system, as demonstrated by Huang *et al.* [50], but the LB formalism assumes non-defected leads. These non-defected leads are required for the spin-polarisation to be converged back to the ideal to prevent discontinuities. If there are discontinuities between the spin-polarisation in the leads and the spin-polarisation in the device then spin-scattering occurs leading to changes in the LB transport properties. To prevent artificial spin-scattering, a non-defected region is required in the device of sufficient length to prevent discontinuities from forming [152]. The convergence was initially carried out using unstrained notch devices (devices patterned along one edge to include a notch shape) and a region of 5 atoms was determined to be sufficient [155]. It was discovered that the introduction of strain greatly increases the distance from the disorder over which the spin-polarisation is perturbed and therefore requires longer non-defected regions when compared to unstrained systems. The insufficient ideal region led to artificial back scattering and reduced the transport gaps more than was physical [155]. To find the relevant non-defected region required, the spin-polarisation of the edge atoms at the device/lead boundary is converged to the ideal result with increasing region length.

### 2.7.2 GRUI

Due to the large number and complexity of the systems studied, the **GR**aphene **U**ser **I**nterface (GRUI) [156] is used to automate the generation of structures with random edge-disorder, and to visualise the asymmetrical systems used. The GRUI also allows the superposition of known structures, either relaxed DFT systems or experimental images, in order to fit the static tight-binding system to a known result. The GRUI also automatically introduces Harrison scaling allowing the hopping parameters to be reparameterised depending on the system.

## 2.8 Uniaxial Strain

Uniaxial strain is another topic that has been studied in depth using both DFT and tight-binding methods. Uniaxial strain can control the properties of graphene devices in a predictable, controllable way [105, 106, 107, 108, 109, 110, 111, 112, 113, 114, 115, 122]. For example, uniaxial strain can lead to a metal/semiconductor transition in both bulk and

nanographene [110, 111], as well as providing a controllable way of perturbing the band-gap [106, 110, 111, 114, 115] and coherent electronic transport [107, 111]. Uniaxial strain can arise due to a lattice mismatch with the substrate [116, 117, 118] or via direct application [119, 120, 121].

### 2.8.1 Harrison Scaling

Uniaxial strain, i.e., uniform strain in one direction, is modelled in the graphene systems though perturbing the hopping parameters. Harrison scaling [109, 123] is the simplest method of perturbing the parameters, assuming a $1/r^2$ dependence on atomic separation. This method is used as it simplest when compared to methods such as exponential scaling which requires parametrisation [123]. Harrison scaling perturbs the hopping parameters such that [123]:

$$t' = t(\frac{r_0}{r})^2 \tag{2.103}$$

where $t(t')$ is the unstrained(strained) hopping parameter and $r_0(r)$ is the unstrained(strained) bond length.

Another option for scaling is exponential scaling [124]. This uses exponential decay to scale the hopping parameters [124],

$$t' = t(exp^{-A\frac{r}{r_0-1}}) \tag{2.104}$$

where $A$ is fitted to the particular system. This fitting is system dependent and thus, for this early exploratory work, the simpler Harrison scaling is used as the interest is in general trends instead of exact, precise, values.

Harrison scaling was initially used for uniaxial strain in bulk, nano and non-graphene [108, 109, 115, 122] devices and was first proposed by Harrison in 1980 [123]. Harrison scaling allows general trends to be probed as uniaxial strain was introduced to various devices. Exponential scaling was introduced in 1998 [124] and was demonstrated to be a more accurate description of uniaxial strain in graphene devices [106]. Currently, exponential scaling is generally used in preference to Harrison scaling for detailed probing of properties, with each author/paper generally using a fitting parameter, $A$, for each system investigated. Due to the various structural perturbations being studied in this work, the Harrison scaling method is used.

### 2.8.2 Poisson Ratio

The Poisson ratio connects the strain in one direction with the compression in the other due to the Poisson effect [123]. This states that a material compressed in one dimension will expand in the other two, and vice-versa. As graphene is assumed to be a 2D material, the Poisson effect does not occur in the out-of-plane direction and thus can be ignored. The

Poisson ratio relates the uniaxial strain in the x- ($\epsilon_x$) and y- ($\epsilon_y$) directions by [123],

$$\epsilon_x = -P\epsilon_y, \tag{2.105}$$

where P is the Poisson ratio and [123],

$$\epsilon_{x(y)} = \frac{(r_{x(y)} - r_{x(y)0)})}{(r_{x(y)0})}, \tag{2.106}$$

where $r_{x(y)}$ is the strained bond length in the x(y)-direction and $r_{x(y)0}$ is the unstrained bond length in the x(y)-direction. For this investigation, a Poisson ratio of 0.186 was used, taken from Liu *et al.* [118], found using DFT LDA calculations with the ABINIT [157, 158] package.

## 2.9 Density Functional Theory

In order to confirm the accuracy of the generalised tight-binding model, in-house DFT calculations using the local spin-density approximation (LSDA) were carried out within the Vienna *Ab-initio* simulation package (VASP) [70] and the Order-N Electronic Total Energy Package (ONETEP) [159, 160]. Density functional theory uses functionals to describe the many-body electron interaction problem and leads to Kohn-Sham potentials [34].

This starts by defining the variational principle [34, 141],

$$E_{model} \geq E_{actual}, \tag{2.107}$$

but defined as a functional of the electron densities [34]:

$$E[n] = min_{\Psi|n} \int \Psi^* \bar{H} \Psi d^{3N} r \tag{2.108}$$

subject to the constraint [34]:

$$\int n(r) d^3\mathbf{r} = N \tag{2.109}$$

where $min_{\Psi|n}$ is the minimum with regards to the many-body wave functions $\Psi$ consistent with n(r), the density. N, is the number of electrons and $\bar{H}$ is the total Hamiltonian. The Born-Oppenheimer approximation [161][2] allows the separation of the Hamiltonian into a Hamiltonian for the electrons and an external potential due to the ions. This allows us to separate Equation 2.108 into [161]:

$$E[n] = min_{\Psi|n} \int \Psi^* \bar{H}_0 \Psi d^{3N}\mathbf{r} + \int V_{ext}(\mathbf{r}) n(\mathbf{r}) d^3\mathbf{r} \tag{2.110}$$

where $\bar{H}_0$ is the Hamiltonian of the electron gas and $V_{ext}$ is the external, ion potential. Kohn

[2] An English language translation of the original paper can be found at http://www.ulb.ac.be/cpm/people/scientists/bsutclif/bornopn_corr.pdf. Online as of 070214

and Sham [34] defined the first term of this equation as a functional dependent only on $n$, $F[n]$, and thus removed the dependence on external potential. This functional can therefore be described as a universal functional of the electrons only.

Kohn and Sham [34] separated this unknown universal functional into three components:

$$F[n] = T[n] + \frac{1}{2}\iint \frac{n(\mathbf{r}')n(\mathbf{r})}{|\mathbf{r}-\mathbf{r}'|}d^3\mathbf{r}'d^3\mathbf{r} + E_{xc}[n] \tag{2.111}$$

where $T[n]$ is the kinetic energy functional of a non-interacting system with density $n(r)$, the second term is the coulomb repulsion energy, the third term is the exchange-correlation energy [34] :

$$E_{xc} = E_x + E_c \tag{2.112}$$

where $E_x$ is the exchange energy, $E_c$ is the correlation energy and therefore $E_{xc}$ includes all many-body effects.

The kinetic energy functional is defined as the kinetic energy of a set of non-interacting electrons with the exact same density as the interacting electrons and thus becomes [34] :

$$T = -\frac{1}{2}\nabla^2\psi_j \tag{2.113}$$

where $\psi_j$ are the Kohn-Sham orbitals. Equation 2.108 can now be minimised giving the Kohn-Sham equations [34]:

$$(T + V_{eff})\psi_j = \epsilon_j\psi_j \tag{2.114}$$

$$n(\mathbf{r}) = \sum_j^N |\psi_j(\mathbf{r})|^2 \tag{2.115}$$

$$V_{xc}(\mathbf{r}) = \frac{\delta E_{xc}[n(\mathbf{r})]}{\delta n(\mathbf{r})} \tag{2.116}$$

$$\tag{2.117}$$

Where $V_{eff}$ is an effective potential [34],

$$V_{eff}(\mathbf{r}) = \int \frac{n(\mathbf{r}')}{|\mathbf{r}-\mathbf{r}'|}d^3\mathbf{r}' + V_{xc}(n(\mathbf{r})) + V_{ext}(n(\mathbf{r})), \tag{2.118}$$

and all unknown terms are contained in $V_{xc}$, the exchange correlation potential. If the exact $E_{xc}$ is used then the Kohn-Sham equations are also exact. The only error in the ground state energy will be from the error in $E_{xc}$. The ground state energy is given by [34]:

$$E_0 = \sum_j^N \epsilon_j - \frac{1}{2}\iint \frac{n(\mathbf{r}')n(\mathbf{r})}{|\mathbf{r}-\mathbf{r}'|}d^3\mathbf{r}'d^3\mathbf{r} - \int V_{xc}(\mathbf{r})n(\mathbf{r})d\mathbf{r} + E_{xc}[n(\mathbf{r})] \tag{2.119}$$

where $\epsilon_j$ and $n$ are found self-consistently.

The forces can be found using the Hellmann-Feynman theorem [162]:

$$F_\lambda = \nabla_\lambda E_0(\mathbf{r}) \tag{2.120}$$

$$= \frac{\partial}{\partial\lambda}\langle\Psi_0(\mathbf{r})|H|\Psi_0(\mathbf{r})\rangle \tag{2.121}$$

$$= \langle\Psi_0(\mathbf{r})|\nabla_\lambda H|\Psi_0(\mathbf{r})\rangle \tag{2.122}$$

where $\Psi_0$ is the ground state wavefunction, $\lambda$ the atomic position of an atom at spatial coordinate, $\mathbf{r}$. The forces acting on atoms at $\lambda$ are therefore found via the expectation value of the gradient of $H$. The expectation value of the gradient of $H$ can be calculated when $n_0(r)$ and thus $\Psi_0$ is known. The forces acting on the atoms at $\lambda$ can then used to determine the new value of $n_0(r)$. This self-consistent method is iterated until the forces are minimised.

In this thesis, the local spin density approximation (LSDA) is used for the exchange-correlation functional. The LSDA, developed by Langreth *et al.* [35] assumes a slowly varying density such that [35]:

$$E_{xc}[n_\uparrow(\mathbf{r}), n_\downarrow(\mathbf{r})] = \int d^3\mathbf{r}(n_\uparrow + n_\downarrow)\epsilon_{xc}^{unif}(n_\uparrow(\mathbf{r}), n_\downarrow(\mathbf{r})) \tag{2.123}$$

where $\epsilon_{xc}^{unif}$ must be parametrised via analytic functions, for example, the exchange-correlation energy per particle of an uniform electron gas [35].

The Kohn-Sham [34] equations can be solved by expanding the eigenfunction in terms of the plane-waves [34]:

$$\varphi_j(\mathbf{r}) = \sum_{\mathbf{k}} c_{j\mathbf{k}} exp(i\mathbf{k}.\mathbf{r}) \tag{2.124}$$

where $c_{j\mathbf{k}}$ is the plane wave coefficient. Due to the discrete, non-finite, nature of computational methods, an energy cut off, $E_{cut}$, for the plane-wave basis must be specified along with the resolution of the mesh describing k-space. Analytically, both $E_{cut}$ and the K-point grid resolution are infinite but this will not be viable, both in terms of CPU and memory cost. Therefore, these values must be converged such that a compromise is reached between accuracy and efficiency. For our results, an energy cut-off of 800eV was used along with a k-points grid of {1, 1, 14} in the x, y and z direction due to the 1D nature of the ribbon.

The following secular equation is formed from substituting Equation 2.124 into Equation 2.114 [34]:

$$\sum_{\mathbf{k'}}(\mathbf{k}^2\delta_{\mathbf{k},\mathbf{k'}} + V_{hartree}(\mathbf{k}) + V_{xc}(\mathbf{k}-\mathbf{k'}) + V_{ext}(\mathbf{k}-\mathbf{k'}))c_{j,k} = \epsilon_j c_{j,k} \tag{2.125}$$

and thus can be solved via an iterative matrix solver matrix solver. For VASP [70], the external potentials are described though the projector augmented-wave method (PAW) [163, 164], calculated by Kresse and Joubert [164]. ONETEP [159, 160], on the other hand, limits

electron-electron interactions to a finite range with interaction outside of a cut-off distance assumed to be insignificant. For ONETEP to be efficient, the system has to be bigger than the cut-off distance. In this study, ONETEP is used for systems too large to be computationally tractable for VASP while still requiring the accuracy required for DFT/GTB comparison.

## 2.10 Conclusion

This Chapter has has laid out the important theories required by this investigation. In particular, the GTB model has been derived and the key parameters discussed. The LB formalism and DOS equations have been presented, along with the details of spin-polarisation and edge-magnetisation. Finally, the DFT method is derived and the LSDA introduced. The two DFT packages, VASP and ONETEP, are also discussed. With these theoretical methods laid out, they must be tested against known results before new results can be calculated with any confidence. The next Chapter will present these initial tests and the validity of the methods will be demonstrated.

# Chapter 3

# Model and Convergence Testing

## 3.1 Abstract

Before any new implementation of a model is used, it must first be tested against known results. This chapter compares the band structure and electronic transport of AGNR and ZGNR systems and the spin-polarisation and density of states of ZGNR systems with published work. The effects of 1st, 2nd and 3rd nearest-neighbour hopping and Hubbard-$U$ parameters are investigated and compared to known results. The main features, including the band- and conduction- gaps, and edge-states, in both LSDA and GGA DFT, and existing tight-binding models are reproduced and the accuracy of the model is confirmed.

As previously discussed, the biggest advantage of the mean-field Hubbard model is that it is an extremely efficient, real-space method of producing the band structures, and other physical properties, required of the nanographene system. *Ab-initio* DFT calculations have previously been performed, but these are extremely inefficient for the size and complexities of the systems required [70]. In a real-space tight-binding model, one can introduce defects and impurities, and hence large unit cells, or matrices, can be generated and solved using an efficient, black-box eigensolver. The program developed for this thesis, uses the ZHEEV routine from LAPACK [165] to solve the eigenproblem. The flexibility in the tight-binding model allows us to study interesting effects, such as the role of nanopatterning, for example, constrictions, impurities, edge defects, mixed edges, on GNRs due to the significantly larger system sizes accessible.

In the case of a graphene nanoribbon (GNR), the hopping will be taken up to third nearest-neighbour to allow an acceptable compromise between computational efficiency and accuracy leading to a minimal model. The value of the hopping parameter will also depend on the distance between the connected sites.

## 3.2 Tight-Binding Model Tests

To find the model parameters required for Equation 2.67, i.e., the generalised tight-binding model (GTB), the band structure and band-gap results of the GTB model are fitted to *ab initio* density functional theory (DFT). Previous work by Hancock *et al.* [33], fitted the GTB model to both zig-zag graphene nanoribbons (ZGNRs) and armchair graphene nanoribbons (AGNRs) systems using DFT, local spin-density approximation (LSDA) calculations in the SIESTA package [16]. This allows a reduced generalised Hubbard model to be defined, which is applicable to both AGNR and ZGNR systems. Due to the large number of variables, the fitting was carried out by eye [33].

The parameters determined by Hancock *et al.* [33] are:

$$t_1 = 2.7eV \tag{3.1}$$

$$t_2 = 0.2eV \tag{3.2}$$

$$t_3 = 0.18eV \tag{3.3}$$

$$U = 2.0eV \tag{3.4}$$

Care must be taken when dealing with the result of any calculation as the energy output may not be the lowest energy obtainable by the model for a particular system. By adiabatically converging the Hubbard-$U$ term, the energy landscape can be explored and therefore the lowest energy found. Different starting configurations and multiple tests of each system must be used to make sure the lowest energy state is being explored. Note, due to the variational principle, the lowest energy found by the model will always be equal to or larger than the real ground state and therefore we must compare the energy obtained with other models and experimental results.

The first test carried out with the new version of the GTB model was a rigorous test of its accuracy. The implementation was tested to ensure that results found for the ideal ribbons were in agreement with those found in the literature, in particular the GTB model results calculated by Hancock *et al.* [33]. For this initial investigation both AGNR and ZGNR systems were modelled.

### 3.2.1 Armchair graphene nanoribbons (AGNR)

AGNR systems are affected by the third nearest-neighbour (NN) hopping term, $t_3$ [46]. To test the accuracy of the model, the effects of the extended hopping terms were tested on a AGNR system predicted to be half-metal using the 1st NN tight-binding model. It is possible in the GTB model to turn on the hopping terms and check, for $t = t_1, t_1 + t_2$, and $t_1 + t_2 + t_3$, that the band structure produced agrees with known results for 14-AGNR. As Figure 3.1 shows, there is a breaking of the symmetry and an opening of the band-gap as $t_3$

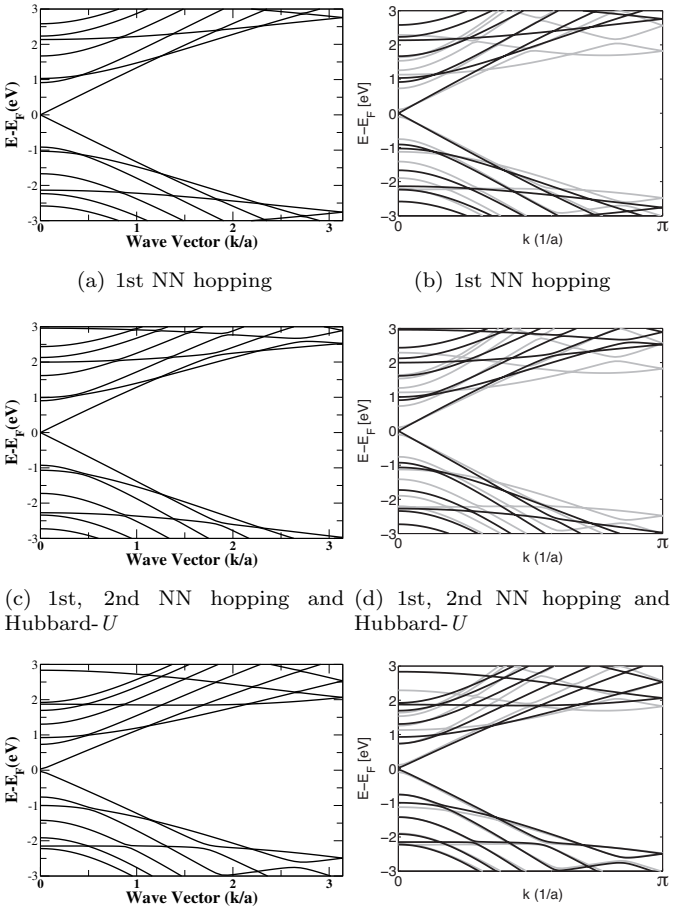


(a) 1st NN hopping

(b) 1st NN hopping

(c) 1st, 2nd NN hopping and Hubbard-$U$

(d) 1st, 2nd NN hopping and Hubbard-$U$

(e) 1st, 2nd, 3rd NN hopping and Hubbard-$U$

(f) 1st, 2nd, 3rd NN hopping and Hubbard-$U$

Figure 3.1: Band structure of a 1-14-AGNR system. The x-axis ranges though k space from 0 to $\frac{\pi}{a}$ in units of $\frac{1}{a}$ and the y-axis gives the energy in eV. This energy is shifted by the Fermi-energy, $E_f$. (a), (c) and (e) were found using this implantation of the GTB model (Equation 2.67) and (b), (d) and (f) were reproduced from the Hancock *et al.* [33] implementation of the GTB model and include the DFT LSDA results calculated via the SIESTA [16] package used for the fitting in grey.

is turned on. The 3rd NN term introduces single-electron interactions across the ribbon, as first demonstrated by White *et al.* [46].

### 3.2.2 Zig-zag graphene nanoribbon (ZGNR)

The ZGNR system, as predicted by theory, has an anti-ferromagnetic spin-structure across the edges and ferromagnetic spin-alignment along an edge [32], demonstrated in the spin-distribution diagram (Figure 3.3). As Figure 3.2 shows, going from the first NN hopping, Figure 3.2(a), to 1st, 2nd and 3rd NN hopping with Hubbard-$U$, Figure 3.2(g), results in an opening of the band-gap for 16-ZGNR. Figure 3.2(a) demonstrates the double edge-state at the Fermi-energy seen in previous published results [40, 42, 43, 44, 45]. Including $t_1$ and the Hubbard-$U$, Figure 3.2(c), leads to the conductance and valence bands around the gap being symmetrical but still includes the open band-gap required. By turning on $t_2$, Figure 3.2(e), the symmetry of the conductance and valence bands is broken. The band gap opening in ZGNR devices is due to the increased edge-localisation of the electrons leading to an anti-ferromagnetic edge-structure. The anti-ferromagnetic nature of ZGNR arises from the flat bands observed in Figure 3.2 leading to a small group velocity.

These investigations on 1-14-AGNR and 1-16-ZGNR have shown that the increased degree of freedom allowed by the 2nd and 3rd NN hopping parameters is required to achieve accurate results but Hancock *et al.* [33] demonstrated that we only need one set of these extended tight-binding model parameters for both ribbon types. It has also been shown that $t_1$ and $t_3$ are the important parameters for AGNR whereas $t_1$, $t_2$ and the Hubbard-$U$ term are the important parameters for ZGNR.

The final band structure test carried out was on bulk graphene, carried out to confirm that the model is still accurate in the bulk limit. As Figure 3.4 demonstrates, the GTB model, Figure 3.4(a), recreates the bulk band structure seen in Figure 3.4(b) between $K$ and $\Gamma$. In addition, Figure 3.4(a) demonstrates the linear dependence of the bands near the Fermi-level combined with the semi-metal nature of the band structure.

## 3.3 Transport Tests

Transport tests were performed on non-primitive ZGNR (Figure 3.5) unit cell sizes used in later investigations. These studies allowed comparisons of the transport properties with published results and also confirmed that taking these systems to larger unit cells did not introduce finite size effects. As Figure 3.5 shows, when compared to literature results (Figure 3.5(b)) there is a qualitative agreement with S.M.-M. Dubois *et al.* [81]. In particular, the edge states due to the flat bands in the ZGNR band structure are observed either side of the band-gap in ZGNR systems and the conduction steps far from the Fermi-energy. There

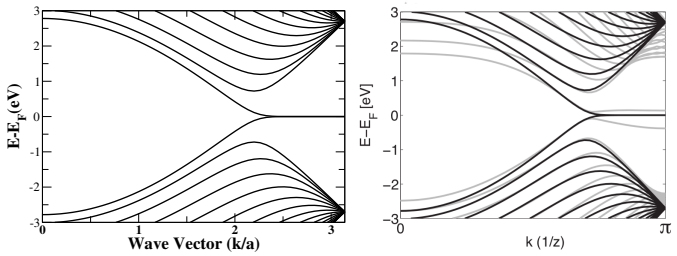


(a) 1st NN hopping (b) 1st NN hopping

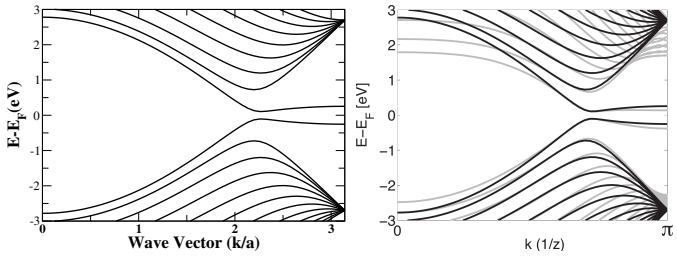


(c) 1st NN hopping and Hubbard-$U$ (d) 1st NN hopping and Hubbard-$U$

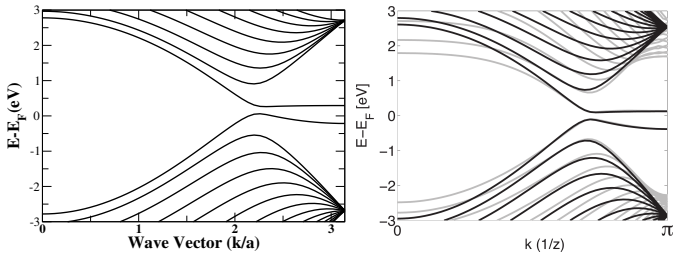


(e) 1st, 2nd NN hopping and Hubbard-$U$ (f) 1st, 2nd NN hopping and Hubbard-$U$

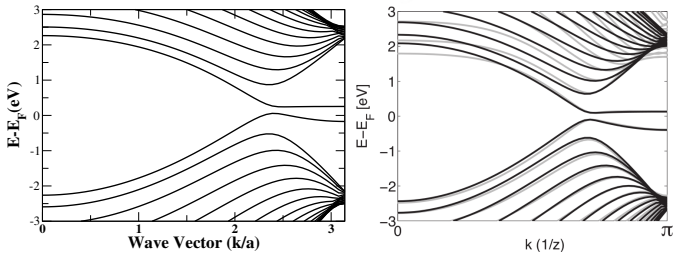


(g) 1st, 2nd, 3rd NN hopping and Hubbard-$U$ (h) 1st, 2nd, 3rd NN hopping and Hubbard-$U$

Figure 3.2: Band structure of a 1-16-ZGNR system. The x-axis ranges though k space from 0 to $\frac{\pi}{a}$ and the y-axis gives the energy in eV. This energy is shifted by the Fermi-energy, $E_f$. (a), (c), (e) and (g) were found using the GTB model (Equation 2.67) and (b), (d), (f) and (h) were reproduced from Hancock *et al.* [33] and include the DFT LSDA results calculated via the SIESTA [16] package results used for the fitting in grey.

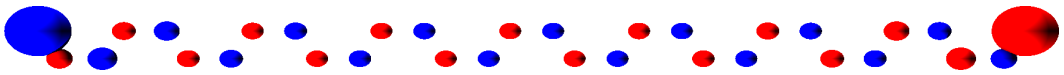

Figure 3.3: Spin-distribution diagram of the ideal 1-16-ZGNR system used in Figure 3.2(g). Red gives spin-up and blue spin-down. The radius of the spheres gives the relative magnitude of $|n_{occupancy}|$ (Equation 2.82). Produced using the GTB model (Equation 2.67).

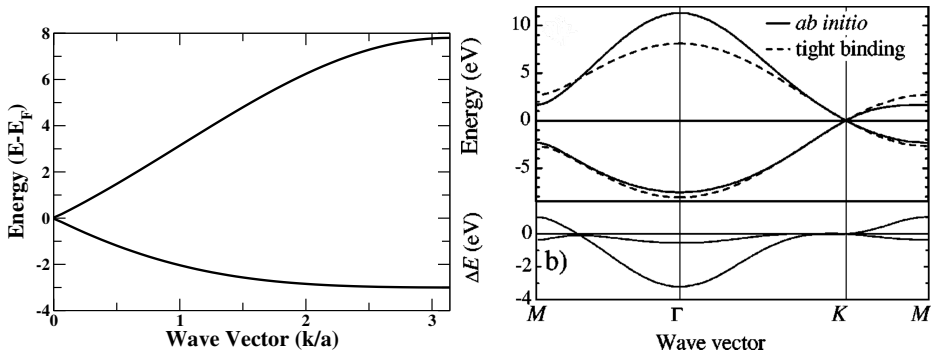


(a) 1st, 2nd, 3rd NN hopping and Hubbard-$U$ (b) Reich *et al.* [15]

Figure 3.4: Band structure of a graphene. The x-axis ranges though k space from 0 to $\frac{\pi}{a}$ and the y-axis gives the energy in eV. This energy is shifted by the Fermi-energy, $E_F$. (a) was found using the GTB model (Equation 2.67) and (b) was reproduced from Reich *et al.* [15]. Figure 3.4(a) maps the wave vector from $K$ to $\Gamma$.

is a slight difference in band gap due to the difference between LSDA and generalised gradient approximation (GGA) DFT scheme. In particular, the edge-states either side of the conductance gap and the energy steps occurring at asymmetrical intervals either side of the conductance results are correctly reproduced.

## 3.4 Conclusion

The chapter has demonstrated the accuracy of the GTB implementation of the tight-binding model. The model has faithfully recreated previous tight-binding results for the band structures and has qualitatively recreated DFT GGA results for transport properties, including band- and conduction-gaps and edge-states in ZGNR systems. The recreation of these results provides confidence that new work presented in the main body of the thesis is correct and accurate. Further more, due to a single set of tight-binding parameters being used for both AGNR and ZGNR, it is possible to investigate the mixed edge structures required in notched systems as well as edge-disordered systems, investigated in the next chapter. The opening of the band-gap in ZGNR with the introduction of the Hubbard-$U$ parameter has also been demonstrated, a key result that will be investigated in the main body of the thesis.

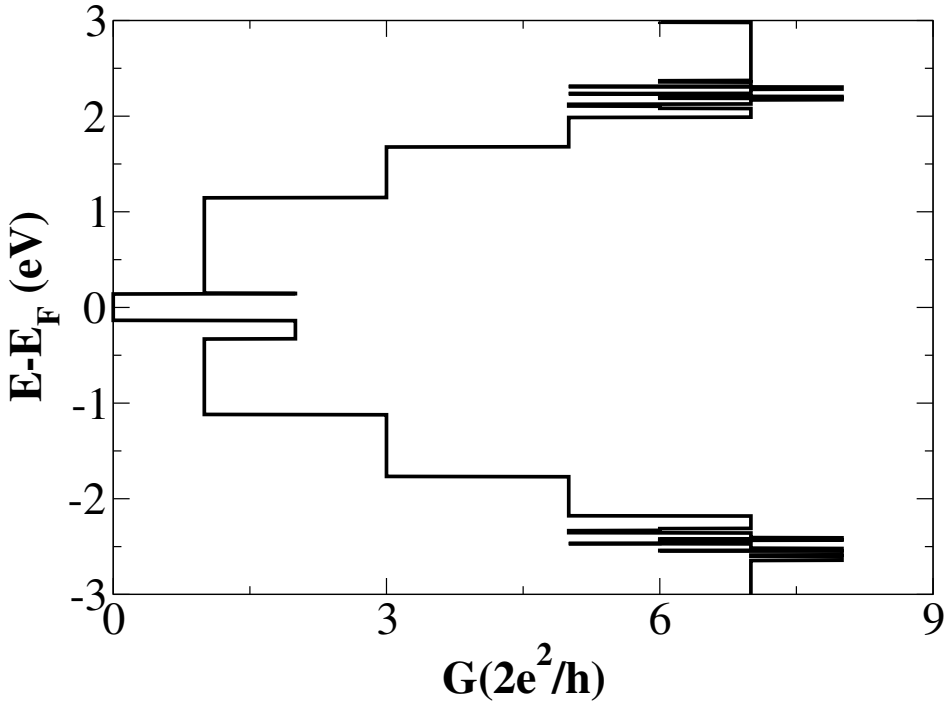


(a) 4-8-ZGNR

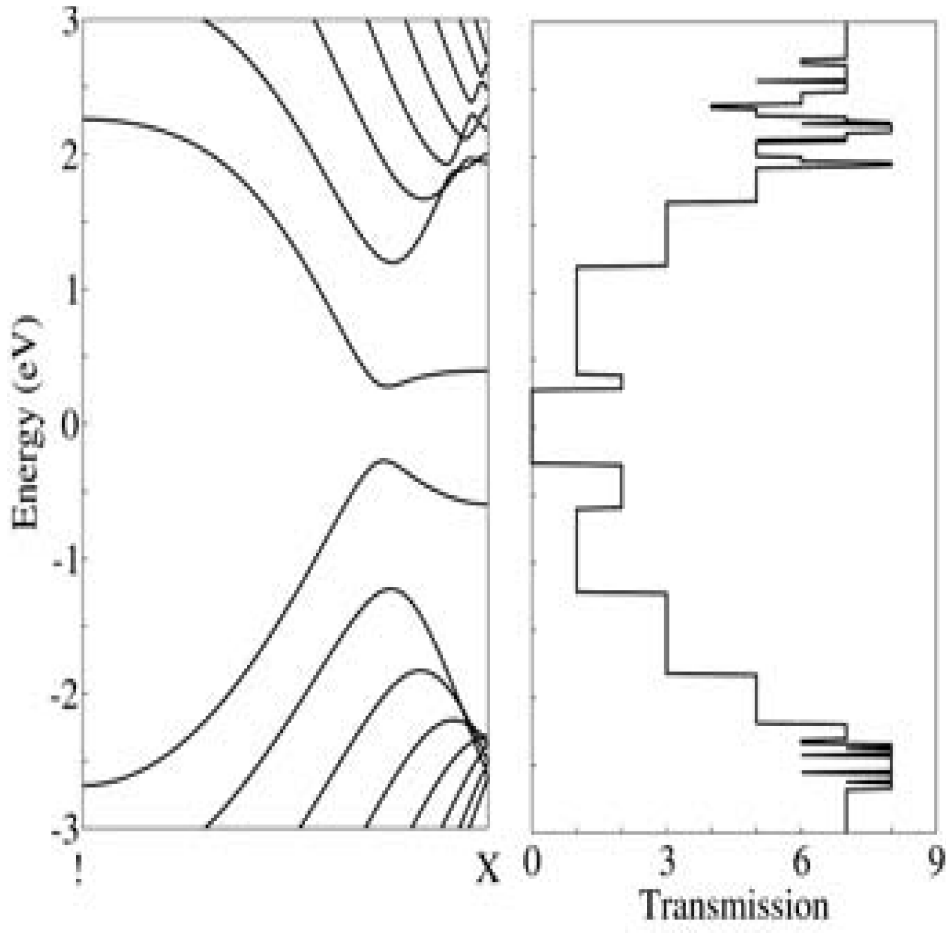


(b) 4-8-ZGNR

Figure 3.5: Spin-dependent transport for 20-5-ZGNR. For perfect systems there is no difference in spin up and spin down transport. (a) was produced using the GTB model (Equation 2.67) whereas (b) was reproduced from S.M.-M. Dubois *et al.* [81] using *ab inito* DFT calculations under the GGA approximation.

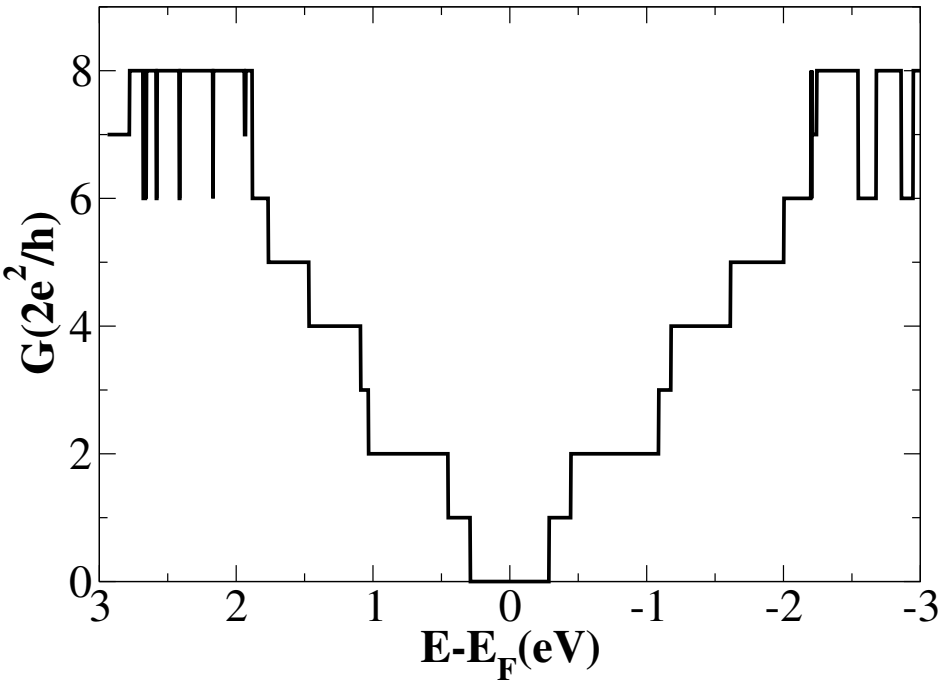


(a) 2-16-AGNR

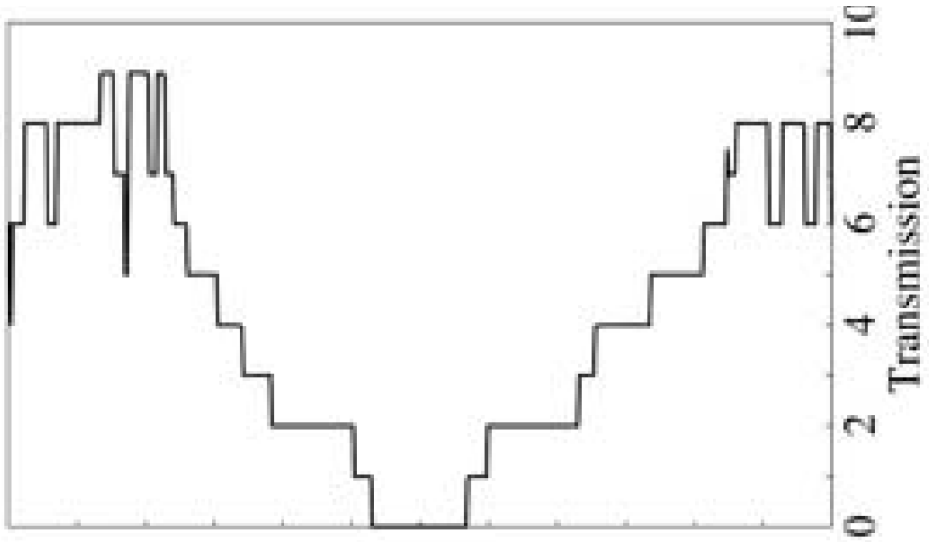


(b) 2-16-AGNR

Figure 3.6: Spin-dependent transport for 20-16-AGNR. For perfect systems there is no difference in spin up and spin down transport. (a) was produced using the GTB model (Equation 2.67) whereas (b) was reproduced from S.M.-M. Dubois *et al* [81] using *ab inito* DFT calculations under the GGA approximation

# Chapter 4

# The Effects of Edge-Vacancies on the Spin-dependent Properties of Zig-zag Graphene Nanoribbons

## 4.1 Abstract

The local magnetisation of 12-6-ZGNRs containing 0%, 8.33%, 16.67% and 33.33% systematic (regularly spaced) edge-vacancies were calculated using the GTB model. Comparison of these results to DFT VASP calculations within the LSDA performed by Huang *et al.* showed that the GTB model faithfully reproduces the DFT results pertaining to the local magnetic properties, including the DFT prediction of the loss of magnetism at 33.33% edge-vacancy concentration. Differences in the edge-magnetism seen in the two models could be attributed to the GTB model not taking into account ionic relaxation. This was confirmed though fitting the positions of the atoms in the GTB model to the relaxed positions found though DFT ONETEP calculations.

Random edge-vacancies, defined as the random removal of carbon atoms along the edges of the device taken over an ensemble average, were also studied to assess their effect on the magnetisation. It was found that, in contrast to the systematic defects, antiferromagnetism was preserved at all edge-vacancy concentrations. This is due to the increased chance of the system containing 3 ideal zig-zag unit cells in a row, in accordance with Clar's theory.

The effects of random edge-vacancies taken over an ensemble average were also investigated to study the spin-dependent coherent transport properties as a function of energy. The dependence of the coherent transport properties on random edge-vacancies has been studied in detail using the STB model in previous literature and has been used to explain the experimental band- and conductance-gaps found in etched GNRs. The issue is that both pristine GNRs created though chemical synthesis and ideal ZGNR devices modelled with the

GTB model, have been found to also contain a band- and conductance-gap, and therefore not requiring random edge-vacancies.

The transport properties of 20-5-ZGNR devices with random edge-vacancies were investigated using the STB, ETB and GTB models to determine if the properties observed in previous STB studies were due to edge-vacancies or from the approximations used in the STB model. It was found that outside of the GTB conductance-gap, the three models follow a similar trend implying that the perturbations observed can be approximated using the non-interacting ETB model. The stability of the GTB conductance gap was also investigated and found to be unperturbed by the introduction of edge-vacancies implying that, at least in terms of conductance gap trends, the GTB model is still more accurate for describing the physics of the system. The differences between the STB model and the ETB and GTB models were further investigated using the energy dependent localisation lengths. It was found that the larger degrees of kinetic freedom of the ETB and GTB models increased the localisation lengths compared to the STB model. For example, at low edge-vacancy concentration (7.5%), the STB model was shown to be fully within the localisation regime, i.e., the regime in which the device is considered weakly disordered, whereas the ETB and GTB models are not.

Finally, the effects of increasing device length were also investigated. It was found that, with increasing device length, there was a exponential decrease in conductance at the Fermi energy for devices modelled with the ETB and STB devices, in agreement with Anderson localisation. Using this exponential decrease in conductance at the Fermi energy, an Anderson localisation length of 47 Å and 49 Å was found for the STB and ETB models respectively. In addition, the onset of the non-interacting, STB and ETB conductance gap was compared to that of the interacting, GTB conductance gap and it was found that, above 120 Å, the trends in conductance gap were similar for all three models.

The results in this Chapter lead to the conclusion that the interacting GTB model is required for the edge-disordered ZGNRs studied, with the intrinsic gap only being overtaken by the disorder-induced conductance gap at device lengths $> 120$ Å. The stability of the intrinsic conductance gap in the GTB model compared to the disorder-induced conductance gap of the STB and ETB models suggests that the experimentally observed band-gap can be attributed to the electron-electron interactions, not the effects of edge-disorder.

## 4.2 The effect of Systematic Edge-Vacancies on the magnetic properties of ZGNRs

Huang *et al.* [50] determined the effect of systematic (regularly spaced) edge-vacancies on the magnetic properties of ZGNRs using VASP DFT [70, 166] within the LSDA. Figure 4.1 shows Huang *et al.*'s results for the local magnetic properties of 12-6-ZGNRs having 0%,

8.33%, 16.67% and 33.33% systematic edge-vacancy concentrations. At 33.33% edge vacancy concentration, the 12-6-ZGNR loses its antiferromagnetic spin-structure and becomes paramagnetic.

The GTB model (Equation 2.67) was applied to these systems and tested against Huang *et al.*'s simulations. Similar to the DFT calculations of Huang *et.al.*, the "edge" in the GTB systems was defined as the first row of carbon atoms along each edge of the ribbon. Thus, the edge-vacancy concentration has been defined as

$$C_{edge} = 100 * \frac{N_{vacancies}}{N_{edge}}, \tag{4.1}$$

where $C_{edge}$ is the % edge-vacancy concentration, $N_{vacancies}$ is the number of edge-vacancies and $N_{edge}$ is the total number of edge-atoms in the non-defected system. The local magnetisation in each structure determined by the GTB model has been calculated using Equation 2.81 (Figure 4.2). Here, the radii of the circles represents the local net-spin $\langle n_{i,}\rangle_{net}$, which have been scaled by $0.5+5*\langle n_i\rangle_{net}$ to allow ease of visualisation. The GTB spin-distributions show a decreasing local magnetisation in each system as the number of edge-vacancies increases, in good qualitative agreement with the results produced by Huang *et al.*(*c.f.,* Figures 4.1 and 4.2). The GTB result also shows that the system becomes paramagnetic at 33.33% edge-vacancy concentration, in agreement with Huang *et al.*'s DFT prediction.

A site-dependent comparison of the edge-magnetisation as a function of the % edge-vacancy concentration is shown in Figure 4.3 comparing Huang *et al.*'s DFT results [50] and the GTB solutions. In general, the GTB results are in good quantitative agreement with Huang *et al.*'s calculations. The Huang *et al.* and GTB solutions both show an overall decrease in edge-magnetisation as the number of edge-defects increases, with the largest decreases occurring around the edge-vacancy sites. An increased local edge-magnetisation compared to the DFT result can be seen in the GTB prediction for all sites at 0% edge-vacancy concentration, sites 4-10 at 8.33% edge-vacancy concentration and sites 3-5 at 16.67% edge-vacancy concentration (Figure 4.3). The loss of edge magnetism is found in both sets of results at 33.33% edge-vacancy concentration (shown previously in Figures 4.1 and 4.2) to be due to the system becoming paramagnetic.

For the ideal system, the difference between the GTB and DFT results can be attributed to slight variations in the ionic relaxation between the SIESTA [16] package used by Hancock *et al.* for the parametrisation of the GTB model [33] and the VASP [70] package used by Huang *et al.* [50]. In addition, the GTB model in this study uses the minimum parametrisation suggested in Hancock *el. al.* [33] and thus ignores the hopping perturbation ($t_{edge}$) along the edge of the system. For the edge-disordered systems, the differences can most likely be accounted for by there being no further ionic relaxation in the GTB model with the introduction of vacancies. Figure 4.4 compares the relaxed DFT result from Huang *et. al.*

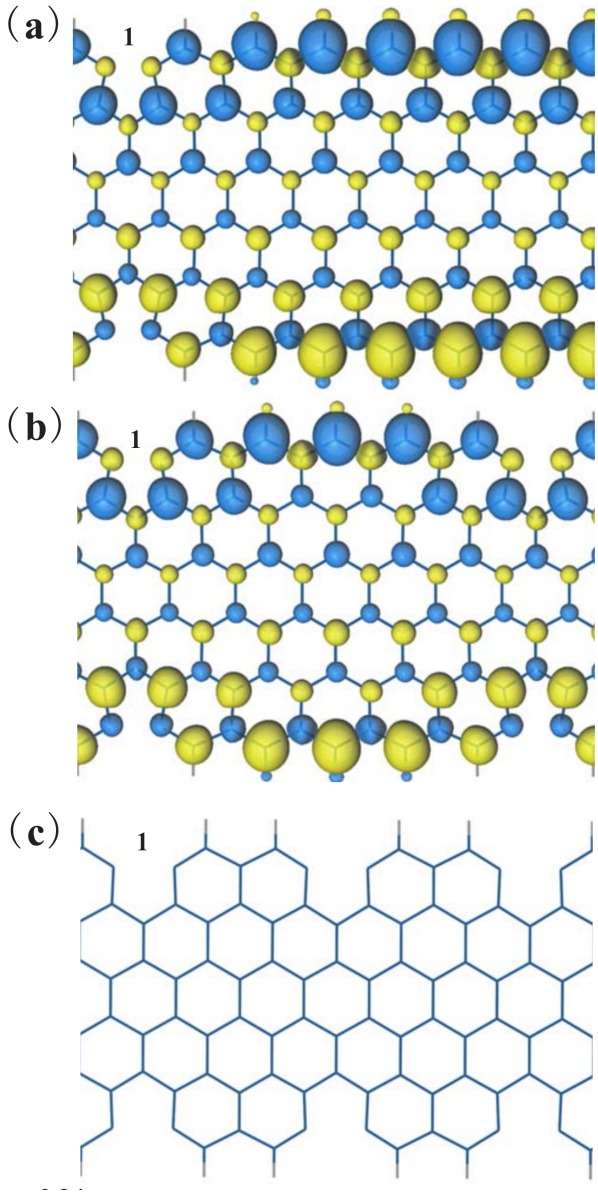


Figure 4.1: The effect of systematic edge-vacancies on the local magnetisation of a 12-6-ZGNR as a function of increasing edge-vacancy concentration calculated using DFT VASP within the LSDA (reproduced from Huang *et al.* [50]). The results show the decrease in magnitude of the edge-magnetisation as the number of systematic edge-vacancy defects increases from (a) 8.33%, (b) 16.67% and (c) 33.33% edge-vacancy concentration. Yellow circles denote net spin-up and blue circles denote net spin-down. Note, only half of the system is shown in (a)-(c). In real-space, a 12-6-ZGNR unit cell describes a system of width 11.38 Å and length 28.34 Å.

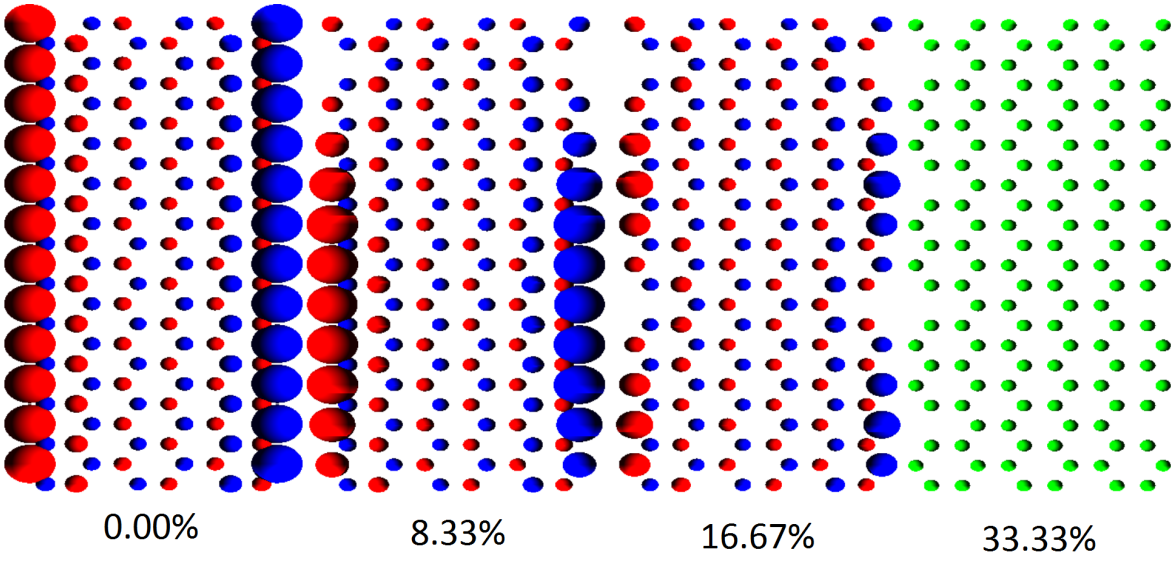


Figure 4.2: Spin-distribution of a systematically edge-defected 12-6-ZGNR calculated using the GTB model (Equation 2.67) within the unit cell approximation. The edge-vacancy concentration, from right to left, is 0%, 8.33%, 16.67% and 33.33%, respectively. Net spin-up circles are blue, net spin-down circles are red and net spin-neutral is green. The radius of each circle gives the relative magnitude of the net local-spin. As the % concentration of edge-defects increases, the magnitude of the edge-magnetisation is shown to decrease.

and the unrelaxed GTB result for 8.33% edge-vacancy concentration and demonstrates the lack of structural relaxation, in particular around the edge-vacancy.

To confirm the effects of further ionic relaxation, ONETEP [159, 160] was used to carry out DFT LSDA ionic relaxation on the 8.33% systematic edge-vacancy system. Using the relaxed atomic structure found through ONETEP [159, 160] (Figure 4.5), the input structure of the relaxed GTB model can be found and the hopping parameters perturbed using exponential scaling. Exponential scaling is used in this instance due to the increased accuracy of this scaling method compared to Harrison scaling (Section 2.8). The GTB fitting is carried out by comparing the relaxed and nonrelaxed LSDA DFT results from ONETEP and scaling the hopping parameters via Equation 2.104. For exponential scaling (Equation 2.104) a fitting parameter, $A$, the value of which was taken as 3.37 from Pereira *et. al.* [106] derived from experimental results. The relaxed 8.33% systematic edge-vacancy structure leads to a decrease in magnetisation (Figure 4.6) far from the defect, in qualitative agreement with Huang *et.al* [50]. The decrease occurs due to the reordering of spin-polarisation around the defect leading to an overall decrease in spin-polarisation far from the defect. Due to computational constraints, only the relaxed ionic positions were calculated for the 8.33% edge-vacancy structure with ONETEP.

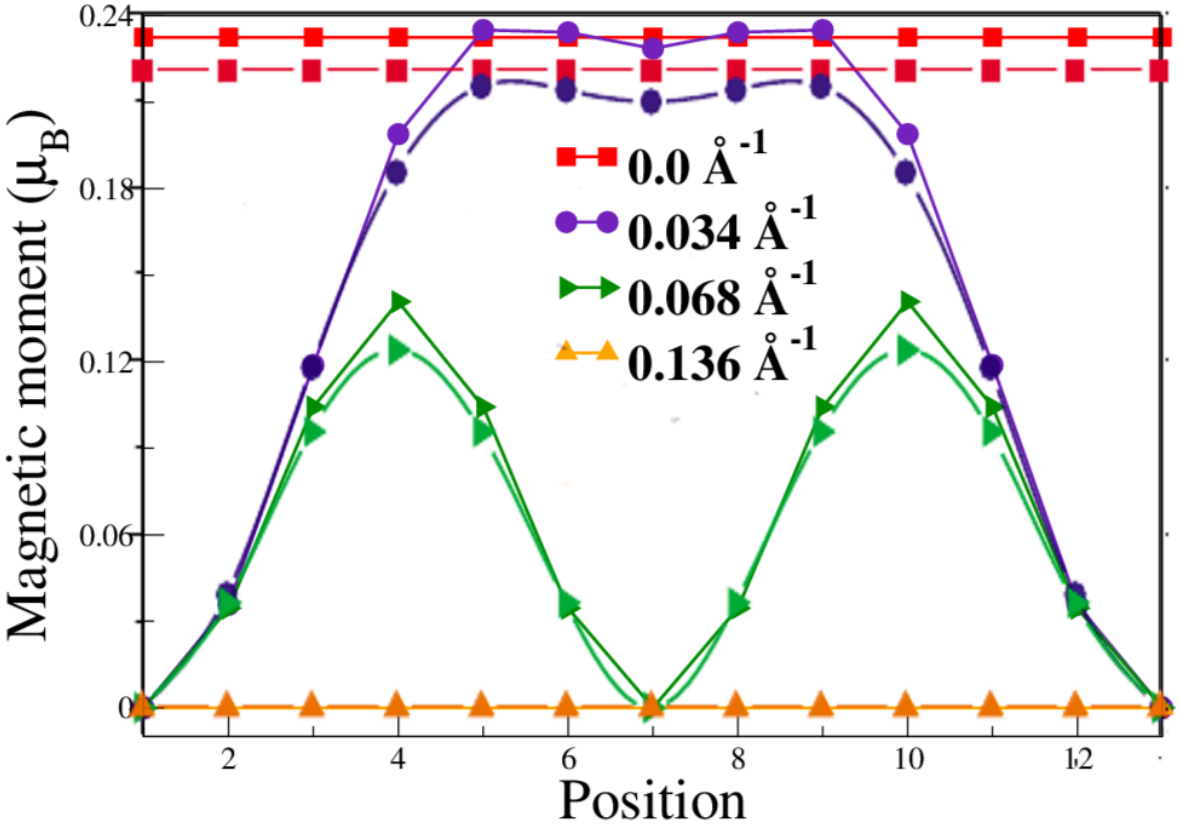


Figure 4.3: The effect of systematic edge-vacancies on the local edge-magnetisation of a 12-6-ZGNR comparing the GTB results with Huang *et al.*'s DFT LSDA simulations [50]. Continuous lines correspond to the GTB solutions and broken lines correspond to Huang *et al.*'s results. The legend in the figure has been based on the one used in Huang *et al.* in Ref. [50], corresponding to edge-vacancy concentrations, from top to bottom, of 0%, 8.33%, 16.67% and 33.33%. Within the unit cell approximation, site 1 is equivalent to site 13 in this system (Figure 4.1). In real-space, a 12-6-ZGNR system has a width of 11.38 Å and length of 28.34 Å.

## 4.3 The Effects of Random Edge-Vacancy Defects on the Magnetic Properties of Zig-zag Graphene Nanoribbons

Systematic edge-vacancy defects, such as those studied in Section 4.2, are not a realistic model for describing experimental edge-disorder in GNRs. A more realistic approach would entail the study of randomly distributed edge-vacancy defects, whereby the calculated properties of the ribbon are determined using ensemble averaging. To investigate the effect of random edge-vacancy defects in ZGNRs, a representative 20-5-ZGNR device of length 48.02 Å and width 9.24 Å was chosen (Figure 4.7). The dimensions of this device were chosen as its length enables a good range of edge-vacancy concentrations to be probed. The size of the device (length to width) is also computationally tractable with respect to the total number of atoms against the efficiency of the Hubbard-$U$ convergence in the GTB calculations.

Random edge-disorder was introduced in the 20-5-ZGNR by randomly removing edge-atoms with equal probability weighting until the required edge-vacancy concentration (Equation 4.1) was obtained. Klein defects [58, 59, 167, 168, 169], which arise when two neighbour-

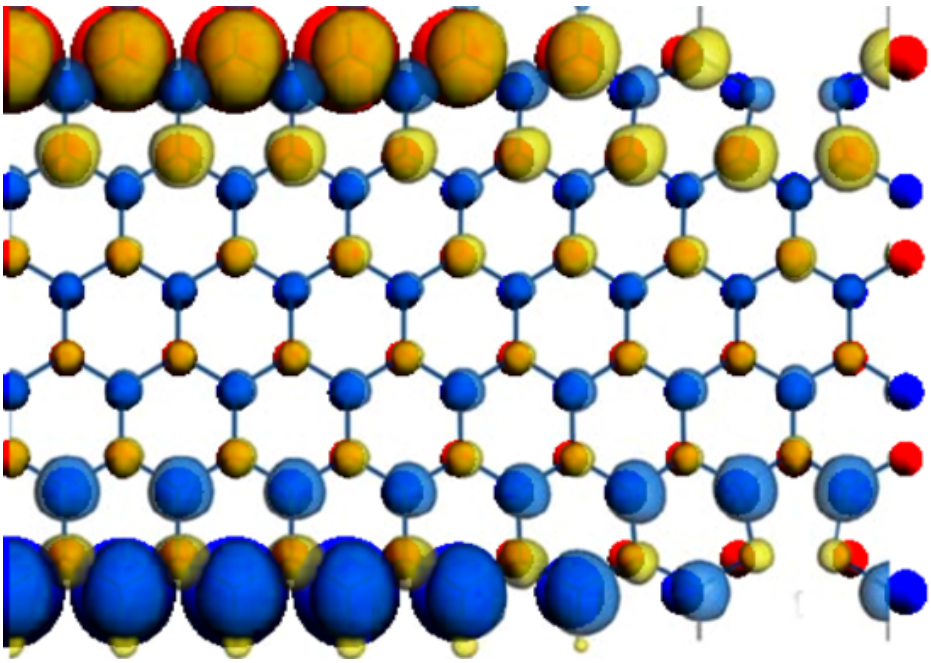

Figure 4.4: The difference between the ionic positions of a relaxed and nonrelaxed edge-vacancy defected 12-6-ZGNR at 8.33% edge-vacancy concentration. Transparent yellow(blue) circles denote spin-up(-down) and bold red(blue) circles denote spin-up(-down) for the relaxed Huang *et. al.* result [50] and the nonrelaxed GTB result, respectively.

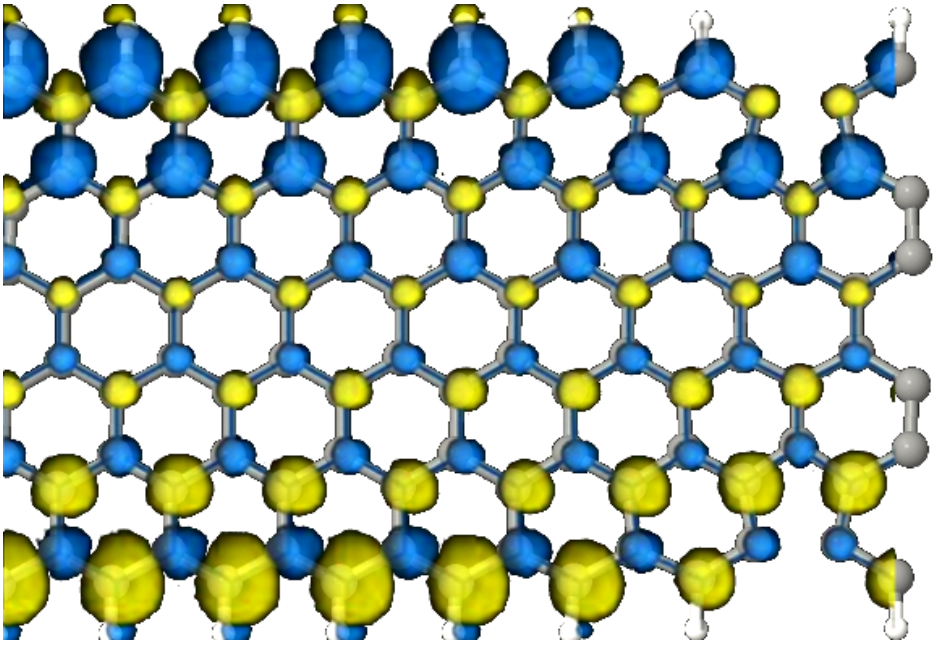

Figure 4.5: The difference between the ionic positions of two further relaxed edge-vacancy defected 12-6-ZGNR at 8.33% edge-vacancy concentrations. Transparent yellow(blue) circles denote spin-up(-down) for the relaxed Huang *et. al.* result [50] and grey circles denote the relaxed ONETEP ionic positions.

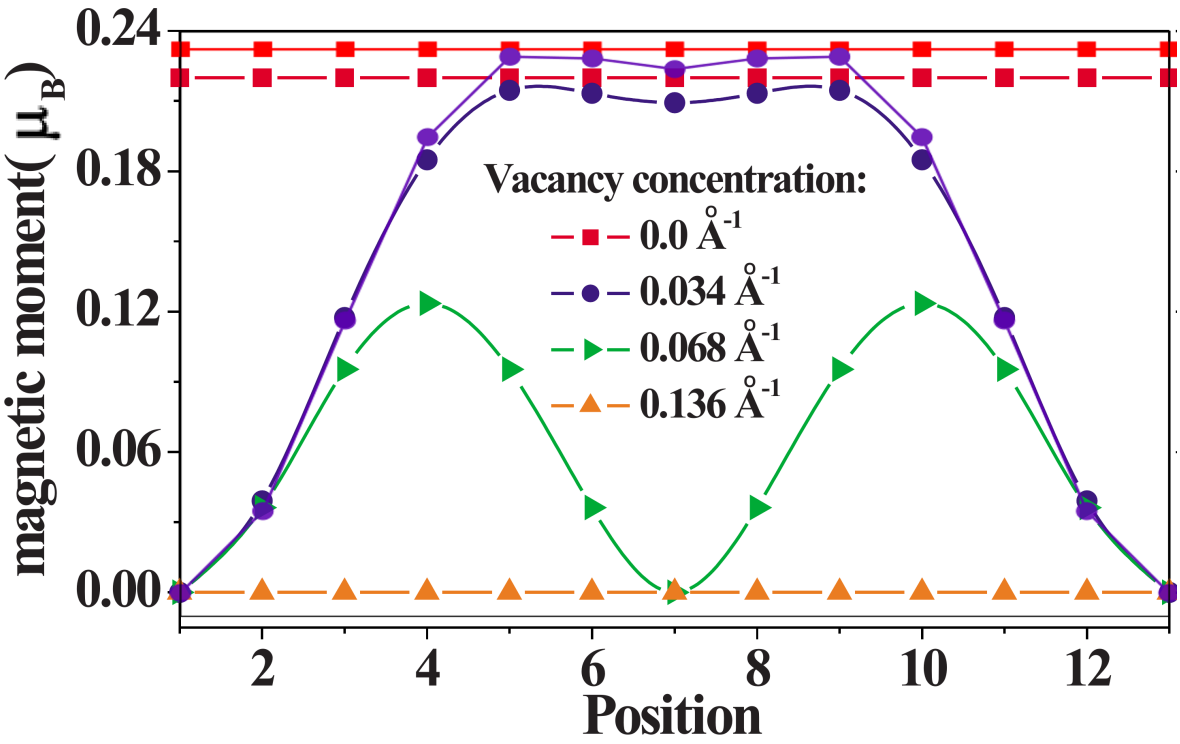


Figure 4.6: The effect of systematic edge-vacancies on the local edge-magnetisation of a relaxed 12-6-ZGNR comparing the GTB with Huang *et al.*'s DFT LSDA results [50]. Continuous lines correspond to the relaxed GTB solution obtained using ONETEP's relaxed structural input with exponential scaling at 8.33% edge-vacancy concentration and broken lines correspond to Huang *et al.*'s results. The legend in the figure has been based on the one used in Huang *et al.* [50], corresponding to edge-vacancy concentrations, from top to bottom, of 0%, 8.33%, 16.67% and 33.33%. Within the unit cell approximation, site 1 is equivalent to site 13 in this system (Figure 4.1).

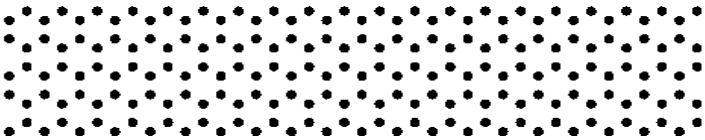

Figure 4.7: Schematic of the ideal 20-5-ZGNR device used as the basis for investigating the effects of random edge-vacancy disorder. In real-space, the 20-5-ZGNR device describes a system of width 9.24 Å and length 48.02 Å.

ing edge-atoms are removed (Figure 4.8(a)), were excluded in the tight-binding simulations. The exclusion was due to these defects being difficult to model within the tight-binding formalism as experimentally the single C-C bond has been observed to vibrate [170] and thus would introduce time dependent hopping parameters. If a Klein defect did occur during the edge-atom removal process, then the dangling carbon atom was removed leading to a small notch (Figure 4.8(b)). Each edge-atom was equally weighted and chosen for removal using a simple random number generator [171], the details of which can be found in Appendix A. The inclusion of edge-vacancies in the second layer caused by the notch has led to the definition of the "edge" in this work being the first two rows of the ZGNR.

In order to calculate the effect of random edge-vacancies on the magnetism, coherent

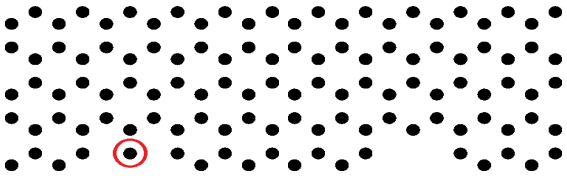

(a) (b)

Figure 4.8: Schematic of (a) an edge-vacancy defected portion of a 20-5-ZGNR system used to demonstrate a Klein defect (circled area), and (b) a notched system with the Klein defect removed.

transport properties (Equation 2.98) and charge-carrier localisation (Equation 4.7) of the defected ZGNR devices, an ensemble average must be taken. The ensemble average needs to include a significant sample size to be representative of the total population of edge-defected systems for a given % edge-defect concentration, such that,

$$\bar{\chi} \approx \bar{x} = \frac{1}{N}\sum_{i=1}^{N} x_i \tag{4.2}$$

where $x_i$ is the property being measured for the $i$th system in the ensemble, $\bar{x}$ is the average value of that property taken over the sample size, $N$, and $\bar{\chi}$ is the ensemble average for the entire population [172]. Each system in the ensemble average is equally weighted as the variation in the total energies associated with these systems is very small ($\pm 10^{-4}$ eV), hence any weighting within the ensemble average would be negligible.

As the sample mean only describes the mean of the sample and not the mean of the population, the confidence in the sample mean must also be stated. The confidence in the sample mean is taken from the standard error [172],

$$SE = \frac{\sigma}{\sqrt{N}}, \tag{4.3}$$

$$\sigma = \sqrt{\frac{1}{N-1}\sum_{i}^{N}(\bar{x} - x_i)^2} \tag{4.4}$$

is the standard deviation from the property under consideration. A further source of uncertainty arises from the energy resolution pertaining to the energy dependent quantities. To minimise this uncertainty, a fine energy-step of 0.008eV was chosen, leading to a systematic error in energy of $\pm$0.008eV .

To determine the minimum sample size $N$ required to adequately describe the ensemble as per Equation 4.2, a convergence test pertaining to the standard error associated with the spin-dependent coherent transport (Equation 2.98) was performed (Figure 4.9). A minimum of $N = 50$ samples was deemed to be large enough to ensure adequate accuracy of the ensemble average spin-dependent coherent transport as determined by the converged maximum

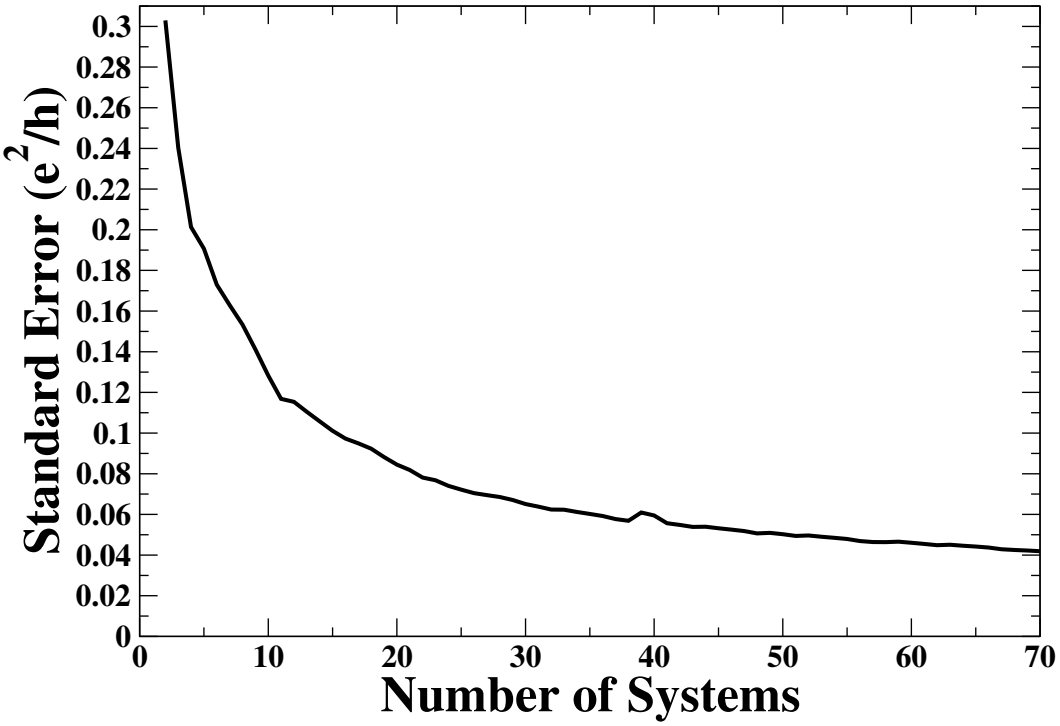


Figure 4.9: Convergence of the standard error (Equation 4.3) associated with the ensemble averaged spin-dependent coherent transport (Equations 2.98 and 4.2) for a 7.5% edge-vacancy defected 20-5-ZGNR calculated using the GTB model (Equation 2.67).

standard error ($\pm 0.06 e^2/h$) taken within the calculation between -1.5 eV$< E - E_F <$1.5 eV. This number of calculations, with a minimum of $N = 50$, also remains computationally tractable.

In the following studies, a range of edge-vacancy concentrations from 0% to 100% (the latter with a total of 80 edge-atoms removed) were investigated, with three edge-vacancy concentrations at 7.5% (6 atoms removed), 42.5% (34 atoms removed) and 90% (72 atoms removed) being investigated in more detail. The selection of these three systems was justified as 7.5%/90% denote the smallest/largest edge-vacancy concentrations examined due to Klein defects, with 42.5% edge-vacancy concentration representing a significantly edge-disordered system. Figure 4.10 shows examples of 20-5-ZGNR used within the ensemble average for each of the edge-vacancy concentrations of interest. *N.B.,* 42.5% was considered significantly edge-disordered as above 50% edge-vacancy concentration the system becomes more ordered due to a greater number of edge-vacancies occurring in the second atomic row (*cf.* Figures 4.10(b) and 4.10(c)).

### 4.3.1 Effects of Random Edge-Vacancies on Magnetic Properties of ZGNRs

Huang *et al.* [50] showed for a 12-6-ZGNR that 33.3% systematic edge-vacancy concentration was sufficient to lead to a change from an antiferromagnetic to a paramagnetic spin configuration (Section 4.2). As a comparison, Figure 4.11 shows the ensemble-averaged, spin-polarisation per atom measured over the entire 20-5-ZGNR unit call as a function of increas-

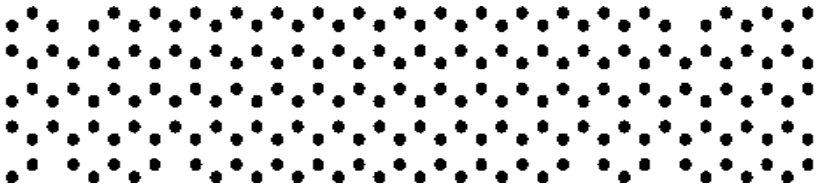

(a) 7.5%

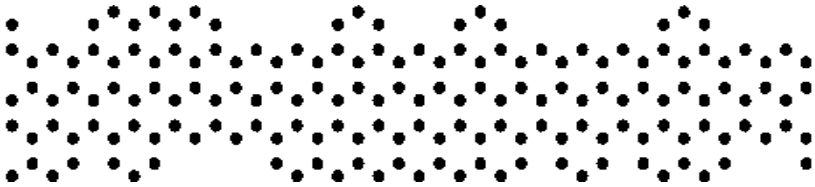

(b) 42.5%

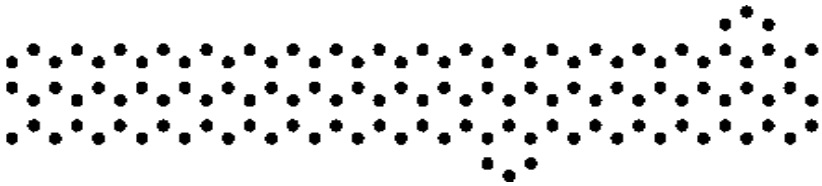

(c) 90%

Figure 4.10: Example schematics of 20-5-ZGNRs used in the ensemble averages (Equation 4.2) with (a) 7.5% edge-vacancy defect concentration (6 atoms removed), (b) 42.5% edge-vacancy defect concentration (34 atoms removed) and (c) 90% edge-vacancy defect concentration (72 atoms removed). The systems at 42.5% and 90% edge-vacancy concentrations provide examples of notch formation caused by the removal of a Klein defect. The edge of these systems is defined as the first two atomic rows.

ing random edge-vacancy concentration determined using the GTB model (Equation 2.82). With the introduction of random edge-vacancies, the shift from an ensemble-averaged, antiferromagnetic lowest energy spin-configuration to an ensemble-averaged, paramagnetic lowest energy spin-configuration is not seen to occur—this being despite the decreased width of the 20-5-ZGNR compared to the 12-6-ZGNR examined in the systematic edge-vacancy defect study. Figure 4.11 therefore demonstrates that for a ZGNR with random edge-vacancies, the lowest energy-state remains antiferromagnetic in spin-texture independent of the edge-vacancy concentration.

The difference in the values of the spin-up and spin-down net polarisation results shown in Figure 4.11 can be explained by the self-consistent method used to solve the GTB model. The GTB calculations involved the spin-up Hamiltonian being arbitrarily chosen and solved initially in each coupled spin-up/spin-down iteration cycle within the self-consistent Hubbard-$U$ procedure. The redistribution of spin in the system, and hence net spin-up magnetism, is therefore a direct result of the broken spin-symmetry caused by the random edge-vacancies.

The lack of a converged, paramagnetic ensemble-averaged solution can be explained by the fact that the random edge-vacancies will, over an ensemble average, preserve at least three ideal ZGNR unit cells in a row. Figure 4.12 shows that even for highly disordered systems there can still be regions of three or more ideal ZGNR unit cells in a row. These

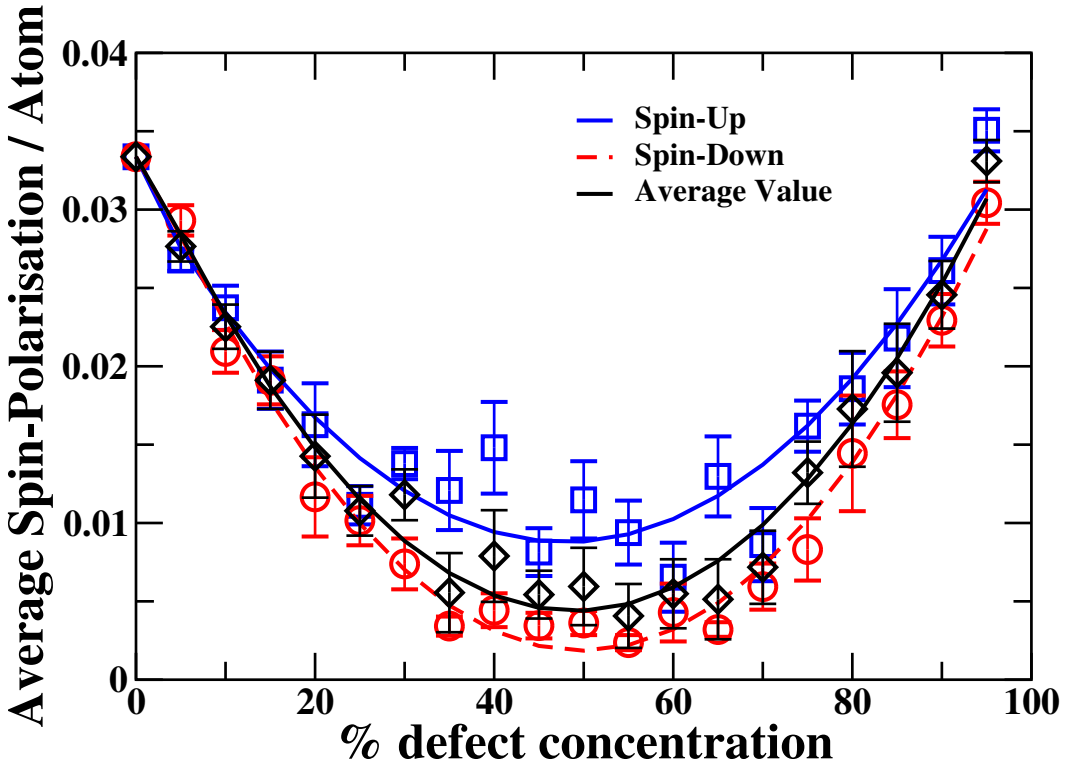


Figure 4.11: The effect of random edge-vacancies on the ensemble averaged value of the spin-polarisation per atom measured over the entire system for a 20-5-ZGNR within the unit cell approximation (Equation 2.82). Blue denotes spin-up, red denotes spin-down, with the average value corresponding to the net spin-polarisation per atom. Error bars represent the calculated standard errors associated with these quantities (Equation 4.3) and lines are added to guide the eye.

stabilising regions preserve the spin-polarisation in the entire system according to Clar's theory [173, 174], thus preventing regions without three ideal ZGNR unit cells in a row from demagnetising (Figure 4.12).

As a direct check with Huang *et. al*'s systematic result, the effect of random edge-vacancies was investigated by doubling the length of the 12-6-ZGNR unit cell to a 24-6-ZGNR to allow for multiple configurations within the ensemble that satisfies Clar's theory of aromaticity [173, 174] of three carbon edge atoms in a row at 33.3% edge-vacancy concentration. Figure 4.13 shows that systematic edge-vacancies, which are distributed with three ideal ZGNR edge-atoms preserved also retain overall spin-polarisation even at the theoretical paramagnetic 33.3% defect concentration. This further emphasises the importance of random edge-vacancy ensemble averaged results in determining the magnetic properties of defected ZGNRs.

### 4.3.2 Effects of Random Edge-Vacancy Defects on the Spin-dependent, Coherent Transport

To calculate the spin-dependent coherent transport (Equation 2.98) the non-defected (black highlighted) region (Figure 4.14) must first be added to each end of the ZGNR device to

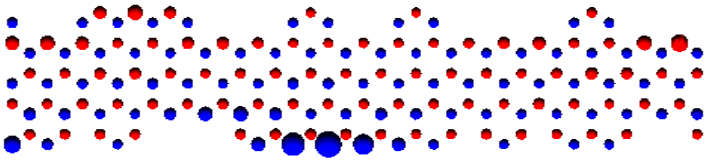

Figure 4.12: Local net spin-polarisation for a systematically defected 20-5-ZGNR determined within the unit cell approximation showing an antiferromagnetic configuration. Blue circles denote spin-up, red circles denote spin-down, with the radius of the circles corresponding to the relative magnitude of the net spin-polarisation (Equation 2.82).

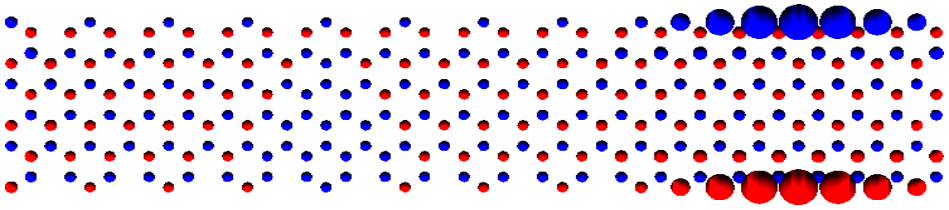

Figure 4.13: Local net spin-polarisation for a systematically defected 24-6-ZGNR determined within the unit cell approximation. Blue circles denote spin-up, red circles denote spin-down, with the radius of the circles corresponding to the relative magnitude of the net spin-polarisation (Equation 2.82).

prevent discontinuities in the spin-polarisation between the disordered device and the semi-infinite ideal leads. The length of the additional non-defected regions was determined such that the edge spin-polarisation on the atoms connecting to the semi-infinite was converged. To test this convergence, a 20-5-ZGNR device with 51.25% edge-vacancy concentration was used. The 51.25% edge-vacancy concentration was chosen as this led to the largest difference in spin-polarisation between the net spin-up and spin-down values (Figure 4.11). Compared to other vacancy defect concentrations, this system would require the longest non-defected region to converge the magnetism into the semi-infinite ideal leads, thus setting the minimum lead length for all other calculations of 20-5-ZGNR defected devices.

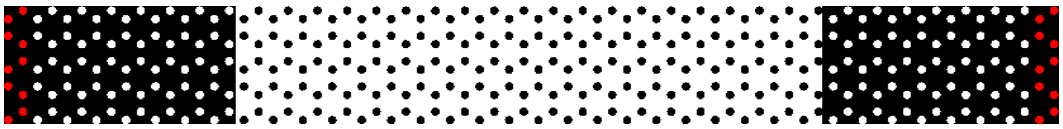

Figure 4.14: A schematic of the set-up used to calculate the coherent transport properties of the random edge-vacancy defected 20-5-ZGNRs. The first and last eight unit cells (black background, white atomic sites) remain structurally ideal, whereas the first and last unit cells (black background, red atomic sites) defines the device-lead boundary. The middle 20 unit cells of 48.02Å length (white background, black atomic sites) defines the disordered region of the device.

Figure 4.15 shows the increase in local spin-polarisation on both an edge atom and internal atom at the device-lead boundary for a 20-5-ZGNR device, with 51.25% edge-vacancy concentration as a function of increasing the ideal (*i.e.,* non-defected) region of the device. The local net spin-polarisation of the edge atom at the device-lead boundary is seen to con-

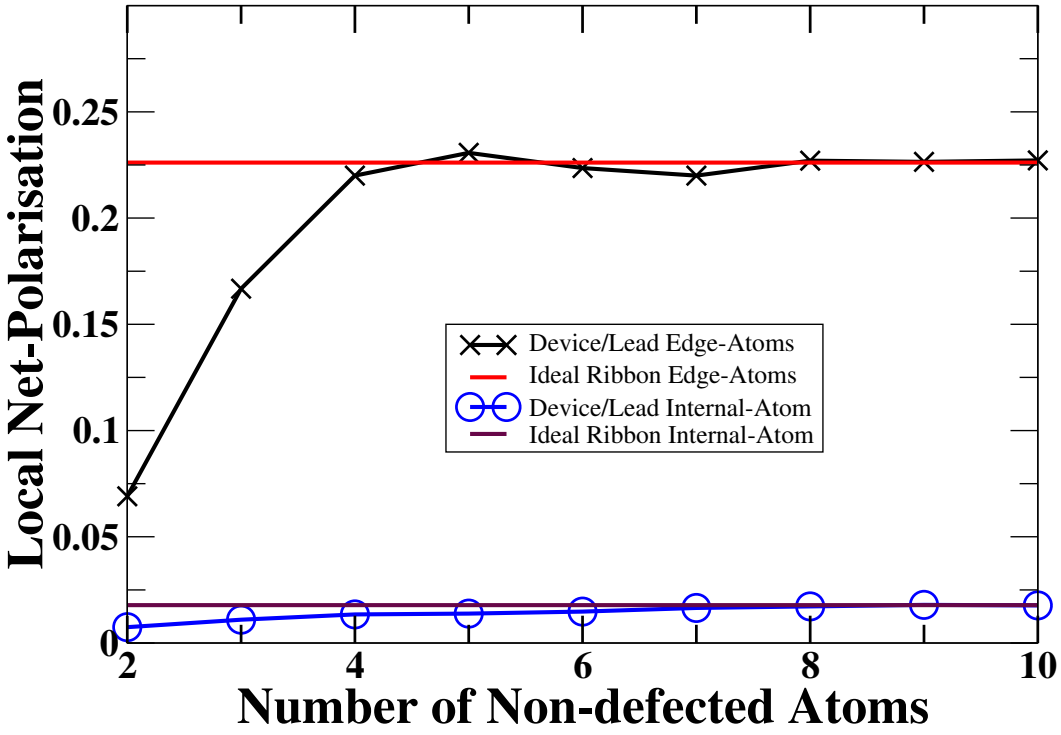


Figure 4.15: Convergence of the local spin-polarisation on the device-lead edge atoms (Equation 2.81). The red(purple) curve shows the result for an edge(internal) atom on an ideal 5-ZGNR (convergence criterion). The black(blue) curve corresponds to the local spin-polarisation on the edge(internal) atom at the device-lead boundary for a 20-5-ZGNR device with 51.25% edge-vacancy concentration as a function of the increasing non-defected region. In both of these systems, the internal-atom is an atom that is positioned half way across the device width. Convergence is shown to occur at an additional non-defected length of eight 5-ZGNR unit cells.

verge to that of an ideal 5-ZGNR system at a non-defected region length of eight 5-ZGNR unit cells, thus meeting the convergence criterion. The magnitude of the converged net local spin-polarisation is 0.227 for the spin-up(+ve) and spin-down (-ve) edges. Convergence also occurs for the net local spin-polarisation on the internal-atom defined as an atom positioned half way across the width of the device. The device/lead internal-atom converges to the net spin-polarisation of an ideal 5-ZGNR internal-atom of 0.018 at a non-defected region length of seven 5-ZGNR unit cells. To ensure lead convergence of the magnetism an additional length of eight 5-ZGNR unit cells was applied to all edge-disordered 20-5-ZGNRs used in the following studies.

Due to the lack of an intrinsic conductance gap in the non-interacting tight-binding model, previous studies that involve the STB model applied to edge-vacancy defected GNRs have been extensive [52, 56, 59, 62, 64, 66, 67]. These studies have shown that edge-vacancies suppress the conductance around the Fermi level, thus this is used to explain the conduction gap seen in experimental results [29, 31, 54, 63]. Evaldsson *et al.* [79] assumed for AGNR edge-disordered devices that a conductance of less than $0.01 * 2e^2/h$ was equivalent to zero conductance based on the experimental results of Han *et al.* [29]. This criterion was also later

applied to 16-ZGNR devices studied by Cresti and Roche [59].

Mucciolo *et al.* [67] introduced edge-disorder to a 40-ZGNR device with length 45 nm and width of 4.7 nm width that was modelled using the STB model where edge roughness was defined such that $r = (W - \bar{W})P/a_0$, where $\bar{W}$ is the average ribbon width, $W$ is the undefected ribbon width, $P$ is the probability of an edge-vacancy and $a_0$ is the lattice constant. Mucciolo *et al.* [67] found that the conductance of the 40-ZGNR device was robust to small edge-roughness ($r = 0.01$), however, became more sensitive as the edge-roughness increased ($r = 0.50$). Specifically the conductance at the Fermi energy dropped by approximately four orders of magnitude relative to the undefected device. They were also able to demonstrate the increased sensitivity of the conductance in ZNGRs with 45 nm length on edge-roughness as a function of decreasing ribbon-width with the conductance gap decreasing by half an order of magnitude as the width of the ribbon was increased from $\sim 2.5 - 12$ nm.

Other studies into the conductance of ZGNR devices have found that at larger widths, the conductance is more stable around the Fermi-level. Areshkin *et al.* [52] studied 64-ZGNR devices of length 1 $\mu$m that had random edge-vacancies, random edge-disorder (implemented by random variations in the on-site atomic energies), and variable bond lengths using the STB model. In these studies, the ballistic conductance of the significantly wide 64-ZGNR systems was determined to be robust even at a large edge-vacancy concentration of 50% and with an "edge" defined as 4 atoms deep. In comparison, Cresti and Roche [59] used the STB model to show that a 16-ZGNR device having a smaller width and length of 500nm exhibited greater sensitivity to the effect of edge-vacancies with significant perturbation to the conductance at only 7.5% edge-vacancy concentration. Specifically, they demonstrated that the spin-independent conductance in 16-ZGNR devices would be significantly reduced to below the $0.01 * 2e^2/h$ criterion, thereby approximating a conductance gap of $\approx 1.75$ eV at lengths greater than 470nm. This suggests that the intrinsic conduction gap found using the GTB model is more significant in determining the conduction properties than random edge-vacancies.

The increased robustness of conduction at increased device width compared to the 16-ZGNR studied by Cresti and Roche [59] has also been demonstrated using the STB model by Haskins *et al.* [64] for a 70-ZGNR system with a length of 100 nm. Li and Lu [62] used the STB model to study ZGNR devices with increasing widths from 5 Å to 55 Å and demonstrated that, for edge-vacancies with one, two or three edge-atoms, the conductance remained unperturbed as a function of the increasing device-width. In comparison, AGNR devices of equivalent widths demonstrated greater relative perturbation to the conductance compared to ZGNRs having same number of edge-vacancies. ZGNRs in this study became immune to edge-vacancy perturbation at widths $> 30$ Å, thereby providing further evidence of the robustness of ZGNRs against edge-vacancy perturbation.

With increasing concentration of edge-vacancies (*i.e.*, greater than 50%) the device resembles a thin ribbon with protrusions instead of a wide ribbon with edge-vacancies (due to Klein defects). Saloriutta *et al.* used the TranSIESTA package that employs spin-dependent, non-equilibrium Green's function-density functional theory (NEGF-DFT) within the PBE-GGA [80] to demonstrate that a hydrogen-passivated structural protrusion on the edge of a 12-5-ZGNR device reduced the transport conduction relative for both spin directions. A significant decrease in spin-conduction near the first conductance step within the range of $\pm 1.5$ eV along with a decrease in the conductance spikes either side of the conductance gap was observed. The largest decrease in spin-conduction was close to 100% at $\pm$ 1.4 eV. Saloriutta *et al.* also demonstrated a stability in the conductance gap, with the gap staying the same size independent of the introduction of these protrusions. Such protrusions are relevant to the work in this thesis as these can occur in random edge-vacancy systems having edge-vacancy concentrations greater than 50%.

Molitor *et al.* [54] carried out experimental transport and band gap measurements on etched GNRs. Similar to Han *et al.* [29], the edge-type (AGNR or ZGNR) could not be determined, however, a band gap and conductance gap was measured at all widths. Molitor *et al.* [54] use edge-roughness to explain the presence of the measured gaps, however, this explanation is not in agreement with other experimental studies, for example Li *et al.* [31], who measured a band gap in structurally pristine, chemically derived GNRs. As the GTB model predicts a intrinsic gap [32], edge-vacancies will be incorporated into the GTB model to test the stability of the transport-gap upon the introduction of edge-vacancies.

As these previous studies show, decreasing the ribbon-width increases the sensitivity of the device to edge-vacancies, thus the small ribbon-widths used in this thesis should also be sensitive to the effects of edge-vacancies, thereby the small sizes enhancing any trends seen. The properties observed in the previous literature were also determined using the spin-independent STB model, thus this thesis also compares non-interacting system results to those obtained using the more generalised, spin-dependent GTB model. The results presented in this chapter were calculated with all three models (STB, ETB and GTB) to determine if the features and edge-effects observed in the STB model from previous studies in the literature are universal to all three models, or artefacts caused by the approximations made in the STB model, *i.e,* first nearest-neighbour hopping and no Coulomb interactions. In particular, the stability of the intrinsic conduction gap in the GTB model will also be studied to determine if the more efficient non-interacting models (STB/ETB) can be used at high edge-disorder.

### 4.3.3 Comparison of the conductance for 20-5-ZGNRs with random edge-vacancy disorder as a function of the model type (STB, ETB and GTB)

Regardless of the model used (STB, ETB or GTB), a reduction in electronic conductance is found for the 20-5-ZGNR at each of the random edge-vacancy concentrations (7.5%, 42.5% and 90%) investigated relative to the ideal 20-5-ZGNR device (Figures 4.16(a), 4.16(b) and 4.16(c)). Tables 4.1, 4.2 and 4.3 contain the largest and smallest relative decreases in conductance for the STB, ETB and GTB models for edge-vacancy concentrations at 7.5% (Table 4.1), 42.5% (Table 4.2) and 90% (Table 4.3), respectively, taken between the range -1.5eV $< E - E_f <$ 1.5eV. The decrease in the overall conductance has been linked in previous studies on the STB model to reductions in conductance channels and an increased charge localisation [52, 54, 56, 59, 62, 64, 66, 67, 73]. Within this context, localisation is defined as an increase in resistivity (and therefore decrease in conductivity) in a semi-conductor [175].

Comparing lightly disordered 20-5-ZGNRs at 7.5% and 90% edge-vacancy concentrations with the highly disordered 42.5% edge-vacancy concentration 20-5-ZGNR, it is possible to observe a decrease in the difference between the maximum and minimum relative conductance compared to an ideal 20-5-ZGNR. For example, the STB model at 7.5% edge-vacancy concentration has a maximum decrease in conductance of 90±3% and minimum decrease in conductance of 65±4%, resulting in a net difference of ∼25%. The STB model at 90% edge-vacancy concentration has a range of values between the largest relative decrease in conductance of 87±3% and the smallest relative decrease in conductance of 65±4%, resulting in a net difference of ∼22%. In comparison, the STB model at 42.5% edge-vacancy disorder exhibits a range of values between the largest relative decrease in conductance of 100±3% and a minimum suppression in conductance of 87±3%, resulting in a net difference of ∼13%.

Compared to the STB, the ETB model, which has a greater degree of kinetic freedom, exhibits the largest range of values associated with the relative net difference in conductance for the low-disorder systems, namely, ∼55% and ∼94% for 7.5%, and 90% random edge-vacancy concentrations, respectively. For the GTB model at low disorder, the relative net difference in conductance is spin-independent with ∼38% and ∼59% at 7.5%, and 90% random edge-vacancy concentrations, respectively. These values for the GTB model are greater than the STB values, but however, lower than the ETB values due to the effects of increased kinetics (i.e., the increased hopping parameters) combined with the localisation effects of the Hubbard-$U$. At high edge-vacancy disorder (42.5%), the STB and ETB models show the same relative net difference in conductance ∼13-14% as increased kinetics in the ETB has no gain due to the removal of a larger number of conduction channels. The GTB result shows a similar trend with a ∼18% relative net difference in the spin-independent conductance. The slight increase in this value against the STB and ETB results can be attributed to the effects

| Model | | 7.5% | | | |
|---|---|---|---|---|---|
| | | Maximum relative reduction | | Minimum relative reduction | |
| | | E (eV) | Con. (% red.) | E. (eV) | Con. (% red.) |
| STB | | 1.41±0.01 | 90±3 | 0.33±0.01 | 65±4 |
| ETB | | 1.36±0.01 | 95±3 | 0.01±0.01 | 40±5 |
| GTB | Spin-Down | 1.34±0.01 | 93±5 | 0.174±0.008 | 56±2 |
| | Spin-Up | 1.41±0.01 | 94±1 | -0.298±0.008 | 58±5 |

Table 4.1: Relative decrease in the ensemble-averaged electronic conductance for a 20-5-ZGNR device with 7.5% random edge-vacancy concentration investigated within the range $-1.5eV < E < 1.5eV$ (Equations 4.2 and 2.98). The conductance values in the defected device were taken relative to the ideal 20-5-ZGNR conductance determined for each model. "E" denotes the energy value at which the reduction occurs and "Con." denotes the relative decrease in conductance (% red.). For the GTB model, the maximum and minimum relative reductions were taken outside of the ideal 20-5-ZGNR conduction gap (±0.165eV) otherwise the minimum decrease would be zero as the conductance gap is not affected by the addition of edge-vacancies.

| Model | | 42.5% | | | |
|---|---|---|---|---|---|
| | | Maximum relative reduction | | Minimum relative reduction | |
| | | E (eV) | Con. (%) | E (eV) | Con. (%) |
| STB | | -0.048±0.008 | 100±3 | 1.47±0.01 | 87±3 |
| ETB | | -0.042±0.008 | 100±3 | -1.03±0.01 | 85±1 |
| GTB | Spin-Down | 1.40±0.01 | 99.5±0.1 | 1.37±0.01 | 82±1 |
| | Spin-Up | 1.39±0.01 | 99.3±0.1 | -1.37±0.01 | 80±4 |

Table 4.2: Relative decrease in the ensemble-averaged electronic conductance for a 20-5-ZGNR device with 42.5% random edge-vacancy concentration investigated within the range $-1.5eV < E < 1.5eV$ (Equations 4.2 and 2.98). The conductance values in the defected device were taken relative to the ideal 20-5-ZGNR conductance determined for each model. "E" denotes the energy value at which the reduction occurs and "Con." denotes the relative decrease in conductance. For the GTB model, the maximum and minimum relative reductions were taken outside of the ideal 20-5-ZGNR conduction gap (±0.165eV) otherwise the minimum decrease would be zero as the conductance gap is not affected by the addition of edge-vacancies.

| Model | | 90% | | | |
|---|---|---|---|---|---|
| | | Maximum relative reduction | | Minimum relative reduction | |
| | | E (eV) | Con. (%) | E (eV) | C (%) |
| STB | | 1.50±0.01 | 87±3 | −0.286±0.008 | 52±4 |
| ETB | | 1.50±0.01 | 95±1 | 0.014±0.008 | 2±2 |
| GTB | Spin-Down | 1.50±0.01 | 96±1 | −0.284±0.008 | 38±4 |
| | Spin-Up | 1.50±0.01 | 96±1 | 0.176±0.008 | 36±4 |

Table 4.3: Relative decrease in the ensemble-averaged electronic conductance for a 20-5-ZGNR device with 90% random edge-vacancy concentration investigated within $-1.5eV < E < 1.5eV$ (Equations 4.2 and 2.98). The conductance values in the defected device were taken relative to the ideal 20-5-ZGNR conductance determined for each model. "E" denotes the energy value at which the reduction occurs and "Con." denotes the relative decrease in conductance. For the GTB model, the maximum and minimum relative reductions were taken outside of the ideal 20-5-ZGNR conduction gap (±0.165eV) otherwise the minimum decrease would be zero as the conductance gap is not affected by the addition of edge-vacancies.

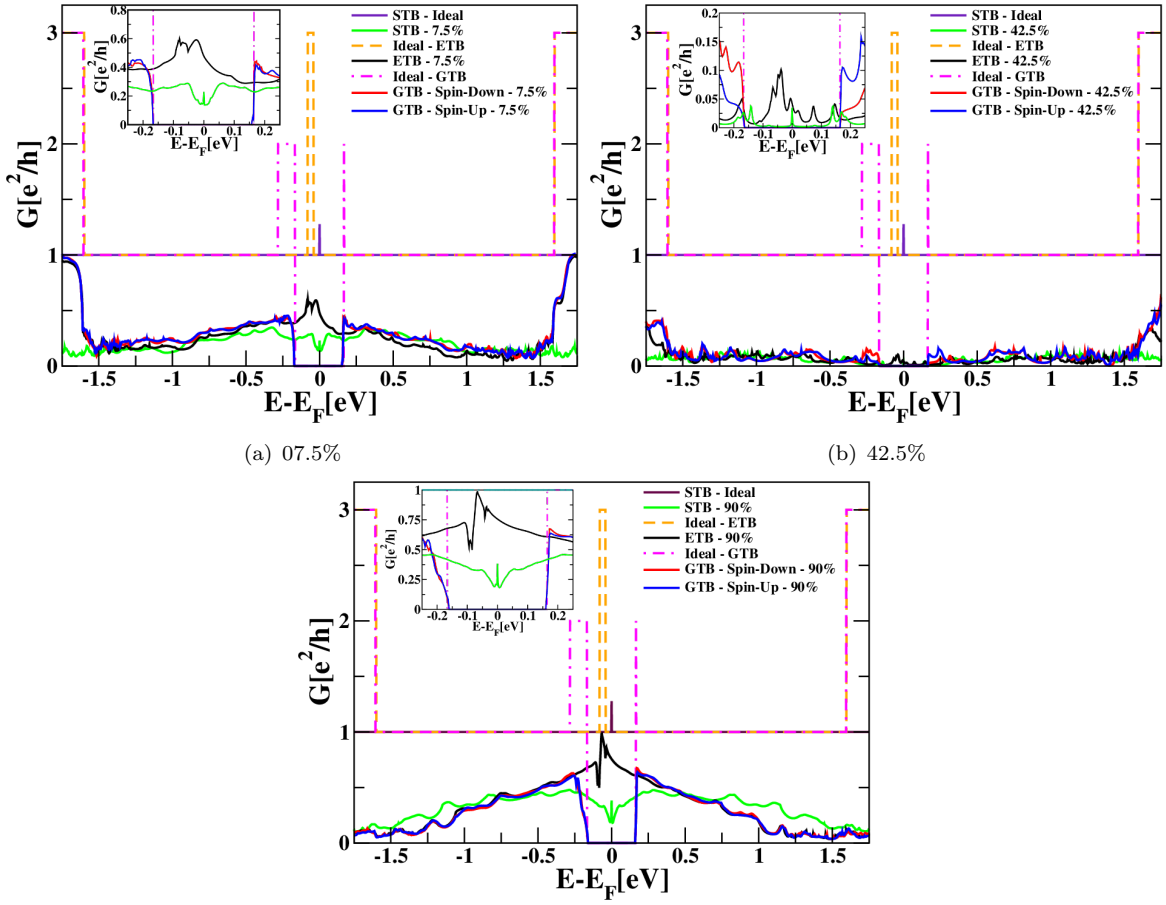


(a) 07.5%

(b) 42.5%

(c) 90.0%

Figure 4.16: Ensemble averaged electronic conductance vs. energy relative to the Fermi-energy for a 20-5-ZGNR device at (a) 7.5%, (b) 42.5% and (c) 90% edge-vacancy concentrations. Insert shows a zoom of the conductance around the Fermi energy. For the non-interacting models (STB and ETB) and for the ideal GTB device, the results are spin-independent. Green, black, red(blue) corresponds to the disordered STB, ETB, GTB spin-down(-up) result respectively. Purple, dashed orange and dashed pink gives the ideal 20-5-ZGNR STB, ETB and GTB result respectively. The energy, E, is taken relative to the Fermi energy, $E_F$. Standard error (Equation 4.3) not included for clarity. The largest error in the results is $\pm 0.05 e^2/h$ (Equation 4.3).

of the Hubbard-$U$ charge-carrier localisation.

The relative decrease in the overall conductance in the STB, ETB and GTB models as a function of increasing edge-vacancy disorder observed here is in agreement with the general trends seen in previous studies [52, 54, 56, 59, 62, 63, 64, 66, 67, 68, 73, 74]. In particular, the largest relative decrease in conductance occurs close to 1.5 eV (*i.e.* close to the first conduction step) at 7.5% and 90% edge-vacancy concentrations (Figures 4.16(a) and 4.16(c)) is in agreement with Li and Lu [62], Areshkin *et al.* [52], Haskins *et al.* [64] and Mucciolo *et al.* [67], who all demonstrate that the largest decrease in conductance occurs near the first conduction step for low edge-disorder. At 42.5% edge-vacancy concentration (Figure 4.16(b)), the conduction is sufficiently suppressed throughout the entire energy range independent of the STB, ETB or GTB model studied. The large decrease in conductance for the STB and ETB models near the Fermi energy (∼100%) seen at high (42.5%) edge-vacancy

concentration is also in agreement with Mucciolo *et al.* [67] who studied a larger 40-ZGNR with 45 nm length at high edge-vacancy disorder of 50% edge-vacancy concentration.

Away from the Fermi energy, *i.e.,* outside the GTB conductance gap (±0.2eV), the STB, ETB and GTB models results for the 20-5-ZGNR show, in general, very similar trends in the coherent transport results (Figures 4.16(a), 4.16(b) and 4.16(c)). The GTB and ETB results, in particular, follow the same general trend, with the STB results showing differences due to the shift in the first conduction steps, which are also observed in the ideal system results. The conduction trends diverge inside the GTB conductance gap (-0.2 eV$< E-E_F <$ 0.2 eV), with the non-interacting models preserving non-zero conductance at the Fermi energy, whereas the GTB model gives a conductance gap of 0.328±0.008 eV at all edge-vacancy concentrations considered, equal, to within error, to the ideal 20-5-ZGNR conduction gap of 0.330±0.008 eV.

The invariance in the intrinsic conductance gap with increasing edge-vacancy concentration suggests that, for a 20-5-ZGNR device at high edge-vacancy disorder, for example at 42.5% edge-vacancy concentration, the intrinsic conductance gap for the interacting GTB model is still observed, and, thus, the GTB model, in this case, should be used over the non-interacting models (Figure 4.16(b)). This may, in general, be of importance for low-width and short-length ZGNRs where the Hubbard-$U$ effects are stronger, and where the effects of edge-vacancies are also more pronounced. Having an intrinsic GTB gap in low-width, short-length ZGNRs also means that edge-vacancy disorder is not necessarily required to open the conduction gap observed in experimental results [31]. For example, conductance gaps have been observed in atomically clean experimental GNR devices [31] implying that edge-disorder is not the only mechanism to open a conductance gap in these systems (Figure 1.12).

To further investigate the effect of random edge-vacancy disorder on 20-5-ZGNRs, the conductance at the Fermi energy and the integrated conductance results found via the Simpson's rule [172] were determined as a function of increasing edge-vacancy concentration for the STB, ETB and GTB models within the energy range of -0.5eV$< E - E_F <$0.5eV (Figures 4.17(a) and (b), respectively). The Simpson's rule is encapsulated in the following equation,

$$\int_b^a f(x)dx \approx \frac{b-a}{6}[f(a) + 4f(\frac{a+b}{2}) + f(b)] \tag{4.5}$$

where a and b define two points along the $x$-axis, $f(x)$ is an exact function of $x$ describing the curve to be integrated, $f(a(b))$ is the value of the function at $x = a(b)$ and $f((a+b)/2)$ is the value of the function between $x = a$ and $x = b$.

Figure 4.17(b) shows that at the Fermi energy, an overall decrease in the conductance of 1.21±0.03 $e^2/h$ occurs in the STB model as the edge-vacancy concentration approaches 51.25%. After this, the conductance is shown to increase to 0.947±0.03 $e^2/h$ as the edge-vacancy concentration rises from 51.25% to 100%. The increase in conductance after 51.25% is due to the removal of atomic (*i.e.,* structural) protrusions from the ZGNR that occur in the

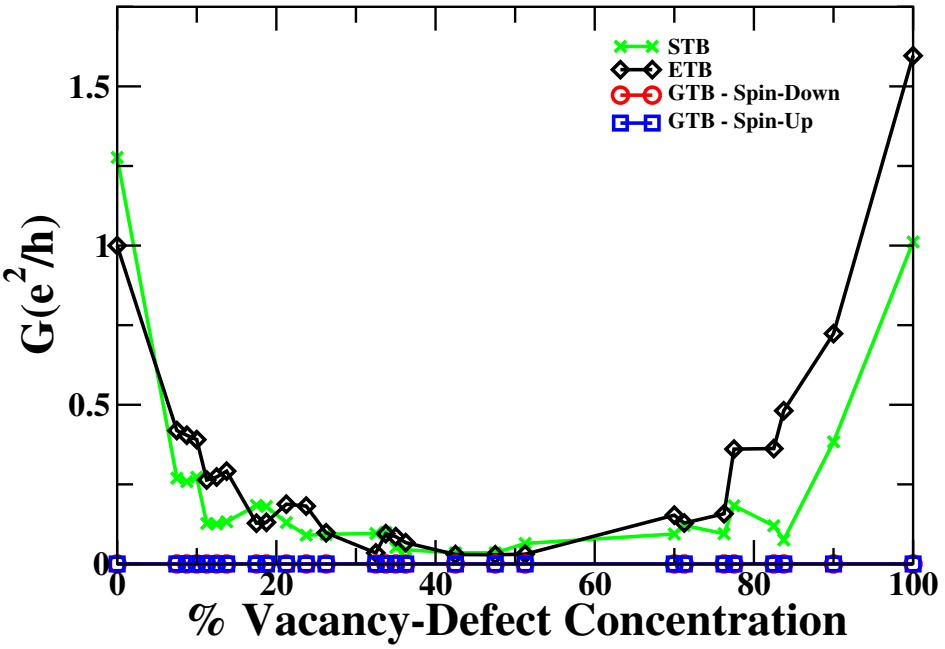


(a)

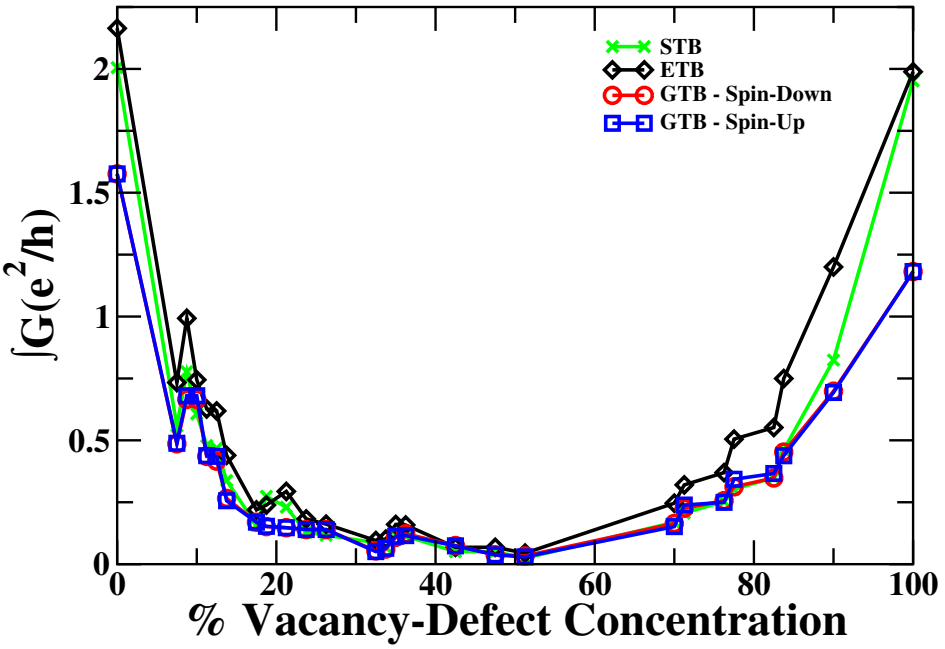


(b)

Figure 4.17: The effect of increasing the edge-vacancy concentration on the ensemble-averaged electronic conductance in a 20-5-ZGNR. Figure (a) shows the conductance at the Fermi energy, and Figure (b) shows the integrated conductance obtained between -0.5 eV$< E - E_F <$0.5 eV via the Simpson's rule for integration. Green, black, red(blue) corresponds to the disordered STB, ETB, GTB spin-down(-up) results, respectively. Purple, dashed orange and dashed pink correspond to the ideal 20-5-ZGNR STB, ETB and GTB results, respectively. For the non-interacting models (STB and ETB) and for the ideal GTB device, the results are spin-independent. The standard errors associated with the ensemble-averaged conductance results have not included for clarity. The largest standard error being $\pm 0.05\ e^2/h$ (Equation 4.3).

first edge-atom layer, thereby resulting in a structurally ideal ZGNR at 100% edge-vacancy concentration. The STB and ETB non-interacting models follow the same overall trend as a function of increasing edge-vacancy concentration, and the same exact trend where the conduction values are in agreement for the two models to within $\pm 0.05\ e^2/h$ between 32.5% and 51.25% edge-vacancy concentration (Figure 4.17(a)). Due to the intrinsic conduction gap in the GTB, the conductance at the Fermi energy is zero. At no point, as a function of the edge-vacancy concentration, do the STB and ETB results enter the zero conductance criterion established by Han *et al.* and Evaldsson *et al.* [29] [79] ($0.01 * e^2/h$ for single-spin).

The integral of the conductance between $-0.5eV < E < 0.5eV$ provides information about the general trend of the overall conductance of the system (Figure 4.17(b)(b)). In this figure, the three models are shown to follow the same overall trend at all % edge-vacancy concentrations, with the integral of the conductance following the same exact trend between 32.5% and 51.25% edge-vacancy concentration. Due to the increased kinetic degrees of freedom in the ETB model and the lack of a conduction-gap compared to the GTB model, the ETB model is therefore shown to have the largest overall conductance and thus the smallest degree of charge-carrier localisation.

The trends observed in the decrease in conductance for the STB model compared to the ETB and GTB models implies that, outside of the GTB conductance gap, the ETB model can be used to approximate the GTB properties (Figure 4.16). The 1st nearest-neighbour hopping only approximation of the STB model is insignificant to properly predict the conductance trends outside of the GTB conductance gap as shown in Figure 4.16. The stability of the GTB conductance gap and edge-magnetisation even for highly edge-disordered devices (42.5%) means that the Coulomb interactions cannot be ignored and must be included in all calculations. The differences between the STB, ETB and GTB models will be further probed by looking at the localisation lengths in the following section, and later as a function of the device length in Section 4.3.5.

### 4.3.4 Effects of Random Edge-Vacancies on Electronic Localisation

#### 4.3.4.1 Localisation Length

The dependence of the charge-carrier conductance on system length within the coherent transport formalism for a disordered chain consisting of a 1D Fermi gas with non-fixed length was first described by Landauer in 1970 [176]. Anderson *et al.* later applied this formalism to the study of disorder in a 1D wire described by a lattice model [177]. The dependence of conductance on system length was later confirmed though rigorous analytical analysis by Johnson and Kunz [178].

At a given energy $E$, the localisation length, $\zeta$, is related to the conductance due to

disorder, $G'$, and the conductance of the ideal system, $G$, via the relation

$$G'(L) = G(L)e^{\frac{-L}{\zeta}} \tag{4.6}$$

where, $L$ denotes the device length [176, 177, 178]. Therefore, at constant L [52]

$$\zeta = (-ln[G/G']/L)^{-1}, \tag{4.7}$$

for a single point measurement. For systems studied as a function of $L$, the localisation length $\zeta$ can be determined from the inverse of the slope of the curve obtained from $-ln[G(L)/G'(L)]$ vs. $L$. Anderson localisation [60] occurs when the localisation length, $\zeta$, is smaller than the device length, $L$. The weak-scattering limit is defined when $\zeta$ is equal to the mean-free path length [179], which implies that if $\zeta$ is smaller than the device then the charge carriers in the system are localised.

The exponential decay in conductance as a function of GNR device length has been demonstrated in detail using the STB model [52, 59, 62, 67]. Li and Lu verified the applicability of Equation 4.6 for random edge-disordered 8- and 12-ZGNR devices between 50 Å and 200 Å in length [62]. In this study edge-disorder was introduced by randomly perturbing the on-site energy of each edge atom by $\pm$ $V$, where $V$ denotes the edge-disorder strength. The study determined localisation lengths of 59 Å and 51 Å for 12-ZGNRs with random edge-disorder of V=$\pm$0.25 eV and $\pm$1.0 eV, respectively, and 53 Å and 45 Å for 8-ZGNRs with edge-disorder of V=$\pm$0.25 eV and $\pm$1.0 eV, respectively. N.B. Values of V were taken relative to the onsite energy of graphene in a homogeneous system, 0.0eV. This suggests that for GNRs, the localisation length increases as the edge-perturbation decreases or if the ribbon width is increased.

Cresti and Roche studied changes to the STB model calculated conductance as a function of increasing device length in randomly edge-vacancy defected 16-ZGNR devices using the STB model [59]. A conductance gap of $\sim$1.75 eV was found at device lengths greater than 470 nm, increasing to $\sim$2.4 eV at 1250 nm [59]. In this study, Cresti and Roche also demonstrated a decrease in mean-free path length (hence, localisation length) as a function of increasing edge-vacancy probability suggesting that the localisation length is dependent on both device length and edge-vacancy concentration. In their study, the edge-vacancy probability was defined as the probability that each edge-atom is removed. For example, at an edge vacancy concentration of 7.5%, each edge-atom has a 7.5% probability of being removed.

Areshkin *et al.* [52] calculated the localisation length for both 52-AGNR and 64-ZGNR devices using the STB model and found that AGNRs are significantly more sensitive than ZGNRs to random edge-vacancy perturbation. The 52-AGNR was found to be within the Anderson localisation regime at 5% edge-vacancy concentration, where the edge-vacancies

were taken to four atomic edge layers deep. In comparison, the 64-ZGNR device required edge-vacancies up to eight atomic layers and a higher edge-vacancy concentration of 50% before the Anderson localisation regime was reached [52]. The localisation length for the AGNR was determined as being 0.6$\mu$m, whereas for the ZGNR the localisation length was determined to be much larger at 7$\mu$m. In general, the fact that the localisation length is found to be inversely dependent on ribbon width [52, 59, 62, 67], coupled with the insensitivity of ZGNRs to edge-perturbation at large widths [52, 59], again provides strong supporting evidence for the choice of thin ZGNRs in this thesis study.

For the 20-5-ZGNR studied in this work, the marked decrease in conductance around 51.25% edge-vacancy concentration can therefore be directly linked to the increased charge-carrier localisation in the device (Figure 4.17(b)). Figure 4.18 compares the ensemble averaged localisation length vs. energy calculated using the STB, ETB and GTB models for the 20-5-ZGNR at two example edge-vacancy concentrations of 7.5% and 42.5%. The 90% random edge-vacancy concentration system was not included here as there is an increase in the fraction of structurally ideal edge due to the increased number of edge-vacancies that leads to a similar effect on the conductance as the 7.5% result as per Figure 4.17. Comparison of Figures 4.18(a) and (b) shows a significant increase in charge-carrier localisation in the device as the edge-vacancy concentration is increased from 7.5% to 42.5%, independent of the model used (to within a maximum uncertainty of 3Å(Equation 4.3)).

The results for the STB model show that the 20-5-ZGNR device of length of 48.02 Å is within the Anderson localisation regime at all energies, and that this occurs even at the low edge-vacancy concentration of 7.5% (Figure 4.18). These trends are in agreement with Mucciolo *et al.* [67], who concluded for devices with width 4.7 nm that the conduction gap opening in edge-disordered systems is evidence of Anderson disorder, and Cresti and Roche [59], who found localisation lengths that were less than the device length (470nm) for edge-vacancies at >5% concentration for single hexagonal defects or when Klein defects were included. A conductance gap is opened in devices studied by Cresti and Roche [59], and Mucciolo *et al.* [67], when the conductance is suppressed significantly (conductance less than $0.01 * 2e^2/h$ [29, 79]) due to Anderson localisation. The fact that the STB results demonstrates Anderson localisation implies that at longer device lengths, a conductance gap may form as discussed later in Subsection 4.3.5.

The increased kinetic degrees of freedom in the ETB and GTB models leads to regions at -0.450 eV< $E - E_F$ <-0.100 eV and -0.060 eV< $E - E_F$ <0.030 eV for the ETB model, and at -0.776 eV< $E - E_F$ <-0.296 eV and 0.168 eV< $E - E_F$ <0.440 eV for the GTB model, where the localisation length for the 20-5-ZGNR at 7.5% edge-vacancy concentration is shown to be outside of the Anderson localisation regime (Figure 4.18(a)). The spin-dependent GTB results show spin-up having longer localisation lengths compared to spin-

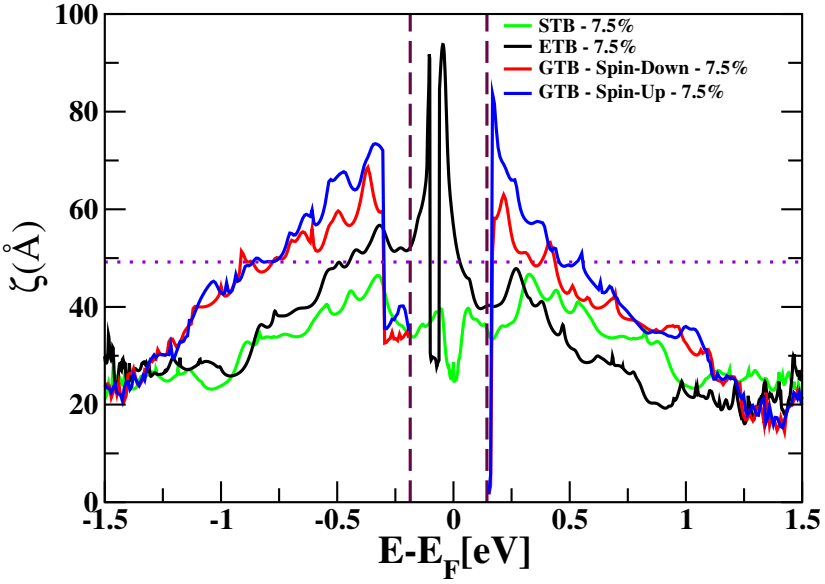


(a) 7.5%

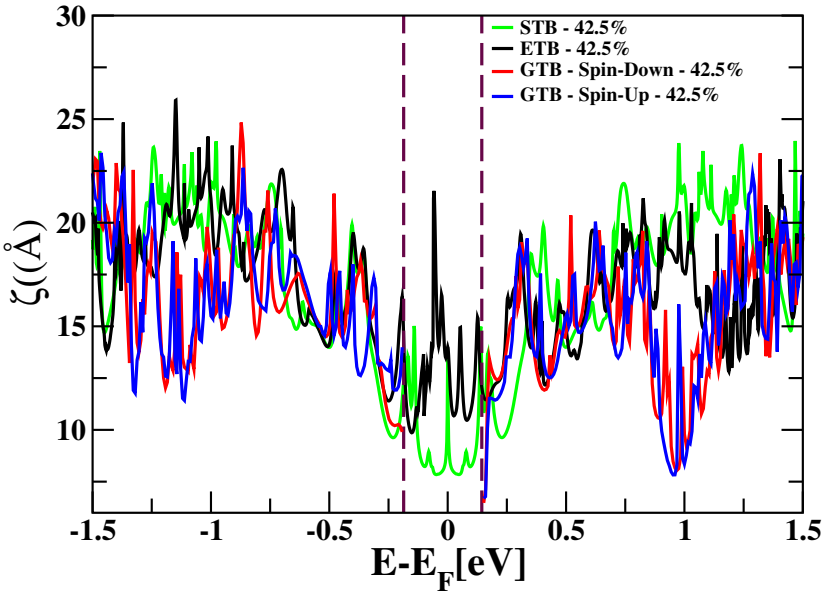


(b) 42.5%

Figure 4.18: The effect of increasing the edge-vacancy concentration on the ensemble-averaged localisation length calculated for a 20-5-ZGNR with (a) 7.5%, and (b) 42.5% edge-vacancy concentration. Green, black, red(blue) denote the STB, ETB, GTB spin-down(-up) results, respectively, for the edge-vacancy defected 20-5-ZGNR. Purple, dashed orange and dashed pink denote the ideal 20-5-ZGNR STB, ETB and GTB results, respectively. In (a), a purple dotted line has been included to signify the overall device length of 48.02 Å. For the non-interacting models (STB and ETB) and for the ideal GTB device, the results are spin-independent. The energy, $E$, is taken relative to the Fermi energy, $E_F$ and has an uncertainty of $\pm 0.008$ eV associated with it. The maximum uncertainty associated with the localisation lengths determined within the ensemble average is 3Å(Equation 4.3)

down outside of the Anderson localisation regime due to spin-up being the majority spin in the Hubbard-$U$ convergence (Figure 4.18). Inside the Anderson localisation regime, the trend is predominantly to exhibit no spin-dependence.

At 42.5% edge-vacancy concentration, the STB, ETB and GTB models are shown to follow the same general trend, with the calculated localisation lengths being within the Anderson localisation regime (Figure 4.18(b)). There is no spin-dependence discernible in the GTB results at 42.5% random edge-vacancy concentration. A limitation of the work in this section is that only a single length of 48.03 Å was analysed therefore providing only a general indicator for Anderson localisation. In the next section, the conductance of 7.5%, 42.5% and 90% edge-vacancy defected 5-ZGNRs will be studied as a function of device length, therefore providing a more accurate estimation of localisation lengths in these systems.

### 4.3.5 Effects of Variable Device Length on the Charge-carrier Localisation

Cresti and Roche [59] showed that the charge-carrier localisation in GNRs, and therefore conductance, is dependent on the system dimensions. As shown in Section 4.3.2 (Figure 4.17(a)), the charge-carrier conductance at the Fermi energy, which was calculated using the non-interacting models for random edge-vacancy defected 20-5-ZGNRs (STB and ETB models), is not suppressed sufficiently at all edge-vacancy concentrations to meet the $0.01 * 2e^2/h$ conduction-gap criterion [29, 79]. In this section, the length-dependence associated with the coherent transport properties of the 5-ZGNR, with lengths, 48.03 Å (20-5-ZGNR), 72.05 Å (30-5-ZGNR), 96.06 Å (40-5-ZGNR), 120.08 Å (50-5-ZGNR) and 144.09 Å (60-5-ZGNR), is investigated using the STB, ETB and GTB models to better understand the interplay between length, the kinetics of the model, and Hubbard-$U$ effects.

As an initial investigation, the non-interacting STB and ETB models were compared (Figure 4.19) to determine if the conductance at the Fermi energy drops below the $0.01 * e^2/h$ conduction-gap criterion, thus indicating the on-set of a conductance gap as a function of the increasing system length. For 7.5% and 90% edge-vacancy concentrations, there is an inverse linear dependence of the conductance at the Fermi energy as a function of increasing device length. In addition, the conductance at the Fermi energy is shown to be larger for the ETB model than for the STB model for all device lengths. The trend whereby the ETB conductance is greater than the STB conductance coincides with previous trends seen in the conduction results shown in Section 4.3.2.

The inverse linear nature of the trends shown in Figure 4.19 means that Anderson localisation is not occurring at 7.5% and 90% edge-vacancy concentrations as an exponential decrease in the conductance would be expected as per Equation 4.6 [177]. These results support those shown in Section 4.3.4, which demonstrate that the 20-5-ZGNR is not Anderson localised for all energies considered between -1.5 and 1.5 eV. The study here will therefore fo-

cus on the 42.5% edge-vacancy defected devices (Figure 4.20), which are Anderson localised, such that the competition between the Anderson localisation and Hubbard-$U$ effects can be probed using the GTB model. The importance of the 42.5% edge-vacancy concentration was also highlighted previously in the study of the 20-5-ZGNR, where this device was shown to be Anderson localised for all models (STB, ETB and GTB) independent of the energy considered.

For highly disordered 42.5% edge-vacancy defected 5-ZGNRs, a logarithmic decrease in conductance at the Fermi energy can be seen between lengths 48.02 Å and 96.06 Å (Figure 4.20). The logarithmic decrease is in agreement with the general trends reported by Li and Lu [62] and Mucciolo *et al.* [67] using the STB model for defected GNR devices that are Anderson localised. Specifically, Mucciolo *et al.* [67] results infers a logarithmic decrease in conductance for a randomly edge-disordered 4.7 nm-wide ZGNR device as a function of increasing device length, where the $G_{on/off}$ ratio (*i.e.,* the ratio between the conductance at the Fermi energy ($G_{off}$) and conductance at the first conductance step ($G_{on}$)) is shown to increase exponentially as the device length increases. Li and Lu [62] studied random edge-disorder (due to perturbed on-site energies) in 8- and 12-ZGNR devices and demonstrated a logarithmic decrease in conductance at the Fermi energy above device lengths of 50 Å.

For devices longer than 96.06 Å (40-5-ZGNR), the individual spin-conductance drops below the conductance-gap criterion value of $0.01 * e^2/h$, within an ensemble averaging uncertainty of maximum $\pm 0.01 * e^2/h$ for both the STB and ETB models (Figure 4.20). This result is in general agreement with Cresti and Roche [59], who demonstrated a decrease in conductance at the Fermi energy for a 7.5% randomly edge-disordered 16-ZGNR up to a device length of 470 nm, at which point the conductance was shown to fall below the $0.01 * 2e^2/h$ [79, 29] conduction value. A conductance gap of 1.75 eV was showed to form for this system which increased in size as the device length was increased.

Compared to the minimum gap-opening length of 96.06 Å needed for the 5-ZGNR (Figure 4.20) at 42.5% edge-vacancy concentration, the significantly larger (2 orders of magnitude) device length of 470 nm studied by Cresti and Roche for the 16-ZGNR [59] with 7.5% edge-vacancy concentration was required for the conductance gap to open due to a combination of the increased device width (leading to a decrease in vacancy sensitivity [52, 62, 67]) and a decrease in edge-vacancy concentration. The fact that Cresti and Roche [59] demonstrates both a logarithmic decrease in conductance and the eventual opening of a edge-vacancy gap suggests that 7.5% edge-vacancy 5-ZGNR devices studied using the STB and ETB models will eventually enter the Anderson regime at significantly larger device lengths.

To determine the localisation length for the 42.5% random, edge-defected 5-ZGNR, the Anderson localisation equation (Equation 4.6) was fitted to the conductance at the Fermi energy vs. length results (Figure 4.20). From these fits, localisation lengths of 47 Å and

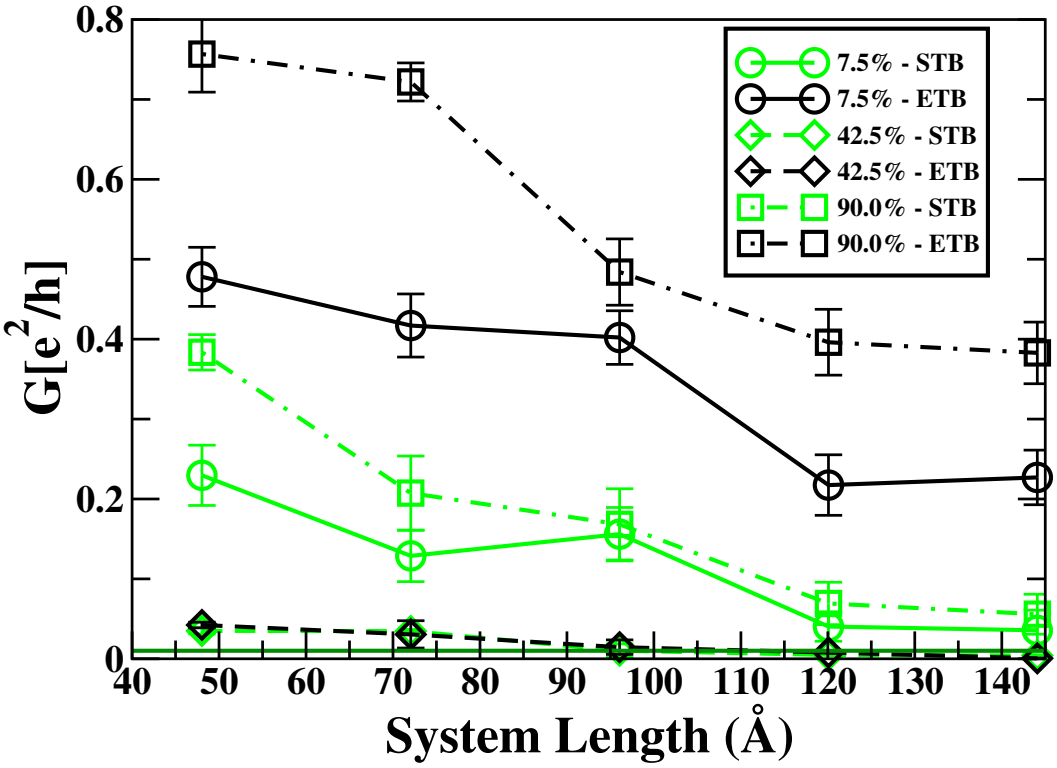


Figure 4.19: Effect of device-length on the charge-carrier conductance measured at the Fermi energy for random edge-disordered 5-ZGNRs. Light green(black) symbols represents the STB(ETB) model. Circles, diagonals and squares correspond to 7.5%, 42.5% and 90% edge-vacancy concentrations, respectively. When the conductance drops below the dark green line ($0.01 * 2e^2/h$ threshold) it is assumed to be zero, indicating a conductance gap as per the criterion established [29, 79] . In real-space, a 5-ZGNR has a system-width of 9.24 Å.

49 Å having a maximum uncertainties of ± 3 Å (Equation 4.3) were determined for the STB and ETB models, respectively. These localisation lengths are in agreement with the general trends discussed previously (Subsection 4.3.4), namely that the STB model demonstrates greater charge-carrier localisation than the ETB model (Figure 4.18).

Using the criterion in Refs [180, 181, 182], Cresti and Roche [59, 58] were able to demonstrate the onset of the localisation regime. Using Refs [180, 181, 182], the diffusion regime is determined to be well established when,

$$\frac{\Delta G(0)}{< G(0) >} < 1 \tag{4.8}$$

whereas, using Equation 4.6, the localisation regime is well defined when,

$$\frac{\Delta G(0)}{< G(0) >} > 1 \tag{4.9}$$

and

$$\frac{\Delta ln(G(0))}{< ln(G(0)) >} < 1 \tag{4.10}$$

where $\Delta G(0)$ is the standard error in the ensemble average transport results at the Fermi

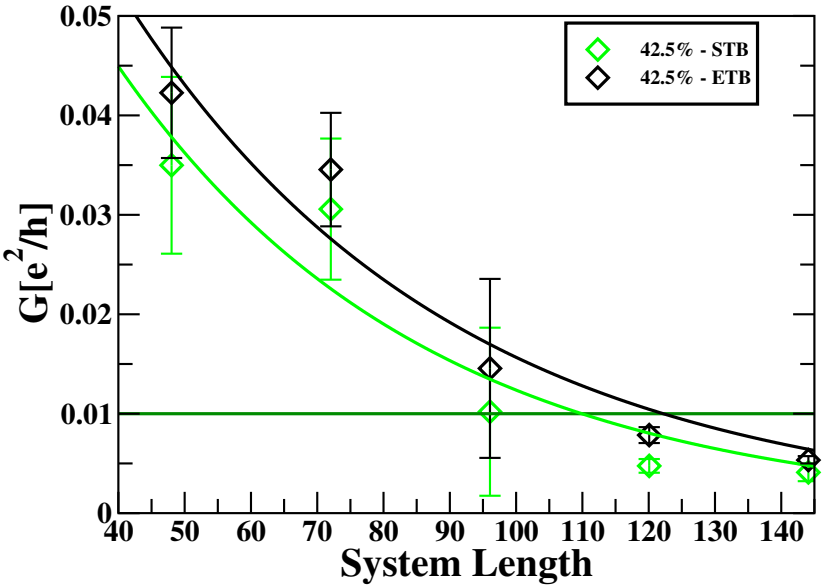


(a)

Figure 4.20: Effect of device-length on the charge-carrier conductance measured at the Fermi energy for 5-ZGNR devices with 42.5% edge-vacancy concentration. Light green(black) symbols correspond to the STB(ETB) model results. When the conductance drops below the dark green line ($0.01 * 2e^2/h$ threshold) it is assumed to be zero, indicating a conductance gap as per the criterion established [29, 79]. In real-space, a 5-ZGNR has a system-width of 9.24 Å.

energy and $< G(0) >$ is the ensemble average transport at the Fermi energy.

Figure 4.21 shows the effects of device length on the diffusion-localised regimes. For 7.5% random edge-vacancy concentration (Figure 4.21(a)), there is no transition from the diffusion regime to the localisation regime, with Equation 4.8 increasing above 1 for both the ETB and STB models and Equation 4.10 remaining above 1 for all device lengths. The fact that Equation 4.10 can be below 1 without Equation 4.8 being greater than 1 is in agreement with Cresti and Roche [58].

The 5-ZGNR with 42.5% edge-vacancy concentration (Figure 4.21(b)), on the other hand, is within the localisation regime for device lengths greater than 48 Å. This increased localisation with increased random edge-vacancy concentration is in agreement with both the work in this document (Figure 4.18) and in the established work discussed above, for example, Cresti and Roche [59, 58], Mucciolo *et al.* [67] and Li and Lu [62]. In addition, the approximate point of transition between diffusion and localised (i.e., between 40 Å and 50 Å) is in agreement with the Anderson localisation length calculations carried out above (Figure 4.21).

In terms of published literature, Cresti and Roche [59, 58] use the regimes, and thus the localisation lengths determined from Refs [180, 181, 182] whereas Mucciolo *et al.* [67] and Li and Lu [62] determined the localisation lengths from the Anderson localisation equation [176, 177, 178] (Equation 4.6). As demonstrated in this document, these two localisation methods, the fitting of the Anderson localisation equation and through the statistics of the ensemble average, are in agreement with each other.

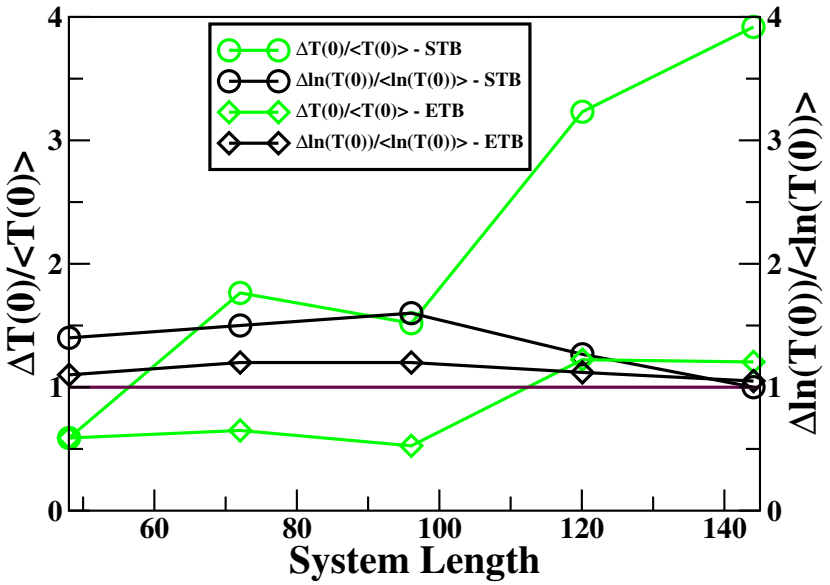


(a) 7.5%

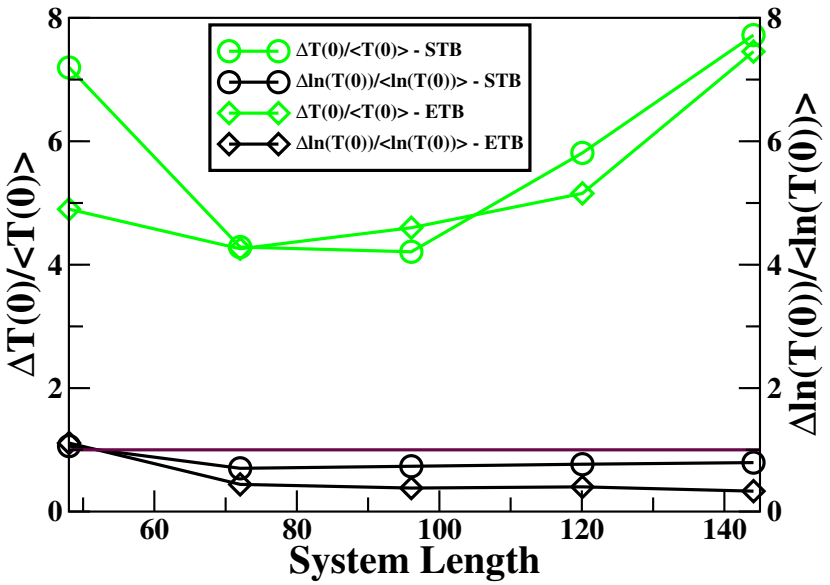


(b) 42.5%

Figure 4.21: Effect of device-length on Equation 4.8 (light green) and Equation 4.10 (black) for random edge-disordered 5-ZGNRs with (a) 7.5% and (b) 4.2% edge-vacancy concentration. Circle(Diamond) symbols represents the STB(ETB) model. Solid horizontal lines denote the point at which a trend fulfills the regimes criterion (Equation 4.10).

As discussed in subsection 4.3.4, Equation 4.7 had been previously fitted using the 20-5-ZGNR conductance results, where it was shown that for the GTB, ETB and STB models, the system was entirely charge-carrier localised at 42.5% edge-vacancy concentration (Figure 4.18). The fact that both STB and ETB systems fall below the $0.01 * e^2/h$ zero conductance criterion at the Fermi energy is the equivalent to the onset of a conductance gap. The edge-vacancy disorder-induced conductance gaps in the non-interacting models can be compared to the interacting GTB conductance gaps. Such a comparison will determine if there is a point as a function of the system parameters (edge-vacancy concentration and device length), where the non-interacting, disorder-induced conductance gap could be equivalent to, or extend beyond the interacting GTB system conductance gap (Figure 4.23).

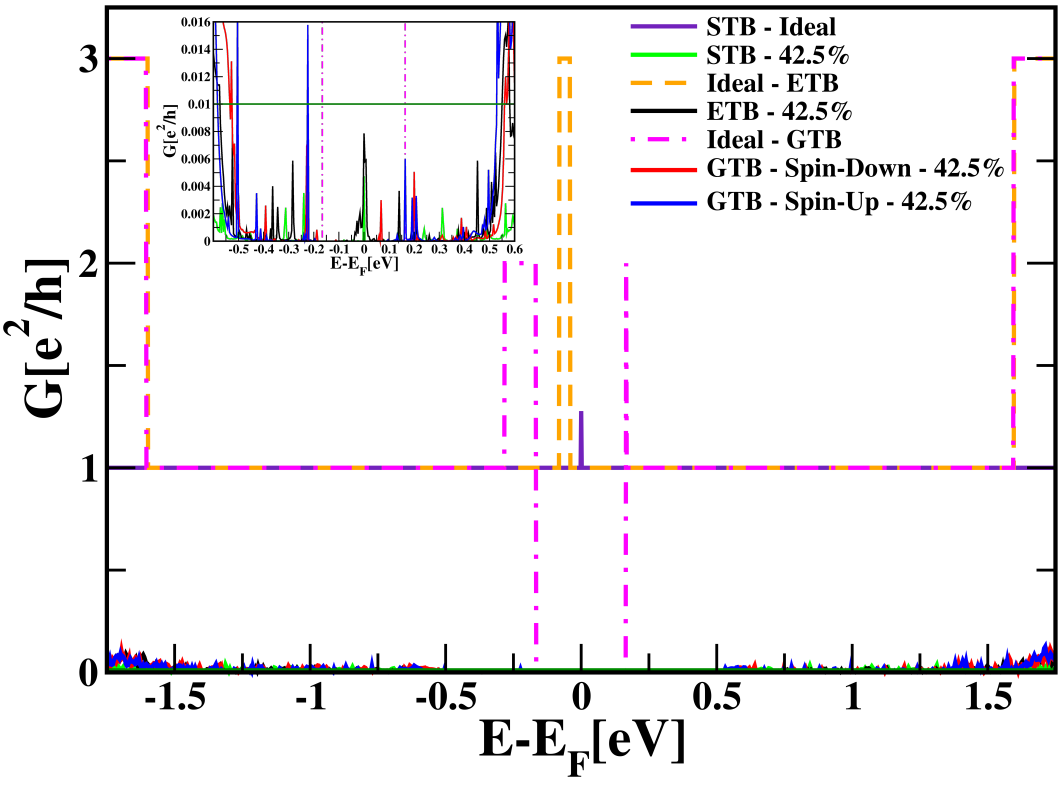


Figure 4.22: Transport result for a 50-5-ZGNR of length 120.075 Å with 42.5% random edge-vacancy concentration demonstrating the conductance gaps that are observed. When the conductance drops below the dark green line ($0.01 * 2e^2/h$) it is assumed to be zero (See zoomed in insert).

Figure 4.19 showed that only the 50- and 60-5-ZGNR non-interacting devices (120.075 Å and 144.09 Å, respectively) with 42.5% edge-vacancy disorder have a conductance at the Fermi energy that is less than the $0.01 * 2e^2/h$ gap forming criterion. To understand these results within the context of the transport results, Figure 4.22 shows the conductance of a 50-5-ZGNR device with 42.5% random edge-vacancy concentration. A 50-5-ZGNR device was chosen as it is the shortest device length investigated to have both non-interacting models (STB & ETB) below the zero conductance criterion of $0.01 * e^2/h$ (Figure 4.22). The dark green line in this figure denotes the $0.01 * e^2/h$ conduction criterion, and thus it is possible to see the point at

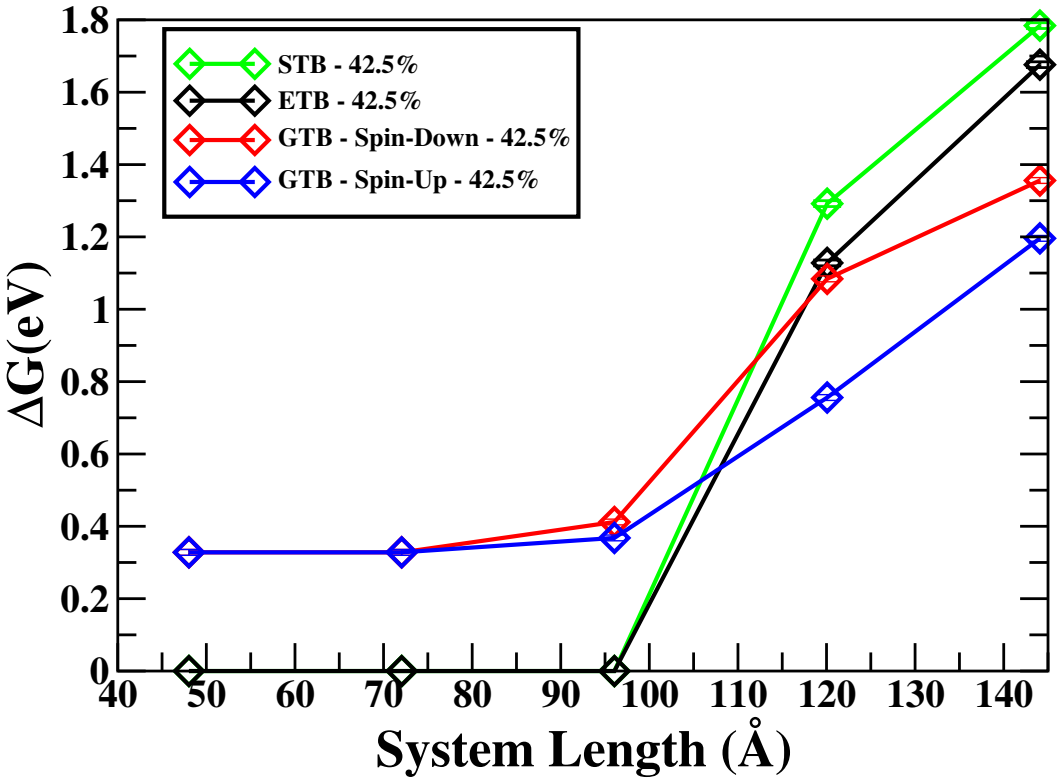


Figure 4.23: Effect of device-length on the conductance gap for 42.5% random edge-vacancy disordered 5-ZGNRs. Light green, black, blue(red) symbols represents the STB, ETB, GTB spin-up(-down) results, respectively.

which the smallest gap result, namely the spin-up conductance (blue), becomes greater than the zero conductance criterion of $0.01 * e^2/h$ which occurs at 0.224±0.008 eV.

The ideal system result in Figure 4.22 can be used as a benchmark to demonstrate the increase in the interacting (GTB) system's conductance gap due to disorder as a function of the increasing length compared to the intrinsic ideal gap. Specifically, in comparison to the GTB result, the non-interacting system conductance gap is shown to increase from 1.292±0.008 eV for the 50-5-ZGNR to 1.784±0.008 eV for the 60-5-ZGNR in the STB model, and from 1.128±0.008 eV for the 50-5-ZGNR to 1.676±0.008 eV for the 60-5-ZGNR for the ETB model (Figure 4.23). Note that the interacting GTB model maintains the intrinsic conductance gap of 0.328±0.008 eV for the 20- and 30-5-ZGNR systems having lengths of 48.03 Å and 72.04 Å, respectively (Figure 4.23). The intrinsic conductance gap caused by the Hubbard-$U$ starts to open for the 40-5-ZGNR system (96.06 Å length), and shows symmetry-breaking upon comparison of the results pertaining to the spin-up and spin-down results (Figure 4.23).

The edge-vacancy induced GTB conductance gap increases in size as the device length increases following a similar trend as the non-interacting models (STB & ETB). For 50-5-ZGNR length devices and for longer 5-ZGNR device lengths, the largest interacting conductance gap (in this case, for spin-down) is smaller than the non-interacting conductance gaps, implying that the non-interacting system is more localised than the interacting one (Figure 4.23). For

a device length of 40-5-ZGNR and for longer devices, the GTB conductance gaps continue to increase in size as the device length increases, following a similar trend as the non-interacting models. For the 40-5-ZGNR device there is a slight increase in the interacting conductance gaps of 0.412eV for spin-down and 0.368eV for spin-up compared to the intrinsic GTB gap of 0.33eV. As a function of increasing device length, the edge-vacancy induced gap increases to 1.08(0.756)eV for spin-down(-up) at 50-5-ZGNR and 1.36(1.20)eV for spin-down(-up) at 60-5-ZGNR (Figure 4.23).

At a fixed device length, more conduction channels are removed with increasing edge-vacancy concentration leading to a decrease in the charge-carrier conductance within the -1.5eV$< E - E_F <$1.5eV range. In removing these conductance channels the probability of charge-carrier scattering becomes greater than the probability of charge-carriers passing though the device. Increasing the device length for a fixed edge-vacancy concentration does not change the number of conduction channels though the device. Instead, as the length of the conduction channels increases for increasing device length, the probability that a single charge-carrier will encounter a scattering site (*i.e.,* edge-vacancy), and thus get scattered, increases. When the device length is longer than the charge-carrier localisation length, the number of charge-carriers scattered become sufficient for Anderson localisation to occur [177].

The non-interacting systems require longer device lengths for edge-vacancy perturbation effects to appear (*i.e.,* via the opening conduction gap) due to the non-interacting edge-states being more robust to edge-vacancy perturbations compared to the edge-states in the GTB interacting system. For example, for 5-ZGNR devices at 42.5% edge-vacancy concentration, the defect-induced spin-conductance gaps in the GTB results are larger than the intrinsic GTB gap commencing at a device length of 40-5-ZGNR (*c.f.* Figure 4.23). In comparison, the non-interacting models (STB & ETB), show edge-vacancy induced conduction gaps starting to open at a greater device length of 50-5-ZGNR. The onset of edge-vacancy perturbation effects at a shorter device length for the GTB model relative to the non-interacting models is due to the Hubbard-U term in the model introducing competition between the scattering localisation and the magnetic localisation.

The fact that these systems are Anderson localised even at lengths smaller than 120.075Å, *i.e.,* the length at which conductance drops below the critical value, means that the conductance does not need to drop below $0.01 * 2e^2/h$ to be considered localised. The fact that this localisation can occur at conductance greater than $0.01 * 2e^2/h$ means that it is not sufficient to use the critical value of conductance to determine if a system is localised. Instead, the localisation length is a more accurate description of the onset of localisation. This is in agreement with Li and Lu [62], Areshkin *et al.* [52] and Mucciolo *et al.* [67]. All three studies find conductances at the Fermi energy above the zero conductance criterion of $0.01 * 2e^2/h$ at device lengths greater than the Anderson localisation length.

Anderson localisation does not depend on the formation of an approximate conductance gap or a critical reduction in conduction to occur [60]. The condition for Anderson localisation is that the mean-free path of the charge-carriers is less than that of the system length, and, thus, there is an increasing probability that charge-carriers will be localised within the device and not traverse the device [60]. This separates the disorder-induced localisation [59], which leads to the opening of a conductance gap, from Anderson localisation.

## 4.4 Conclusion

In this chapter, it was demonstrated that there is an overall decrease in conductance of GNRs with the introduction of edge-vacancies. In particular, it has been shown that there is an overall increase in localisation along the ribbon-edge up to a critical edge-vacancy concentration of 51.25%. When comparing the three models, the simple tight-binding (STB) model, the extended tight-binding (ETB) model, and the generalised tight-binding (GTB) model, the general trend of decreasing electronic transport is observed in all three models, with convergence of the conductance occurring between 32.5% and 51.25% edge-vacancy concentration. It has also been shown that at 42.5% edge-vacancy all three models are within the localisation regime, with the STB model being fully within the localisation regime at low edge-vacancy concentrations (7.5% edge-vacancy concentration). The stability of the conduction-gap in the GTB model and of the non-zero conductance at the Fermi energy for the non-interacting models with the introduction of edge-vacancies implies that, even at high edge-vacancies concentrations, the GTB model is sufficiently different that it should be used over the simpler, non-interacting, models. When compared to the experimental, chemically derived nanographene gap there is a better agreement with the GTB model due to the stability of the model conductance gap. The effect of random edge-vacancies compared to systematic edge-vacancies was also investigated and it was found that random edge-vacancies stabilise the edge-polarisation and prevent the antiferromagnetic/paramagnetic transition observed in the systematic edge-vacancies study, implying that the GTB is preferred over the non-interacting models to calculate the effects of these edge-defects.

In addition, the effects of increasing device length was probed and Anderson localisation lengths of 47Å and 49Å were found for the STB and ETB models respectively. The difference between localisation and Anderson localisation was also discussed, with Anderson localisation requiring longer devices. Finally, the onset of the non-interacting conductance gap was investigated, with the conductance gap calculated via the STB and ETB models following the same trend as the GTB model above 120Å.

The results in this Chapter lead to the conclusion that the interacting GTB model is required for the edge-disordered ZGNRs studied, with the intrinsic gap only being overtaken by the disorder-induced conductance gap at device lengths $>$ 120 Å. The stability of the

intrinsic conductance gap in the GTB model compared to the disorder-induced conductance gap of the STB and ETB models suggests that the experimentally observed band gap can be attributed to the electron-electron interactions, not the effects of edge-disorder.

# Chapter 5

# Effects of Asymmetrical Edge Perturbations and Uniaxial Strain on the Spin-dependent, Coherent Transport of ZGNRs

## 5.1 Abstract

The effects of asymmetric edge-patterning and uniaxial strain were investigated, with notch properties investigated. The effects of a square and V-notch in 5-ZGNR devices were calculated using the GTB model. Both notch types were shown to decrease the overall conductance, with a decrease of up to 98% between -1.5eV and 1.5eV.

The effects of increasing notch bottom length was also investigated and it was demonstrated that there is an overall increase in localisation as the notch bottom length increases. For a three atom long V-notch bottom 5-ZGNR device there is a decrease in the spin-up conductance gap of 0.7eV and a increase in the spin-down conductance gap of 0.002eV when compared to the ideal 5-ZGNR device. For a six atom long V-notched bottom 5–ZGNR device there is a decrease in conductance gap for both spin-directions, 0.048eV and 0.022eV for spin-up and spin-down, respectively. In particular, there is an increase in the localisation of spin-up electrons, in agreement with the increase in spin-up localisation sites.

Uniaxial strain was then introduced to both notched and ideal systems, with systems producing an inverse dependence of spin-independent coherent conductance gap on uniaxial strain in the y-direction, in agreement with published literature [115, 126, 125].

Finally, the effects of both edge-notches and uniaxial was probed, with the uniaxially strained notched 5-ZGNR devices demonstrating the same (within error) trends as the ideal 5-ZGNR device, with the spin-dependent conductance gap decreasing from 0.328eV at 0%

uniaxial strain for both spin-directions in the V-notched 5-ZGNR to 0.232eV and 0.236eV for spin-up and spin-down, respectively, at 20% uniaxial strain.

## 5.2 Effects of Asymmetrical Notches in ZGNRs on the Spin-dependent, Coherent Transport

Chapter 4 demonstrated how the transport stops being spin-independent due to random edge-vacancies, which is an important consideration in the design of future spintronic devices. This chapter will investigate structural asymmetric edge-perturbations, *i.e.*, notches, in order to probe possible spin-dependent effects. Uniaxial strain is also introduced to these devices to exploit the direct correlation between strain and band-gap [105, 106, 107, 108, 109, 110, 111, 112, 113, 114, 115]. The combination of these two properties (asymmetrical edge-perturbations and uniaxial strain) may allow the onset and enhancement of the spin-dependent transport properties. Before these perturbations can be probed in combination, they must be investigated separately.

Hancock *et al.* [33], Zhang *et al.* [83] and Wimmer *et al.* [84] showed spin-dependent properties of notched ZGNR devices both in the coherent transport and in the local spin-distribution of notched ZGNR devices. This section will investigate square notched and V-notched asymmetric-edge devices, where a square notch combines both ZGNR and AGNR edge types and a V-notched device contains ZGNR edge-type only. Figure 5.1 shows these two edge-structures in the notch. The ability to simulate the mixed edge-structure systems is one of the advantages of the GTB model [33].

Following the method in Chapter 4 (section 4.3.2), an ideal ZGNR region is required either side of the edge-perturbation (in this case the notch). The ideal region is calculated for both square and V-notch devices. For the spin-dependent, coherent transport results (Equation 2.98) the non-defected region must first be added to each end of the device in order to prevent discontinuities in the spin-polarisation between the asymmetrically notched device and semi-infinite ideal leads (Figure 5.1). The non-defected regions were converged for a 5-ZGNR device with a square notch of 4-ZGNR deep (7.39Å) and three unit cells long (7.38Å) (Figure 5.1(b)). These regions were also converged for a V-shaped notched device that was 4-ZGNR deep, one unit cell long (2.46Å) at the shortest point and three unit cells (7.38Å) at the longest point (Figure 5.1(a)). 5-ZGNR was chosen as edge-effects are enhanced due to it being a narrower system system.

Figure 5.2 shows the increase in spin-polarisation of the device-lead boundary edge-atoms as the ideal (i.e., non-defected) region at each end of the defected device is increased in length. The local net spin-polarisation of the edge-atoms at the device-lead boundary approaches that of the ideal system until they converge at a non-defected region nine atoms long (22.1Å) with

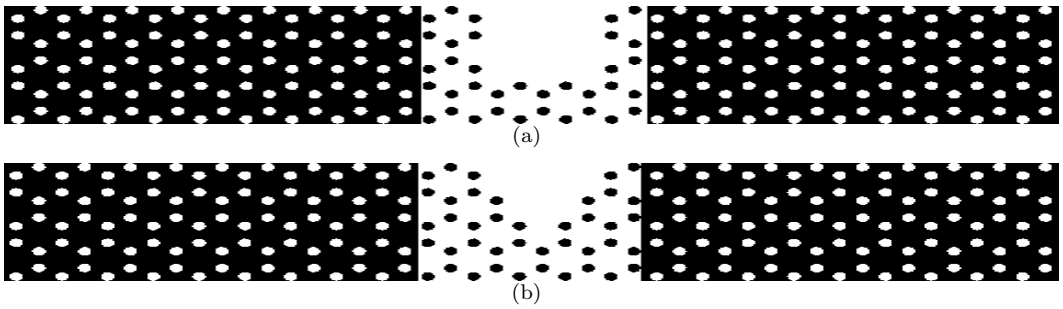


Figure 5.1: Schematic of the systems used for transport calculations (a) a square notched 5-ZGNR device, and (b) a V-notched 5-ZGNR device. The first and last nine (22.14Å) unit cells (black background, white atomic sites) in the system are ideal, and the middle five (12.3Å) unit cells (white background, black atomic sites) defines the notched device region. In real-space, 5-ZGNR has a width of 9.24Å. The entire device length is 34.4Å.

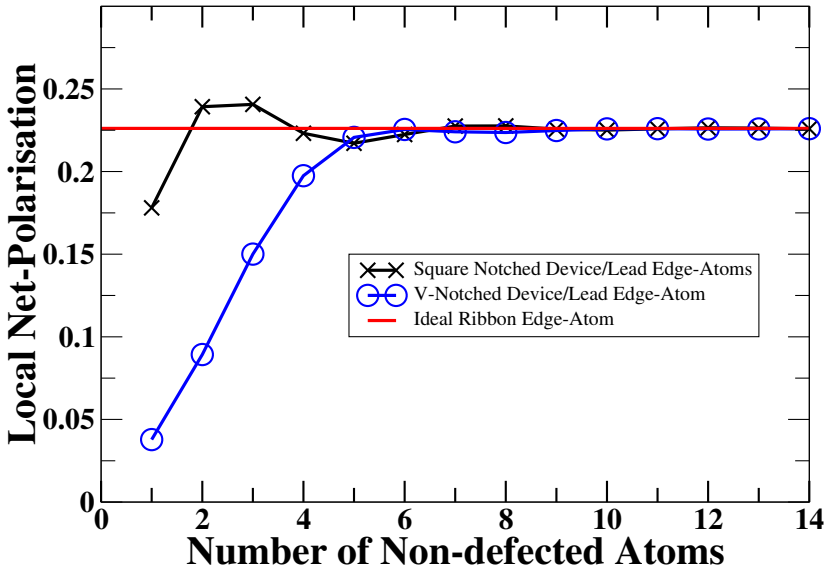


Figure 5.2: Convergence of the local net spin-polarisation (Equation 2.81) of the device/lead edge atoms for the two asymmetrical notched 5-ZGNR devices using the GTB model (Equation 2.67). The red line shows the ideal result for a 5-ZGNR that is required for accurate and continuous device-lead coupling of the edge-atom. The black(blue) curve corresponds to the local net-occupancy of the device-lead boundary edge-atom for a square(V-) notched 5-ZGNR device with increasing ideal region.

a net local spin-polarisation of $|\pm 0.227|$ for the spin-up(+ve) and spin-down (-ve) edges for both notch types investigated (square, Figure 5.1(a) and V-notch, Figure 5.1(b)). As discussed in the previous chapter (Section 4.2) when compared to the DFT LSDA results by Huang *et al.* [50], the effects of atomic relaxation around the defect (i.e, the notch in this situation) are insignificant compared to the effects of the notch and therefore can be ignored.

### 5.2.1 Square Notched ZGNR

With the introduction of the square notch to the 5-ZGNR device (Figure 5.1(a)), there is an overall decrease in conductance relative to the ideal device, consistent with the introduction of edge-vacancies (Figure 5.3). Specifically there is a decrease in conductance of $1.01e^2/h$

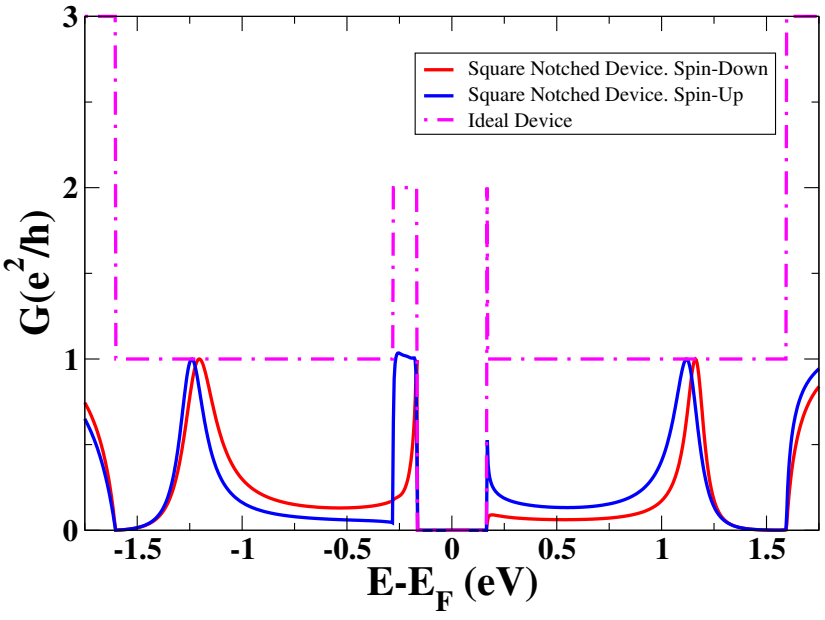


Figure 5.3: Conductance (Equation 2.98) vs energy relative to the Fermi-energy for the square notched 5-ZGNR device (Figure 5.1(a)) using the GTB model (Equation 2.67). For the ideal 5-ZGNR device, the result is spin-independent. Red(blue) gives the square notched GTB spin-down(-up) result. Dashed pink gives the ideal 5-ZGNR GTB result.

from the top of the ideal 5-ZGNR conductance peek and the highest point of the spin-down conductance peak at $E - E_f$ = -0.167eV, and a decrease of $1.82e^2/h$ from the top of the ideal 5-ZGNR conductance peek and the lowest point of the spin-down conductance peak at -0.179eV (Figure 5.3). For the spin-up conductance, the conductance peak between -0.167eV and -0.179eV decreases less overall relative to the ideal device, with the largest decrease being $1.08e^2/h$ at -0.171eV and the smallest decrease of $0.965e^2/h$ at -0.255eV. (N.B., errors in energy ($\pm$0.008V) arise due to the width of the energy steps and should be assumed for all measurements).

The reduction in the conductance is due to the loss of conductance channels in the device, in particular along the spin-down (notched) edge (Figure 5.1(a)). The decrease in channels along the spin-down edge leads to the larger decease in conductance about the conductance gap (Figure 5.1(a)) compared to the spin-up (ideal) edge. The decrease in conductance to zero near the first conductance step for both spin-directions, in addition to the decrease in overall size of the top of the conductance step, is in agreement with the effects of random edge-vacancies where this was also shown (Figure 4.16). The reduction in the conductance step is more evident in these studies due to the increased number of edge-vacancies in a notch. Finally, the symmetry of the spin-up and spin-down conductance away from the electronic conductance gap is broken due to the broken symmetry of the device and thus the conductance channels. Figure 5.4 shows the decrease in the local net spin-down polarisation either side of the notch and the slight decrease in local net spin-up polarisation along the edge opposite to the notch.

The asymmetrical decrease in spin-dependent conductance is in agreement with work by Hancock *et al.* [33] who demonstrated similar peaks and dips in the spin-dependent conductance using the GTB model applied to a square notched 5-ZGNR device with a notch depth of 4-ZGNR and width of three unit cells. Hancock *et al.* [33] also compared the square notched GTB result with DFT, LSDA calculations using the TranSIESTA package [16, 183] and showed that the GTB model faithfully reproduces the DFT, LSDA results.

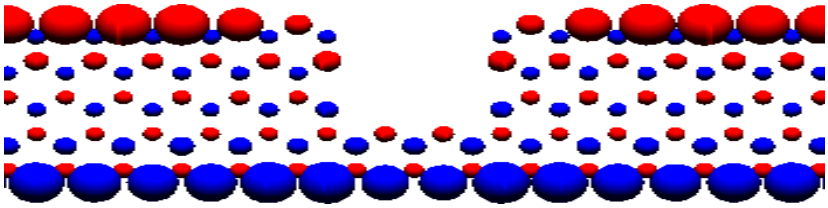

Figure 5.4: Spin-distribution of a square notched 5-ZGNR device calculated using the GTB model (Equation 2.67). Net spin-up circles are blue and net spin-down circles red. The radius of each circle gives the magnitude of the net local-spin (Equation 2.81). In real-space, 5-ZGNR describes a system of width 9.24Å and the entire device length is 34.4Å.

### 5.2.2 V-Notched ZGNR

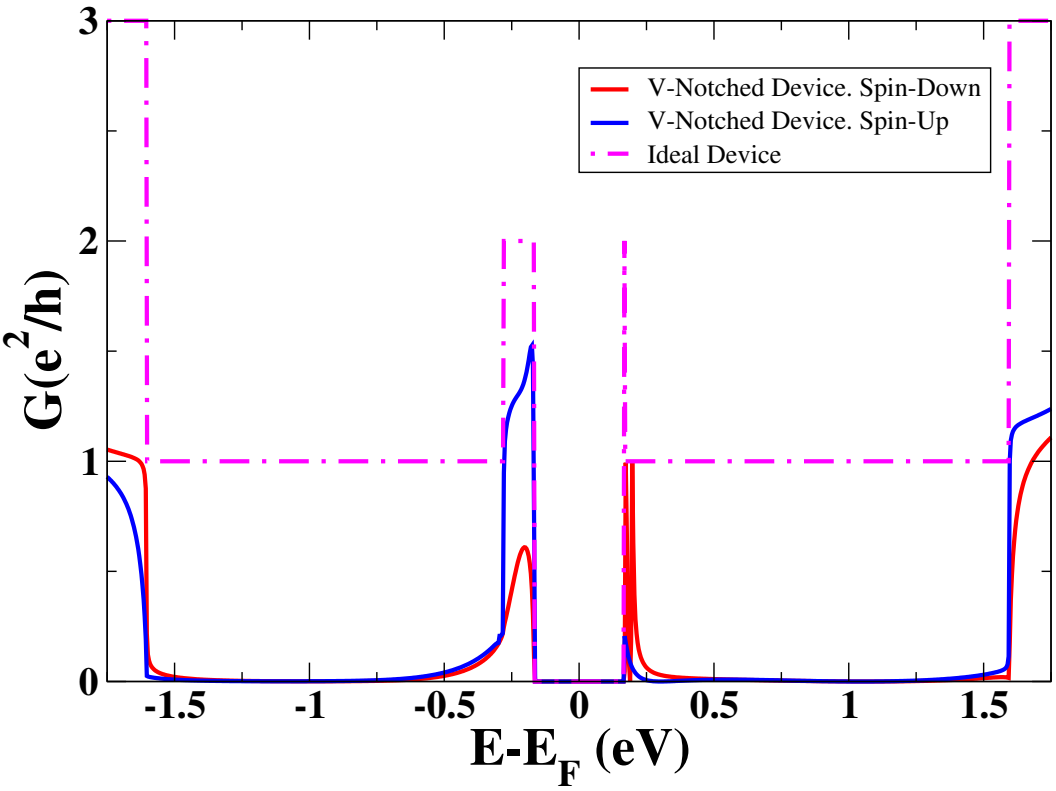


Figure 5.5: Conductance (Equation 2.98) vs energy relative to the Fermi-energy for a V-notched 5-ZGNR device (Figure 5.1(a)) calculated using the GTB model (Equation 2.67). For the ideal 5-ZGNR device, the result is spin-independent. Red(blue) gives the square notched GTB spin-down(-up) result. Dashed pink gives the ideal 5-ZGNR GTB result.

With the introduction of a V-notch to the 5-ZGNR device (Figure 5.1(b)), a similar overall decrease to the conductance occurs compared to the square notch result. In particular, the

smallest decrease relative to the ideal conductance peak for the spin-down conductance is $1.3914e^2/h$ at -0.203eV and the largest decrease is $1.75e^2/h$ at -0.279eV. For the spin-up conductance, the overall conductance again reduces less relative to the spin-down results, with the smallest decrease of $0.4753e^2/h$ occurring at -0.175eV and largest of $1.05e^2/h$ occurring at -0.279eV (Figure 5.5).

The notch removes conductance channels leading to the overall reduction in conductance for both spin-directions. Figure 5.6 shows the spin-polarisation of the 5-ZGNR V-notch device, with the decrease in net spin-down polarisation along the notch-edge and an increase in net spin-up polarisation along the ideal edge. This increase in net spin-up polarisation is due to there being more than three ZGNR edge-atoms in a row, in agreement with Clar's theory [173, 174] as discussed in Chapter 4.

Hancock *et al.* [82] compared the GTB model and DFT LSDA calculations using the TranSIESTA [16, 183] package for a 7-ZGNR device with a V-notch 5-ZGNR deep, five unit cells long at the longest and one unit cell at the shortest. They found faithful agreement in the conductance results between the GTB and DFT LSDA models. In addition, there is qualitative agreement between Hancock *et al.* [82] and the results presented in this section. The main difference is that lack of a conductance spike between approximately $\pm$1eV and $\pm$1.5eV, observed in Hancock *et al.* [82] due to the increased relative depth of the notch (2-ZGNR between the notch and ribbon edge in Hancock *et al.* [82] compared to 1-ZGNR in this work). The spin-polarisation also qualitatively agrees with the effects of the V-notch on spin-polarisation observed by Wimmer *et al.* [84] for a 10-ZGNR device with a 6-ZGNR deep random edge-vacancy defected V-notch using the interacting Hubbard model parameterized to ZGNR only. In addition, the asymmetrical decrease in conductance in a 5-ZGNR V-notched system was found by Zhang *et al.* [83] via DFT calculations using nonequilibrium Greens functions (NEGFs) within the ATOMISTIX TOOLKIT [80, 184][1]. The zero conductance between the conductance spikes around the electronic conductance gap and the conductance steps are also observed in Zhang *et al.* [83].

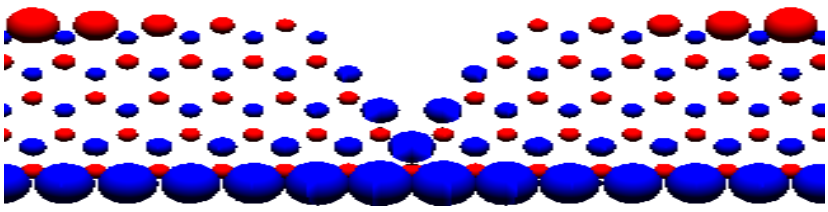

Figure 5.6: Spin-distribution of a V-notched 5-ZGNR device calculated using the GTB model (Equation 2.67). Net spin-up circles are blue, net spin-down circles red. The radius of each circle gives the relative magnitude of the net local-spin, Equation 2.81. In real-space, 5-ZGNR describes a system of width 9.24Å and the entire device length is 34.44Å. Only the region around the notch has been included for clarity.

[1]See http://quantumwise.com/ for ATOMISTIX TOOLKIT, online as of 100214

The increased spin-dependence relative to the square notch, both in terms of the spin-polarisation and spin-conductance, along with the significant decrease in spin-up conductance on the edge of the electronic conductance gap (Figure 5.5) implies that the V-notched system might demonstrate peculiar properties with increasing notch base length and thus the possibility of increased spin-polarisation along the bottom of the notch. Due to computational restrictions, along with a limit in achievable variation in notch depth at this ribbon width, means that only the effect of notch length will be investigated in more detail (Figure 5.7).

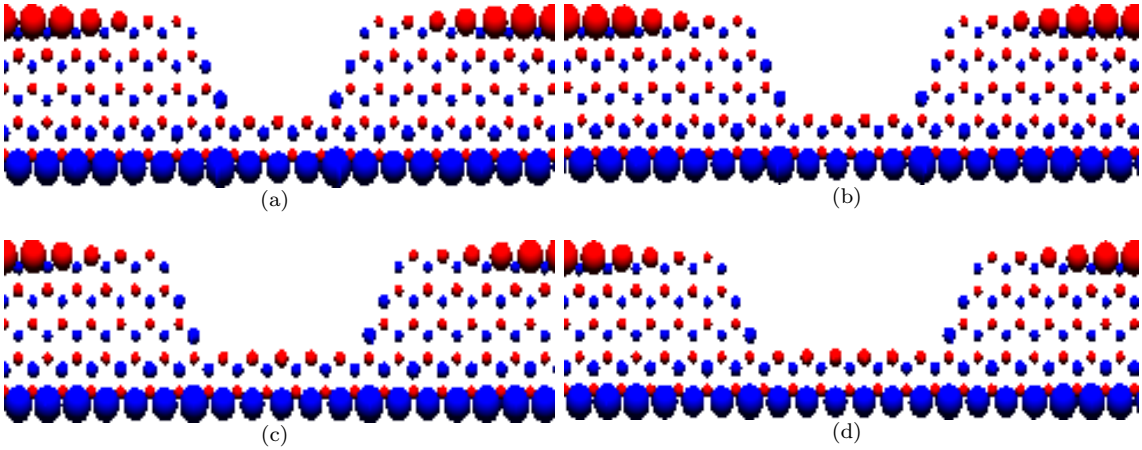


Figure 5.7: Spin-distribution of a series of V-notched 5-ZGNR devices calculated using the GTB model (Equation 2.67). Net spin-up circles are blue and net spin-down circles red. The radius of each circle gives the relative magnitude of the net local-spin (Equation 2.81). Only the region around the notch has been included for clarity.

The devices looked at in the increasing notch length study are shown in Figure 5.7 along with the local net spin-distribution results. The shortest notch bottom was chosen to be large enough that Clar's theory [173, 174] of three ZGNR unit cells in a row is observed both along the device and notch edge, and within the notch. This should introduce extra localisation in the spin-down direction, as demonstrated along the bottom of the notch (Figure 5.7(a)). In terms of the magnetisation per atom, there is an insignificant change in the spin-up and spin-down system wide magnetisation per atom, with a slight decrease in the spin-down magnetisation due to the increase in spin-down localisation inside the notch being smaller than the loss of spin-down localisation with increasing notch size.

Figure 5.8 demonstrates the spin-dependent coherent transport results for a V-notched device with a three atom long bottom (Figure 5.7(a)) and a six atom long bottom (Figure 5.7(d)). In the three atom long V-notch bottom device, the spin-up conductance gap decreases relative to the ideal 5-ZGNR device by 0.7eV, with an increase in the size of the spin-down gap of $0.002eV$ consistent with an increased localisation of the spin-up electrons compared to the spin-down electrons. In the six atom long V-notch bottom device, the relative change in electronic conductance gaps compared to an ideal 5-ZGNR are -0.048eV and -0.022eV for spin-up and spin-down, respectively.

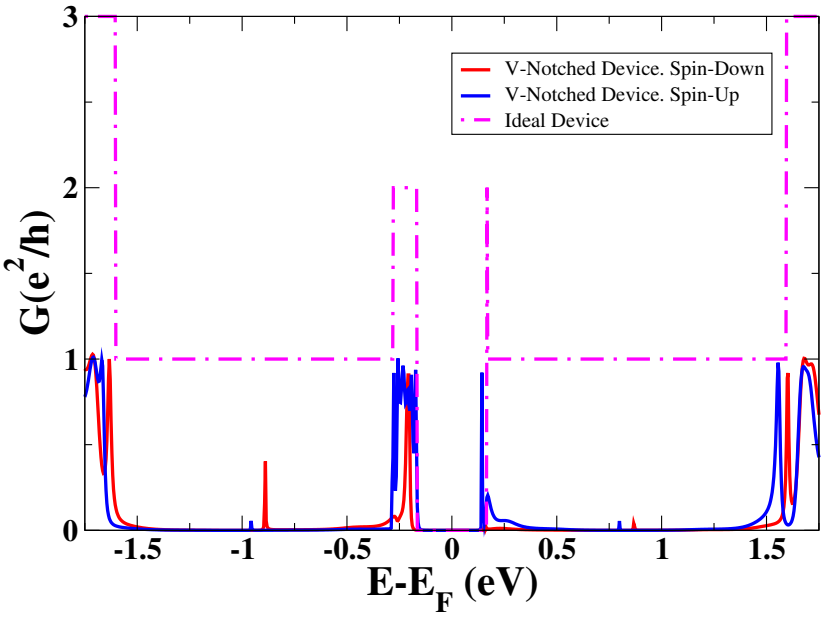


(a)

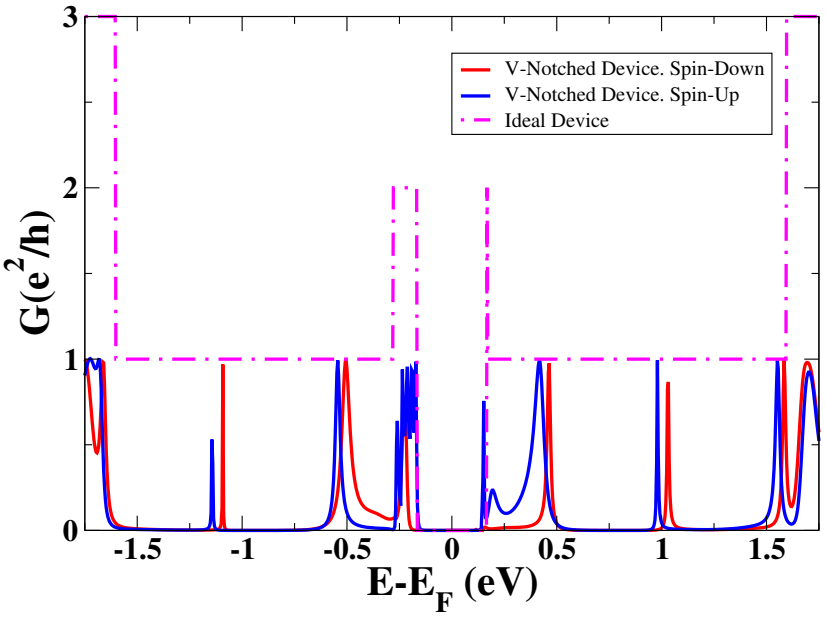


(b)

Figure 5.8: Electronic conductance (Equation 2.98) vs energy relative to the Fermi-energy for a V-notched 5-ZGNR device with (a) a three atom long bottom (Figure 5.7(a)) and (b) a six atom long bottom (Figure 5.7(d)) calculated using the GTB model (Equation 2.67). For the ideal 5-ZGNR device (also shown), the result is spin-independent. Red(blue) gives the V-notched GTB spin-down(-up) result. Dashed pink gives the ideal 5-ZGNR GTB result.

Figure 5.9 shows the change in integrated conductance as the notch bottom length increases. The integrated conductance, calculated using Simpson's rule (Equation 4.5) in the range -1eV< $E - E_f$ <1eV, is shown to initially decrease then increase as the notch bottom length increases (Figure 5.9). The initial decrease is due to the loss of 2nd and 3rd nearest neighbour hopping allowed across the notch and the following increase is due to the shifting position and size of the conductance spikes as previously discussed (Figure 5.8).

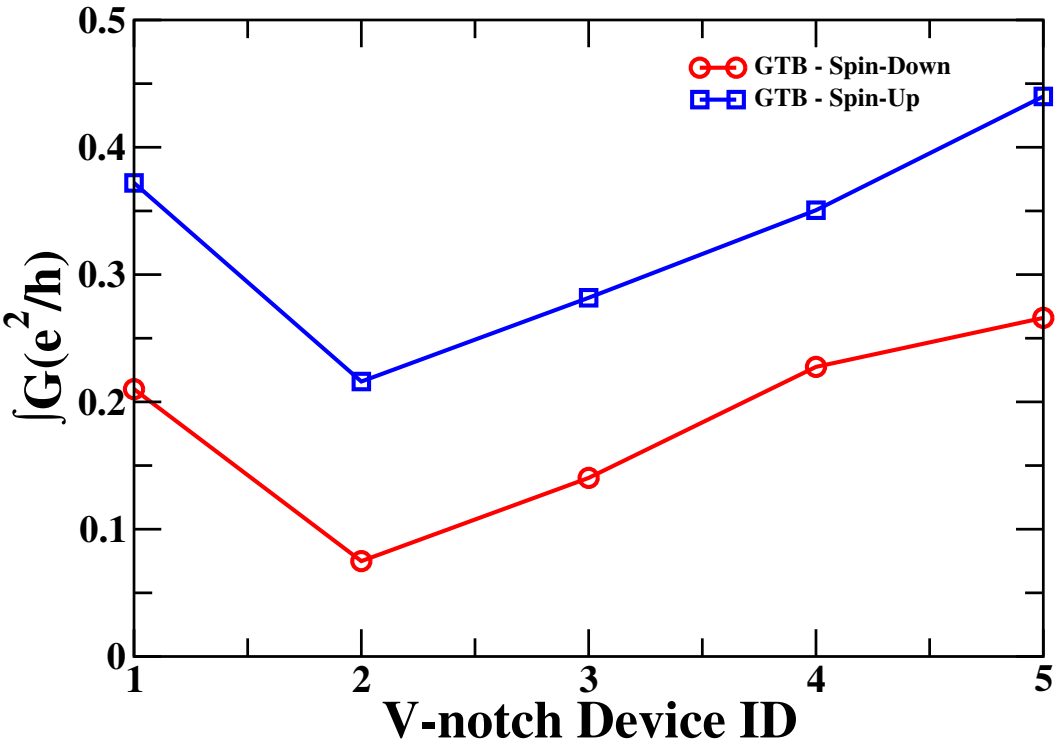


Figure 5.9: Integral of the electronic conductance (Equation 2.98) between -1eV< $E - E_f$ <1eV vs V-notch bottom length for a V-notched 5-ZGNR device using the GTB model (Equation 2.67). Red(blue) gives the V-notched GTB spin-down(-up) result. Devices 1, 2, 3, 4 and 5 corresponds to Figure 5.1(b), and Figures 5.7(a), 5.7(b), 5.7(c) and 5.7(d), respectively.

The integral of the spin-down conductance is smaller than the integral of the spin-up conductance (Figure 5.9) meaning that, overall, the spin-down electrons are more localised for all V-notch bottom lengths investigated. This supports the conclusion that the spin-down electrons are more localised due to the Hubbard-$U$ term and Clar's theory [173, 174]. As the length of the bottom of the V-notch increases, the system starts to approach that of a smaller ribbon between two larger ribbons connected via sloping edges.

The increasing integral of the conductance between -1eV< $E - E_f$ <1eV about the Fermi level suggests that the conductance channels are becoming less localised (Figure 5.9), with both the integral of the conductance increasing and the electronic conductance gaps decreasing. When compared to the general trends for the direct band gap vs ribbon width, for example in Hancock *et al.* [33] and Son *et al.* [32] [2], which shows a decrease in the band

[2]Note, band gap and electronic conductance gap can be compared in zero bias

gap for ideal ZGNR devices at very small widths (Figures 1.8(b) and 1.10), it can be argued, for the ribbon width investigated here, that as the length of the V-notch bottom increases the system will start to approximate the electronic conductance gap of a small 2-ZGNR device attached to two large 5-ZGNR leads. Due to the limitations of this investigation, this effect can not be probed in detail, but it is a potential avenue for future work.

## 5.3 Effects of Uniaxial Strain in ZGNRs on the Spin-dependent, Coherent Transport

To investigate the effects of uniaxial strain, three ZGNR devices were modelled; 2-6-ZGNR (Figure 5.10(a)), 2-7-ZGNR (Figure 5.10(b)) and 2-8-ZGNR (Figure 5.10(c)) with unstrained widths 11.1Å, 12.9Å and 14.7Å respectively and unstrained length of 4.92Å. These widths were chosen to give a range of values to to test the sensitivity of ribbon width as a function of uniaxial strain. Uniaxial strain is applied in the y(x)- direction (perpendicular(along)) the ribbon length and with values from -50% to 50%. Negative values of uniaxial strain in the y-direction is equivalent to positive strain in the x-direction due to the Poisson effect [123] (Equation 2.106). ±50% was chosen to investigate strain exceeding the physical extremes of uniaxial strain.

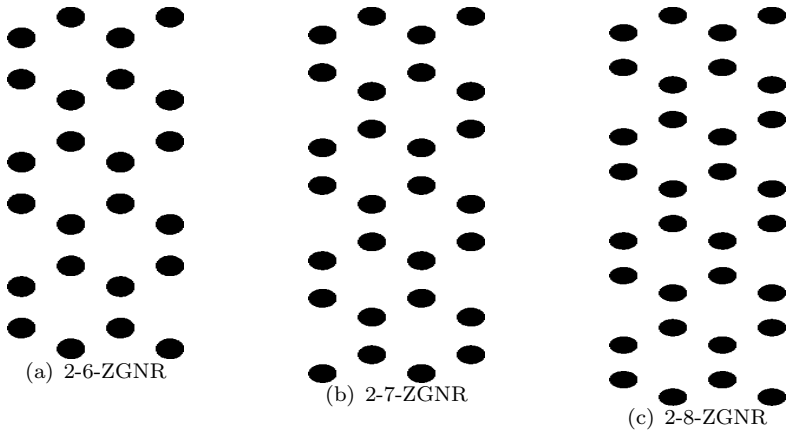

(a) 2-6-ZGNR (b) 2-7-ZGNR (c) 2-8-ZGNR

Figure 5.10: Schematic of the system used for transport (Equation 2.98) calculations of (a) 2-6-ZGNR device, (b) 2-7-ZGNR device, (c) 2-8-ZGNR device. In real-space, 6-ZGNR, 7-ZGNR and 8-ZGNR describes a device of unstrained widths 11.1Å, 12.9Å and 14.7Å respectively, and the entire unperturbed device length is 4.92Å for all ZGNR ribbons.

Figure 5.11(a) demonstrates the effects of uniaxial strain on the coherent conductance gap relative to the unstrained, ideal, device (0% uniaxial strain). As uniaxial strain in the y-direction decreases from 0% to -50%, the conductance gap increases by 1.1eV, 1.12eV and 1.14eV for 6-ZGNR (11.088Å), 7-ZGNR (12.936Å) and 8-ZGNR (14.784Å) respectively. As the strain approaches -50%, the coherent conductance gaps converge to $1.41e^2/h$ for all three ribbon widths. As uniaxial strain in the y-direction increase from 0% to 50%, the coherent conductance gap decreases for all ribbon widths investigated. These conductance gaps are

within error of each other and thus, as the conductance gaps do not converge to a single value at 50% for all three widths, the gaps decrease by the same relative amount. The difference in conductance gap between the three widths does decrease with increasing strain (0.036eV at 0% uniaxial strain in the y-direction compared to 0.02eV at 50% uniaxial strain in the y-direction) suggesting that the three widths will converge at a % uniaxial strain in the y-direction at a large, and thus extremely unrealistic, amount of uniaxial stain.

For strain in the x-direction (Figure 5.11(a), a trend which is inverse to the y-direction trend is observed between -20% and 20% uniaxial strain. For uniaxial strain greater than $|\pm 20\%|$ the inverse agreement breaks down. This can be seen more clearly in Figure 5.11(b) where the x-axis for the y-direction uniaxial strain graph has been reversed. This shows clearly a good inverse agreement between uniaxial strain in the x-direction and uniaxial strain in the y-direction between -20% and 20%. This inverse agreement is expected as compression in the x-direction (negative uniaxial strain) is equivalent to expansion in the y-direction (positive uniaxial strain) due to the Poisson ratio [123] (Equation 2.106). For strain in both directions, there is a slight linear dependence of electronic conductance on uniaxial strain within $|\pm 10\%|$, with a the linear dependence curving as it approaches $|\pm 10\%|$. Figure 5.11(b) is limited to $-20\% < strain < 20\%$ due to the break down in agreement in between uniaxial strain in the x-direction and y-direction. In addition, 10-ZGNR, 12-ZGNR, 14-ZGNR and 16-ZGNR have been included for completeness and to compare with DFT results later in the Section.

The change in electronic conductance gap with varying uniaxial strain is due to the variation in distances between atoms and thus perturbations in the hopping parameters (Equation 2.103). As the system is strained in the y-direction, the atoms are compressed in the x-direction (and thus the conductance direction) due to the Poisson ratio (Equation 2.106). This compression in the conductance direction will increase the number of energetically favorable conductance channels and thus decrease the conductance gap. Similarly, if the system is compressed in the perpendicular y-direction, the atomic sites will move further apart in the conductance direction lowering the number of energetically favorable channels and thus increasing the conductance gap.

The linear dependence of the electronic conductance gap (which is equivalent to the energy band gap at zero bias) on unixaial strain has been demonstrated by Li *et al.* [115] for12-ZGNR using DFT with GGA via VASP [70] for small uniaxial strain in the x-direction (less than 10%). The slightly curving linear dependence was also shown for 6-ZGNR by Zhang *et al.* [125] with DFT, GGA and HSE06 via VASP [70] between $|\pm 10\%|$ in the y-direction. Lu and Guo [126] used the interacting tight-binding model to calculate energy band gaps for 5-, 10-, 16- and 32-ZGNR and found a slightly curved linear dependence between $|\pm 15\%|$ in the x-direction (Figure 5.12(a)). Lu and Guo [126] parametrised the model using the hopping and Hubbard-$U$ values found by Gunlycke and White [127], thus leading to a slight difference

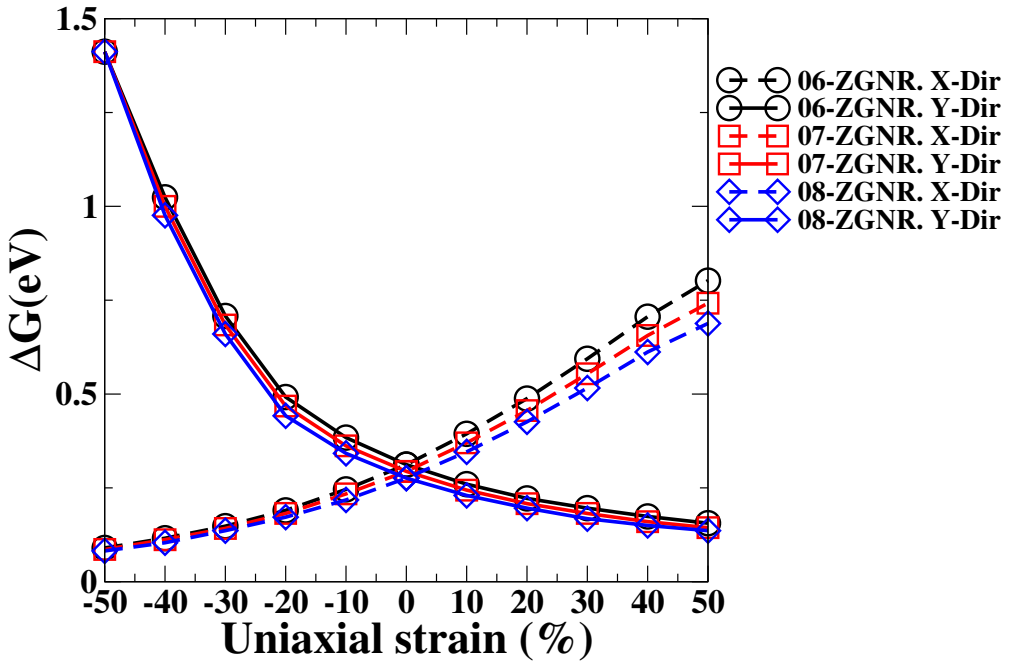


(a)

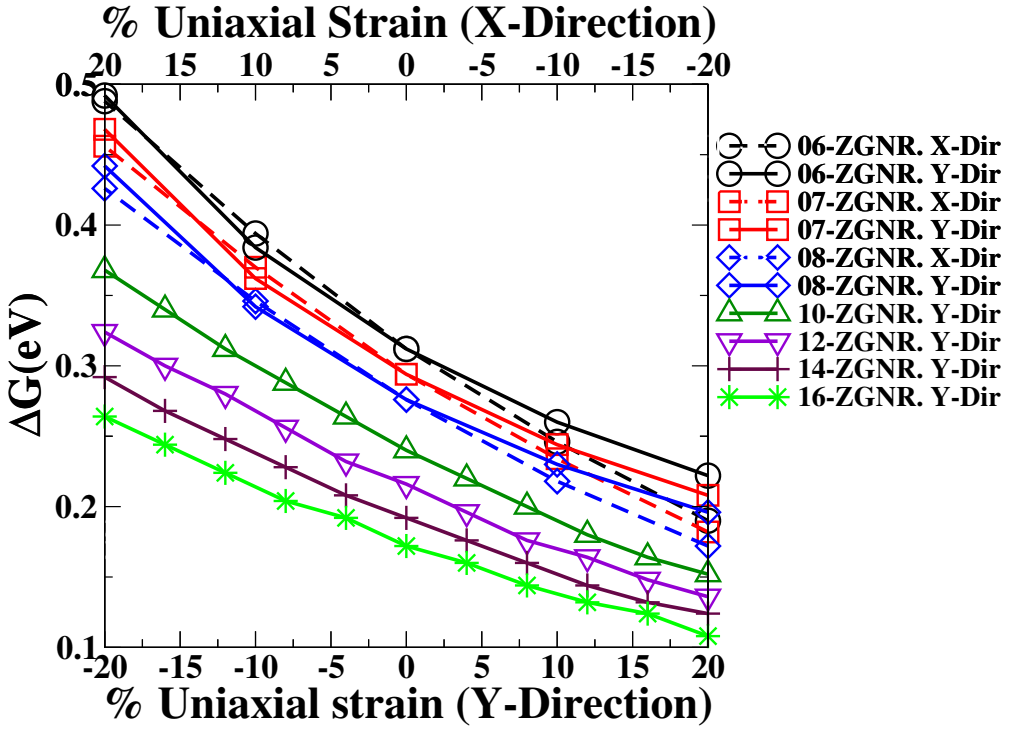


(b)

Figure 5.11: Electronic conductance gap (Equation 2.98) vs uniaxial strain (Equation 2.103) calculated using the GTB model (Equation 2.67). Solid(dashed) lines gives uniaxial strain perpendicular(parallel) to the ribbon width (y(x)-direction) for three different ribbons widths, 6-ZGNR (black circle), 7-ZGNR (red square) and 8-ZGNR (blue diamond). The entire unperturbed device length is 4.92Å for all ribbons. In (b), the x-axis for uniaxial strain in the y-direction has been reveresed to compare the inverse relationship between uniaxial strain in the x- and y-directions.

between the conductance gaps found here and the energy gaps found by Lu and Guo [126]. Lu and Guo [126] used Harrison scaling and a Poisson ratio of 0.165. It must be noted that energy gaps and transport gaps are equivalent under zero voltage bias.

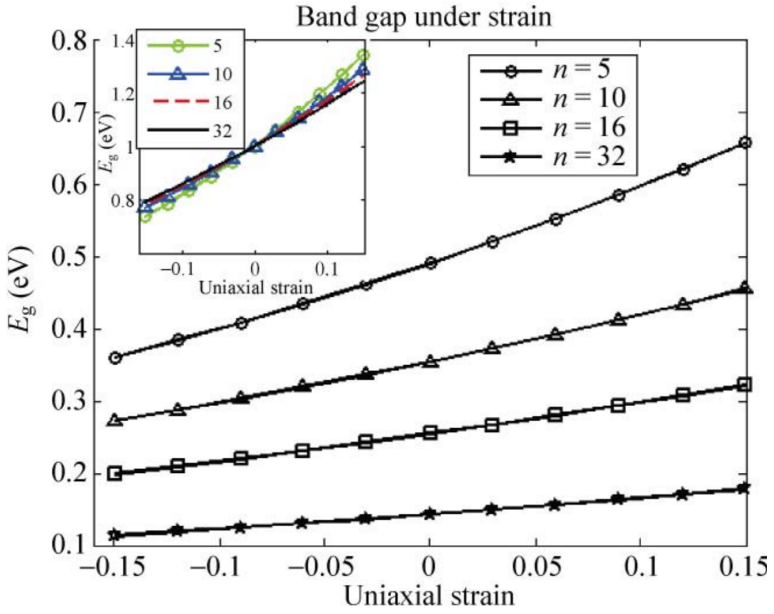


(a)

Figure 5.12: Energy gaps calculated by Lu and Guo [126] via the interacting tight-binding model, using Gunlycke and White [127] parameters for a 5-, 10- 16- and 32-ZGNR device. Insert demonstrates the normalised energy band gap. Note, in zero voltage bias, energy and electronic conductance gaps are equivalent.

Poetschke *et al.* uses the STB model to model a 10-ZGNR device under strain but finds no metallic/semiconductive transition in the ZGNR device. When compared to the DFT results of Li *et al.* [115], Zhang *et al.* [125] and Su *et al.* [128] it is clear to see that the STB model is insufficient to accurately model the effects of strain on a ZGNR system. The lack of an interacting term is sufficient enough that is possible to disregard the STB model for these studies.

The change in conductance gap implies a change in conductance around the conductance gap. Figure 5.13 demonstrates an increase in the Simpson's rule integral of the conductance (Equation 4.5) with increasing uniaxial strain in the y-direction. The increasing Simpson's rule integral of the conductance is in agreement with the decreasing conductance gap, as a smaller conductance gap implies more conductance around the gap. Again, the increased conductance as the uniaxial strain increases in the y-direction is due to the relative compression in the electronic conductance direction.

This section has demonstrated the spin-dependent transport of notched devices and the predictable control of the conductance using uniaxial strain. The ability to control the spin-dependent transport predictably would be extremely powerful in spintronic devices (i.e. devices that use the intrinsic spin of electrons). Therefore the combination of asymmetrical

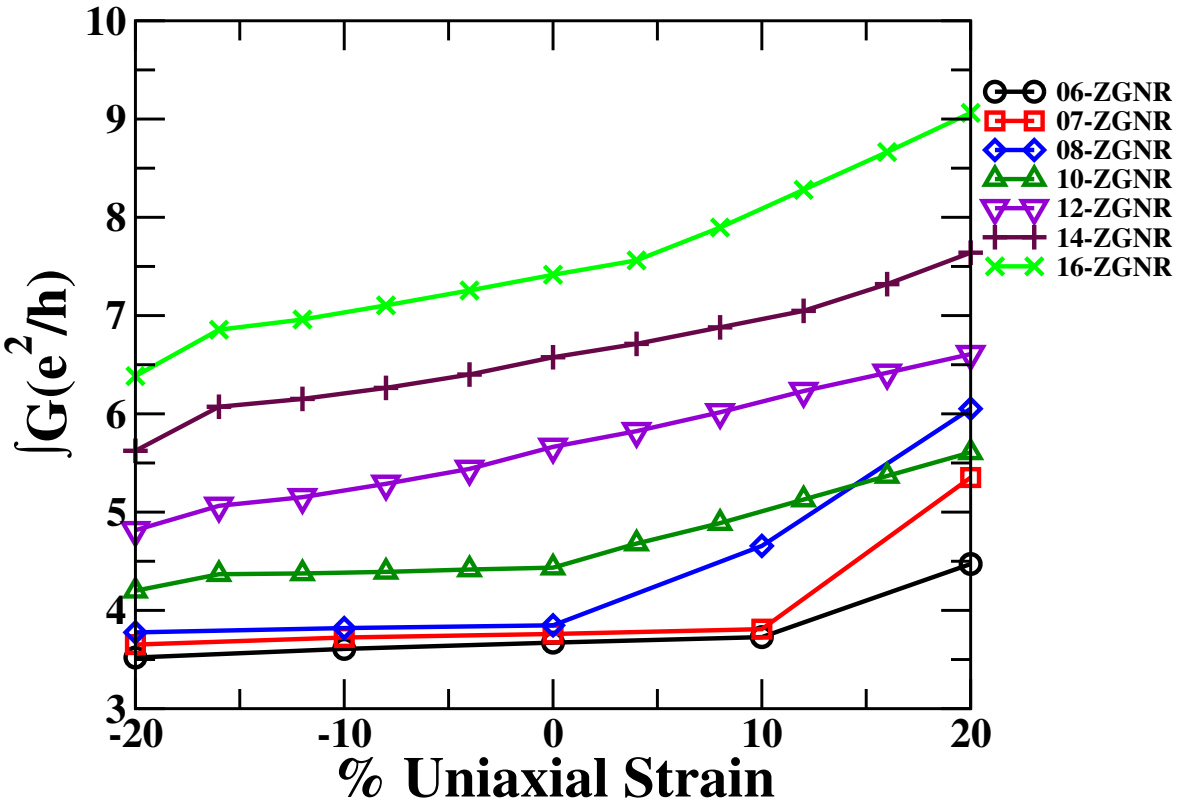


(a)

Figure 5.13: Integral of the electronic conductance (Equation 2.98) between $\pm 1eV$ vs uniaxial strain (Equation 2.103) in the y-direction calculated using the GTB model (Equation 2.67). Uniaxial strain is perpendicular to the ribbon width (y-direction) for 7 different ribbons widths, 6-ZGNR, 7-ZGNR, 8-ZGNR, 10-ZGNR, 12-ZGNR, 14-ZGNR and 16-ZGNR. The entire unperturbed device length is 4.92Å for all ribbons.

notches and uniaxial strain is investigated, focusing on positive strain in the y-direction (due to the decreasing trend in coherent conductance gap and thus the possibility of a spin-dependent semi-conductor in one spin-direction and insulator in the other) and maximum strain of 20% (due to the theoretical critical strain predicted in Su *et al.* [128]).

## 5.4 Effects of Strain on Notched ZGNRs

In this section, V-notched and square notched devices are perturbed using uniaxial strain and the conductance results compared to ideal results. Due to the physical limits in these devices, strain will be limited to 0-20% in the y-direction. This range is used both due to the physical limits of the uniaxial strain in GNRs, along with the fact that the trends in conductance are consistent between -20-20% and thus only 0-20% can be considered.

Similar to Section 5.2, the non-defected region, the black highlighted region in Figure 5.14, must first be added to each end of the device to converge the edge-magnetism of the lead-device boundary. The non-defected region, defined as the region of ideal ribbon between the asymmetrically notched device and the semi-infinite lead, was converged using a device with a square notch (Figure 5.14(a)) and a device with a V-shaped notch (Figure 5.14(b)) with

20% uniaxial strain in the y-direction.

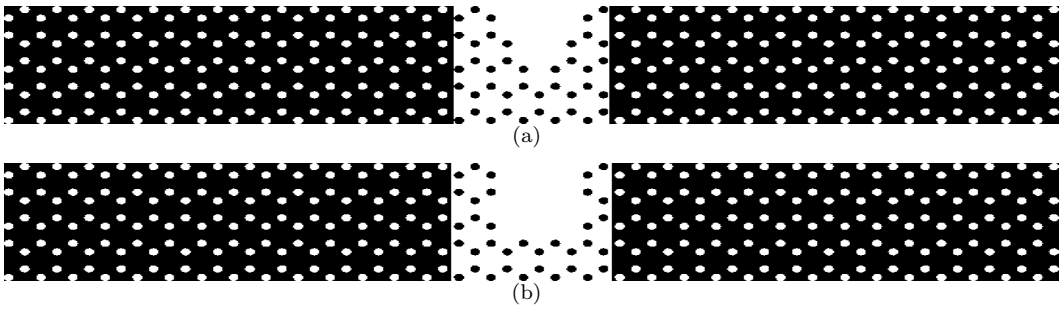


Figure 5.14: Schematic of the systems used for transport calculations of (a) a square notched 5-ZGNR device and (b) a V-notched 5-ZGNR device. The first and last 14 (34.4Å) unit cells (black background, white atomic sites) in the system are kept ideal, and the middle five (12.3Å) unit cells (white background, black atomic sites) defines the notched 5-ZGNR devices. In real-space, 5-ZGNR describes a system of width 9.24Å and the entire device length is 46.7Å.

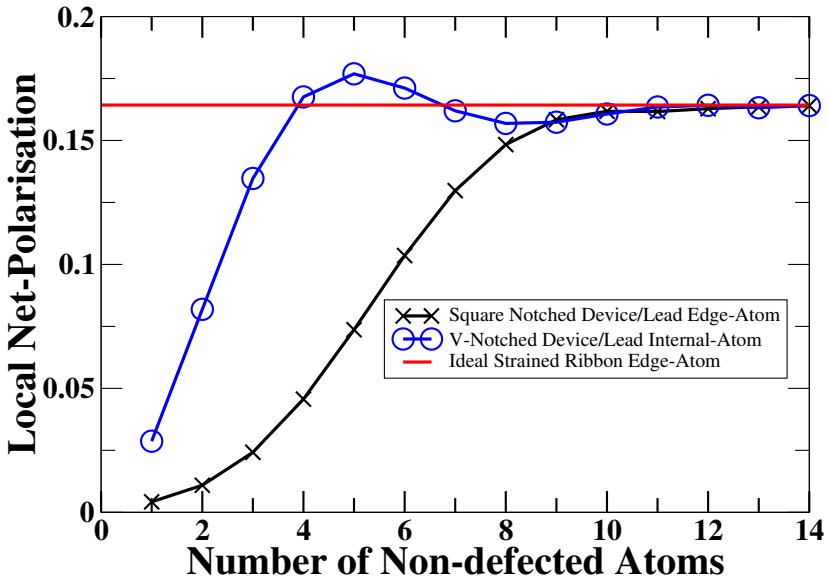


Figure 5.15: Convergence of the local net-polarisation (Equation 2.81) of the device/lead edge atoms for two asymmetrical notches in 5-ZGNR with 20% uniaxial strain in the y-direction calculated using the GTB model (Equation 2.67). The red curve shows the ideal result for a 5-ZGNR that is required for accurate and continuous device-lead coupling for the edge-atom. The black(blue) curve corresponds to the local net-occupancy of the device-lead boundary edge-atom for a square(V-) notched 5-ZGNR device with increasing non-defected region.

Figure 5.15 shows the increase in spin-polarisation of the device-lead boundary edge-atoms as the ideal (i.e., non-defected) region at each end of the uniaxial strained notched devices is increased. As the non-defected region increases in length, the local net spin-polarisation of the edge-atoms at the device-lead boundary approaches that of the ideal system until they converge at a non-defected region of 14 atoms long (34.4Å) with a net local spin-polarisation of $|\pm 0.164|$ for the spin-up(+ve) and spin-down (-ve) edges for both notch types investigated (V-notched, Figure 5.14(a) and square, Figure 5.14(b)). It must be noted that the uniaxial strained notched systems are not relaxed after uniaxial strain is introduced.

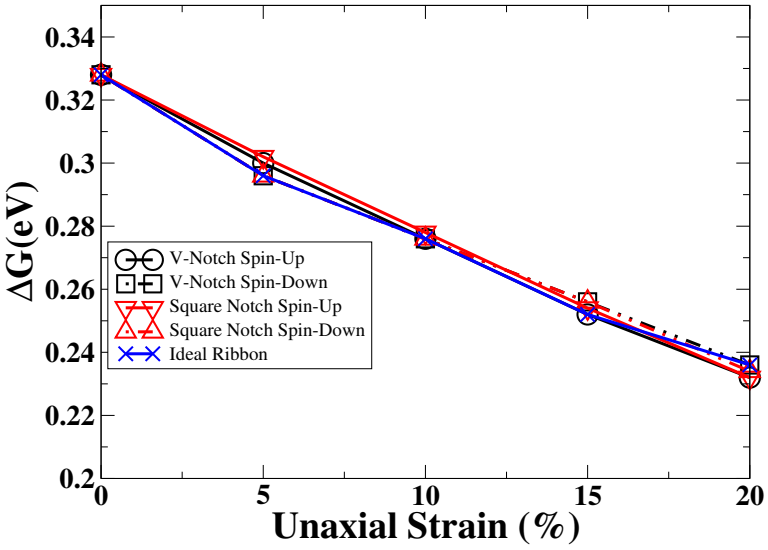


Figure 5.16: Electronic conductance gap (Equation 2.98) vs uniaxial strain (Equation 2.103) calculated using the GTB model (Equation 2.67) for two different notch types, V-notched 5-ZGNR device (black) and square notched 5-ZGNR device (red). Spin-up(-down) is full(dashed) line with circle(square) and full(dashed) line with triangle down(up) for V-notch and square notch respectively. The result for an ideal 5-ZGNR ribbon is in blue with crosses. In real-space, 5-ZGNR describes a system of width 9.24Å and the entire device length is 46.7Å.

Figure 5.16 presents the same trend in the decrease of the spin-dependent coherent conductance gap for the ideal 5-ZGNR, V-notched 5-ZGNR and square notched 5-ZGNR devices within error. For example, the spin-up coherent conductance gap for the V-notched system decreases from 0.328eV for 0% uniaxial strain to 0.232eV for 20% uniaxial strain and the spin-down coherent conductance gap decreases from 0.328eV for 0% uniaxial strain to 0.236eV for 20% uniaxial strain. Again, the two spin-directions follow the same trend for all three systems within error. N.B. error in energy ($\pm$0.008eV) is due to the resolution of the energy step and is constant throughout this study.

The fact that there is an agreement within error between the notched and ideal trend with varying strain means that the only effect influencing the conductance gap is the uniaxial strain. This suggests that asymmetrical notches will not introduce spin-dependent coherent transport gaps without additional inhomogeneity. Figure 5.17 gives examples of the decrease in local net spin-polarisation as the uniaxial strain in the y-direction increases from 0% to 20% for a V-notched 5-ZGNR (Figures 5.17(a) and 5.17(b), respectively) and a square notched 5-ZGNR (Figures 5.17(c) and 5.17(d), respectively). For both notched 5-ZGNRs, there is a decrease in the overall net spin-polarisation from 0% to 20% uniaxial strain in the y-direction. The range over which the notch has an effect on the spin-polarisation around the notch is also increased with the introduction of strain (as demonstrated by the lead/device convergence length, Figure 5.15). The sensitivity of spin-polarisation to strain suggests that magnetic inhomogeneities may also effect the coherent transport properties of the device. These mag-

netic inhomogeneities can be introduced by perturbing the site dependent Hubbard-$U$, using a similar method to perturbing the onsite energy to introduce impurities as discussed in Chapter 6.

## 5.5 Conclusion

This Chapter has demonstrated that structural inhomogeneities can break the spin-independence of the coherent conductance of GNRs. In particular, it is possible to increase both the degree of spin-dependence and create a spin-dependent conductance gap by increasing the length of the bottom of the notch. Unixaxial strain is also shown to controllably and predictably perturb the conductance gap in both ideal and notched devices. In terms of introducing notches to the strained device, the only real effect of notches is to remove conduction channels and reduce the overall conductance by up to 98% close to the Fermi level. Due to the degree of spin-dependence in both the overall conductance and the conductance gap, being dependent on notch bottom length, a length that would be hard to control in top-down synthesis, notches should not be relied on for spintronic devices and inhomogeneous magnetic impurities are a better option.

Next Chapter will probe three different methods of perturbing the conductance via structure, both using bottom-down and top-up synthesis methods.

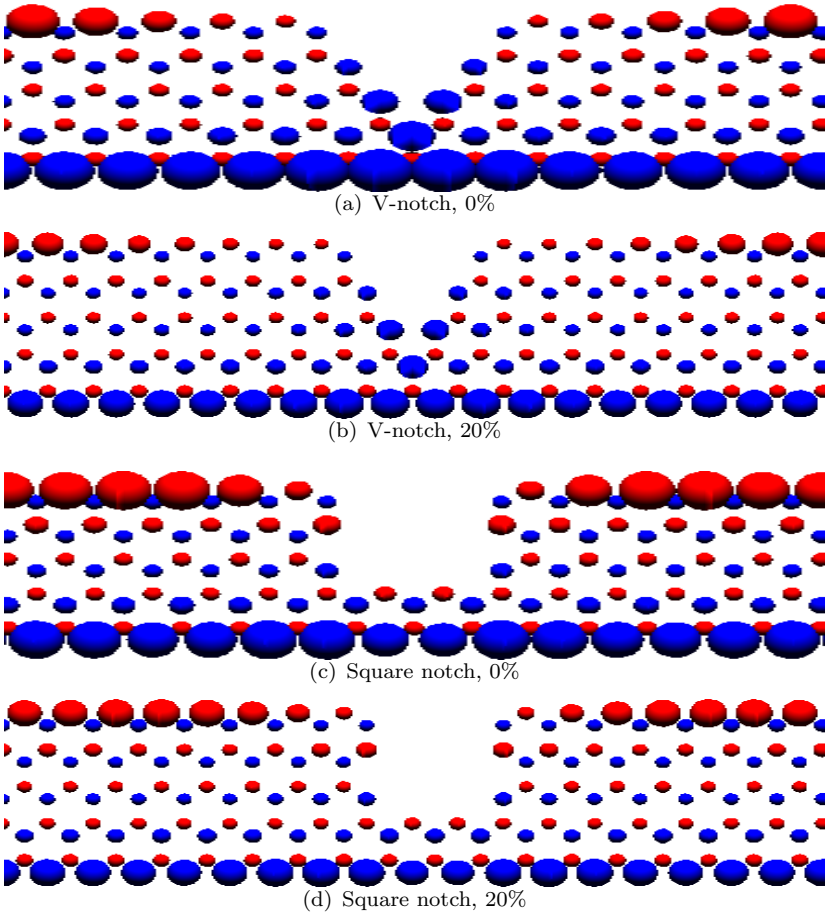

(a) V-notch, 0%

(b) V-notch, 20%

(c) Square notch, 0%

(d) Square notch, 20%

Figure 5.17: Spin-distribution of notched 5-ZGNR devices calculated using the GTB model (Equation 2.67) under uniaxial strain (Equation 2.103). (a) V-notched 5-ZGNR device with 0% uniaxial strain (b) V-notched 5-ZGNR device with 20% uniaxial strain (c) square notched 5-ZGNR device with 0% uniaxial strain (b) square notched 5-ZGNR device with 20% uniaxial strain. Net spin-up circles are blue, net spin-down circles red. The radius of each circle gives the relative magnitude of the net local-spin, Equation 2.81. In real-space, 5-ZGNR describes a system of width 9.24Å and the entire device length is 46.7Å. Image length has been cropped for clarity.

# Chapter 6

# Feasibility Studies into Structural Perturbations

## 6.1 Abstract

Three methods of perturbing the structure of a graphene nanoribbon device were probed in order to investigate the potential of these structures as electronic devices.

Asymmetrical magnetic inhomogeneities were first introduced, with one edge containing a magnetic inhomogeneity though perturbations to the Hubbard-$U$ along the edge of the device. Using this method of perturbation, it was possible to demonstrate a significant spin-dependence in the conductance gap of these devices, with the device transitioning from semi-conductive to half-metallic to metallic with increasing strain, width and edge-perturbation strength.

In addition, the structure produced via two bottom-up synthesis methods was probed. These feasibility studies demonstrate that controllable properties can be predicted, i.e., the spin-localisation, overall spin-dependent conductance and spin-independent conductance gap.

Chevron devices demonstrate a dependence on spin-dependent and spin-independent conductance with chevron length. In addition, it is possible to control the spin-dependent conductance gap with varying lead width.

Patterned devices demonstrate a strong dependence of the conductance gap with length-/width ratio. Compared to the ideal device dependence on just width, a dependence on just length/width ratio allows devices to be constructed without need for angstroms precise dimensions.

## 6.2 Effects of Asymmetrical Inhomogeneities and Uniaxial strain in ZGNRs on the Spin-dependent, Coherent Transport

### 6.2.1 Introduction and Background

Magnetic inhomogeneities can be introduced into the GTB model by perturbing site-specific Hubbard-$U$ values in ZGNR devices relative to the value for carbon atoms, which is set at 2.0eV [82]. This section investigates asymmetrical magnetic inhomogeneities by perturbing the Hubbard-$U$ of an ideal ZGNR ribbon and with the introduction of uniaxial strain (Equation 2.103) to this system. Widths of 3-ZGNR (5.54Å), 7-ZGNR (12.9Å) and 9-ZGNR (16.63Å) were probed to determine the effects of ribbon width on the spin-dependent properties and to investigate a range of devices from large to small edge-atom to internal-atom ratio. In particular, transitions from metallic to half-metallic and from half-metallic to semiconductive states were studied and the spin-polarisation associated with these transitions was also investigated.

Magnetic inhomogeneity has been studied in bulk graphene that has magnetic impurities by Hu *et al.* [85] using quantum Monte Carlo methods within the STB model. Hu *et al.* [85] found that the magnetic moment of the impurity atom could be controlled through an applied chemical potential via an electric field. Yang et. al. [86] introduced perturbations to the Hubbard-$U$ value in bulk graphene via a proximity effect to a metallic substrate and calculated an opening of the band-gap of 98meV and 134meV for spin-down and -up respectively. Pedersen and Pedersen [87] introduced B and N doping into a self-consistent TB model for bulk graphene and determined that an on-site Hubbard-$U$ can be used to describe these impurities, with $U$ equal to 7.8eV, 9.7eV and 11.5eV for B, C, and N respectively (N.B. The Pedersen and Pedersen [87] Hubbard-$U$ value for C is different from the one used in this study as the Hubbard-$U$ is fitted directly to the system investigated). This supports the approximation used in this study that magnetic inhomogeneities can be added to ZGNRs via perturbations to the local atomic Hubbard-$U$ values.

In nanographene, Power *et. al.* [88] explored magnetic inhomogeneities using a first nearest neighbour Hubbard model and DFT, GGA calculations within the SIESTA program to investigate the introduction of single magnetic impurity into ZGNR and AGNR systems. In this work, a good agreement of the segregation function between DFT for a Mn impurity and the first nearest neighbour Hubbard model for a defected 6-ZGNR was made. In addition, Power *et. al.* [88] showed that it is energetically favorable for magnetic impurities to be absorbed along the edge of the GNR system, not the middle. Power *et. al.* [88] assumed that the only non-zero value of $U$ in the device is for the transition metal impurity. This assumption would, however, lead to zero magnetic properties when applied to a ZGNR system without impurities.

Krychowski *et. al.* [89] carried out DFT, GGA calculations within the VASP program for a single Co adatom in 4-ZGNR. The Co adatom in this investigation is placed on a "hollow site", i.e., in the middle of a hexagonal ring of carbon. Mao *et. al.* [90] introduced K adatoms at various concentrations using GGA-PBE DFT calculations within the VASP program to 8-ZGNR and found that, at 1.56% adatom concentration, the device becomes FM instead of AFM. Zhang *et. al.* [91] introduces regular Fe adatoms to the "hollow site" both at the edge and in the middle of a 4-ZGNR device. GGA-PBE DFT calculations are carried out using the atomistix toolkit (ATK). For regular Fe atoms along the edge "hollow sites", there is a decrease in the magnetic moment near to the Fe adatom, and the introduction of a spin-dependent transport gap.

Aryasetiawan *et. al.* [185] used random phase approximation and LDA DFT first principles calculations to determine the Hubbard-$U$ values of 3d metals, including Fe and Co. Aryasetiawan *et. al.* found Hubbard-$U$ values of 4.0eV and 4.1eV for Fe and Co respectively. In addition, Aryasetiawan *et. al.* demonstrated that all 3d transition metals have Hubbard-$U$ values greater than 2.0eV (i.e., the Hubbard-$U$ value of nanographene). This result was also found by Nakamura *et. al.*[186], Gunnersson [187] and, Soloveyev and Dederichs [188] using DFT LSDA methods. Soloveyev and Dederichs [188] also determined screened Hubbard-$U$ values from 2.4eV for Ta to 4.4eV for Pd for 5d and 4d impurities. Fukushima *et. al.* [189] calculated the Hubbard-$U$ value for a Mn impurity within GaN of between 3.30 and 3.77eV using LDA+U DFT methods. It must be noted these are calculated for the LDA+U first principle approximation and thus may not be applicable to the GTB model. Cox *et. al.* [190] determined the Hubbard-$U$ values for the TB model via the fitting of the d electron eigenvalues giving values between 1.35eV for scandium to 3.3 for nickel, with Fe falling within this range. The values calculated by Cox *et. al.* are smaller than the values calculated via the LDA-U approach (3.0eV compared to 4.0eV for Fe) which may be due to the fact Cox *et. al.* assumed 100% screening between neighboring sites. Anisimov and Gunnarsson [191] investigated the screening in Fe and found only $\tilde{5}0\%$ screening between neighboring Fe sites and thus calculated a value of $U$ of 6.0eV. Anisimov and Gunnarsson [191] determined that, in general, the screening was very efficient.

### 6.2.2 Results and Discussion

Asymmetrical magnetic inhomogeneities have been introduced by perturbing the on-site Hubbard-$U$ value at the edge ($U_{edge}$) in small-width ZGNRs (N.B. small-widths are chosen due to computational expense). For a 7-ZGNR there are interesting trends in the conductance gap with increasing $U_{edge}$ value (Figure 6.1). Below $U_{edge}$=0.8 eV, the transport-gap is spin-independent, between 0.8eV $< U_{edge} <$ 1.4eV the system is half metallic or metallic, and between 1.4eV $< U_{edge} <$ 3.7eV there is a linear decrease in the spin-up transport gap

and a non-linear increase in the spin-down transport gap. Above $U_{edge}$=3.7eV the transport gap becomes spin-independent again. For 2.0eV< $U_{edge}$ < 3.7eV there is a qualitatively similar, but opposite, trend in results compared to the 1.4eV< $U_{edge}$ < 2.0eV range, which implies that magnetic inhomogeneities that increase the $U_{edge}$ value would be more useful for allowing control over the conductance gap. The trends for $U_{edge}$ greater than 2.0eV observed in Figure 6.1 are consistent with published literature, with Zhang *et. al.* [91] and Krychowski *et. al.* [89] finding spin-dependent electronic transport gaps with the introduction of Fe (Hubbard-$U$ = 4.0eV [185]) and Co (Hubbard-$U$ value of 4.1eV [185]) respectively.

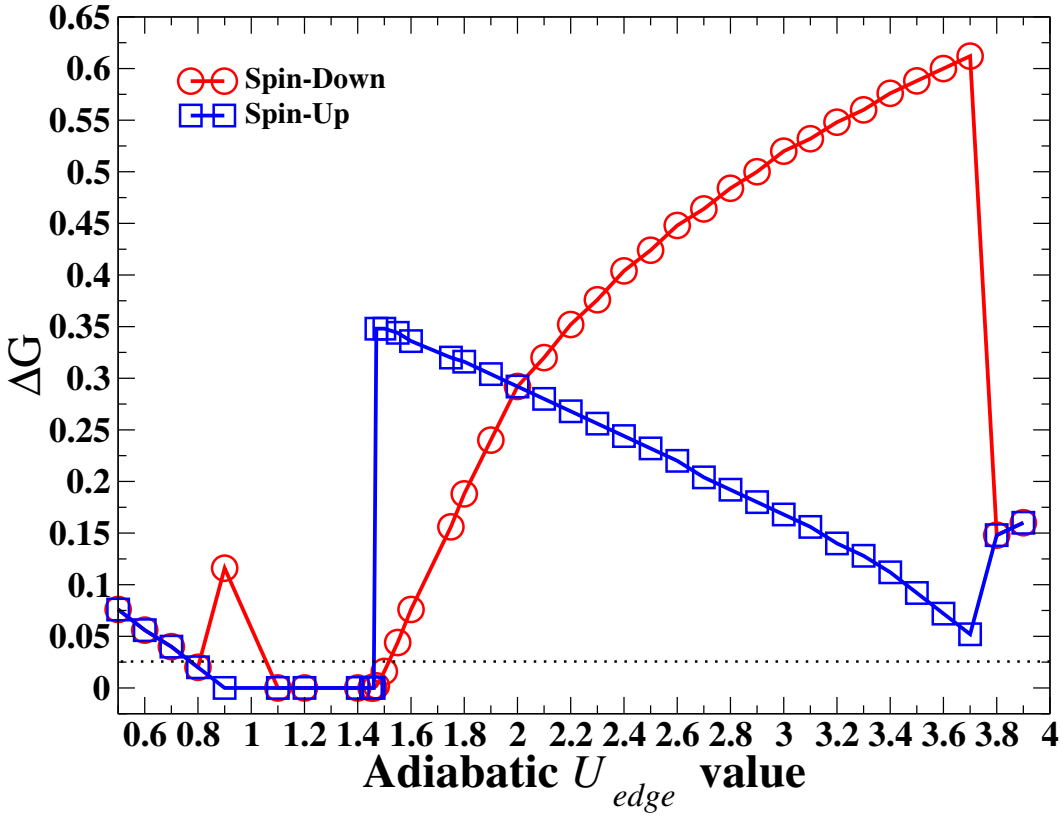


Figure 6.1: Spin-dependent conductance gap (Equation 2.98) vs. $U_{edge}$ value calculated using the GTB model (Equation 2.67) for a 7-ZGNR device with magnetic-edge inhomogeneity. Spin-up(-down) is blue(red) line with circle(square). The dotted line is $k_BT$=0.026 eV.

A 7-ZGNR device with an inhomogeneous $U_{edge}$ of 1.47eV (Figure 6.2(a)) is first probed due to the transition from a spin-dependent transport gap to a spin-independent metallic state observed at this point in Figure 6.1. The spin-up coherent conductance gap for this system at 0% uniaxial strain is 0.002eV, which is less than $K_BT$ (0.026eV), where $K_B$ is the Boltzmann constant and $T$ is room temperature (300K) (Figure 6.2(d)). Thus this system can be assumed to be conducting in the spin-down channel.

The decrease in the spin-down conductance gap of 0.29eV at 0% uniaxial strain is significant relative to the conductance gap of the ideal 7-ZGNR device. The spin-up coherent conductance gap, however, has increased in size by 0.056eV to 0.348eV relative to the ideal 7-ZGNR. With the introduction of a small amount of uniaxial strain in the y-direction (5%),

the inhomogeneous system becomes conducting for both spins (Figure 6.2(d)). In addition, the system transitions from a lowest energy antiferromagnetic state at 0% uniaxial strain (Figure 6.2(b)) to a lowest energy ferromagnetic state at 5% uniaxial strain (Figure 6.2(c)). At 0% uniaxial strain in the y-direction, a decrease in the total local net spin (Equation 2.82) occurs on the edge atoms, from $0.24\mu_b$ for the homogeneous 7-ZGNR device to $0.22\mu_b$ and $0.23\mu_b$ for net spin-down and spin-up respectively.

The decrease in local net spin on the edge atoms is due to an increase in charge-carrier itinerancy, which also introduces non-zero spin-dependent conductance within $K_BT$. The introduction of uniaxial strain in the y-direction to this device closes the conductance gap for both spin-directions due to the decrease in Hubbard-$U$ effects through the separation of the edges and a decrease in the site separation in the conducting direction (Poisson effect). The 7-ZGNR inhomogeneous device demonstrates a transition from a single-spin conductor to a spin-independent conductor allowing the control of the spin-conductance with just the uniaxial strain and thus providing a new method of turning on or off spin-dependent properties.

Unlike Mao *et. al.* [90], who demonstrated using GGA-PBE DFT an AFM to FM transition of the opposite edges with the introduction of 1.56% K impurities, the AFM to FM transition occurs in the 7-ZGNR device with the introduction of both uniaxial strain and impurities. By adding the larger K atom to the device and relaxing the structure as normal in DFT studies, strain will occur from the addition of the adatom, suggesting that the transition occurring in Mao *et. al.* [90] is due to the combined interaction between the strain and K adatoms. The sensitivity of the transition in this study (i.e., between 0% and 5%) supports this conclusion. Compared to Zhang *et. al.* [91], the agreement is very good, with the spin-dependent conductance gap predicted by Zhang *et. al.* for a 4-ZGNR device with the introduction of Fe adatoms [91] observed in this study (Figure 6.2).

Reducing the device-width to a 3-ZGNR (Figure 6.3(a)) requires a smaller $U_{edge}$ of 1.40 eV to overcome the increased quantum confinement. At 0% uniaxial strain, the system is antiferromagnetic with spin-up localised along the inhomogeneous edge, whereas at 5% uniaxial strain in the y-direction, the system is paramagnetic (Figure 6.3(c)). The change to a paramagnetic state corresponds to the formation of the spin-down coherent conductance gap and a decrease in the spin-up conductance gap from 0.21 eV to 0.06 eV (Figure 6.3(d)). As the uniaxial strain in the y-direction increases from 5% to 20%, the spin-independent conduction gap increases from 0.06 eV to 0.08 eV. The conduction gaps at all values of uniaxial strain are smaller than the homogeneous conduction gap suggesting an increase in charge-carrier itinerancy. The large quantum confinement found in uniaxially strained 3-ZGNR also means that, due to the lowest-energy paramagnetic state, that Pauli Exclusion effects are dominating. Compared to the 7-ZGNR devices with $U_{edge}$ perturbation the 3-ZGNR device allows for

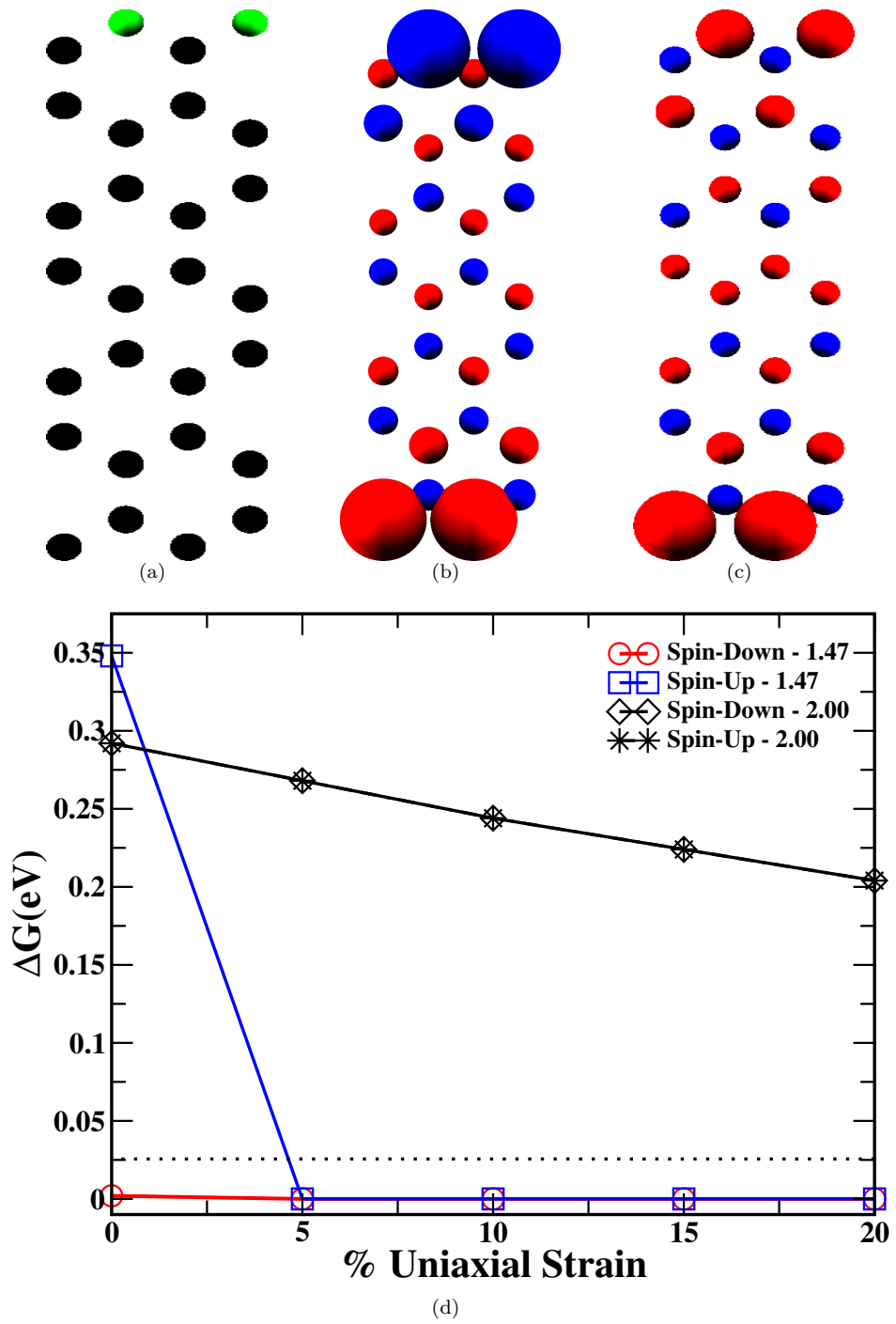


Figure 6.2: The effects of $U_{edge}$ = 1.47eV, on the magnetic properties and spin-dependent coherent transport gap of a 7-ZGNR device under uniaxial strain. (a) Spin-distribution for the device. Net spin-up(-down) circles are blue(red). The radius of each circle gives the relative magnitude of the net local-spin. (b) Spin-distribution for the 7-ZGNR device with 5% uniaxial strain. (c) Dependence of the spin-dependent conductance gap as a function of uniaxial strain. Where red(blue) denotes spin-up(-down) results for the inhomogeneous device, and black denotes the spin-independent results for an ideal 7-ZGNR device. The dotted line is $K_BT$=0.026 eV.

switching from a single-spin conductor to a spin-independent semiconductor state as a function of increasing uniaxial strain. Such tuneability implies that ZGNRs of different widths and $U_{edge}$ perturbations can be used for different types of spin-conductance switching.

The formation of a spin-dependent conductance gap with the initial introduction of edge-adatoms (i.e., $U_{edge}$ perturbations) to the 3-ZGNR device is in agreement with the GGA-PBE DFT calculations of Zhang *et. al.* [91]. Zhang *et. al.* [91] calculated a spin-dependent band gap with the introduction of Fe adatoms. In comparison with this study, Zhang *et. al.* [91] added a single Fe adatom to the device and found a decrease in magnetic moment around the adatom. This conclusion is in agreement with both work carried out by Huang *et al.* and with work presented in Chapter 4 of this thesis. Huang *et al.* added B adatoms to both sides of a 6-ZGNR device and found a paramagnetic state forming at impurity concentration of 33.33%. Huang *et al.* carries out DFT LSDA calculations and, similar to Mao *et. al.* [90],introduces strain though the introduction of the smaller B atoms. Zhang *et. al.* [91] introduces adaoms above the "hollow" sites at the edge of the ribbon and thus strain will not be introduced though their addition.

The 9-ZGNR inhomogeneous device with $U_{edge}$=1.60eV (Figure 6.4(a)) has a lowest energy antiferromagnetic state for uniaxial strain of 0% to 15% applied in the y-direction (Figure 6.4(d)). Due to the increased width, and therefore decreased quantum confinement, a smaller decrease in $U_{edge}$ is required when compared to a 7-ZGNR device (1.60eV compared to 1.47eV) for a semi-metal to metallic state transition. In addition, a larger strain (20%) is needed before the increased charge carrier itinerancy and decreased quantum confinement becomes significant for a ferromagnetic change in the lowest-energy state (Figure 6.4(c)). The inhomogeneous 9-ZGNR device shows a similar type of spin-dependent switching as the 7-ZGNR (Figure 6.2), with the system changing from a spin-dependent semiconductor state at 0% uniaxial strain, to a single-spin conductor at 5% uniaxial strain (Spin-down conductance gap = 0.016eV) and finally to a spin-independent conductor at 20% uniaxial strain.

The inhomogeneous 9-ZGNR study has similarities to both Mao *et. al.* [90] and Zhang *et. al.* [91]. As strain is increased in the device, a spin-dependent conductance gap is formed, with a decrease in spin-localisation along the perturbed edge in agreement with Zhang *et. al.* [91]. Similar to 3-ZGNR, strain is not required to introduce a spin-dependent conductance gap in these devices, but strain does increase the spin-dependence of the conductance gap. As the uniaxial strain increases to 20%, the device becomes FM, in agreement with Mao *et. al.* [90]. Like the 7-ZGNR device, uniaxial strain is required to create the results found by Mao *et. al.* [90]. The increased strain required supports the idea that the 8-ZGNR device with K adatoms requires the strain introduced by the adatoms in addition to the impurity.

The 3D colour plot (Figure 6.5) provides more information into the strain effects. The angled transition between 60% and 80% in the spin-down results with increasing uniaxial

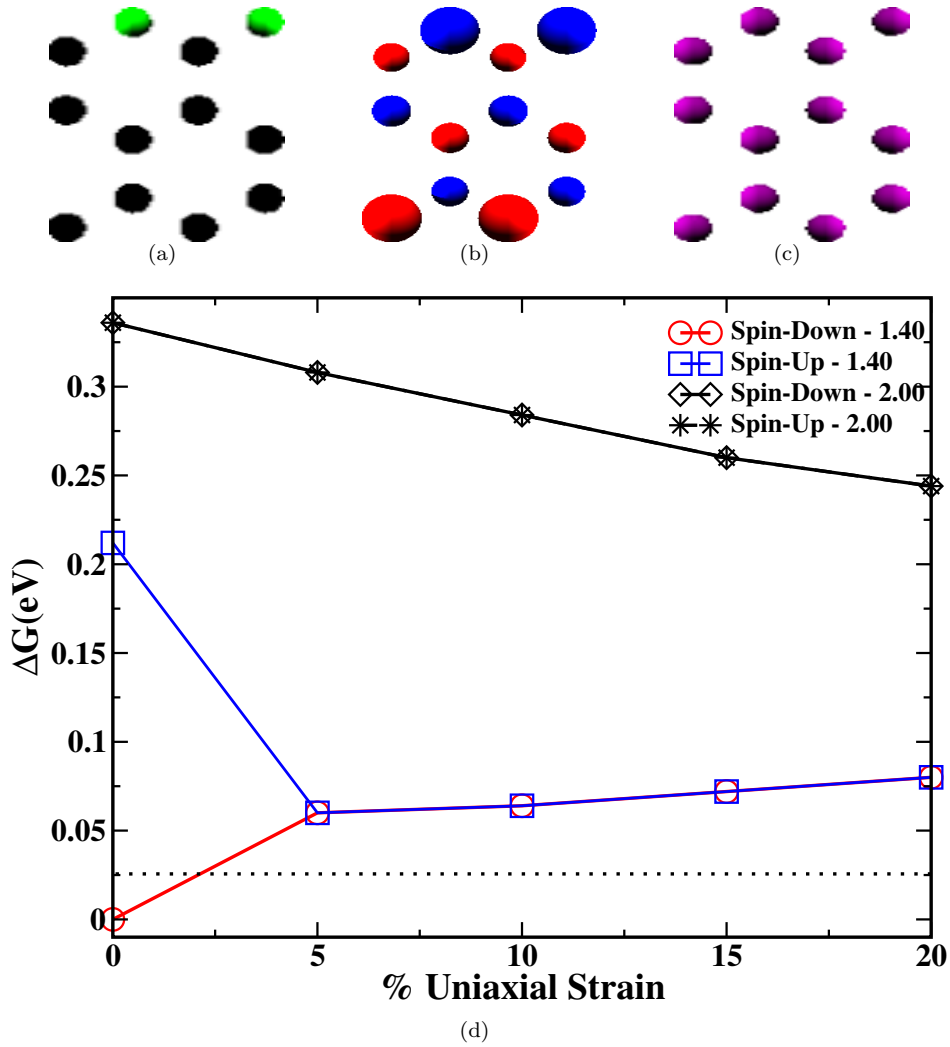


Figure 6.3: The effects of $U_{edge}$ = 1.40eV, on the magnetic properties and spin-dependent coherent transport gap of a 3-ZGNR device under uniaxial strain. (a) Spin-distribution for the device. Net spin-up(-down) circles are blue(red). The radius of each circle gives the relative magnitude of the net local-spin. (b) Spin-distribution for the 3-ZGNR device with 5% uniaxial strain. Purple circles are net paramagnetic (c) Dependence of the spin-dependent conductance gap as a function of uniaxial strain. Where red(blue) denotes spin-up(-down) results for the inhomogeneous device, and black denotes the spin-independent results for an ideal 3-ZGNR device. The dotted line is $K_BT$=0.026 eV.

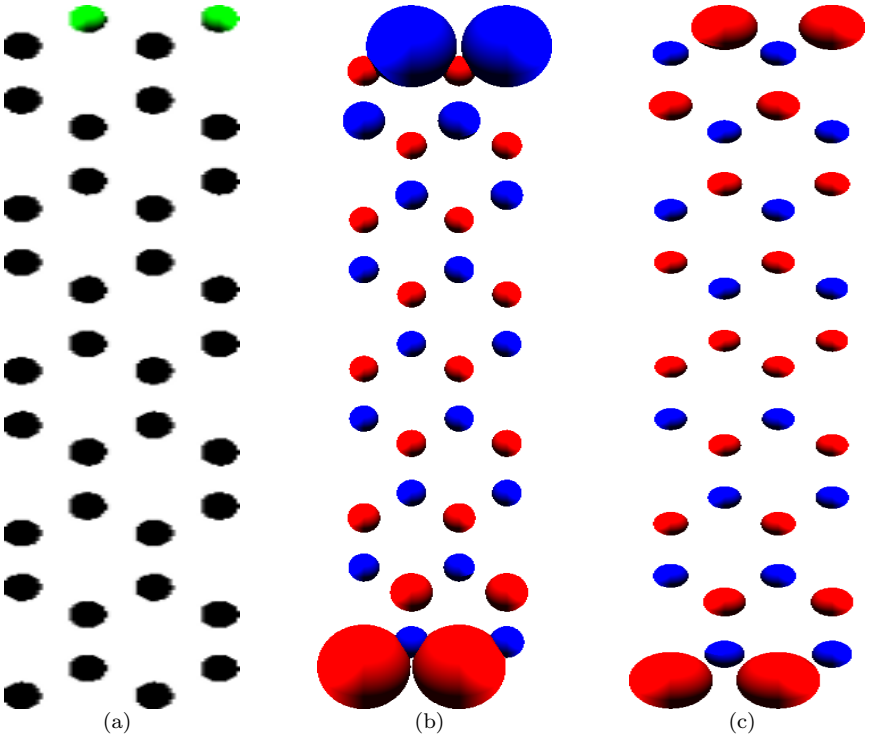

(a) (b) (c)

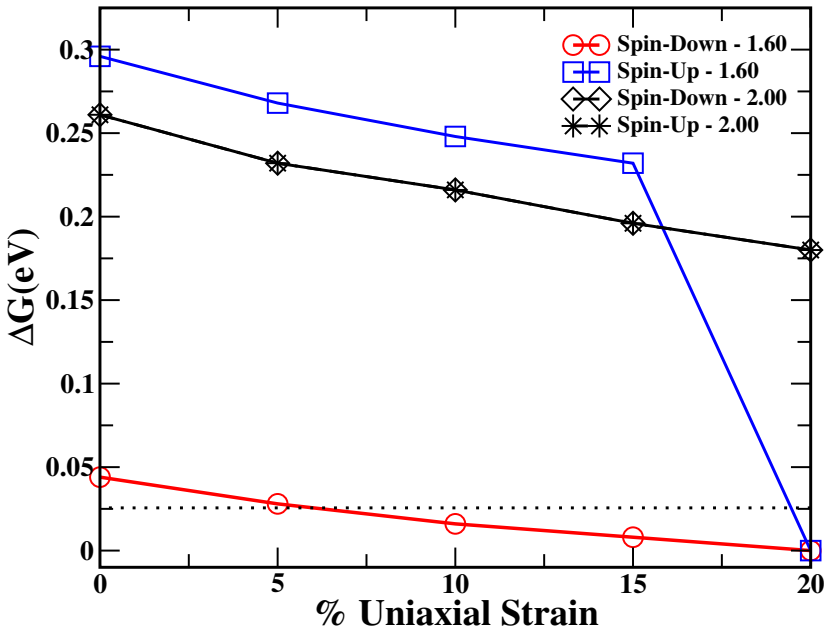


(d)

Figure 6.4: The effects of $U_{edge}$ = 1.60eV, on the magnetic properties and spin-dependent coherent transport gap of a 9-ZGNR device under uniaxial strain. (a) Spin-distribution for the device. Net spin-up(-down) circles are blue(red). The radius of each circle gives the relative magnitude of the net local-spin. (b) Spin-distribution for the 9-ZGNR device with 20% uniaxial strain. (c) Dependence of the spin-dependent conductance gap as a function of uniaxial strain. Where red(blue) denotes spin-up(-down) results for the inhomogeneous device, and black denotes the spin-independent results for an ideal 9-ZGNR device. The dotted line is $K_BT$=0.026 eV.

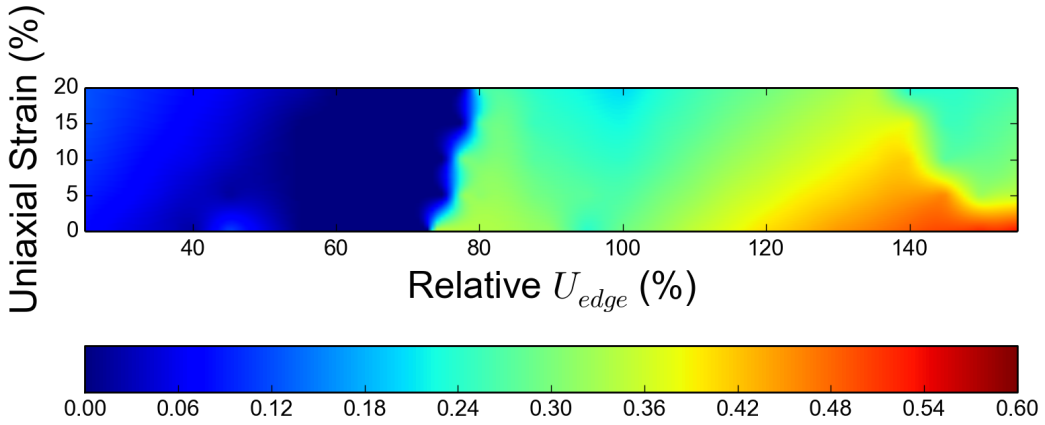


(a)

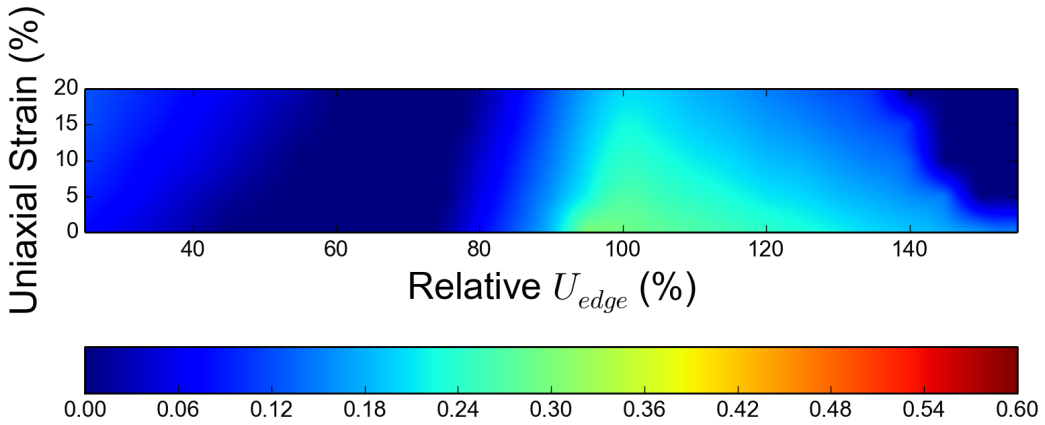


(b)

Figure 6.5: Spin-dependent conductance gap (Equation 2.98) vs. uniaxial strain (Equation 2.103) and $U_{edge}$ (relative to the homogeneous ZGNR value of 2.0eV) calculated using the GTB model (Equation 2.67) for a 7-ZGNR device. (a) Spin-down result, (b) spin-up result. Colour of the graph indicates the size of the spin-dependent conductance gap.

strain demonstrates a strain dependent transition from metallic to half metallic (compared to the spin-down result). The strain-dependent transition occurs due to the slight alteration in the width due to the strain. The fact a metallic/half-metallic transition occurs is of interest as it would allow a strain sensor to be developed, with the conductance turning on at a certain strain.

### 6.2.3 Summary

The effects of magnetic adatoms observed in this section are consistent with DFT calulcations carried out by Mao *et. al.* [90] and Zhang *et. al.* [91]. Figures 6.2(c) and 6.4(c) show a transition from AFM to FM ground state, similar to Mao *et. al.* [90]. It must be noted that for this work, the transition is brought on by the increase in strain, but the strain in this investigation acts as a fine tuning effect that allows one to carefully probe certain effects. In the case of the AFM-FM transition, it can be argued that the addition of K adatoms would cause the strain in the device required for the AFM-FM transition. The transport

properties also demonstrate similar results to those of Zhang *et. al.* [91]. In particular, the spin-dependent transport and transport-gap observed throughout this section, was predicted though DFT calculations by Zhang *et. al.* [91]. Again, Zhang *et. al.* [91] assumes Fe adatoms above the ''hollow sites" along the edge of the ZGNR device, but it seems like there is fair agreement between Zhang *et. al.* [91] and the approximations made in this section.

## 6.3 Chevron Device

### 6.3.1 Introduction and Background

Chevron GNRs (C-GNRs) (Figure 6.6) are grown using chemical self-assembly methods (bottom-up fabrication) from small precursor hydrocarbon molecules to construct atomically clean systems [78, 92]. 6'11-dibromo-1,2,3,4-tetraphenyltriphenylene, for example, is double annealed on a Au(111) substrate to produce chevron AGNR (C-AGNR) with alternating N=6 and N=9 widths [78], where N is defined at the number of dimer lines crossed. C-GNRs have been investigated using both DFT [93, 94, 95] and TB methods [96], with AGNR edged chevrons being the focus of most theoretical studies [92, 94, 78, 96].

The section probes the effects of various shapes of C-ZGNR and uses the GTB model to calculate the spin-dependent properties such as conductance and magnetisation. C-ZGNR devices require a detailed nomenclature to describe the various lengths and widths that are investigated. A and B (Figure 6.6) describes the lead and chevron widths, respectively, which are defined by the number of zig-zag chains. C to G denote the chevron length, chevron depth, length between lead and first chevron peak, length between neighboring chevron peaks, and length of chevron peak respectively and is the number of ideal ZGNR unit cells that required for these lengths. Following this convention, the device in Figure 6.6 is described as a 8/4/16/6/4/8/2 C-ZGNR.

Wang and Wang [94] used DFT, LDA methods to investigate optical properties of C-AGNR, and found that there as an overall increase in the band gap of the chevron GNR compared to the ideal GNR. Fa and Zhou [93] investigated oxygen terminated ZGNR chevron devices (C-ZGNR) using DFT, GGA with spin-polarisation and demonstrated a transition from AFM to FM spin-localisation. Unfortunately, this paper does not draw any conclusions for ideal chevron ZGNR. Finally, Cuong *et. al.* [95] investigated 120 degree angled C-ZGNR devices using DFT LDA methods but ignored the spin degrees of freedom and determined that the formation energies of these C-ZGNR devices was less than that of straight ZGNR devices. This supports the idea that C-ZGNR devices would occur during the bottom-up synthesis of ZGNR devices and that it would be more energetically favorable than ideal, straight ZGNR devices. Cuong *et. al.* [95] also determined that a band-gap opening would occur but, as spin-degrees of freedom are ignored, conclusions can not be drawn until compared to spin-polarised

calculations.

In terms of TB calculations, Chen *et. al.* [96] focuses on thermal properties of CAGNR devices but they do determine a decrease in conductance compared to ideal AGNR devices due to the reduction in conductance channels. Girao *et. al.* [97] has investigated both AGNR and mixed edge ZGNR using the Hubbard-$U$ model in term of band gaps and magnetic structure. The main conclusion drawn in this study is that different spin-properties demonstrate different conductance results, with various AFM and FM magnetic orders probed: (i) In the AFM case, a large spin-independent conductance gap, (ii) for the FM case, spin-dependent conductance and (iii) in the PM case, metallic conductance. Girao *et al.* [97] probes two C-ZGNR devices, a $(5_Z, 8_Z)$ Zig-zag/Zig-zag graphene-nanowiggle and a $(5_Z, 13_A)$ Zig-zag/Armchair graphene-nanowiggle and one CAGNR devices, a $(11_A, 6_Z)$ Armchair/Zig-zag graphene-nanowiggle. This study puts forward possible structural perturbations for Zig-zag/Zig-zag C-ZGNRs and defines various dimensions that can be varied. In addition, Girao *et. al.* [97] does not compare C-ZGNRs with the ideal ribbon. The groundwork layed out by Girao *et al.* [97] is built upon in this work and further structural perturbations are probed.

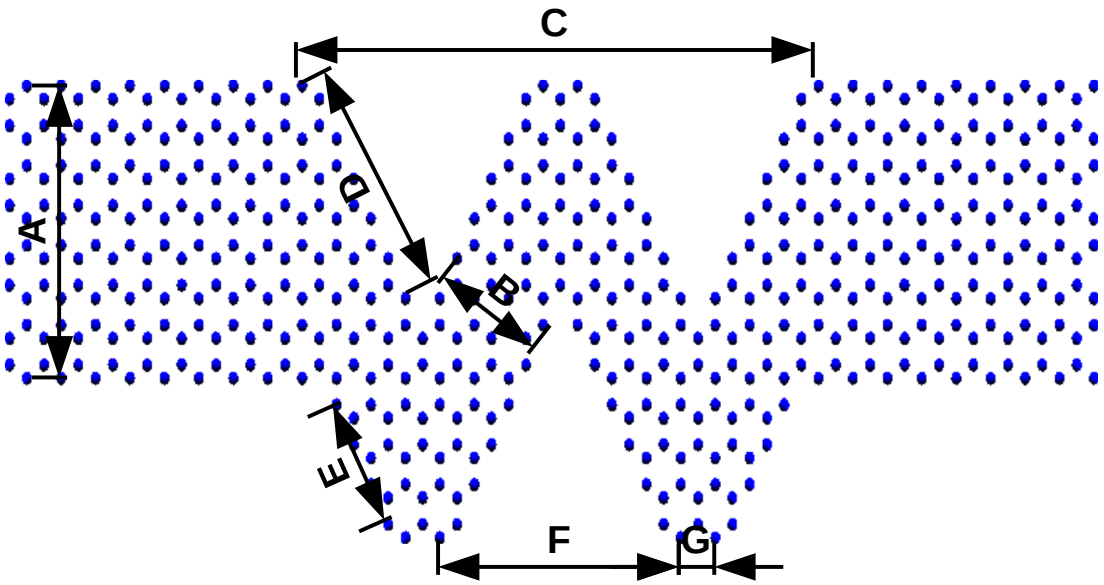


Figure 6.6: Schematic of the C-ZGNR device used in this investigation. The distances defined are: A - width of the lead. B - width of the chevron. C - length of the chevron region. D-depth of the chevron. E - length between the lead and first chevron peak. F - length between neighboring chevron peaks. G - length of the chevron peak. The naming convention for the above device is A/B/C/D/E/F/G = 8/4/16/6/4/8/2 C-ZGNR.

### 6.3.2 Results and Discussion

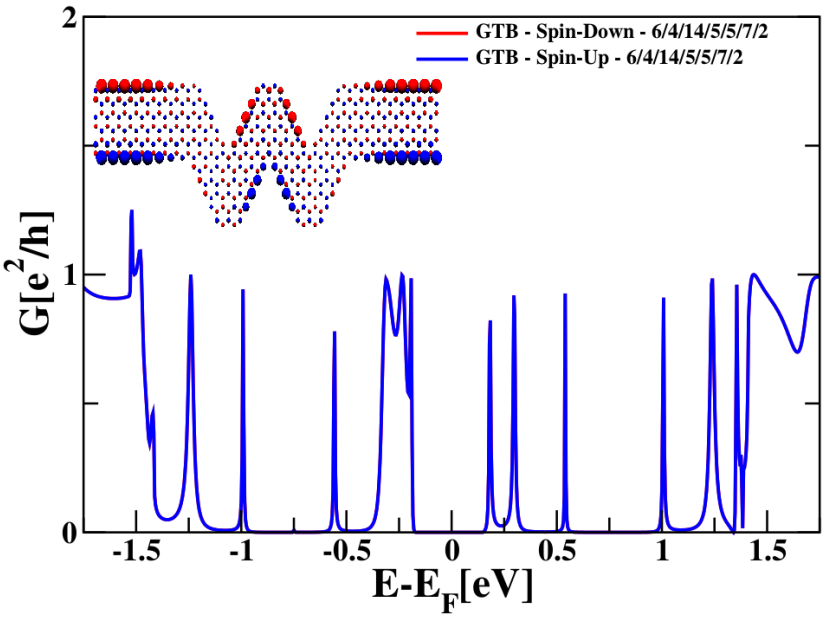


Figure 6.7: Electronic conductance (Equation 2.98) vs. energy relative to the Fermi-energy for a 6/4/14/5/5/7/2 C-ZGNR device (insert) calculated using the GTB model (Equation 2.67). Red(blue) denotes the spin-down(-up) results. Insert: Spin-distribution diagram for the 6/4/14/5/5/7/2 C-ZGNR device. Net spin-up circles are blue, and net spin-down circles red where the radius of each circle is the relative magnitude of the net local-spin (Equation 2.81).

Figure 6.7 shows the electronic conductance of a 6/4/14/5/5/7/2 C-ZGNR device. The electronic conductance properties of this system are spin-independent with discrete conductance spikes implying a loss of conductance channels resulting in charge-carrier localisation. As the depth of the chevron (D) is increased from 5 to 9 atoms (Figure 6.8), the number of conductance spikes either side of the electronic conductance gap has doubled, however the conductance result remains spin-independent. The introduction of conductance spikes is in agreement in general literature on edge-defected GNRs, for example Girao *et al.* [97], who investigated the coherent transport properties of both mixed edge AGNR and ZGNR devices.

A further increase to the depth of the chevron to 10 atoms (Figure 6.9) results in a similar trend previously observed such that the overall number of conductance spikes increases. Also observed is that the wide conductance spike on the negative side of the electronic conductance gap is decreasing in size and becoming more discrete, as well as an increase in asymmetry above the conductance gap. This carries on the trend seen in Figures 6.7 and 6.8 which implies that the charge carriers are significantly localised with the increasing depth of chevron due to increasing number of atoms occurring in the isolated regions of the chevron. The spin-independence, seen in other systems (Figures 6.7 and 6.8 ) is also broken most likely due to the fact that the depth has an even number of atoms, compared to the odd number of atoms in Figures 6.7 and 6.8.

Table 6.1 summaries a quantitative comparison of the electronic conductance gaps and

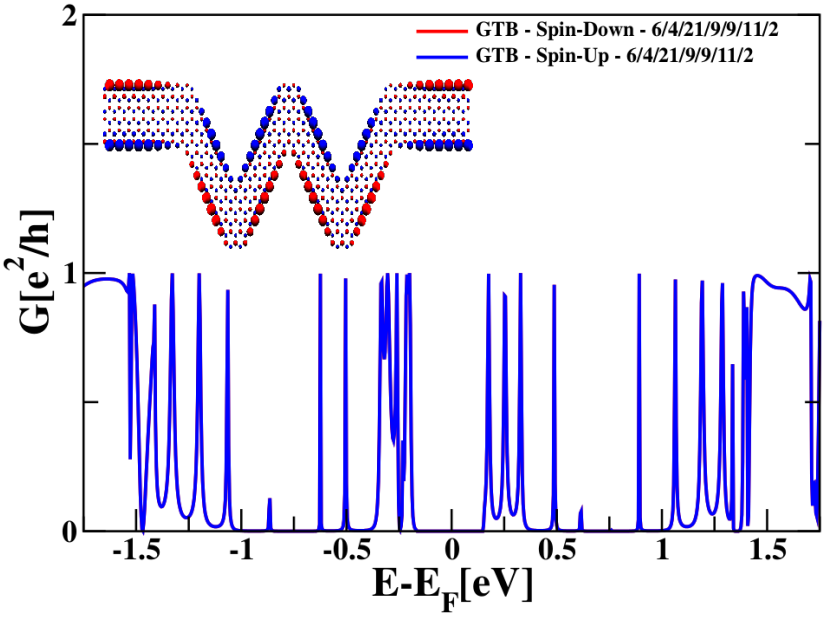


Figure 6.8: Electronic conductance (Equation 2.98) vs. energy relative to the Fermi-energy for a 6/4/21/9/9/11/2 C-ZGNR device (insert) calculated using the GTB model (Equation 2.67). Red(blue) denotes the spin-down(-up) results. Insert: Spin-distribution diagram for the 6/4/21/9/9/11/2 C-ZGNRdevice. Net spin-up circles are blue, and net spin-down circles red where the radius of each circle is the relative magnitude of the net local-spin (Equation 2.81).

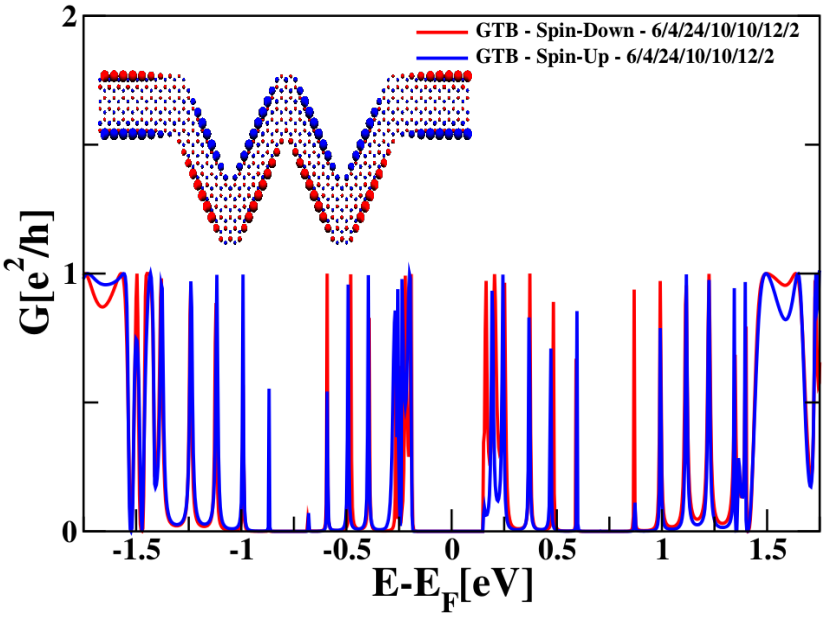


Figure 6.9: Electronic conductance (Equation 2.98) vs. energy relative to the Fermi-energy for a 6/4/24/10/10/12/2 C-ZGNR device (insert) calculated using the GTB model (Equation 2.67). Red(blue) denotes the spin-down(-up) results. Insert: Spin-distribution diagram for the 6/4/24/10/10/12/2 C-ZGNR device. Net spin-up circles are blue, and net spin-down circles red where the radius of each circle is the relative magnitude of the net local-spin (Equation 2.81).

the Simpson's rule integrated conductance (Equation 4.5) between -1eV< $E - E_F$ <1eV for the C-ZGNRS (Figure 6.7, 6.8 and 6.9.

| Device | Electronic Conductance Gap (eV) | | Integral of the Conductance ($e^2/h$) | |
|---|---|---|---|---|
| | Spin-Up | Spin-Down | Spin-Up | Spin-Down |
| 6/4/14/5/5/7/2 C-ZGNR | 0.32 | 0.32 | 0.426 | 0.426 |
| 6/4/21/9/9/11/2 C-ZGNR | 0.328 | 0.328 | 0.335 | 0.335 |
| 6/4/24/10/10/12/2 C-ZGNR | 0.34 | 0.336 | 0.301 | 0.315 |

Table 6.1: Change in electronic conductance gap and the Simpson's rule integrated conductance (Equation 4.5) between $-1eV < E < 1eV$.

As the depth of the chevron increases (D), the electronic conductance gap increases and the integral of the conductance decreases. This implies that the path through the device is becoming more difficult with the decreasing number of channels. The large drop in the integral in the conductance from 6/4/14/5/5/7/2 C-ZGNR to 6/4/21/9/9/11/2 C-ZGNR can be explained by the 6/4/14/5/5/7/2 C-ZGNR having an almost direct conductance path from one lead to the other via energetically favorable first nearest neighbour hopping. The path from one lead to the other for the other two devices via first nearest neighbour hopping is significantly longer and thus increases the probability that the charge carrier will be scattered. This conclusion is in agreement with Chen *et. al.* [96], who determined a decrease in overall conductance in C-AGNR devices compared to ideal AGNR devices. Chen *et. al.* [96] compares chevron devices to ideal devices, but as the devices in this study are becoming increasingly chevron like with increasing depth, a comparison can be made.

The electronic conductance gap arises due to the Hubbard-$U$ term and thus will be less affected by the specific path of the conductance. This is observed in the previous sections, both in notched ZGNR devices (Figure 5.5) and in low edge-disordered devices (Figure 4.16) which show a stability in the electronic conductance gap as a function of various structural edge-perturbations. The most significant change in electronic conduction gap is between the 6/4/21/9/9/11/2 C-ZGNR and the 6/4/24/10/10/12/2 C-ZGNR, which also corresponds with a breaking of the spin-symmetry. The breaking of the spin-symmetry means that the spin-distribution is also asymmetric (Insert of Figure 6.9), possibly also leading to the increase in the magnitude of the spin-dependent electronic conductance gaps (Table 6.1). The slight increase in electronic conductance gap with increasing chevron depth is consistent with Wang and Wang [94] and Cuong *et. al.* [95], with both papers calculating an increase in conductance and band gap relative to the ideal system with the introduction of chevron perturbations.

Finally, the width of the lead (width A in Figure 6.6) is varied. At this point, there are two devices to compare, a relatively thin 4/4/16/6/9/8/2 C-ZGNR (Figure 6.10) and a wider 8/4/16/6/4/8/2 C-ZGNR (Figure 6.11). It must be noted that by varying A, the dimension E is also varied.

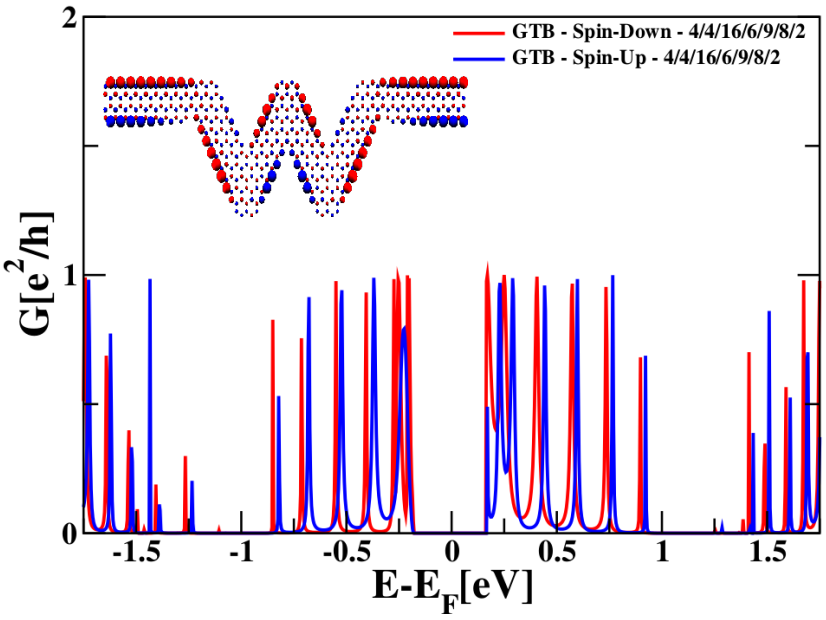


Figure 6.10: Electronic conductance (Equation 2.98) vs. energy relative to the Fermi-energy for a 4/4/16/6/9/8/2 C-ZGNR device (insert) calculated using the GTB model (Equation 2.67). Red(blue) denotes the spin-down(-up) results. Insert: Spin-distribution diagram for the 4/4/16/6/9/8/2 C-ZGNR device. Net spin-up circles are blue, and net spin-down circles red where the radius of each circle is the relative magnitude of the net local-spin (Equation 2.81).

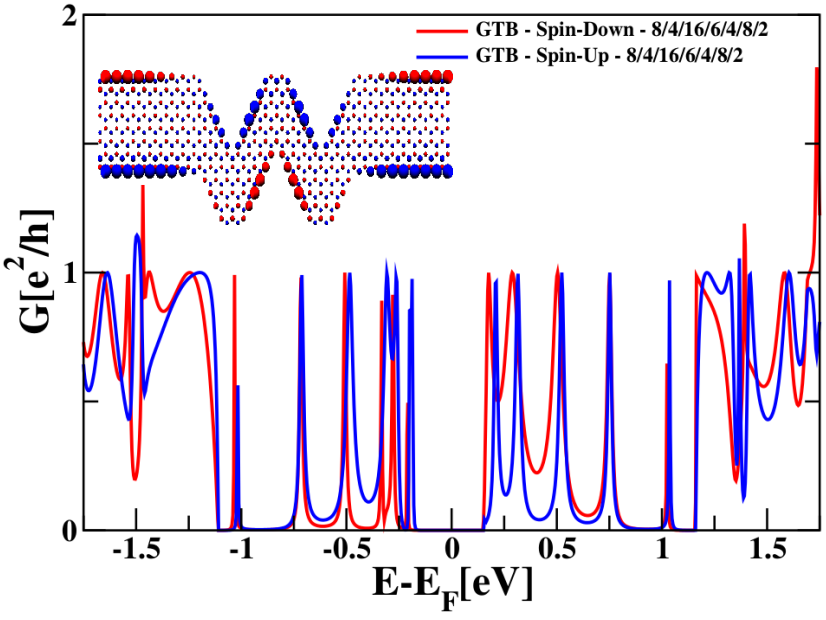


Figure 6.11: Electronic conductance (Equation 2.98) vs. energy relative to the Fermi-energy for a 8/4/16/6/4/8/2 C-ZGNR device (insert) calculated using the GTB model (Equation 2.67). Red(blue) denotes the spin-down(-up) results. Insert: Spin-distribution diagram for the 8/4/16/6/4/8/2 C-ZGNR device. Net spin-up circles are blue, and net spin-down circles red where the radius of each circle is the relative magnitude of the net local-spin (Equation 2.81).

Figure 6.10 shows a system with a relatively narrow (4-ZGNR) lead, i.e., the same width as the chevron (width B in Figure 6.6). The conductance spikes between the electronic conductance gap and the first conductance step are observed, similar to previous systems, for example the 6/4/14/5/5/7/2 C-ZGNR (Figure 6.7). In addition, the spin-independence of the electronic conductance is observed, similar to the 6/4/14/5/5/7/2 C-ZGNR (Figure 6.7) and the 6/4/21/9/9/11/2 C-ZGNR (Figure 6.8), again supporting the evidence that the spin-independence is due to an even value for the dimension D rather than being dependent on the lengths of C or F.

The 8/4/16/6/4/8/2 C-ZGNR device (Figure 6.11) demonstrates similar conductance spike features up to $\pm 1eV$ with the conductance stabilising at $E - E_F <$ -1eV and $E - E_F >$ 1eV with the conductance no longer trending to zero. The conductance spikes are also wider and taller leading to increased integral conductance compared to other systems (Table 6.2).

| Device | Electronic Conductance Gap (eV) | | Integral of the Conductance ($e^2/h$) | |
|---|---|---|---|---|
| | Spin-Up | Spin-Down | Spin-Up | Spin-Down |
| 4/4/16/6/9/8/2 C-ZGNR | 0.356 | 0.348 | 0.425 | 0.477 |
| 8/4/16/6/4/8/2 C-ZGNR | 0.356 | 0.332 | 0.692 | 0.656 |

Table 6.2: Change in electronic conductance gap and the Simpson's rule integral of the conductance (Equation 4.5) -1eV$< E - E_F <$1eV. Device nomenclature explained in Figure 6.6.

As the width of the lead increases from A=4 (Figure 6.10) to A=8 (Figure 6.11) (Table 6.2), the Simpson's rule integral of the conductance (Equation 4.5) increases significantly (i.e., by 0.27 $e^2/h$). The 8/4/16/6/4/8/2 C-ZGNR has a more direct conductance path though the device and thus an increase in conductance occurs about the electronic conductance gap. This is in keeping with the results from Figure 6.7 where the 6/4/14/5/5/7/2 C-ZGNR had a direct conductance path with a smaller lead and chevron depths. In addition, systems in Table 6.2 have a slight differences in the spin-down dependent electronic conductance gap, which is consistent with the trends in Table 6.1 being due to the change in spin-polarisation along length E. As the lead increases in these devices, length E decreases. This reduces the degree of spin-down localisation along the edge and thus shrinks the spin-down electronic conductance gap. As there are no changes in the degree of spin-up localisation, the spin-dependent spin-up gap stays the same.

### 6.3.3 Summary

The general trends seen here are in agreement with Girao *et al.* [97] who investigated different types of chevron using the GTB model, mainly mixed armchair and zig-zag edge-types. Building on the work by Girao *et al.* [97] this work has suggested possible avenues of investigation into C-GNRs, in particular, demonstrating the dependent and independent dimensions within the C-ZGNR device. The overall decrease in conductance compared to ideal ZGNR

devices in in agreement with conclusions drawn by Chen *et. al.* [96] with regards to CAGNR devices.

## 6.4 Patterned Graphene Nanoribbon

### 6.4.1 Introduction and Background

Patterned AGNR (P-AGNR) devices are internally patterned AGNRs with atomic-precision patterning that can be made by chemical self-assembly. One possible route to making a P-AGNR would be to combine Tetrabenzathracence and benzene molecules, to form the patterned devices in Figure 6.12. Based on the relative coupling strength (X-X and Y-Z), the width and length of the P-AGNR can be controlled [99]. The band and transport gaps of P-AGNRs are compared to ideal AGNRs using the GTB model. Due to the lack of long ZGNR edges within the P-AGNRs, magnetic properties are not predicted due to Clar's theory [173, 174] and thus only the spin-independent band and transport gaps are investigated.

Experimentally, patterned devices have been probed in depth [99, 100, 101], but with fewer studies into the theoretical electronic properties. Geraets *et. al.* has carried out preliminary kinetic self-assembly modeling into the energy-gap and transport properties of these patterned devices, with the key results discussed in this section [98].

Due to the regular nature of the patterning, along with the shape of the hole, the closest studies being carried out computationally to those studied here are antidots. Due to the size of the devices probed in this section, large scale anti-dots will not sufficiently describe the finite size effects investigated in this work. Topsakal *et. al.* [102] carried out DFT GGA-PAW calculations using the VASP package on AGNR systems with small antidots. The devices investigated by Topsakal *et. al.* [102] assume a single antidot in a wide device and with the location of the anti-dot being varied throughout the width. The closest approximation to the P-AGNR in Figure 6.12 is that of a antidot in location 1, i.e., the center of the device for the smallest widths investigated by Topsakal *et. al.* [102]. For 34- 36- and 38-AGNR devices, an increase in band gap is observed with the introduction of the antidot [102].

Ma *et. al.* [103] carried out transport calculations on AGNR and ZGNR devices with two triangular antidots. Ma *et. al.* [103] used the STB model, and assumed that the introduction of the two triangular anti-dots opened a conductance gap in the device. Rosales *et. al.* [104] carried out STB model transport calculations on antidots within 11-AGNR devices. The antidots are repeated along the length of the device with period d. Rosales *et. al.* [104] showed that, as the period of the antidots increased, the conductance gap decreased, with there being a large increase in the gap for the small period (d=3) system. Again, Rosales *et. al.* [104] used the STB model for their calculations, modelling a semi-conductive (within the

STB model) AGNR device. This allows easier comparison with the GTB model compared to a metallic (within the STB model) device.

### 6.4.2 Results and Discussion

The first investigation for P-AGNRs is to determine the width dependence of the band gap calculated using the GTB model and compares this to the ideal AGNR results of the same width (Figure 6.13). The results show that the band gap for the ideal AGNR decreases inversely, however, only a single ideal AGNR trend is observed due to the reduced set of results that are calculated. The band gap for the P-AGNR is significantly larger compared to the ideal AGNRs (1.6eV compared to 0.7eV at a width of 9.8Å). In addition the P-AGNR band gap is independent of device width suggesting that the band gap in these devices is dominated by the single X-X coupling bond observed in Figure 6.12. The increase in band gap with the introduction of patterning is in agreement with Topsakal *et. al.* [102] and Rosales *et. al.* [104], with both demonstrating an increase in band/conduction gap with the introduction of antidots in 34- 36- and 38-AGNR devices, and 11-AGNR devices, respectively.

The effect of width with constant device length (Figure 6.14) and length to width ratio on the transport gap is also examined (Figure 6.15). For these devices, an ideal AGNR lead is attached to each end of the device (i.e., at the X-X coupling sites, Figure 6.12). Due to the lack of spin-polarisation in these devices, only a single ideal AGNR unit cell is required to approximate for the leads. As the length of the P-AGNR devices increases, the width at which the transport gap becomes metallic increases (Figure 6.14). In addition, a step occurs, similar to that in the length/width ratio graph (Figure 6.15) where the transport gap for the P-AGNR drops by an order of magnitude for 32.7 Å and 49.8 Å length devices. The order of magnitude drop for 32.7 Å is shown in more detail in the zoomed insert (Figure 6.14). In comparison, the transport gap for the ideal AGNR never drops to zero in the widths examined.

The decrease in transport gap and eventual semi-conductive/metal transition in P-AGNR occurs due to the loss of third NN hopping within the device due to the patterned holes. In terms of pathways though the device in the direction of the leads, the only path is via the X-X coupling which includes 1st and 2nd NN hopping terms. As demonstrated for ideal AGNR, it is the 3rd NN hopping parameter that opens the metallic AGNR gap (Chapter 3). Finally, the fact that longer devices stay semi-conductive for larger widths is due to longer devices including more possible 3rd NN hopping sites (i.e., within the building block molecule). Thus a longer device is required for the 3rd NN hopping to become insignificant and thus close the gap.

The steps in the conduction gaps are due to additional channels forming as the width of the devices increases (Figure 6.14). For each length, there is a certain width that is required for

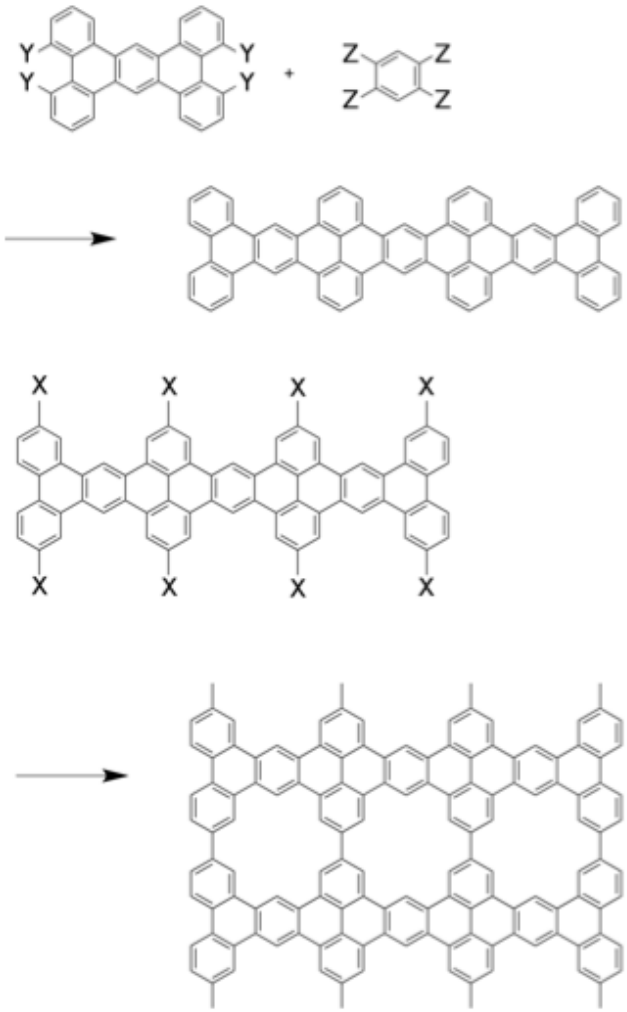


Figure 6.12: Self assembly example for the formation of the patterned AGNR device. Ribbon grows in the direction of the x-x coupling resulting in regular holes along the device. Reproduced from Gerates *et. al.* [98]

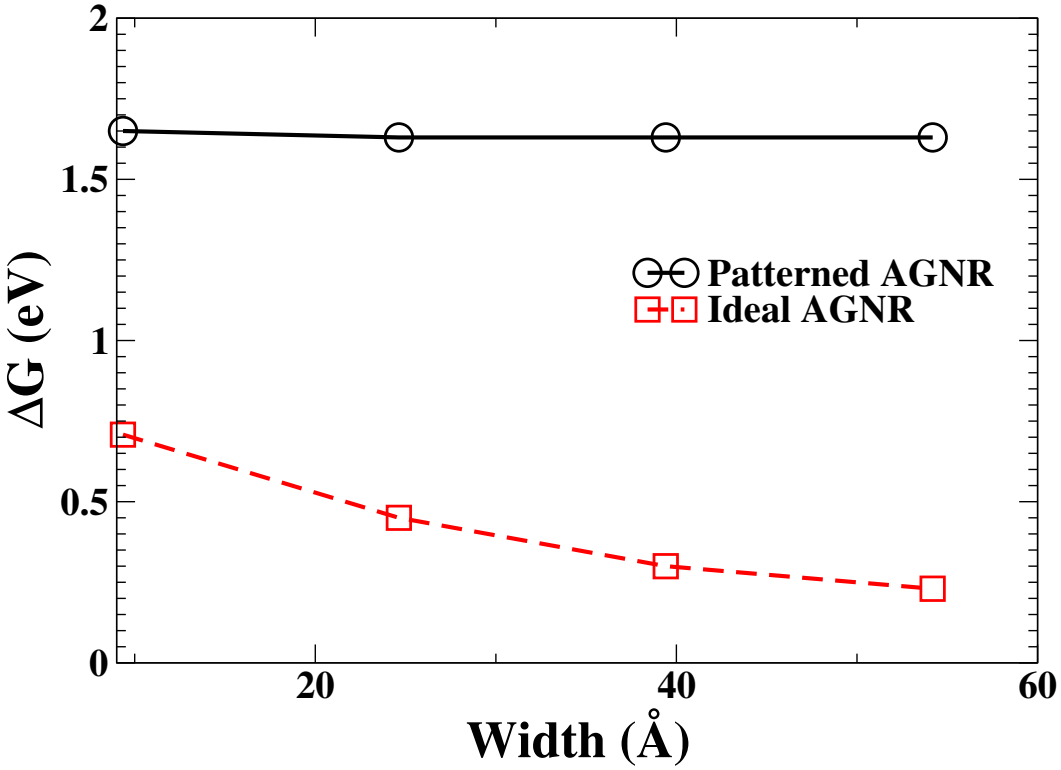


Figure 6.13: Width dependence of the band gap for P-AGNR (circles) compared to ideal AGNRs (squares) calculated using the ETB model (Equation 2.67).

this "new" conductance channel to form via increasing the number of X-X pathways through the device as a function of increasing width. The fact that the conductance gap decreases with increasing width is in agreement with Topsakal *et. al.* [102], who showed that as the width increases from 36-AGNR to 60-AGNR, there is a decrease in the conductance gap. This alone would not be significant as the general trend for AGNRs is that the band gap decreases with increasing width. Topsakal *et. al.* [102], however, also demonstrated that when the width increased from 36-AGNR to 60-AGNR, the introduction of the antidot increased the band gap for 36-AGNR but decreased it for 60-AGNR. This agrees with Figure 6.14, which demonstrates a point at which the conductance gap for the ideal AGNR becomes bigger than that of a P-AGNR device of length 49.8Å. The initial increase is due to the removal of conductance channels though the device leading to less conductance occurring though the system. As the width increases, the fact that there is a reduction in 3rd NN hopping leads to a decrease in conductance gap.

As the length to width ratio increases, so does the conductance gap (Figure 6.15). The strong dependence of the conductance gap on the length to width ratio shows that it would be possible to fine tune the transport properties of these devices using this parameter. In addition, as the trend in the transport gap is based on length to width ratio, it removes the preciseness required in ideal AGNRs for a certain transport gap leading to increased tune-ability for P-AGNRs compared to AGNRs . For example, if a gap of 0.6eV is required, a length width ratio of 1.67 is needed, instead of a length and width of precise dimension.

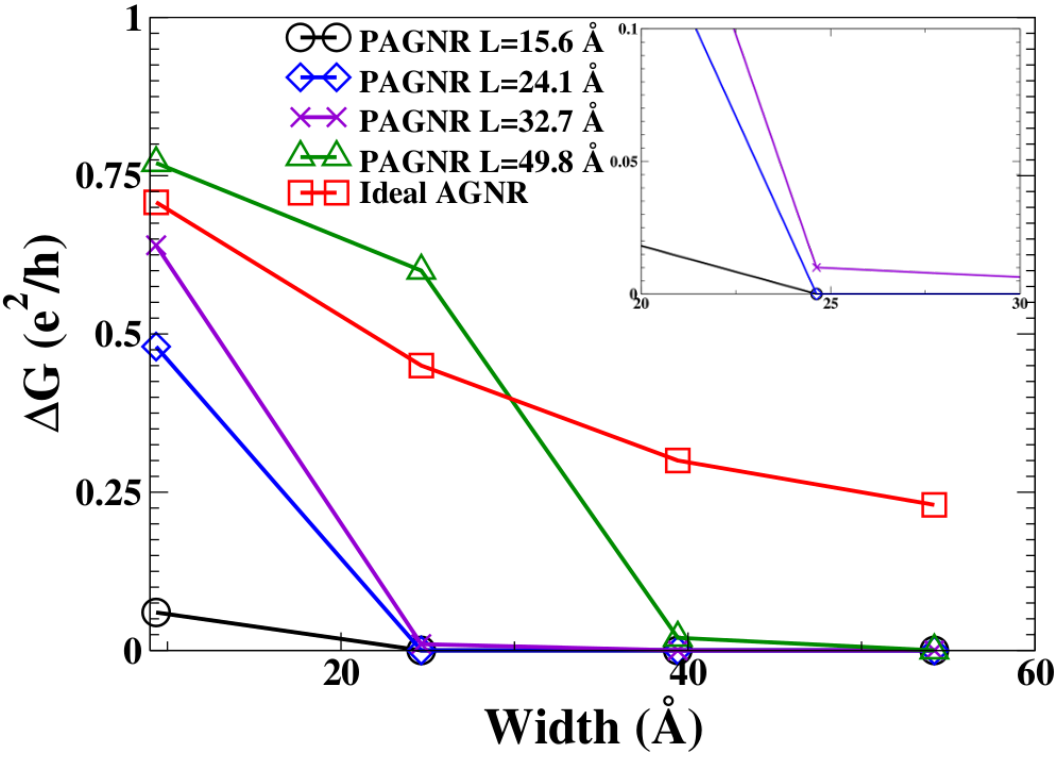


Figure 6.14: Width dependence of the electronic transport gap for P-AGNR calculated using the ETB model (Equation 2.67). Insert demonstrates the none-zero value if the L=32.7 ÅP-AGNR device.

Finally, as the length/width ratio increases, the transport gap converges to the band gap of the infinitely long patterned device (Figure 6.15).

## 6.5 Conclusion

This Chapter has demonstrated that the three types of edge perturbation investigated here, asymmetrical magnetic inhomogeneities, chevron GNRs and patterned AGNRs, each have a potential in future device designs.

Asymmetrical magnetic inhomogeneities demonstrate a controllable method of transitioning from semi-conductive, to half-metallic, to metallic via edge-perturbation strength, width and uniaxial strain. In addition, a transition from antiferromagnetic, to ferromagnetic, to paramagnetic is also observed.

Chevron devices have been shown to transition from spin-dependent to spin-independent transport properties via chevron length. In addition the spin-dependent conductance gap is shown to be dependent on the lead width. This study also outlines potential avenues to take this work further.

Finally, the conductance gap in patterned AGNR devices is shown to be dependent on length/width ratio, with the band gap independent of width. This suggests that for a sufficiently long device, the conductance gap would also be width independent. The dependence of conductance gap on length/width ratio removes the need for Angstroms precise measure-

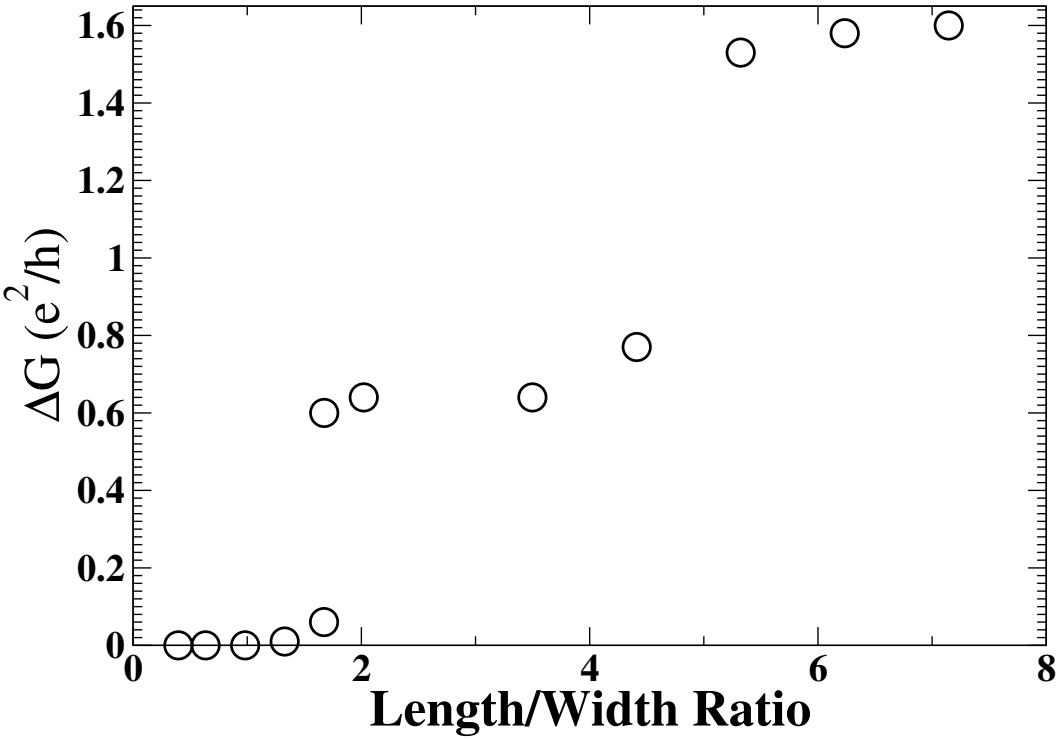


Figure 6.15: Length/Width dependence of the electronic transport gap for patterned AGNR devices calculated with the GTB model (Equation 2.67)

ment of the width when determining the conductance gap. Instead, a certain conductance gap can be requested and a device of a certain length/width ratio produced.

It must be noted that the work presented in this Chapter is preliminary work only. This preliminary work lays out the potential of the GTB model in predicting and designing potential new devices. Further probing the effects of edge-inhomogeneity and varying different chevron dimensions has potential for further work.

# Chapter 7

# Conclusion

In Chapter 4, it was demonstrated that there is an overall decrease in conductance of GNRs with the introduction of edge-vacancies. In particular, it was shown that there is an overall increase in localisation along the ribbon-edge up to a critical edge-vacancy concentration of 51.25%. When comparing the three models, the simple tight-binding (STB) model, the extended tight-binding (ETB) model, and the generalised tight-binding (GTB) model, the general trend of decreasing electronic transport is observed in all three models, with convergence of the conductance occurring between 32.5% and 51.25% edge-vacancy concentration. It has also been shown that at 42.5% edge-vacancy all three models are within the localisation regime, with the STB model being fully within the localisation regime at low edge-vacancy concentrations (7.5% edge-vacancy concentration). The stability of the conduction-gap in the GTB model and of the non-zero conductance at the Fermi energy for the non-interacting models with the introduction of edge-vacancies implies that, even at high edge-vacancies concentrations, the GTB model is sufficiently different that it should be used over the simpler, non-interacting, models. The effect of random edge-vacancies compared to systematic edge-vacancies was also investigated and it was found that random edge-vacancies stabilise the edge-polarisation and prevent the antiferromagnetic/paramagnetic transition observed in the systematic edge-vacancies study, implying that the GTB is preferred over the non-interacting models to calculate the effects of these edge-defects.

In addition, the effects of increasing device length was probed and Anderson localisation lengths of 47 Å and 49 Å were found for the STB and ETB models respectively. The difference between localisation and Anderson localisation was also discussed, with Anderson localisation requiring longer devices. Finally, the onset of the non-interacting conductance gap was investigated, with the conductance gap calculated via the STB and ETB models following the same trend as the GTB model above 120Å.

The results in Chapter 4 lead to the conclusion that the interacting GTB model is required for the edge-disordered ZGNRs studied, with the intrinsic gap only being overtaken by the disorder-induced conductance gap at device lengths $>$ 120 Å. The stability of the intrinsic

conductance gap in the GTB model compared to the disorder-induced conductance gap of the STB and ETB models suggests that the experimentally observed band gap can be attributed to the electron-electron interactions, not the effects of edge-disorder.

Chapter 5 demonstrated that structural inhomogeneities can break the spin-independence of the coherent conductance of GNRs. In particular, it is possible to increase both the degree of spin-dependence and create a spin-dependent conductance gap by increasing the length of the bottom of the notch. Unixaxial strain is also shown to controllably and predictably perturb the conductance gap in both ideal and notched devices. In terms of introducing notches to the strained device, the only real effect of notches is to remove conduction channels and reduce the overall conductance by up to 98% close to the Fermi level. Due to the degree of spin-dependence in both the overall conductance and the conductance gap, being dependent on notch bottom length, a length that would be hard to control in top-down synthesis, notches should not be relied on for spintronic devices and inhomogeneous magnetic impurities are a better option.

Chapter 6 demonstrated that the three types of edge perturbation investigated, asymmetrical magnetic inhomogeneities, chevron GNRs and patterned AGNRs, each have a potential in future device designs.

Asymmetrical magnetic inhomogeneities demonstrate a controllable method of transitioning from semi-conductive, to half-metallic, to metallic conductance via edge-perturbation strength. The same trend can also be observed by varying the device width while keeping the edge-perturbation strength constant. Applied uniaxial strain can also be used to fine tune the width allowing more control over the onset of the observed transitions. In general, these transitions in the conduction properties are linked to a similar transition from antiferromagnetic, to ferromagnetic, to paramagnetic states. The antiferromagnetic state generally occurs with the spin-dependent semi-conductive and half-metal regimes, the ferromagnetic state generally occurs with the spin-independent metallic regime and the paramagnetic state generally occurs with the spin-independent semi-conductive regime in the systems probed. Further work needs to be carried out to probe more devices to confirm these trends.

Chevron devices have been shown to transition from spin-dependent to spin-independent transport properties via chevron length. In addition the spin-dependent conductance gap is shown to be dependent on the lead width. This study also outlines potential avenues to take this work further.

Finally, the conductance gap in patterned AGNR devices is shown to be dependent on length/width ratio, with the band gap independent of width. This suggests that for a sufficiently long device, the conductance gap would also be width independent. The dependence of conductance gap on length/width ratio removes the need for Angstrom precise measurement of the width when determining the conductance gap. Instead, a certain conductance

gap can be requested and a device of a certain length/width ratio produced.

# Appendix

# Appendix A

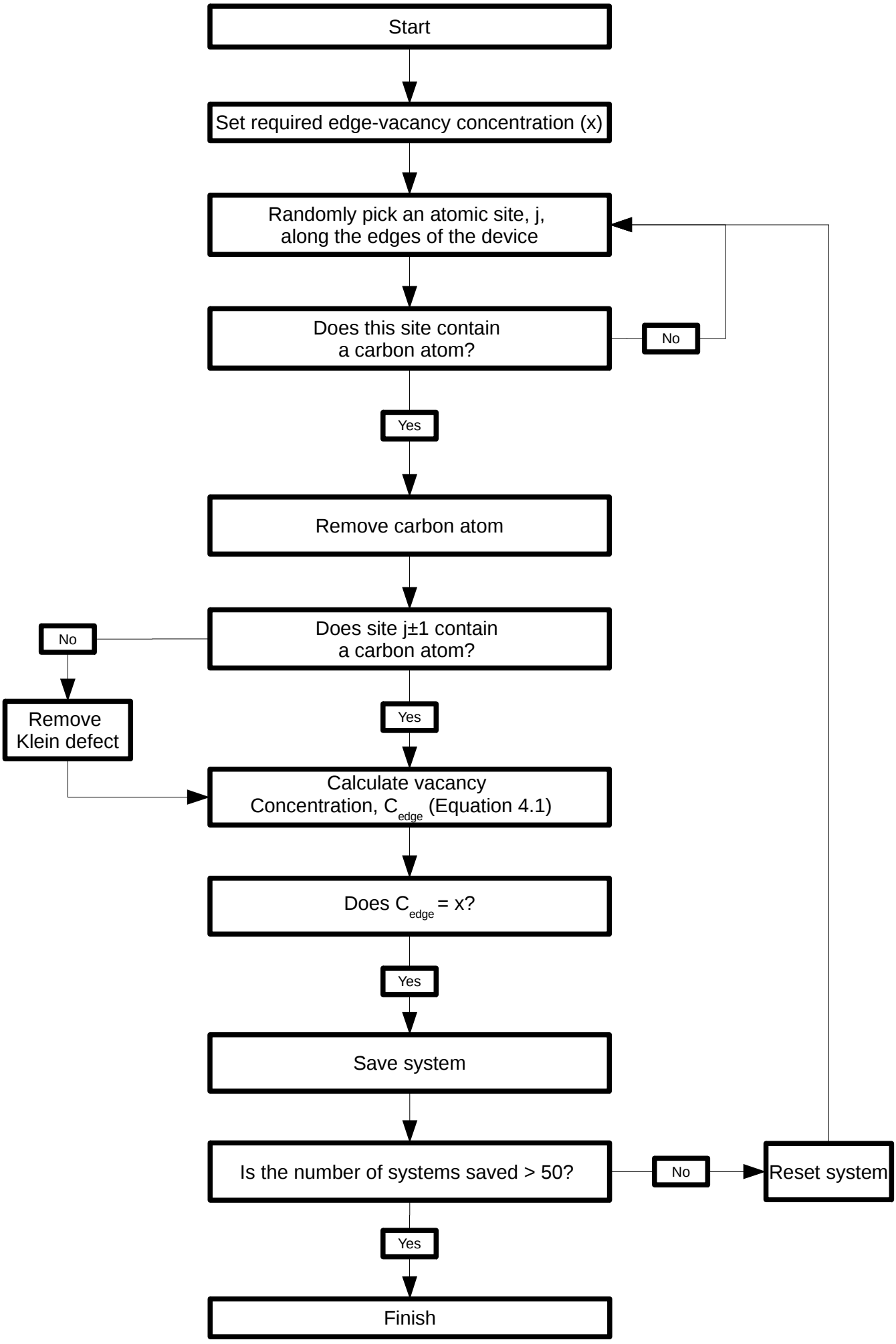
Start
Set required edge-vacancy concentration (x)
Randomly pick an atomic site, j, along the edges of the device
Does this site contain a carbon atom?
No
Yes
Remove carbon atom
Does site j±1 contain a carbon atom?
No
Remove Klein defect
Yes
Calculate vacancy Concentration, $C_{edge}$ (Equation 4.1)
Does $C_{edge}$ = x?
Yes
Save system
Is the number of systems saved > 50?
No
Reset system
Yes
Finish

# List of References


[1] Schaller R. Moore's law: past, present and future. IEEE spectrum. 1997;34(6):52–59.

[2] Hassan S, Humaira, Asghar M. Limitation of Silicon Based Computation and Future Prospects. In: Communication Software and Networks, 2010. ICCSN '10. Second International Conference on; 2010. p. 559 –561.

[3] Schulz M. The end of the road for silicon. Nature. 1999;399(6738):729–730.

[4] Savio A, Monfray S, Charbuillet C, Skotnicki T. On the Limitations of Silicon for I-MOS Integration. Electron Devices, IEEE Transactions on. 2009 may;56(5):1110 –1117.

[5] Ieong M, Doris B, Kedzierski J, Rim K, Yang M. Silicon Device Scaling to the Sub-10-nm Regime. Science. 2004;306(5704):2057–2060.

[6] Novoselov K, Geim A, Morozov S, Jiang D, Zhang Y, Dubonos S, et al. Electric field effect in atomically thin carbon films. Science. 2004;306(5696):666.

[7] Novoselov K, Geim A, Morozov S, Jiang D, Katsnelson M, Grigorieva I, et al. Two-Dimensional Gas of Massless Dirac Fermions in Graphene. Nature. 2005;438:197.

[8] Sirdeshmukh DB, Sirdeshmukh L, Subhadra K. Atomistic Properties of Solids. vol. 147. Springer Verlag; 2011.

[9] Katsnelson MI. Graphene: carbon in two dimensions. Materials today. 2007;10(1-2):20–27.

[10] Wallace PR. The Band Theory of Graphite. Phys Rev. 1947 May;71:622–634.

[11] Zhang Y, Tan YW, Stormer HL, Kim P. Experimental observation of the quantum Hall effect and Berry's phase in graphene. Nature(London). 2005;438(7065):201–204.

[12] Ashcroft NW, Mermin ND. Solid State Physics. Holt, Rinehart and Winston, New York, 1976; 1976.

[13] Vonsovskiæi S. Quantum solid-state physics. Springer-Verlag (Berlin and New York); 1989.

[14] Slonczewski JC, Weiss PR. Band Structure of Graphite. Phys Rev. 1958 Jan;109:272–279.

[15] Reich S, Maultzsch J, Thomsen C, Ordejón P. Tight-binding description of graphene. Phys Rev B. 2002 Jul;66(3):035412.

[16] Soler JM, Artacho E, Gale JD, García A, Junquera J, Ordejón P, et al. The SIESTA method for ab initio order- N materials simulation. Journal of Physics: Condensed Matter. 2002 Mar;14(11):2745–2779.

[17] Geim AK, MacDonald AH. Graphene: Exploring carbon flatland. Physics Today. 2007;60:35.

[18] Semenoff GW. Condensed-Matter Simulation of a Three-Dimensional Anomaly. Phys Rev Lett. 1984 Dec;53:2449–2452.

[19] DiVincenzo DP, Mele EJ. Self-consistent effective-mass theory for intralayer screening in graphite intercalation compounds. Phys Rev B. 1984 Feb;29:1685–1694.

[20] Shankar R. Principles of quantum mechanics. Springer; 1994.

[21] Herbut IF. Interactions and phase transitions on graphenes honeycomb lattice. Physical review letters. 2006;97(14):146401.

[22] Li X, Zhang G, Bai X, Sun X, Wang X, Wang E, et al. Highly conducting graphene sheets and Langmuir–Blodgett films. Nat Nanotechnol. 2008;3(9):538–542.

[23] Katsnelson M, Novoselov K, Geim A. Chiral tunnelling and the Klein paradox in graphene. Nature Physics. 2006;2(9):620–625.

[24] Lamata L, León J, Schätz T, Solano E. Dirac Equation and Quantum Relativistic Effects in a Single Trapped Ion. Phys Rev Lett. 2007 Jun;98(25):253005.

[25] De Martino A, Dell'Anna L, Egger R. Magnetic Confinement of Massless Dirac Fermions in Graphene. Phys Rev Lett. 2007 Feb;98(6):066802.

[26] Geim A, Novoselov K. The rise of graphene. Nature materials. 2007;6(3):183.

[27] Mayorov AS, Gorbachev RV, Morozov SV, Britnell L, Jalil R, Ponomarenko LA, et al. Micrometer-Scale Ballistic Transport in Encapsulated Graphene at Room Temperature. Nano Letters. 2011;.

[28] Miao F, Wijeratne S, Zhang Y, Coskun U, Bao W, Lau C. Phase-coherent transport in graphene quantum billiards. Science. 2007;317(5844):1530.

[29] Han MY, Ozyilmaz B, Zhang Y, Kim P. Energy band-gap engineering of graphene nanoribbons. Physical review letters. 2007;98(20):206805.

[30] Heersche H, Jarillo-Herrero P, Oostinga J, Vandersypen L, Morpurgo A. Manifestations of phase-coherent transport in graphene. The European Physical Journal-Special Topics. 2007;148(1):27–37.

[31] Li X, Wang X, Zhang L, Lee S, Dai H. Chemically Derived, Ultrasmooth Graphene Nanoribbon Semiconductors. Science. 2008;319(5867):1229–1232.

[32] Son YW, Cohen ML, Louie SG. Energy gaps in graphene nanoribbons. Physical review letters. 2006;97(21):216803.

[33] Hancock Y, Uppstu A, Saloriutta K, Harju A, Puska MJ. Generalized tight-binding transport model for graphene nanoribbon-based systems. Phys Rev B. 2010 Jun;81(24):245402.

[34] Kohn W, Sham LJ. Quantum Density Oscillations in an Inhomogeneous Electron Gas. Phys Rev. 1965 Mar;137:A1697–A1705.

[35] Langreth DC, Mehl MJ. Beyond the local-density approximation in calculations of ground-state electronic properties. Phys Rev B. 1983 Aug;28:1809–1834.

[36] Perdew JP, Chevary JA, Vosko SH, Jackson KA, Pederson MR, Singh DJ, et al. Atoms, molecules, solids, and surfaces: Applications of the generalized gradient approximation for exchange and correlation. Phys Rev B. 1992 Sep;46:6671–6687.

[37] Perdew JP, Burke K, Ernzerhof M. Generalized gradient approximation made simple. Physical Review Letters. 1996;77(18):3865–3868.

[38] Dalosto SD, Levine ZH. Controlling the band gap in zigzag graphene nanoribbons with an electric field induced by a polar molecule. The Journal of Physical Chemistry C. 2008;112(22):8196–8199.

[39] Du A, Smith SC, Lu G. Formation of Single-Walled Carbon Nanotube via the Interaction of Graphene Nanoribbons: Ab Initio Density Functional Calculations. Nano Lett. 2007;7(11):3349–3354.

[40] Fujita M, Wakabayashi K, Nakada K, Kusakabe K. Peculiar Localized State at Zigzag Graphite Edge. Journal of the Physical Society of Japan. 1996;65(7):1920–1923.

[41] Gunlycke D, White CT. Tight-binding energy dispersions of armchair-edge graphene nanostrips. Phys Rev B. 2008 Mar;77(11):115116.

[42] Ezawa M. Peculiar width dependence of the electronic properties of carbon nanoribbons. Phys Rev B. 2006 Jan;73:045432.

[43] Nakada K, Fujita M, Dresselhaus G, Dresselhaus MS. Edge state in graphene ribbons: Nanometer size effect and edge shape dependence. Physical Review B. 1996;54(24):17954–17961.

[44] Finkenstadt D, Pennington G, Mehl MJ. From graphene to graphite: A general tight-binding approach for nanoribbon carrier transport. Phys Rev B. 2007 Sep;76:121405.

[45] Zheng H, Wang ZF, Luo T, Shi QW, Chen J. Analytical study of electronic structure in armchair graphene nanoribbons. Phys Rev B. 2007 Apr;75:165414.

[46] White CT, Li J, Gunlycke D, Mintmire JW. Hidden one-electron interactions in carbon nanotubes revealed in graphene nanostrips. Nano letters. 2007;7(3):825–830.

[47] Yamashiro A, Shimoi Y, Harigaya K, Wakabayashi K. Spin- and charge-polarized states in nanographene ribbons with zigzag edges. Phys Rev B. 2003 Nov;68:193410.

[48] Fernández-Rossier J. Prediction of hidden multiferroic order in graphene zigzag ribbons. Phys Rev B. 2008 Feb;77:075430.

[49] Kan E, Li Z, Yang J. Magnetism IN Graphene Systems. Nano. 2008;03(06):433–442.

[50] Huang B, Liu F, Wu J, Gu BL, Duan W. Suppression of spin polarization in graphene nanoribbons by edge defects and impurities. Physical Review B. 2008;77(15):153411.

[51] Datta S. Electronic transport in mesoscopic systems. Cambridge Univ Pr; 1997.

[52] Areshkin DA, Gunlycke D, White CT. Ballistic transport in graphene nanostrips in the presence of disorder: Importance of edge effects. Nano Lett. 2007;7(1):204–210.

[53] Dubois SMM, Lopez-Bezanilla A, Cresti A, Triozon F, Biel B, Charlier JC, et al. Quantum transport in graphene nanoribbons: Effects of edge reconstruction and chemical reactivity. ACS nano. 2010;4(4):1971–1976.

[54] Molitor F, Jacobsen A, Stampfer C, Güttinger J, Ihn T, Ensslin K. Transport gap in side-gated graphene constrictions. Phys Rev B. 2009 Feb;79(7):075426.

[55] Kim WY, Kim KS. Carbon nanotube, graphene, nanowire, and molecule-based electron and spin transport phenomena using the nonequilibrium Green's function method at the level of first principles theory. Journal of Computational Chemistry. 2008;29(7):1073–1083.

[56] Cresti A, Nemec N, Biel B, Niebler G, Triozon F, Cuniberti G, et al. Charge transport in disordered graphene-based low dimensional materials. Nano Research. 2008;1:361–394.

[57] Lherbier A, Biel B, Niquet YM, Roche S. Transport Length Scales in Disordered Graphene-Based Materials: Strong Localization Regimes and Dimensionality Effects. Phys Rev Lett. 2008 Jan;100(3):036803.

[58] Cresti A, Roche S. Range and correlation effects in edge disordered graphene nanoribbons. New Journal of Physics. 2009;11:095004.

[59] Cresti A, Roche S. Edge-disorder-dependent transport length scales in graphene nanoribbons: From Klein defects to the superlattice limit. Phys Rev B. 2009 Jun;79(23):233404.

[60] Anderson PW. Absence of Diffusion in Certain Random Lattices. Physical Review. 1958 Mar;109(5):1492–1505.

[61] Anderson PW. Absence of Diffusion in Certain Random Lattices. Phys Rev. 1958 Mar;109:1492–1505.

[62] Li T, Lu SP. Quantum conductance of graphene nanoribbons with edge defects. Physical Review B. 2008;77(8):085408.

[63] Gallagher P, Todd K, Goldhaber-Gordon D. Disorder-induced gap behavior in graphene nanoribbons. Physical Review B. 2010 Mar;81(11):115409.

[64] Haskins J, Knac A, Sevik C, Sevinçli H, Cuniberti G, Can T. Control of thermal and electronic transport in defect-engineered graphene nanoribbons. ACS nano. 2011 May;5(5):3779–87.

[65] Ihnatsenka S, Kirczenow G. Conductance quantization in strongly disordered graphene ribbons. Physical Review B. 2009 Nov;80(20):201407.

[66] Martin I, Blanter Y. Transport in disordered graphene nanoribbons. Physical Review B. 2009 Jun;79(23):235132.

[67] Mucciolo E, Castro Neto A, Lewenkopf C. Conductance quantization and transport gaps in disordered graphene nanoribbons. Physical Review B. 2009 Feb;79(7):1–5.

[68] Zheng XH, Rungger I, Zeng Z, Sanvito S. Effects induced by single and multiple dopants on the transport properties in zigzag-edged graphene nanoribbons. Physical Review B. 2009 Dec;80(23):235426.

[69] Lagendijk A, van Tiggelen B, Wiersma DS. Fifty years of Anderson localization. Physics Today. 2009;62(8):24.

[70] Kresse G, Furthmuller J. Efficiency of ab-initio total energy calculations for metals and semiconductors using a plane-wave basis set. Computational Materials Science. 1996;6(1):15–50.

[71] Broers AN, Hoole ACF, Ryan JM. Electron beam lithographyResolution limits. Microelectronic Engineering. 1996 Sep;32(1-4):131–142.

[72] Bai J, Huang Y. Fabrication and electrical properties of graphene nanoribbons. Materials Science and Engineering: R: Reports. 2010 Nov;70(3-6):341–353.

[73] Ihnatsenka S, Zozoulenko I, Kirczenow G. Band-gap engineering and ballistic transport in edge-corrugated graphene nanoribbons. Physical Review B. 2009 Oct;80(15):155415.

[74] Saloriutta K, Hancock Y, Kärkkäinen A, Kärkkäinen L, Puska MJ, Jauho AP. Electron transport in edge-disordered graphene nanoribbons. Physical Review B. 2011;83(20):205125.

[75] Berger C, Song Z, Li T, Li X, Ogbazghi AY, Feng R, et al. Ultrathin epitaxial graphite: 2D electron gas properties and a route toward graphene-based nanoelectronics. The Journal of Physical Chemistry B. 2004;108(52):19912–19916.

[76] Jiao L, Zhang L, Wang X, Diankov G, Dai H. Narrow graphene nanoribbons from carbon nanotubes. Nature. 2009 Apr;458(7240):877–80.

[77] Kosynkin DV, Higginbotham AL, Sinitskii A, Lomeda JR, Dimiev A, Price BK, et al. Longitudinal unzipping of carbon nanotubes to form graphene nanoribbons. Nature. 2009 Apr;458(7240):872–6.

[78] Cai J, Ruffieux P, Jaafar R, Bieri M, Braun T, Blankenburg S, et al. Atomically precise bottom-up fabrication of graphene nanoribbons. Nature. 2010 Jul;466(7305):470–3.

[79] Evaldsson M, Zozoulenko IV, Xu H, Heinzel T. Edge-disorder-induced Anderson localization and conduction gap in graphene nanoribbons. Phys Rev B. 2008 Oct;78:161407.

[80] Brandbyge M, Mozos JL, Ordejón P, Taylor J, Stokbro K. Density-functional method for nonequilibrium electron transport. Phys Rev B. 2002 Mar;65:165401.

[81] Dubois SMM, Zanolli Z, Declerck X, Charlier JC. Electronic properties and quantum transport in Graphene-based nanostructures. The European Physical Journal B-Condensed Matter and Complex Systems. 2009;72(1):1–24.

[82] Hancock Y, Saloriutta K, Uppstu A, Harju A, Puska MJ. Spin-Dependence in Asymmetric, V-Shaped-Notched Graphene Nanoribbons. Journal of Low Temperature Physics. 2008;153(5):393–398.

[83] Zhang XJ, Chen KQ, Tang LM, Long MQ. Electronic transport properties on V-shaped-notched zigzag graphene nanoribbons junctions. Physics Letters A. 2011 Aug;375(37):3319–3324.

[84] Wimmer M, Adagideli I, Berber S, Tománek D, Richter K. Spin currents in rough graphene nanoribbons: Universal fluctuations and spin injection. Physical review letters. 2008;100(17):177207.

[85] Hu FM, Ma T, Lin HQ, Gubernatis JE. Magnetic impurities in graphene. Phys Rev B. 2011 Aug;84:075414.

[86] Yang HX, Hallal A, Terrade D, Waintal X, Roche S, Chshiev M. Proximity effects induced in graphene by magnetic insulators: First-principles calculations on spin filtering and exchange-splitting gaps. Physical review letters. 2013;110(4):046603.

[87] Pedersen TG, Pedersen JG. Self-consistent tight-binding model of B and N doping in graphene. Physical Review B. 2013;87(15):155433.

[88] Power S, de Menezes V, Fagan S, Ferreira M. Magnetization profile for impurities in graphene nanoribbons. Physical Review B. 2011;84(19):195431.

[89] Krychowski D, Kaczkowski J, Lipinski S. Kondo effect of a cobalt adatom on a zigzag graphene nanoribbon. Physical Review B. 2014;89(3):035424.

[90] Mao Y, Hao W, Wei X, Yuan J, Zhong J. Edge-adsorption of potassium adatoms on graphene nanoribbon: A first principle study. Applied Surface Science. 2013;280:698–704.

[91] Zhang Z, Chen Y, Xie Y, Zhang M, Zhong J. Spin-polarized transport properties of Fe atomic chain adsorbed on zigzag graphene nanoribbons. Journal of Physics D: Applied Physics. 2011;44(21):215403.

[92] Linden S, Zhong D, Timmer a, Aghdassi N, Franke JH, Zhang H, et al. Electronic Structure of Spatially Aligned Graphene Nanoribbons on Au(788). Physical Review Letters. 2012 May;108(21):216801.

[93] Fa W, Zhou J. Electronic and magnetic properties of chevron-type graphene nanoribbon edge-terminated by oxygen atoms. Physics Letters A. 2012 Dec;377(1-2):112–117.

[94] Wang S, Wang J. Quasiparticle Energies and Optical Excitations in Chevron-Type Graphene Nanoribbon. The Journal of Physical Chemistry C. 2012 May;116(18):10193–10197.

[95] Cuong NT, Otani M, Okada S. Absence of edge states near the 120 corners of zigzag graphene nanoribbons. Physical review B. 2013;87(4):045424.

[96] Chen Y, Jayasekera T, Calzolari a, Kim KW, Nardelli MB. Thermoelectric properties of graphene nanoribbons, junctions and superlattices. Journal of physics Condensed matter : an Institute of Physics journal. 2010 Sep;22(37):372202.

[97] Girao EC, Cruz-Silva E, Meunier V. Electronic transport properties of assembled carbon nanoribbons. ACS nano. 2012;6(7):6483–6491.

[98] Gerates J, Baldwin J, Twarock R, Hancock Y. A proposed method for directed self-assembly of graphene nanoribbons. In Preparation;.

[99] Björk J, Hanke F. Towards Design Rules for Covalent Nanostructures on Metal Surfaces. Chemistry-A European Journal. 2014;20(4):928–934.

[100] Cai J, Ruffieux P, Jaafar R, Bieri M, Braun T, Blankenburg S, et al. Atomically precise bottom-up fabrication of graphene nanoribbons. Nature. 2010;466(7305):470–473.

[101] Chen L, Hernandez Y, Feng X, Müllen K. From nanographene and graphene nanoribbons to graphene sheets: chemical synthesis. Angewandte Chemie International Edition. 2012;51(31):7640–7654.

[102] Topsakal M, Aktürk E, Sevinçli H, Ciraci S. First-principles approach to monitoring the band gap and magnetic state of a graphene nanoribbon via its vacancies. Physical Review B. 2008;78(23):235435.

[103] Ma K, Yan X, Xiao Y, Chen Y. Electronic transport properties of metallic graphene nanoribbons with two vacancies. Solid State Communications. 2010;150(29):1308–1312.

[104] Rosales L, Pacheco M, Barticevic Z, León A, Latgé A, Orellana P. Transport properties of antidot superlattices of graphene nanoribbons. Physical Review B. 2009;80(7):073402.

[105] Rostami H, Asgari R. Electronic ground-state properties of strained graphene. Physical Review B. 2012 Oct;86(15):155435.

[106] Pereira V, Castro Neto a, Peres N. Tight-binding approach to uniaxial strain in graphene. Physical Review B. 2009 Jul;80(4):045401.

[107] Zhang XH. Coherent transport in strained zigzag graphene nanoconstriction. The European Physical Journal B. 2012 Jul;85(7):228.

[108] Mei H, Yong Z, Hong-Bo Z. Effect of Uniaxial Strain on Band Gap of Armchair-Edge Graphene Nanoribbons. Chinese Physics Letters. 2010 Mar;27(3):037302.

[109] Lee SH, Chiu CW, Ho YH, Lin MF. Uniaxial-stress effects on electronic structures of monolayer and bilayer graphenes. Synthetic Metals. 2010 Dec;160(23-24):2435–2441.

[110] Ni ZH, Yu T, Lu YH, Wang YY, Feng YP, Shen ZX. Uniaxial strain on graphene: Raman spectroscopy study and band-gap opening. ACS nano. 2008;2(11):2301–2305.

[111] Poetschke M, Rocha CG, Foa Torres LEF, Roche S, Cuniberti G. Modeling graphene-based nanoelectromechanical devices. Physical Review B. 2010 May;81(19):193404.

[112] Pellegrino F, Angilella G, Pucci R. Dynamical polarization of graphene under strain. Physical Review B. 2010 Sep;82(11):115434.

[113] Viana-Gomes J, Pereira VM, Peres NMR. Magnetism in strained graphene dots. Physical Review B. 2009 Dec;80(24):245436.

[114] Sun L, Li Q, Ren H, Su H, Shi QW, Yang J. Strain effect on electronic structures of graphene nanoribbons: A first-principles study. The Journal of chemical physics. 2008 Aug;129(7):074704.

[115] Li Y, Jiang X, Liu Z, Liu Z. Strain effects in graphene and graphene nanoribbons: The underlying mechanism. Nano Research. 2010 Jul;3(8):545–556.

[116] Bruna M, Vaira a, Battiato a, Vittone E, Borini S. Graphene strain tuning by control of the substrate surface chemistry. Applied Physics Letters. 2010;97(2):021911.

[117] Tsoukleri G, Parthenios J, Papagelis K, Jalil R, Ferrari AC, Geim AK, et al. Subjecting a graphene monolayer to tension and compression. Small (Weinheim an der Bergstrasse, Germany). 2009 Nov;5(21):2397–402.

[118] Liu F, Ming P, Li J. *Ab initio* calculation of ideal strength and phonon instability of graphene under tension. Phys Rev B. 2007 Aug;76:064120.

[119] Frank IW, Tanenbaum DM, van der Zande aM, McEuen PL. Mechanical properties of suspended graphene sheets. Journal of Vacuum Science & Technology B: Microelectronics and Nanometer Structures. 2007;25(6):2558.

[120] Xu P, Yang Y, Barber S, Ackerman M, Schoelz J, Qi D, et al. Atomic control of strain in freestanding graphene. Physical Review B. 2012 Mar;85(12):121406.

[121] Lee C, Wei X, Kysar JW, Hone J. Measurement of the elastic properties and intrinsic strength of monolayer graphene. Science (New York, NY). 2008 Jul;321(5887):385–8.

[122] Lu Y, Guo J. Band gap of strained graphene nanoribbons. Nano Research. 2010 May;3(3):189–199.

[123] Harrison WA. Solid state theory. Dover Pubns; 1980.

[124] Papaconstantopoulous DA, Mehl MJ, Erwin SC, Pederson MR. Tight-binding Approach to Computational Materials Science: Symposium Held December 1-3, 1997, Boston, Massachusetts, U.S.A. Materials Research Society symposia proceedings. Materials Research Society; 1998.

[125] Zhang Y, Wu X, Li Q, Yang J. Linear Band-Gap Modulation of Graphane Nanoribbons under Uniaxial Elastic Strain: A Density Functional Theory Study. The Journal of Physical Chemistry C. 2012 Apr;116(16):9356–9359.

[126] Lu Y, Guo J. Band gap of strained graphene nanoribbons. Nano Research. 2010;3(3):189–199.

[127] Gunlycke D, Areshkin D, White C. Semiconducting graphene nanostrips with edge disorder. Applied physics letters. 2007;90:142104.

[128] Su WS, Wu BR, Leung TC. A first-principles study on the electromechanical effect of graphene nanoribbon. Computer Physics Communications. 2011 Jan;182(1):99–102.

[129] Slater JC, Koster GF. Simplified LCAO Method for the Periodic Potential Problem. Phys Rev. 1954 Jun;94:1498–1524.

[130] Mahan GD. Many-Particle Physics. Physics of Solids and Liquids. Springer; 2000.

[131] Pauli W. Selected topics in field quantization. vol. 6. Courier Dover Publications; 2000.

[132] Jordan P, Pauli Jr W. Zur Quantenelektrodynamik ladungsfreier Felder. Zeitschrift für Physik. 1928;47(3-4):151–173.

[133] Callaway J. Energy band theory. vol. 16. Academic Pr; 1964.

[134] Hubbard J. Electron correlations in narrow energy bands. Proceedings of the Royal Society of London Series A Mathematical and Physical Sciences. 1963;276(1365):238.

[135] Kittel C. Introduction to solid state physics. Wiley; 1986.

[136] Madelung O. Introduction to Solid-State Theory. Springer Series in Solid-State Sciences. Springer; 1996.

[137] Wannier GH. The Structure of Electronic Excitation Levels in Insulating Crystals. Phys Rev. 1937 Aug;52(3):191–197.

[138] Penn DR. Stability theory of the magnetic phases for a simple model of the transition metals. Physical Review. 1966;142(2):350–365.

[139] Hirsch J. Two-dimensional Hubbard model: Numerical simulation study. Physical Review B. 1985;31(7):4403–4419.

[140] Kittel C, Kroemer H. Thermal Physics. W. H. Freeman; 1980.

[141] Rae AIM. Quantum mechanics. Taylor & Francis Group; 2008.

[142] Abramowitz M, Stegun IA. Handbook of Mathematical Functions: With Formulas, Graphs, and Mathematical Tables. Applied mathematics series. Dover Publications; 1964.

[143] Lieb E, Mattis D. Ordering Energy Levels of Interacting Spin Systems. Journal of Mathematical Physics. 1962;3(4):749–751.

[144] Lieb EH, Wu FY. Absence of Mott Transition in an Exact Solution of the Short-Range, One-Band Model in One Dimension. Phys Rev Lett. 1968 Jun;20:1445–1448.

[145] Mott NF. The Basis of the Electron Theory of Metals, with Special Reference to the Transition Metals. Proceedings of the Physical Society Section A. 1949;62(7):416.

[146] Nagaoka Y. Ferromagnetism in a Narrow, Almost Half-Filled s Band. Phys Rev. 1966 Jul;147:392–405.

[147] Tasaki H. The Hubbard model-an introduction and selected rigorous results. Journal of Physics Condensed Matter. 1998;10:4353–4378.

[148] Peres NMR, Araújo MAN, Bozi D. Phase diagram and magnetic collective excitations of the Hubbard model for graphene sheets and layers. Phys Rev B. 2004 Nov;70:195122.

[149] Sorella S, Tosatti E. Semi-Metal-Insulator Transition of the Hubbard Model in the Honeycomb Lattice. EPL (Europhysics Letters). 1992;19(8):699.

[150] Hanisch T, Kleine B, Ritzl A, Mller-Hartmann E. Ferromagnetism in the Hubbard model: instability of the Nagaoka state on the triangular, honeycomb and kagome lattices. Annalen der Physik. 1995;507(4):303–328.

[151] Fisher DS, Lee PA. Relation between conductivity and transmission matrix. Phys Rev B. 1981 Jun;23(12):6851–6854.

[152] Muñoz-Rojas F, Jacob D, Fernández-Rossier J, Palacios J. Coherent transport in graphene nanoconstrictions. Physical Review B. 2006;74(19):195417.

[153] Saloriutta K. Electron transport in graphene nanostructures. PhD Thesis, Aalto University; 2013.

[154] Guinea F, Tejedor C, Flores F, Louis E. Effective two-dimensional Hamiltonian at surfaces. Phys Rev B. 1983 Oct;28(8):4397–4402.

[155] Baldwin J, Hancock Y. Effects of Strain on Notched Zigzag Graphene Nanoribbons. Crystals. 2013;3(1):38–48.

[156] Taylor R. Flexible graphene electronics - Linking Experiment and theory. MPhys Thesis, University of York; 2011.

[157] Gonze X, Amadon B, Anglade PM, Beuken JM, Bottin F, Boulanger P, et al. ABINIT: First-principles approach to material and nanosystem properties. Computer Physics Communications. 2009;180(12):2582–2615.

[158] Gonze X. A brief introduction to the ABINIT software package. Zeitschrift für Kristallographie. 2005;220(5/6/2005):558–562.

[159] Hine NDM, Robinson M, Haynes PD, Skylaris CK, Payne MC, Mostofi AA. Accurate ionic forces and geometry optimization in linear-scaling density-functional theory with local orbitals. Phys Rev B. 2011 May;83:195102.

[160] Skylaris CK, Haynes PD, Mostofi AA, Payne MC. Introducing ONETEP: Linear-scaling density functional simulations on parallel computers. The Journal of Chemical Physics. 2005;122(8):–.

[161] Born M, Oppenheimer R. Zur quantentheorie der molekeln. Annalen der Physik. 1927;389(20):457–484.

[162] Feynman RP. Forces in Molecules. Phys Rev. 1939 Aug;56:340–343.

[163] Blöchl PE. Projector augmented-wave method. Phys Rev B. 1994 Dec;50:17953–17979.

[164] Kresse G, Joubert D. From ultrasoft pseudopotentials to the projector augmented-wave method. Phys Rev B. 1999 Jan;59:1758–1775.

[165] Anderson E. LAPACK Users' guide. vol. 9. Siam; 1999.

[166] Kresse G, Furthmuller J. VASP the Guide. Computational Physics, Faculty of Physics, Universit$^2$at Wien, Sensengasse. 2001;8.

[167] Niimi Y, Matsui T, Kambara H, Tagami K, Tsukada M, Fukuyama H. Scanning tunneling microscopy and spectroscopy of the electronic local density of states of graphite surfaces near monoatomic step edges. Physical Review B. 2006 Feb;73(8):085421.

[168] Kobayashi Y, Fukui Ki, Enoki T. Edge state on hydrogen-terminated graphite edges investigated by scanning tunneling microscopy. Physical Review B. 2006 Mar;73(12):125415.

[169] Klein DJ. Graphitic polymer strips with edge states. Chemical Physics Letters. 1994;217(3):261 – 265.

[170] Liu Z, Suenaga K, Harris PJF, Iijima S. Open and Closed Edges of Graphene Layers. Phys Rev Lett. 2009 Jan;102:015501.

[171] Knuth DE. Art of Computer Programming, Volume 2: Seminumerical Algorithms, The. Addison-Wesley Professional; 2014.

[172] Atkinson KE. An introduction to numerical analysis. Wiley; 1989.

[173] Clar E, Schoental R. Polycyclic hydrocarbons. vol. 2. Springer; 1964.

[174] Wassmann T, Seitsonen AP, Saitta AM, Lazzeri M, Mauri F. Clars theory, $\pi$-electron distribution, and geometry of graphene nanoribbons. Journal of the American Chemical Society. 2010;132(10):3440–3451.

[175] Altshuler BL, Khmel'nitzkii D, Larkin AI, Lee PA. Magnetoresistance and Hall effect in a disordered two-dimensional electron gas. Phys Rev B. 1980 Dec;22:5142–5153.

[176] Landauer R. Electrical resistance of disordered one-dimensional lattices. Philosophical Magazine. 1970 Apr;21(172):863–867.

[177] Anderson P, Thouless D, Abrahams E, Fisher D. New method for a scaling theory of localization. Physical Review B. 1980 Oct;22(8):3519–3526.

[178] Johnston R, Kunz H. The conductance of a disordered wire. Journal of Physics C: Solid State Physics. 1983 Jul;16(20):3895–3912.

[179] Thouless DJ. Localization distance and mean free path in one-dimensional disordered systems. Journal of Physics C: Solid State Physics. 1973;6(3):L49.

[180] Beenakker CW. Random-matrix theory of quantum transport. Reviews of modern physics. 1997;69(3):731.

[181] Avriller R, Roche S, Triozon F, Blase X, Latil S. Low-dimensional quantum transport properties of chemically-disordered carbon nanotubes: from weak to strong localization regimes. Modern Physics Letters B. 2007;21(29):1955–1982.

[182] Thouless D. Maximum metallic resistance in thin wires. Physical Review Letters. 1977;39(18):1167.

[183] Ordejón P, Artacho E, Soler JM. Self-consistent order-N density-functional calculations for very large systems. Phys Rev B. 1996 Apr;53:R10441–R10444.

[184] Taylor J, Guo H, Wang J. *Ab initio* modeling of quantum transport properties of molecular electronic devices. Phys Rev B. 2001 Jun;63:245407.

[185] Aryasetiawan F, Karlsson K, Jepsen O, Schönberger U. Calculations of Hubbard U from first-principles. Physical Review B - Condensed Matter and Materials Physics. 2006;74(12):1–9.

[186] Nakamura K, Arita R, Yoshimoto Y, Tsuneyuki S. First-principles calculation of effective onsite Coulomb interactions of 3d transition metals: Constrained local density

functional approach with maximally localized Wannier functions. Physical Review B - Condensed Matter and Materials Physics. 2006;74(23):1–5.

[187] Gunnarsson O. Calculation of parameters in model Hamiltonians. Physical Review B. 1990;41(1):514–518.

[188] Solovyev IV, Dederichs PH. Ab initio calculations of Coulomb U parameters for transition-metal impurities. Physical Review B. 1994;49(10):6736–6740.

[189] Fukushima T, Katayama-Yoshida H, Sato K, Bihlmayer G, Mavropoulos P, Bauer DSG, et al. Hubbard U calculations for gap states in dilute magnetic semiconductors. Journal of physics Condensed matter : an Institute of Physics journal. 2014;26(27):274202.

[190] Cox BN, Coulthard Ma, Lloyd P. A calculation of the Coulomb correlation energy, U, for transition metals in Hubbard's model. Journal of Physics F: Metal Physics. 1974 Jun;4(6):807–820.

[191] Anisimov VI, Gunnarsson O. Density-functional calculation of effective Coulomb interactions in metals. Physical Review B. 1991 Apr;43(10):7570–7574.